

**Time-Resolved Photoluminescence  
Spectroscopy of Semiconductors for Optical  
Applications beyond the Visible Spectral Range**

DISSERTATION

zur

Erlangung des Doktorgrades  
der Naturwissenschaften

(Dr. rer. nat.)

dem

Fachbereich Physik  
der Philipps-Universität Marburg



vorgelegt von

**Alexey A. Chernikov**

aus

Sankt-Petersburg

Marburg/Lahn, 2011

Vom Fachbereich Physik der Philipps-Universität Marburg  
als Dissertation angenommen am:

Erstgutachter: Prof. Dr. Martin Koch

Zweitgutachter: Prof. Dr. Stephan W. Koch

Tag der mündlichen Prüfung:



"H: *What is this one?*

R: It's blue light

H: *What does it do?*

R: Turns blue."

John J. Rambo



# Zusammenfassung

Seit der Erfindung der ersten Leuchtdiode (LED) Ende der 1960-er [1, 2], schritt die technologische Entwicklung der Halbleiter-basierten Optoelektronik im Laufe der letzten fünfzig Jahre rapide voran. In der heutigen Zeit werden daher fast alle Aspekte der Lichterzeugung, -Kontrolle und -Detektion durch Halbleiterbauelemente abgedeckt, da sie eine einzigartige Kombination aus Flexibilität, preiswerter Herstellung und kompakter Bauweise bieten. Seit Jahren werden halbleiterbasierte Lichtquellen und Strahlungsdetektoren von Seiten der Industrie erfolgreich in der Materialbearbeitung und Qualitätskontrolle eingesetzt [3]. Zudem profitieren auch wissenschaftliche Anwendungen von der hohen Durchstimmbarkeit und Ausgangsleistung von Halbleiter-Laserdioden sowie von der Empfindlichkeit von Detektoren über einem breiten spektralen Bereich zwischen dem Ultravioletten (UV) und dem Infraroten (IR) [4].

Auch in unserem Alltag sind wir ständig von halbleiterbasierter Technologie umgeben. Diese ist zwar oft subtil integriert und daher auf den ersten Blick kaum bemerkbar, sie bildet jedoch meistens das Herzstück der jeweiligen Anwendung. Prominentestes Beispiel ist sicherlich der CD-Player, der die Vorgängertonträger quasi restlos verdrängt hat. Zusätzlich ermöglichen kompakte Halbleiterlaser den Übertrag von Informationen innerhalb weniger Augenblicke über den gesamten Globus [5], LED-Bildschirme hoher Brillanz sorgen für ein intensives und realitätsnahes Kinoerlebnis [6] und kaum ein Photograph verlässt sich nicht auf hoch-empfindliche Silizium-Detektoren, die sogenannten charge-coupled devices (CCDs) [7], die in fast jeder modernen Kamera integriert sind. Die Entwicklung der CCD wurde im Jahre 2009 sogar mit dem Nobelpreis gewürdigt [8].

Allerdings ist die Erfolgsgeschichte der Halbleitertechnologie damit noch lange nicht vorbei. Aufgrund des stets wachsenden Bedarfes nach energiesparender Beleuchtung, schneller optischer Telekommunikation oder vielseitiger Laserquellen für das wachsende Feld der Biophotonik sowie für die medizinische Anwendungen werden weitere technologische Entwicklungen antizipiert und sogar gefordert. Ziele der Forschung sind u.A. die Entwicklung kompakter, intensiver und verstimmbarer Laser für die NIR und UV Spektralbereiche, effizienter LEDs für die Abdeckung des gesamten sichtbaren Spektrums, transparenter Optoelektronik und Lichtemitter auf der Nanometerskala. Zur Bewältigung dieser und vieler weiterer Herausforderungen sind mehrere Schritte notwendig. Als erstes, bleibt das Verständnis und die korrekte Beschreibung grundlegender physikalischer

Phänomene in Halbleitern für die Realisierung von optischen Bauelementen unerlässlich. Weiterhin ist die Synthese und Charakterisierung neuartiger Materialsysteme für die anvisierten Anwendungen von der zentralen Bedeutung. Schließlich werden auf dieser Basis die eigentlichen Halbleiterbauelemente entwickelt und systematisch optimiert, um das volle Potenzial der Technologie auszuschöpfen sowie ihre fundamentalen Grenzen zu erschließen.

In dieser Arbeit habe ich mich daher mit experimentellen Studien aus drei übergeordneten Bereiche beschäftigt: (1) Untersuchung grundlegender physikalischer Vorgänge, (2) Charakterisierung neuartiger Materialien und (3) Optimierung von Halbleiterlasern. Es versteht sich von selbst, dass nur Teile dieser umfangreichen wissenschaftlichen Gebiete bearbeitet wurden. Für die Bewältigung der Fragestellungen wurde in allen drei Fällen die experimentelle Methode der Photolumineszenz (PL)-Spektroskopie gewählt [9]. Diese Technik basiert auf der Detektion von Lichtemission optisch angeregter Halbleiter. Die angewandte Methode beinhaltet weiterhin spektral-, zeitlich, und orts-aufgelöste Untersuchungen und bietet somit einen flexiblen, vor allem aber einen zerstörungsfreien Zugang zu den optischen Eigenschaften verschiedener Materialsysteme.

Die einzelnen Abschnitte der Arbeit sind wie folgt gegliedert. In dem nachfolgenden Kapitel 2 werden die für die spätere Diskussion relevante PL Eigenschaften von Halbleitern zusammengefasst. Der erste Teil behandelt intrinsische Prozesse in einem idealen direkten Halbleiter inklusive einer kurzen Einführung in die zugrundeliegende Theorie und einer Übersicht der Resultate eines repräsentativen PL Experimentes. In dem zweiten Teil wird die Rolle von Gitterschwingungen, der Einfluss interner elektrischer Felder und der dielektrischen Umgebung sowie die Lumineszenz indirekter Halbleiter diskutiert. Das Kapitel endet mit der Beschreibung extrinsischer PL Eigenschaften wie Defekte und Unordnung in realen Materialien.

Die experimentelle Durchführung spektroskopischer Untersuchungen wird in dem Kapitel 3 dargestellt. Der experimentelle Aufbau für zeitaufgelöste PL wird im Detail erklärt, wobei auf die Beschreibung des verwendeten Lasersystems, der Anordnung für Frequenzmischung und die Funktionsweise einer ultra-schnellen Schmierbildkamera besonderen Wert gelegt wird. Abschließend folgt die Darstellung unterstützender Experimente wie zeitintegrierte PL und lineare Absorption.

In dem Kapitel 4 wird die Wechselwirkung der Ladungsträgern mit den Gitterschwingungen (Phononen) in CdS, CdSe, ZnS und ZnO Volumenmaterial untersucht, welche für das Verständnis der Ladungsträgerdynamik sowie für den Wärmetransport relevant ist. Die experimentellen Studien befassen sich mit den Vielteilcheneffekten in phonon-unterstützter Emission unter der Anwesenheit der Elektron-Elektron Coulomb-Streuung [10]. Der entsprechende theoretische Hintergrund wird in Detail in Kapitel 2 diskutiert. Die Untersuchungen widmen sich den Fragestellungen nach dem möglichen Beitrag von Elektron-

Loch Plasma zu der Licht-Materie Kopplung an den exzitonischen Übergängen und dem Einfluss der Coulomb-Korrelationen auf die Ladungsträger-Phonon Streuung. Der erste Teil dieser Studien liefert einen klaren experimentellen Nachweis für die phonon-assistierte Lumineszenz von Plasma, womit die theoretischen Vorhersagen [11] bestätigt werden. Die exzitonische PL an den entsprechenden Phonon-Übergängen kann damit nicht als Zeichen exzitonischer Besetzung verstanden werden, womit die traditionelle Interpretation der sogenannten Phonon-Seitenbanden korrigiert und erweitert wird. Ferner wird es gezeigt, dass die relativen Beiträge der Exzitonen und Plasma durch die Wahl experimenteller Bedingungen deutlich beeinflusst werden. In dem zweiten Teil des Kapitels wird der Einfluss der Coulomb-Wechselwirkung auf die Stärke der inelastischen Streuung zwischen den Ladungsträgern und Phononen untersucht und mit den Ergebnissen der mikroskopischer Theorie [11] verglichen. Im Rahmen dieser Studien wird gezeigt, dass die Fröhlich-Kopplung im Falle von Exzitonen ineffektiv wird und die Deformationspotential-Streuung sogar in stark polaren Materialien wie ZnO dominieren kann. Interessanterweise ist dies der Fall, obwohl in allen untersuchten Systemen die Wechselwirkung einzelner Ladungsträger mit den Phononen durch die Fröhlich-Kopplung bestimmt wird.

In dem Kapitel 5 werden zeitaufgelöste PL Experimente an neuartigen Materialsystemen, wie ZnO/(ZnMg)O Heterostrukturen, Ga(AsBi) Quantenfilme und GaN Quantendrähte, diskutiert. Sowohl das ZnO/(ZnMg)O System als auch die GaN-Quantendrähte sind vielversprechende Kandidaten für mögliche opto-elektronische Anwendungen im UV Spektralbereich [12, 13]. Auf der anderen Seite, werden die Bi-haltigen Halbleiter auf der GaAs-Basis für mögliche Anwendungen bei den sogenannten Telekom-Wellenlängen von  $1.3 \mu\text{m}$  and  $1.55 \mu\text{m}$  im nah-IR Bereich vorgeschlagen [14]. Die Besonderheit des Materialsystems ist die ungewöhnlich starke Abhängigkeit der Bandlücke von dem Bi-Gehalt, etwa eine Größenordnung höher als in den "üblichen" ternären Verbindungen [15]. Das Ziel der durchgeführten PL Studien an diesen Systemen dient der optischen Charakterisierung der Materialien und dem besseren Verständnis der Ladungsträgerdynamik für einen optimierten Design von Bauelementen.

Die Experimente zeigen deutlich, dass die Lokalisierung von Ladungsträgern die optischen Eigenschaften von einzelnen (ZnMg)O Schichten als auch von ZnO Quantenfilmen stark beeinflusst. Allerdings stellt sich die Relaxation von Elektronen und Löchern aus den (ZnMg)O Barrieren in die ZnO Quantenfilme mit einer Streuzeit kleiner als 3 ps als extrem effizient heraus, trotz der potenziellen Lokalisierung der Ladungsträger in (ZnMg)O. Dieses Ergebnis wird erzielt, indem für eine direkte Beobachtung der Ladungsträgerpopulation der Aufbau der Abschirmung interner elektrischer Felder in den Quantenfilmen ausgenutzt wird. Zusätzlich geben temperaturabhängigen PL Studien einen starken Hinweis darauf, dass die strahlende Rekombination zumindest bei den Gittertem-

peraturen kleiner als 150 K den Ladungsträgerzerfall dominieren kann. Insgesamt sind die experimentellen Befunde für eine mögliche Realisierung von optischen Halbleiterbauelementen im UV Spektralbereich auf der ZnO/(ZnMg)O-Basis vielversprechend, obwohl es sicherlich noch Raum für die Verbesserung der Materialqualität gibt und eine kontrollierte p-Dotierung von ZnO realisiert werden muss. Einerseits ist die schnelle Ladungsträgerrelaxation aus den Barrieren in die Quantenfilme zusammen mit einer potenziell hohen Quanteneffizienz von einem großen Vorteil für den Laserbetrieb, andererseits würden LEDs mit einzelnen aktiven (ZnMg)O-Schichten von der Ladungsträgerlokalisierung stark profitieren. Für die Zukunft sind Messungen der nichtlinearen Absorption und der optischer Verstärkung an ZnO/(ZnMg)O Strukturen geplant, sowie die Entwicklung eines optisch-gepumpten Halbleiterlasers auf der Basis von ZnO Quantenfilmen.

In den zeitaufgelösten Studien von Ga(AsBi), dargestellt in dem zweiten Teil des Kapitels 5, wird ein starker Einfluss der Unordnung auf die optischen Eigenschaften des Halbleiters beobachtet. Sowohl die spektralen Antwort des Materialsystems als auch die Ladungsträgerdynamik werden durch das charakteristische Zusammenspiel von Relaxations- und Rekombinationsprozessen bestimmt. Kinetische Monte-Carlo Simulationen unterstützen die experimentellen Beobachtungen: Für die quantitative Beschreibung der Unordnung wird ein geeignetes Zwei-Skalen-Modell entwickelt, wobei sowohl die örtlichen Fluktuationen der chemischen Zusammensetzung in Ga(AsBi) als auch die Entstehung von Bi-Clustern beachtet werden. Aus dem Vergleich experimenteller Daten mit den Ergebnissen der Simulationen lassen sich die Unordnungsparameter wie Energieskalen und Streuraten bestimmen. Unter anderem wird eine schnelle Migration von Ladungsträgern innerhalb des fluktuierenden Potentials der Bandlücke in dem Gegensatz zu einer wesentlich langsameren Ladungsträger-Diffusion zwischen den einzelnen Bi-Clustern identifiziert. Zusätzlich läuft der Einfang der Ladungsträger in die Bi-Cluster auf der Zeitskala von 5 ps ab. Insgesamt zeigen die Resultate der PL Untersuchungen, dass bei der Interpretation von optischen Eigenschaften von Ga(AsBi) der Einfluss der Unordnung stets beachtet werden muss, zumindest bei dem heutigen Stand der Entwicklung dieser Strukturen. In der nahen Zukunft, abhängig von der Optimierung der Wachstumsparameter und der erfolgreichen Dotierung von Ga(AsBi), wird das Materialsystem sein Potential für optische Anwendungen im nah-IR Spektralbereich unter Beweis stellen müssen.

In dem dritten Teil des Kapitels 5, zeichnen sich in den PL Untersuchungen deutliche Signaturen von den GaN Quantendrähten ab, die aufgrund eines hohen quantenmechanischen Einschluss-Effektes eindeutig identifiziert werden. Aus den Lumineszenzdaten wird somit der Durchmesser der Drähte von einigen wenigen Nanometern abgeschätzt, welcher mit den Befunden der Transmissions-Elektronen-Spektroskopie gut übereinstimmt. Außerdem wird in der PL der Quantendrähte kein Beleg für das Auftreten

interner elektrischer Felder entlang der Ausrichtung der Drähte gefunden, so dass die Licht-Materie Kopplung von der Ladungsträgertrennung nicht beeinflusst wird. Ein weiterer Vorteil des Materialsystems findet sich in der relativ hohen Stabilität der PL Intensität und der Ladungsträgerlebensdauer mit steigender Gittertemperatur. Da sich dieses Material noch in dem Entwicklungsstadium befindet, sollen weitere Studien optischer und struktureller Eigenschaften folgen. Insgesamt bleiben die GaN Quantendrähte ein viel versprechendes System für die Untersuchung quasi-eindimensionaler Strukturen und bieten mannigfaltige Anwendungsmöglichkeiten vor dem Hintergrund der gereiften GaN-Technologie.

In dem Kapitel 6 wird ein oberflächen-emittierender Halbleiterlaser (engl. VECSEL) optimiert und charakterisiert, welcher auf der Basis des etablierten (GaIn)As Materialsystems für die Anwendungen in dem nah-IR Spektralbereich entwickelt wurde. Diese Art von Lasern wird unter Verwendung einer externen Laser-Kavität betrieben [16, 17] und bietet somit eine optimale Kombination aus einer hohen Ausgangsleistung und einem beugungs-limitierten Strahlprofil. Generell sind VECSEL heute verfügbar in einem breiten Spektralbereich der Emissionswellenlänge [18], werden erfolgreich für die Frequenzmischung und -stabilisierung eingesetzt [19, 20] und können auch im gepulsten Regime mit Pulsdauern unter 500 fs betrieben werden [21]. Für den Großteil dieser Anwendungen ist eine hohe Ausgangsleistung notwendig, welche typischerweise durch das Aufheizen des Halbleiterchips begrenzt ist. In dem Rahmen dieser Arbeit werden daher thermische Eigenschaften eines VECSELS studiert und die Verteilung sowie die Abfuhr der Hitze untersucht und optimiert. Durch die entsprechende Verbesserung der Kühlung wird damit eine maximale Laserleistung von über 70 W erreicht. Außerdem wird die laterale Hitzeverteilung in dem VECSEL-Chip während des Laserbetriebes mit Hilfe der orts-aufgelösten PL Spektroskopie studiert. Die Messungen zeigen deutlich, dass die Laserleistung durch den dreidimensionalen Wärmefluss begrenzt bleibt, im Gegensatz zu der häufigen Annahme eines eindimensionalen Wärmetransportes. Auf der Grundlage dieser Untersuchungen sollen weiterführende, komplexere Konzepte für die Kühlung des Halbleitermaterials entwickelt werden. Dennoch stellte sich der VECSEL in der verwendeten Konfiguration als äußerst leistungsfähig und effizient heraus. Damit ist das Lasersystem optimal geeignet sowohl für die Hochleistungsanwendungen als auch für die intrakavitäre Frequenzmischung.

## Literatur

- [1] R. Hall, G. Fenner, J. Kingsley, T. Soltys, and R. Carlson, "Coherent light emission from GaAs junctions", *Physical Review Letters* **9**, 366 (1962).
- [2] N. Holonyak and S. F. Bevacqua, "Coherent (visible) light emission from Ga(AsP) junctions", *Applied Physics Letters* **1**, 82 (1962).
- [3] J. Singh, *Electronic and optoelectronic properties of semiconductor structures* (Cambridge University Press, 2003), 1st ed.
- [4] J. C. Ion, *Laser processing of engineering materials: principle, procedures and industrial applications* (Elsevier Butterworth-Heinemann, 2005).
- [5] M. M. Rao, *Optical communication* (Universities Press, 2000).
- [6] T. K. Hatwar and J. Spindler, "Development of white OLED technology for application in full-color displays and solid-state lighting", in *Luminescent materials and applications*, A. Kitai, ed. (John Wiley & Sons Ltd., 2008).
- [7] W. S. Boyle and G. E. Smith, "Charge coupled semiconductor devices", *Bell Sys. Tech. J.* **49**, 587 (1970).
- [8] [Http://www.nobelprize.org/nobel\\_prizes/physics/laureates/2009/](http://www.nobelprize.org/nobel_prizes/physics/laureates/2009/)
- [9] C. Klingshirn, *Semiconductor Optics* (Springer, 2007) 2nd ed.
- [10] H. Haug and S. W. Koch, *Quantum theory of the optical and electronic properties of semiconductors* (World Scientific, Singapore, 2009), 5th ed.
- [11] T. Feldtmann, "Influence of phonons on semiconductor quantum emission", Ph.D. thesis, Philipps Universität Marburg (2009).
- [12] C. F. Klingshirn, B. K. Meyer, A. Waag, A. Hoffmann, and J. Geurts, *Zinc Oxide*, vol. 120 of *Springer Series in Materials Science* (Springer, 2010).
- [13] S. Nakamura, S. Pearton, and G. Fasol, *The blue laser diode: the complete story* (Springer, 2010).
- [14] K. Oe and H. Okamoto, "New semiconductor alloy GaAsB grown by metal organic vapor phase epitaxy", *Japanese Journal of Applied Physics* **37**, L1283 (1998).
- [15] S. Paul, J. B. Roy, and P. K. Basu, "Empirical expressions for the alloy composition and temperature dependence of the band gap and intrinsic carrier density in GaInAs", **69**, 827 (1991).



- [16] M. Kuznetsov, F. Hakimi, R. Sprague, and A. Mooradian, "High-power ( $>0.5$ W cw) diode-pumped vertical-external-cavity surface-emitting semiconductor lasers with circular TEM<sub>00</sub> beams", *IEEE Phot. Techn. Lett.* **9**, 1063 (1997).
- [17] A. C. Tropper, H. D. Foreman, A. Garnache, K. G. Wilcox, and S. H. Hoogland, "Vertical-external-cavity semiconductor lasers", *Journal of Physics D: Applied Physics* **37**, R75(2004).
- [18] L. Cerutti, A. Garnache, F. Genty, A. Ouvrard, and C. Alibert, "Low threshold, room temperature laser diode pumped Sb-based VECSEL emitting around 2.1 microns", *Electronics Letters* **39**, 290 (2003).
- [19] J. L. A. Chilla, "Blue and green optically pumped semiconductor lasers for display", *Proc. of SPIE* **5740**, 41 (2005).
- [20] M. Holm, D. Burns, A. Ferguson, and M. Dawson, "Actively stabilized single-frequency vertical-external-cavity AlGaAs laser", *IEEE Photonics Technology Letters* **11**, 1551 (1999).
- [21] A. Garnache, S. Hoogland, A. C. Tropper, I. Sagnes, G. Saint-Girons, and J. S. Roberts, "Sub-500-fs soliton-like pulse in a passively mode-locked broadband surface-emitting laser with 100 mW average power", *Applied Physics Letters* **80**, 3892 (2002).
- [22] S. Tixier, M. Adamcyk, T. Tiedje, S. Francoeur, A. Mascarenhas, P. Wei, and F. Schiettekatte, "Molecular beam epitaxy growth of GaAsBi", *Applied Physics Letters* **82**, 2245 (2003).
- [23] S. Baranovskii, R. Eichmann, and P. Thomas, "Temperature-dependent exciton luminescence in quantum wells by computer simulation", *Physical Review B* **58**, 13081 (1998).



# Contents

<b>1</b>	<b>Introduction</b>	<b>1</b>
<b>2</b>	<b>Photoluminescence spectroscopy</b>	<b>5</b>
2.1	Intrinsic photoluminescence properties of direct-gap semiconductors . . .	6
2.1.1	Microscopic theory of luminescence . . . . .	6
2.1.2	Photoluminescence of an ideal quantum-well structure . . . . .	15
2.1.3	Influence of dimensionality . . . . .	26
2.2	Role of phonons, internal fields, and the dielectric environment . . . . .	31
2.2.1	Phonon-assisted emission . . . . .	31
2.2.2	Internal electric fields . . . . .	42
2.2.3	Influence of the dielectric environment . . . . .	45
2.2.4	Impact of the band structure . . . . .	47
2.3	Extrinsic photoluminescence properties: defects and disorder . . . . .	50
2.3.1	Defects . . . . .	50
2.3.2	Disorder . . . . .	57
<b>3</b>	<b>Experimentals</b>	<b>65</b>
3.1	Time-resolved photoluminescence . . . . .	65
3.2	Linear absorption and continuous-wave photoluminescence . . . . .	71
<b>4</b>	<b>Role of the Coulomb-interaction in phonon-assisted emission</b>	<b>73</b>
4.1	Luminescence sources: plasma contributions . . . . .	73
4.1.1	Material systems . . . . .	73
4.1.2	Resonant vs. non-resonant excitation . . . . .	77
4.1.3	Excitation power dependence: the Mott-transition . . . . .	78
4.2	Interaction mechanisms: Fröhlich vs. deformation potential scattering . .	82
4.2.1	Material systems . . . . .	83
4.2.2	Analysis of phonon-sideband ratios . . . . .	84
<b>5</b>	<b>Ultra-fast luminescence studies of novel semiconductor material systems</b>	<b>89</b>
5.1	Carrier dynamics in ZnO/(ZnMg)O heterostructures . . . . .	89
5.1.1	Carrier localization in (ZnMg)O layers . . . . .	91

## Contents

5.1.2	Screening of the internal-fields as a probe for carrier populations . . . . .	97
5.1.3	Recombination processes in ZnO quantum wells . . . . .	108
5.2	Ga(AsBi): carrier localization and phonon-coupling . . . . .	114
5.2.1	Carrier localization . . . . .	115
5.2.2	Carrier-phonon coupling . . . . .	122
5.3	GaN quantum wires: confinement in a quasi 1D-system . . . . .	126
5.3.1	Carrier confinement . . . . .	128
5.3.2	Influence of the excitation density and the lattice temperature . . . . .	130
5.3.3	Impact of the growth temperature . . . . .	132
<b>6</b>	<b>Vertical-external-cavity surface-emitting lasers for NIR applications</b>	<b>135</b>
6.1	VECSEL Setup . . . . .	136
6.2	Device characterization: cooling concepts and high power operation . . . . .	137
6.2.1	Heat spread . . . . .	137
6.2.2	Heat removal . . . . .	139
6.2.3	Power scaling . . . . .	141
6.3	Study of spatial temperature distribution via PL spectroscopy . . . . .	143
<b>7</b>	<b>Summary and conclusions</b>	<b>149</b>
	<b>Appendix</b>	<b>153</b>
1	Photon density calculator . . . . .	153
2	Decay-time extraction algorithm . . . . .	155

## List of Abbreviations

<b>BBO</b>	Bismut triborate
<b>CW</b>	Continuous-wave
<b>DAP</b>	Donor-acceptor-pair (transition)
<b>DBR</b>	Distributed Bragg reflector
<b>DOS</b>	Density of states
<b>EM</b>	Electro-magnetic
<b>FWHM</b>	Full-width-at-half-maximum
<b>He:Ne</b>	Helium-neon (laser)
<b>IR</b>	Infra-red (spectral range)
<b>LBO</b>	Lithium triborate
<b>LED</b>	Light-emitting diode
<b>Nd:YAG</b>	Neodymium doped yttrium-aluminum-garnet (laser)
<b>NIR</b>	Near infra-red (spectral range)
<b>NA</b>	Numerical aperture
<b>QCSE</b>	Quantum-confined Stark effect
<b>QW</b>	Quantum well
<b>QWires</b>	Quantum wires
<b>OSA</b>	Optical spectrum analyzer
<b>PL</b>	Photoluminescence
<b>PSB</b>	Phonon-sideband
<b>SBE</b>	Semiconductor Bloch equations
<b>SH</b>	Second harmonic
<b>SLE</b>	Semiconductor luminescence equations
<b>SRH</b>	Shockley-Read-Hall (recombination)
<b>Ti:Sa</b>	Titanium-sapphire (laser)
<b>TH</b>	Third harmonic
<b>TRPL</b>	Time-resolved photoluminescence
<b>UV</b>	Ultra-violet (spectral range)
<b>VECSEL</b>	Vertical-external-cavity surface-emitting laser
<b>VIS</b>	Visible (spectral range)



# List of Figures

2.1	Schematic illustration of PL in a semiconductor . . . . .	5
2.2	Calculated PL spectra with and without excitonic population . . . . .	14
2.3	Illustration of different excitation schemes . . . . .	16
2.4	Carrier relaxation after quasi-resonant excitation . . . . .	18
2.5	PL spectra after quasi-resonant excitation . . . . .	19
2.6	PL spectra at different excitation densities and lattice temperatures . . . . .	20
2.7	Characteristic transient PL from excitons and plasma . . . . .	22
2.8	Recombination of excitons . . . . .	23
2.9	Illustration of Auger-recombination . . . . .	25
2.10	Schematic absorption spectrum of a bulk crystal . . . . .	27
2.11	Influence of polariton formation . . . . .	28
2.12	Schematic absorption spectrum of a quantum well . . . . .	29
2.13	Schematic absorption spectrum of a quantum wire . . . . .	30
2.14	Schematic absorption spectrum of a quantum wire . . . . .	31
2.15	Illustration of phonon-assisted luminescence process . . . . .	32
2.16	Phonon-assisted emission from localized and free carriers . . . . .	37
2.17	Phonon-assisted emission from excitons and plasma . . . . .	38
2.18	Electron-phonon interaction mechanisms . . . . .	39
2.19	Momentum dependence of Fröhlich and deformation potential scattering . . . . .	40
2.20	Fröhlich-scattering in presence of carrier-carrier Coulomb-interaction . . . . .	41
2.21	Temperature dependence of $PSB_2/PSB_1$ ratio . . . . .	42
2.22	Quantum-confined Stark effect . . . . .	43
2.23	Influence of QCSE on PL dynamics . . . . .	44
2.24	Emission of a QW inside a dielectric structure . . . . .	46
2.25	Illustration of polarization selection rules . . . . .	48
2.26	Influence of the indirect band-structure on PL emission . . . . .	49
2.27	Overview of the different types of point-defects . . . . .	51
2.28	Typical energy levels of point-defects . . . . .	52
2.29	Exemplary emission spectrum of defects and impurities in a semiconductor . . . . .	53
2.30	Donor-acceptor-pair recombination . . . . .	54
2.31	Non-radiative recombination in power- and temperature-dependent PL . . . . .	56

*List of Figures*

2.32	Influence of disorder on the absorption and emission spectra . . . . .	57
2.33	Influence of relaxation processes on the Stokes-shift . . . . .	58
2.34	Typical luminescence spectrum of a disordered semiconductor . . . . .	59
2.35	Influence of excitation power on the PL from a disordered semiconductor . . . . .	60
2.36	Influence of the temperature on the PL from a disordered semiconductor . . . . .	61
3.1	Time-resolved photoluminescence setup . . . . .	65
3.2	Frequency-tripler layout . . . . .	66
3.3	Spectral response of the streak camera . . . . .	68
3.4	Operation principle of a streak camera . . . . .	69
3.5	Exemplary streak camera image . . . . .	70
3.6	Formation of a PL transient in a streak camera . . . . .	71
3.7	Absorption and photoluminescence setup . . . . .	72
4.1	Emission spectra of bulk CdS and CdSe samples . . . . .	74
4.2	Polarization resolved spectra of the CdS bulk sample . . . . .	75
4.3	Temperature-dependent TRPL data of the CdS bulk sample . . . . .	76
4.4	PL of the CdS sample for resonant and non-resonant excitation . . . . .	77
4.5	Transients of the CdS and CdSe samples as function of the excitation density . . . . .	79
4.6	Relative change of the excitons-plasma ratio as function of excitation density . . . . .	80
4.7	Carrier density scaling of the plasma emission in the CdS sample . . . . .	81
4.8	Emission spectra of bulk ZnO, ZnS, and CdS samples . . . . .	84
4.9	PL spectra of the first two sidebands of CdS and ZnO . . . . .	85
4.10	Different evaluation procedures of relative PSB intensities . . . . .	86
4.11	PSB <sub>2</sub> /PSB <sub>1</sub> ratios of ZnO, ZnS, and CdS as function of temperature . . . . .	87
4.12	PSB <sub>2</sub> /PSB <sub>1</sub> ratios of ZnO and CdS as function of the excitation density . . . . .	88
5.1	Exemplary time-resolved data of a ZnO QW . . . . .	90
5.2	Temperature-dependent emission from the (ZnMg)O layers . . . . .	92
5.3	Temperature-dependent PL transients of the (ZnMg)O layers . . . . .	93
5.4	Temperature-dependent PL decay times of the (ZnMg)O layers . . . . .	94
5.5	PL intensity of the (ZnMg)O samples as function of temperature . . . . .	95
5.6	Analysis of the emission energy-dependent PL decay times . . . . .	96
5.7	PL spectra and transients of ZnO/(Zn <sub>0.8</sub> Mg <sub>0.2</sub> )O QWs . . . . .	98
5.8	PL properties as function of the QW width . . . . .	99
5.9	Strength of the carrier-phonon interaction for varying QW widths . . . . .	100
5.10	PL properties of the ZnO/(Zn <sub>0.8</sub> Mg <sub>0.2</sub> )O QW as function of temperature . . . . .	102
5.11	Energy intervals between the ZPL, PSB <sub>1</sub> and PSB <sub>2</sub> in ZnO . . . . .	103
5.12	Transient PL spectra of a ZnO/(Zn <sub>0.8</sub> Mg <sub>0.2</sub> )O QW . . . . .	104
5.13	PL properties a ZnO/(Zn <sub>0.8</sub> Mg <sub>0.2</sub> )O QW as function of the excitation density . . . . .	105



5.14	Evolution of screening in a ZnO/(Zn <sub>0.8</sub> Mg <sub>0.2</sub> )O QW sample . . . . .	106
5.15	Transient PL properties of a ZnO/(Zn <sub>0.8</sub> Mg <sub>0.2</sub> )O QW . . . . .	107
5.16	PL spectra of a QCSE-free QW sample as function of temperature . . . . .	108
5.17	PSB <sub>1</sub> - ZPL energy spacing in the ZnO/(Zn <sub>0.9</sub> Mg <sub>0.1</sub> )O QW sample . . . . .	110
5.18	Low-temperature TRPL data for homo- and heteroepitaxial ZnO QWs . . . . .	111
5.19	Temperature-dependent TRPL data of homo- and heteroepitaxial ZnO QWs . . . . .	112
5.20	Absorption and emission data from the Ga(AsBi) sample . . . . .	116
5.21	Two-scale carrier hopping model . . . . .	117
5.22	Experimental and simulated Stokes shift and FWHM of the PL . . . . .	118
5.23	Experimental and simulated PL intensity as function of temperature . . . . .	119
5.24	Time-integrated PL spectrum of the Ga(AsBi) sample at T = 10 K . . . . .	120
5.25	Measured and simulated TRPL data of the Ga(AsBi) sample at T = 10 K . . . . .	121
5.26	PL decay time of the Ga(AsBi) sample as function of the emission energy . . . . .	122
5.27	Spectra of the two Ga(AsBi) QWs at T = 10 K . . . . .	123
5.28	Temperature-dependent PL spectra of the Ga(As <sub>0.989</sub> Bi <sub>0.011</sub> ) QW . . . . .	124
5.29	Excitation density-dependent PL spectra of the Ga(As <sub>0.989</sub> Bi <sub>0.011</sub> ) QW . . . . .	125
5.30	Sample structure and TEM images of GaN quantum wire structures . . . . .	127
5.31	Exemplary streak image of a GaN QWires sample . . . . .	128
5.32	Decay time of the GaN QWires PL as function of the emission energy . . . . .	129
5.33	TRPL data of the GaN QWires as function of the excitation density . . . . .	130
5.34	TRPL data of the GaN QWires as function of the lattice temperature . . . . .	131
5.35	TRPL data of the GaN QWires as function of the growth temperature . . . . .	132
5.36	PL properties of GaN QWires as function of the growth temperature . . . . .	133
6.1	Illustration of a basic VECSEL design . . . . .	136
6.2	Study of the heat spreading concepts for the VECSEL device . . . . .	138
6.3	Comparison of two heat removal concepts for the VECSEL device . . . . .	140
6.4	Study of power scaling of the VECSEL device . . . . .	141
6.5	Study of power scaling of the VECSEL device . . . . .	142
6.6	Study of power scaling of the VECSEL device . . . . .	143
6.7	Setup scheme for spatially resolved PL measurements of the VECSEL . . . . .	144
6.8	Exemplary PL spectrum during the VECSEL operation . . . . .	145
6.9	Spatially resolved chip temperature for different pump profiles . . . . .	146
6.10	Spatially resolved chip temperature for different pump spot sizes . . . . .	147



# 1 Introduction

Since the development of the first light-emitting diodes (LEDs) in the early 1960's [1, 2], opto-electronic technology based on the semiconducting materials evolved rapidly in the last half of the century. Today, barely all aspects of the generation, control, and detection of light are potentially covered by the solid-state semiconductor devices. The reason is a unique combination of flexibility, low-cost fabrication, as well as compact packaging dimensions. In particular, scientific applications profit from the large tunability of the semiconductor diodes and lasers as well as from the high sensitivity of the detectors in a broad spectral range from the ultra-violet (UV) to the infra-red (IR) [4]. In addition, numerous industry branches successfully exploit solid-state light-sources for material processing, characterization, and quality testing [3]. Finally, the semiconductor-based emitters and detectors have already found their way into the everyday's life. In many cases, the technology is subtly integrated and barely noticeable, yet it is often the heart of the respective applications. High-brilliance LEDs provide images for the television projectors [6], compact lasers ensure rapid optical communication [5], and almost every photographer relies on cameras with silicon-based detectors, the so-called charge-coupled-devices or CCDs [7], only to name a few. Notably, the invention of the latter was honored with the Nobel Prize in Physics in 2009 [8].

Still, the journey is far from being over. The ever-increasing need for energy-saving lighting, faster optical communication, as well as for versatile optical sources in the growing field of the bio-physics anticipates and almost demands further technological advance. The research is aimed towards compact and low-cost lasers with high repetition rates in the near-infra-red (NIR) spectral range, bright, more efficient LEDs over the complete visible (VIS) spectrum, as well as strong and tunable lasers emitting in the ultra-violet (UV) wavelength region. In addition, transparent opto-electronic devices as well as the light-emitters on a scale as small as several nanometers are envisioned.

To address these challenges, several steps are to be taken. First, a detailed understanding of the fundamental phenomena in semiconductors is required for a proper design of optical devices. The second, equally important procedure is the synthesis and the characterization of novel material systems suited for the desired applications over a broad spectral range. On this basis, semiconductor devices are finally developed and optimized to exploit their respective potential as well as to identify any fundamental restrictions.

## 1 Introduction

The work discussed in this thesis is focused on the experimental studies regarding these three steps: (1) investigation of the fundamental effects, (2) characterization of new material systems, and (3) optimization of the semiconductor devices. It goes without saying that only parts of the broad scientific fields are addressed. In all three cases, the experimental technique of choice is *photoluminescence (PL) spectroscopy* [9]. This method is based on the detection of light emitted by the photo-excited materials. Considering the possibility of spectrally-, temporally- and spatially-resolved measurements, PL spectroscopy remains a flexible and, most-important, a non-destructive probe for the optical response of semiconductors.

The thesis is organized as follows. Chapter 2 gives a summary of the PL properties of semiconductors relevant for this work. The first section deals with the intrinsic processes in an ideal direct band gap material, starting with a brief summary of the theoretical background followed by the overview of a typical PL scenario. In the second part of the chapter, the role of the lattice-vibrations, the internal electric fields as well as the influence of the band-structure and the dielectric environment are discussed. Finally, extrinsic PL properties are presented in the third section, focusing on defects and disorder in real materials.

In chapter 3, the experimental realization of the spectroscopic studies is discussed. The time-resolved photoluminescence (TRPL) setup is presented, focusing on the applied excitation source, non-linear frequency mixing, and the operation of the streak camera used for the detection. In addition, linear spectroscopy setup for continuous-wave (CW) PL and absorption measurements is illustrated.

Chapter 4 aims at the study of the interactions between electrons and lattice-vibrations in semiconductor crystals relevant for the proper description of carrier dynamics as well as the heat-transfer processes. The presented discussion covers the experimental studies of many-body effects in phonon-assisted emission of semiconductors due to the carrier-carrier Coulomb-interaction [10, 11]. The corresponding theoretical background is discussed in detail in chapter 2. The investigations are focused on the two main questions regarding electron-hole plasma contributions to the phonon-assisted light-matter interaction as well as the impact of Coulomb-correlations on the carrier-phonon scattering.

The experiments presented in chapter 5 deal with the characterization of recently synthesized material systems: ZnO/(ZnMg)O heterostructures, GaN quantum wires (QWires), as well as (GaAs)Bi quantum wells (QWs). The former two materials are designed for potential electro-optical applications in the UV spectral range [12, 13]. TRPL spectroscopy is applied to gain insight as well as a better understanding of the respective carrier relaxation and recombination processes crucial for the device operation. The latter material system, Ga(AsBi), is a possible candidate for light-emitting devices in the NIR, at the telecom wavelengths of  $1.3\ \mu\text{m}$  and  $1.55\ \mu\text{m}$  [14]. The main hallmark of this semiconduc-

tor is the giant band gap reduction with Bi content [22], unusually large for more typical compound materials [15]. The aim of the studies is the systematic investigation of carrier dynamics influenced by disorder. The measurements are supported by kinetic Monte-Carlo simulations [23], providing a quantitative analysis of carrier localization effects.

In chapter 6, optimization and characterization studies of semiconductor lasers, based on the well-studied (GaIn)As material system designed for NIR applications, are performed. The device under investigation is the so-called *vertical-external-cavity surface-emitting laser* (VECSEL) [16, 17]. This laser perfectly combines the excellent beam quality of surface emitters and the high output power of semiconductor edge-emitting diode-lasers. VECSELs are available in a broad spectral range [18], offer efficient intra-cavity frequency mixing [19] combined with frequency stabilization [20], and are able to operate in a pulsed regime, emitting ultra-short sub-500 fs pulses [21]. For the majority of the applications high output power of the device remains crucial. The performance of the laser, however, is typically limited by the heating of the device during the operation. The experiments focus on the study of the thermal properties of a high-power VECSEL. The distribution and removal of the excess heat as well as the optimization of the laser for increased performance are addressed applying different heat-spreading and heat-transfer approaches. Based on these investigations, the possibility for power-scaling is evaluated and the underlying restrictions are analyzed. The latter investigations are performed applying spatially-resolved PL spectroscopy. An experimental setup is designed for monitoring the spatial distribution of heat in the semiconductor structure during laser operation.

A brief summary of the experimental findings and the resulting conclusions are given in the chapter 7 in the end of the thesis.



## 2 Photoluminescence spectroscopy

This chapter presents a summary of the PL properties of semiconductors, relevant for this thesis. A simplified picture of the PL process is given in Fig. 2.1 prior to a more detailed discussion. A basic description is also found in standard text-books on semiconductor optics, e.g., in Ref. [9]. The band structure of a semiconductor in the vicinity of the band gap is represented by two parabolic bands in the reciprocal space. In a typical PL experiment, the semiconductor is excited by a light-source that provides photons with an energy larger than the energy of the band gap. The incoming photons are absorbed, creating electrons and holes with finite momenta  $\mathbf{k}$  in the conduction and valence bands, respectively. The excitation process is then followed by energy and momentum relaxation of the charge-carriers towards the band gap minimum. Finally, the electrons recombine with holes under emission of photons. The latter process is called luminescence or more specifically - PL when the carriers are created by photoexcitation.

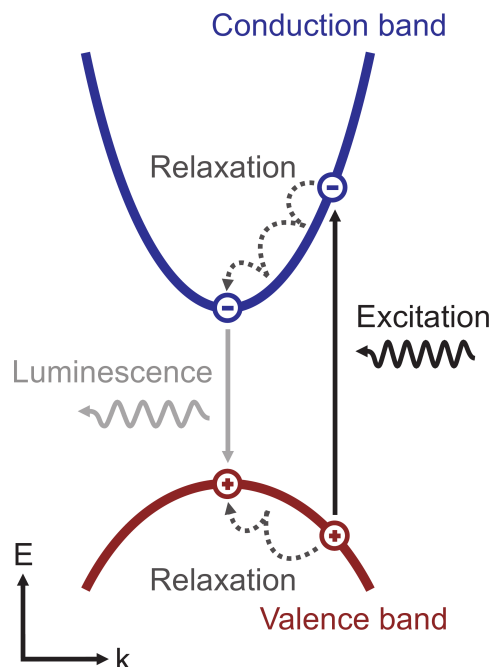


Figure 2.1: Schematic illustration of PL in a semiconductor

Despite the fact that PL is easily observed in most semiconductor materials, a proper theoretical description is generally a challenging task. Already an ideal, defect-free semi-

conductor is a complex many-body system of interacting charge-carriers, lattice vibrations, i.e., phonons, as well as photons, when light-matter coupling is considered. The PL properties are also extremely sensitive to the presence of internal electric fields and to the specifics of the dielectric environment which imposes further complexity. In addition, real material systems incorporate defects in the lattice structure and chemical composition as well as spatial fluctuations of material parameters, i.e., disorder. The treatment of both defects and disorder is extremely challenging for a microscopic theory. In most cases, the main issue is the lack of detailed knowledge regarding the perturbations of an ideal crystal structure. Thus, the influence of the extrinsic effects on the PL is usually addressed phenomenologically.

For all these reasons, it is useful to start with the description of the most fundamental PL properties in an ideal system. The first section thus deals with the intrinsic processes regarding photoexcitation and luminescence in direct band gap materials. It starts with a brief summary of the theoretical background, focused on the influence of the Coulomb-interaction. The latter is inevitable for a proper treatment of the many-particle system of an excited semiconductor. Then, an overview of the complete PL scenario is given using a quasi-two-dimensional structure as an exemplary system; the influence of dimensionality is covered in the end of the section. Here, the illustration of the relevant phenomena is based on the results of the microscopic theory, yet the discussion is kept on a phenomenological level for a better legibility and brevity. In the second part of the chapter, the role of phonons, internal electric fields, as well as the influence of the band-structure and dielectric environment are discussed. Finally, extrinsic PL properties are presented in the third section, focusing on defects and disorder in real materials.

## 2.1 Intrinsic photoluminescence properties of direct-gap semiconductors

### 2.1.1 Microscopic theory of luminescence

#### System Hamiltonian

This subsection presents a brief introduction to the theoretical approach for the microscopic description of the PL in an ideal, direct semiconductor. A detailed derivation and a complete explanation of the involved calculations are found in Refs. [10, 24, 25, 26]. In the overall discussion, the reader is further referred to the standard text-books, like [27, 28], for the general properties of semiconductors as well as the fundamentals of quantum-mechanics.

The interacting many body-system of a defect-free semiconductor crystal coupled to a



## 2.1 Intrinsic photoluminescence properties of direct-gap semiconductors

light-field is represented by the following Hamilton-operator in the second quantization formalism:

$$H = H_{\text{el}} + H_{\text{vib}} + H_{\text{em}} + H_{\text{el-el}} + H_{\text{el-vib}} + H_{\text{el-em}} \quad (2.1)$$

The first three terms describe single-particle contributions: free electrons ( $H_{\text{el}}$ ), lattice vibrations ( $H_{\text{vib}}$ ), and photons, i.e., quantized electro-magnetic field ( $H_{\text{em}}$ ). The last three terms contain the interactions: electron-electron scattering via Coulomb-interaction ( $H_{\text{el-el}}$ ), coupling between electrons and lattice vibrations ( $H_{\text{el-vib}}$ ), as well as light-matter interaction ( $H_{\text{el-em}}$ ). The Hamiltonian  $H_{\text{el}}$  of the non-interacting part accounts for the free charge-carriers:

$$H_{\text{el}} = \sum_{\lambda\mathbf{k}} \varepsilon_{\lambda\mathbf{k}} a_{\lambda\mathbf{k}}^\dagger a_{\lambda\mathbf{k}}. \quad (2.2)$$

Here,  $a_{\mathbf{k}}^\dagger$  and  $a_{\mathbf{k}}$  are the fermionic creation and annihilation operators, respectively, for both electrons and holes. The particle quasi-momentum  $k$  is merged with the spin quantum number  $\sigma$  to  $\mathbf{k} = \{k, \sigma\}$ . The index  $\lambda$  denotes individual band or subband index and can be further simplified to  $\lambda = \text{c}$  or  $\lambda = \text{v}$  in a two-band approximation, when conduction (c) or valence bands (v) are considered. The energy of the particle state corresponding to  $\mathbf{k}$  is given by  $\varepsilon_{\mathbf{k}}$ . This quantity summarizes the influence of the band-structure obtained by, e.g.,  $\mathbf{k}\cdot\mathbf{p}$  multi-band calculations.

The quantized lattice-vibrations field in harmonic approximation is described by the second Hamiltonian:

$$H_{\text{vib}} = \sum_{\mathbf{p}} \hbar\Omega_{\mathbf{p}} \left( D_{\mathbf{p}}^\dagger D_{\mathbf{p}} + \frac{1}{2} \right), \quad (2.3)$$

with the bosonic phonon-creation and -annihilation operators  $D_{\mathbf{p}}^\dagger$  and  $D_{\mathbf{p}}$ , respectively. Again, the quasi-momentum  $p$  and number of the phonon branch  $\alpha$  are merged to  $\mathbf{p} = \{p, \alpha\}$ .  $\hbar\Omega_{\mathbf{p}}$  denotes the phonon energy according to the dispersion-relation of the corresponding branch.

The electro-magnetic (EM) field is included in the last operator of the non-interacting part,  $H_{\text{em}}$ . Here, it is important to stress that only fully quantized radiation field should be used for the description of the PL. The reason for that is given in the following brief discussion. It requires, however, some anticipation of the theoretical results. When coherent phenomena like linear reflection or transmission are considered, it is sufficient to treat light in the classical picture, i.e., as an EM wave. According to Maxwell's equations, the EM field couples to the polarization in the material. On the other hand, the coherent polarization is usually zero in a typical PL experiment under pulsed excitation conditions, and only an incoherent population of electrons and holes is present in the sys-

## 2 Photoluminescence spectroscopy

tem. The latter, however, does not couple directly to classical fields and thus can not act as a source of incoherent spontaneous emission, i.e., the PL. Therefore, the radiation field has to be treated fully quantum-mechanically with photons as quasi-particles. In this case, the corresponding Hamiltonian obtains the following form, analogous to the description of phonons:

$$H_{\text{em}} = \sum_{\mathbf{q}} \hbar\omega_{\mathbf{q}} \left( B_{\mathbf{q}}^{\dagger} B_{\mathbf{q}} + \frac{1}{2} \right). \quad (2.4)$$

The bosonic operators  $B_{\mathbf{q}}^{\dagger}$  and  $B_{\mathbf{q}}$  create and annihilate photons, respectively.  $\mathbf{q} = \{q, \pi\}$  summarizes the wavenumber  $q$  and polarization  $\pi$  of a photon. The well-known dispersion relation determines the photon energy  $\omega_{\mathbf{q}} = cq$ , with  $c$  denoting the speed of light.

The first Hamiltonian of the interacting part describes the Coulomb-scattering between the charge-carriers:

$$H_{\text{el-el}} = \sum_{\lambda\lambda' \mathbf{k}\mathbf{k}' \Delta\mathbf{k}} V_{\Delta\mathbf{k}} a_{\lambda\mathbf{k}}^{\dagger} a_{\lambda'\mathbf{k}'}^{\dagger} a_{\lambda'\mathbf{k}'+\Delta\mathbf{k}} a_{\lambda\mathbf{k}-\Delta\mathbf{k}}. \quad (2.5)$$

Here, the particles in the initial states  $\{\lambda, \mathbf{k} - \Delta\mathbf{k}\}$  and  $\{\lambda', \mathbf{k}' + \Delta\mathbf{k}\}$  scatter to the final states  $\{\lambda, \mathbf{k}\}$  and  $\{\lambda', \mathbf{k}'\}$  under the transfer of momentum  $\Delta\mathbf{k}$ . The strength of the interaction is given by the Coulomb matrix-element  $V_{\Delta\mathbf{k}}$  which is proportional to  $\Delta\mathbf{k}^{-2}$  and independent of the band-indices  $\lambda$  and  $\lambda'$ .

The second operator  $H_{\text{el-vib}}$  accounts for the electron-phonon coupling:

$$H_{\text{el-vib}} = \sum_{\lambda\mathbf{k}\mathbf{p}} \hbar\Omega_{\mathbf{p}} g_{\lambda\mathbf{p}} a_{\lambda\mathbf{k}-\mathbf{p}}^{\dagger} a_{\lambda\mathbf{k}} \left( D_{-\mathbf{p}} + D_{\mathbf{p}}^{\dagger} \right). \quad (2.6)$$

An electron or a hole is scattered between the states  $\{\lambda, \mathbf{k}\}$  and  $\{\lambda, \mathbf{k} - \mathbf{p}\}$  under the emission ( $D_{\mathbf{p}}^{\dagger}$ ) or absorption ( $D_{-\mathbf{p}}$ ) of a phonon. The momentum  $\mathbf{p}$  is transferred from the electronic system to the phonon bath during this process.  $\hbar\Omega_{\mathbf{p}}$  is the phonon energy and  $g_{\lambda\mathbf{p}}$  denotes the electron-phonon interaction strength. The influence of  $\lambda$  and  $\mathbf{p}$  on  $g_{\lambda\mathbf{p}}$  varies strongly for different coupling mechanisms; the latter are discussed in section 2.2.1 in more detail.

Finally, the light-matter interaction is described by:

$$H_{\text{el-em}} = - \sum_{\mathbf{k}\mathbf{q}} i \left( \mathcal{F}_{\mathbf{q}} a_{c\mathbf{k}+\mathbf{q}}^{\dagger} a_{v\mathbf{k}} + \mathcal{F}_{\mathbf{q}}^* a_{v\mathbf{k}}^{\dagger} a_{c\mathbf{k}-\mathbf{q}} \right) B_{\mathbf{q}} + H.C. \quad (2.7)$$

An electron and a hole are created or annihilated under emission or absorption of a photon. The momentum  $\mathbf{q}$  is transferred between the EM field and the electron-hole system. In most cases,  $\mathbf{q}$  is extremely small compared to the quasi-impulse  $\mathbf{k}$  of the

## 2.1 Intrinsic photoluminescence properties of direct-gap semiconductors

charge-carriers. The strength of the light-matter coupling is defined by  $\mathcal{F}_q$  which depends on the dipole-mediated overlap of the electron and hole wavefunctions. H.C. denotes the Hermitian-conjugated part of the operator.

### Equations of motion approach

In general, the physically meaningful properties of the system are always traced down to the expectation values  $\langle O \rangle$  of the quantum-mechanical operators  $O$ . The latter can be classified as N-particle operators  $O_N$ , according to:

$$O_N = B_1^\dagger \dots B_{N_1}^\dagger a_1^\dagger \dots a_{N_2}^\dagger a_{N_2} \dots a_1 B_{N_3} \dots B_1, \quad (2.8)$$

with

$$N = N_1 + N_2 + N_3, \quad (2.9)$$

as well as the bosonic and the fermionic operators  $B_i^\dagger$  and  $a_j^\dagger$ , respectively. Thus, from a purely formal point of view, a single bosonic operator and also a pair of fermionic operators are both considered single-particle quantities. The expectation value of an arbitrary operator  $O_N$  is obtained by calculating the trace  $\langle O_N \rangle = \text{Tr}[O_N \rho]$ , where  $\rho$  is the statistical operator of the system. The dynamics of  $O_N$  are derived applying the Heisenberg equation of motion:

$$i\hbar \frac{\partial}{\partial t} O_N = [O_N, H]. \quad (2.10)$$

However, since the system Hamiltonian is not only composed of single-particle but also of two-particle operators, the expectation value  $\langle O_N \rangle$  couples to the expectation values of N- and (N+1)-particle operators:

$$i \frac{\partial}{\partial t} \langle O_N \rangle = T[\langle N \rangle] + V[\langle N + 1 \rangle]. \quad (2.11)$$

Here, the functionals T and V mainly result from the non-interacting and interacting parts of the Hamiltonian  $H$ , respectively. This coupling leads to an infinite hierarchy of equations with all possible combinations and orders of operators. Thus, a consistent approximation must be applied to obtain a closed equations set. For this purpose, a systematic truncation scheme within the so-called cluster expansion approach is used [29].

## 2 Photoluminescence spectroscopy

### Cluster expansion

The method of cluster expansion is based on consistent factorization of an N-particle quantity  $\langle N \rangle$  into products of: (i) independent single-particle operators or singlets  $\langle 1 \rangle$ , (ii) purely correlated pairs or doublets  $\Delta \langle 2 \rangle$ , as well as (iii) three- (triplets) and up to N-particle clusters  $\Delta \langle N \rangle$ :

$$\langle N \rangle = \langle N \rangle_S + \langle N - 2 \rangle \Delta \langle 2 \rangle + \langle N - 3 \rangle \langle 1 \rangle \Delta \langle 2 \rangle + \cdots + \Delta \langle N \rangle. \quad (2.12)$$

As an example, a three-particle expectation value is decomposed according to this scheme into:

$$\langle 3 \rangle = \langle 3 \rangle_S + \langle 3 \rangle_D + \langle 3 \rangle_T \quad (2.13)$$

with the singlet part  $\langle 3 \rangle_S$  as products of singlets

$$\langle 3 \rangle_S = \sum \langle 1 \rangle \langle 1 \rangle \langle 1 \rangle, \quad (2.14)$$

the doublet containing part  $\langle 2 \rangle_S$  as products of singlets and doublets

$$\langle 3 \rangle_D = \sum \langle 1 \rangle \Delta \langle 2 \rangle, \quad (2.15)$$

and the triplet contribution with pure three-particle correlations:

$$\langle 3 \rangle_T = \sum \Delta \langle 3 \rangle. \quad (2.16)$$

Every part incorporates all possible permutations of the operators up to the corresponding order as well as sign changes. This factorization scheme now allows a consistent truncation up to an arbitrary cluster-order N, when the pure correlations  $\Delta \langle N + 1 \rangle$  are neglected. In the example shown above, a three-particle expectation value, approximated up to the second order, yields:

$$\langle 3 \rangle \approx \langle 3 \rangle_S + \langle 3 \rangle_D = \sum \langle 1 \rangle \langle 1 \rangle \langle 1 \rangle + \sum \langle 1 \rangle \Delta \langle 2 \rangle. \quad (2.17)$$

The truncation of the factorized operators is applied to the hierarchy of Heisenberg equations of motion, see eq. (2.10) and (2.11). Again, as an example, a singlet-doublet approximation leads to the following set of equations for an arbitrary single-particle expectation value  $\langle O_1 \rangle$ :

## 2.1 Intrinsic photoluminescence properties of direct-gap semiconductors

$$i\hbar \frac{\partial}{\partial t} \langle O_1 \rangle = T_1[\langle 1 \rangle] + V_1[\langle 2 \rangle_S] + V_1[\Delta \langle 2 \rangle] \quad (2.18)$$

$$i\hbar \frac{\partial}{\partial t} \Delta \langle 2 \rangle = T_2[\Delta \langle 2 \rangle] + V_2[\langle 3 \rangle] \approx T_2[\Delta \langle 2 \rangle] + V_2[\langle 3 \rangle_S + \langle 3 \rangle_D], \quad (2.19)$$

where  $T_{1,2}$  and  $V_{1,2}$  are known functionals. Together with the Heisenberg equations for the additional operators included in  $\langle 1 \rangle$ ,  $\langle 2 \rangle_S$ ,  $\langle 3 \rangle_S$  and  $\langle 3 \rangle_D$ , truncated in the same manner, the set of the equations is closed.

### Semiconductor luminescence equations

In general, the response of a semiconductor to a radiation field is subdivided into coherent and incoherent parts. As briefly mentioned in section 2.1.1, only coherent contributions are described by the classical EM fields. In that case, the relevant observables are the expectation values  $\langle B_{\mathbf{q}}^\dagger \rangle$  and  $\langle B_{\mathbf{q}} \rangle$ , related to the amplitudes of the EM waves. In analogy to Maxwell's equations these quantities are coupled to the microscopic electron-hole polarizations  $p_{\mathbf{k}} = \langle a_{\mathbf{c}\mathbf{k}}^\dagger a_{\mathbf{v}\mathbf{k}} \rangle$  in a semiconductor. However, in a typical PL scenario, the polarizations have already decayed, yielding  $p_{\mathbf{k}} = \langle B_{\mathbf{q}}^\dagger \rangle = \langle B_{\mathbf{q}} \rangle = 0$ , see 2.1.2. In this regime, the radiation from the semiconductor, i.e., the PL, is purely incoherent. It is given by the expectation value of the photon occupation number within the cluster expansion formalism:

$$\langle B_{\mathbf{q}}^\dagger B_{\mathbf{q}} \rangle = \langle B_{\mathbf{q}}^\dagger B_{\mathbf{q}} \rangle_S + \Delta \langle B_{\mathbf{q}}^\dagger B_{\mathbf{q}} \rangle = \Delta \langle B_{\mathbf{q}}^\dagger B_{\mathbf{q}} \rangle. \quad (2.20)$$

The singlet part  $\langle B_{\mathbf{q}}^\dagger B_{\mathbf{q}} \rangle_S$  contains only single-particle expectation values and is thus zero. In the majority of cases, the relevant observable is the intensity of the PL as function of the photon energy  $\omega_{\mathbf{q}}$ . By the definition, this quantity corresponds to the temporal change of the photon population:

$$I_{PL}(\omega_{\mathbf{q}}) = \frac{\partial}{\partial t} \Delta \langle B_{\mathbf{q}}^\dagger B_{\mathbf{q}} \rangle. \quad (2.21)$$

In the following, a planar QW structure is considered to keep the results consistent with the later discussion in section 2.1.2. The most important implication of a two-dimensional system is the absence of translation symmetry in the  $z$ -direction, perpendicular to the plane of the structure. In this case, momentum conservation rules do not apply with regard to the  $z$ -component and it thus proves convenient to separate the photon momentum in the perpendicular part  $q_z$  and the in-plane momentum  $\mathbf{q}$ . The absolute momentum value is denoted by  $q$ . The evaluation of the corresponding Heisenberg equations of motion in

## 2 Photoluminescence spectroscopy

second-order cluster expansion then leads to the following set of equations:

$$\begin{aligned} \frac{\partial}{\partial t} \Delta \langle B_{q_z, \mathbf{q}}^\dagger B_{q_z, \mathbf{q}} \rangle &= i(\omega_{q_z} - \omega_{q_z^i}) \Delta \langle B_{q_z, \mathbf{q}}^\dagger B_{q_z, \mathbf{q}} \rangle \\ &+ \frac{1}{\hbar} \sum_{\mathbf{k}} [\mathcal{F}_q \Delta \langle B_{q_z, \mathbf{q}} a_{c, \mathbf{k}}^\dagger a_{v, \mathbf{k}-\mathbf{q}} \rangle + \mathcal{F}_q^* \Delta \langle B_{q_z, \mathbf{q}}^\dagger a_{v, \mathbf{k}-\mathbf{q}}^\dagger a_{c, \mathbf{k}} \rangle], \end{aligned} \quad (2.22)$$

$$\begin{aligned} i\hbar \frac{\partial}{\partial t} \Delta \langle B_{q_z, \mathbf{q}}^\dagger a_{v, \mathbf{k}-\mathbf{q}}^\dagger a_{c, \mathbf{k}} \rangle &= [\tilde{\epsilon}_{\mathbf{k}}(\mathbf{q}) - \hbar\omega_q] \Delta \langle B_{q_z, \mathbf{q}}^\dagger a_{v, \mathbf{k}-\mathbf{q}}^\dagger a_{c, \mathbf{k}} \rangle \\ &- [1 - f_{\mathbf{k}}^e - f_{\mathbf{k}-\mathbf{q}}^h] \Omega_{stim}(\mathbf{k}, q_z, \mathbf{q}) \\ &+ i\mathcal{F}_q [f_{\mathbf{k}}^e f_{\mathbf{k}-\mathbf{q}}^h + \sum_l \Delta \langle a_{c, \mathbf{l}+\mathbf{q}}^\dagger a_{v, \mathbf{k}-\mathbf{q}}^\dagger a_{c, \mathbf{k}} a_{v, \mathbf{l}} \rangle] \\ &+ i\hbar \frac{\partial}{\partial t} \Delta \langle B_{q_z, \mathbf{q}}^\dagger a_{v, \mathbf{k}-\mathbf{q}}^\dagger a_{c, \mathbf{k}} \rangle|_{scatt}, \end{aligned} \quad (2.23)$$

$$\frac{\partial}{\partial t} f_{\mathbf{k}}^e = -\frac{2}{\hbar} \sum_{q_z, \mathbf{q}} \text{Re}[\mathcal{F}_q \langle B_{q_z, \mathbf{q}}^\dagger a_{v, -\mathbf{k}-\mathbf{q}}^\dagger a_{c, \mathbf{k}} \rangle] + \frac{\partial}{\partial t} f_{\mathbf{k}}^e|_{SBE}, \quad (2.24)$$

$$\frac{\partial}{\partial t} f_{\mathbf{k}}^h = -\frac{2}{\hbar} \sum_{q_z, \mathbf{q}} \text{Re}[\mathcal{F}_q \langle B_{q_z, \mathbf{q}}^\dagger a_{v, -\mathbf{k}}^\dagger a_{c, \mathbf{k}+\mathbf{q}} \rangle] + \frac{\partial}{\partial t} f_{\mathbf{k}}^h|_{SBE}. \quad (2.25)$$

In the first equation the photon population  $\Delta \langle B_{q_z, \mathbf{q}}^\dagger B_{q_z, \mathbf{q}} \rangle$  couples to the photon-assisted polarization  $\Delta \langle B_{q_z, \mathbf{q}}^\dagger a_{v, \mathbf{k}-\mathbf{q}}^\dagger a_{c, \mathbf{k}} \rangle$  via light-matter interaction matrix-element  $\mathcal{F}_q$ . Hence, the changes in the photon occupation number originate from the inter-band transitions of the charge-carriers. The dynamics of the photo-assisted polarization are determined by the second equation. Here, the first term includes band-structure renormalization effects due to the Coulomb-interaction as well as the excitonic correlations. The renormalized kinetic energy is given by

$$\tilde{\epsilon}_{\mathbf{k}}(\mathbf{q}) \equiv \epsilon_{\mathbf{k}}^e + \epsilon_{\mathbf{k}-\mathbf{q}}^h - \sum_l V_{\mathbf{k}-\mathbf{l}} [f_{\mathbf{l}}^e + f_{\mathbf{l}-\mathbf{q}}^e]. \quad (2.26)$$

The second term resembles the generalized Rabi-frequency in the Semiconductor Bloch Equations (SBE). It includes the phase-space filling factor  $[1 - f_{\mathbf{k}}^e - f_{\mathbf{k}-\mathbf{q}}^h]$  and is a source for the stimulated emission:

$$\Omega_{stim}(\mathbf{k}, q_z, \mathbf{q}) \equiv i \sum_{q_z^i} \mathcal{F}_q \Delta \langle B_{q_z, \mathbf{q}}^\dagger B_{q_z^i, \mathbf{q}} \rangle + \sum_l V_{\mathbf{k}-\mathbf{l}} \Delta \langle B_{q_z, \mathbf{q}}^\dagger a_{v, \mathbf{l}}^\dagger a_{c, \mathbf{l}-\mathbf{q}} \rangle \quad (2.27)$$

Usually, the stimulated contributions are negligible under typical experimental conditions in the weak coupling regime, i.e., when no cavity is applied. The sources of the photo-assisted polarization and thus of the PL are given by the third term. The singlet contri-

## 2.1 Intrinsic photoluminescence properties of direct-gap semiconductors

butions  $f_{\mathbf{k}}^e f_{\mathbf{k}-\mathbf{q}}^e$  account for the recombination of uncorrelated electrons and holes, i.e. an electron-hole plasma. The purely correlated part  $\sum_l \Delta \langle a_{c,l+\mathbf{q}}^\dagger a_{v,\mathbf{k}-\mathbf{q}}^\dagger a_{c,\mathbf{k}} a_{v,l} \rangle$  is the excitonic source for the spontaneous emission. The last term in the Eq. (2.23) includes scattering effects. These are the Coulomb-scattering which can be understood as a phenomenological damping, as well as the coupling to the correlations between the photons and phonons. The latter give rise to the phonon-assisted emission, discussed in section 2.2.1 in more detail. The last two Eqs. (2.24) and (2.25) describe the dynamics of the electron and hole populations, respectively. Changes in the occupation number due to the emission of photons are determined by the first term. The second term  $\frac{\partial}{\partial t} f_{\mathbf{k}}|_{SBE}$  summarizes the dynamics given by the SBE. These include Coulomb-renormalization, phase-space filling, generalized Rabi frequency as well as the Coulomb- and phonon-scattering. The latter are responsible for the thermalization of the carrier distributions as well as relaxation and cooling processes. The complete equations set (2.22) - (2.25) is called *Semiconductor Luminescence Equations (SLE)*.

### Analytic solution

For a wide array of experimentally relevant situations, it is sufficient to calculate the steady-state PL at a constant time interval after the excitation. In this case, the populations of free carriers  $f_{\mathbf{k}}^e$  and  $f_{\mathbf{k}}^h$ , as well as the excitonic correlations  $\Delta \langle a_{c,l+\mathbf{q}}^\dagger a_{v,\mathbf{k}-\mathbf{q}}^\dagger a_{c,\mathbf{k}} a_{v,l} \rangle$  are taken as constant. Further approximations are introduced in the regime of low densities and negligible broadening: (i) the Coulomb-scattering triplets are reduced to a phenomenological dephasing rate  $\gamma$ , (ii) the homogeneous broadening is assumed to be small in comparison to the exciton binding energy. For these assumptions, the SLE are solved analytically and yield a simple expression for the PL intensity:

$$I_{PL}(\omega_q) = \frac{2\mathcal{F}_q^2}{\hbar} \text{Im} \left[ \sum_{\lambda} |\phi_{\lambda}^R(r=0)|^2 \frac{\Delta N_{\lambda}^{exc}(\mathbf{q}) + N_{\lambda}^{eh}(\mathbf{q})}{E_{\lambda} - \hbar\omega_{\mathbf{q}} - i\gamma} \right]. \quad (2.28)$$

Here, the PL signal is proportional to the light-matter coupling  $\mathcal{F}_q^2$ . The absolute energy level of the excitonic state  $\lambda$  is given by  $E_{\lambda}$ ;  $\phi_{\lambda}^R$  is the corresponding wavefunction in real-space coordinates, a right-handed eigenfunction of the Wannier equation.  $\phi_{\lambda}^R$  converges to the initial excitonic eigenfunction  $\phi_{\lambda}$  in case of the vanishing carrier densities. The denominator  $[E_{\lambda} - \hbar\omega_{\mathbf{q}} - i\gamma]$  determines the spectral position as well as the shape of the PL. In general, the emission spectrum is a series of lorentzian-shaped PL peaks at the excitonic resonances  $E_{\lambda}$ , broadened according to  $\gamma$ . Also, due to a stronger coupling to the light-field, the PL from the excitonic ground state  $\lambda = 1s$  is significantly higher than the signal from the excited states and the continuum emission.

The sources of the PL are given by the enumerator  $[\Delta N_{\lambda}^{exc}(\mathbf{q}) + N_{\lambda}^{eh}(\mathbf{q})]$ . Here,  $\Delta N_{\lambda}^{exc}(\mathbf{q})$

## 2 Photoluminescence spectroscopy

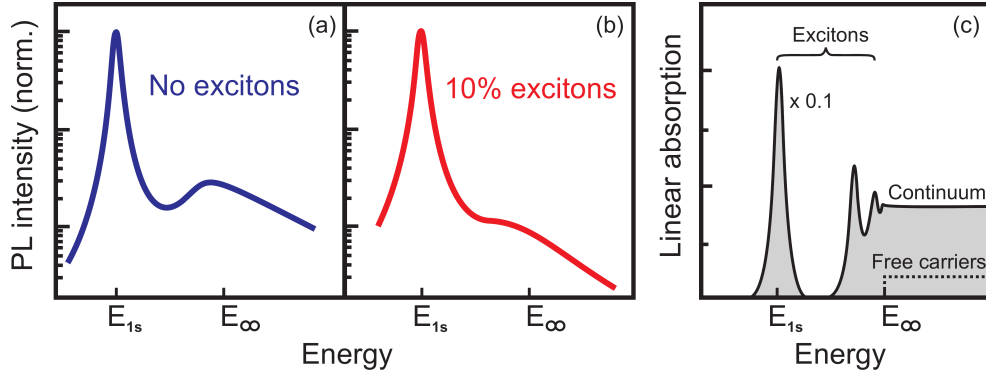


Figure 2.2: Calculated PL spectra in the absence of the excitonic population (a) and for the case, when 10 % of the electrons and holes form excitons (b). The PL results are taken from [26, 30]. The corresponding linear absorption spectrum is shown in (c).

denotes the contribution of the excitonic population in the state  $\lambda$  with the center-of-mass momentum  $\mathbf{q}$ . The second contribution  $N_{\lambda}^{eh}(\mathbf{q})$  comes from the electron-hole plasma, i.e., the unbound charge-carriers:

$$N_{\lambda}^{eh}(\mathbf{q}) \equiv \sum_{\mathbf{k}} \phi_{\lambda}^L(\mathbf{k})^2 f_{\mathbf{k}+\mathbf{q}_e}^e f_{\mathbf{k}-\mathbf{q}_h}^h, \quad (2.29)$$

with  $\mathbf{q}_e + \mathbf{q}_h = \mathbf{q}$  and  $\phi_{\lambda}^L$  as the excitonic left-handed eigenfunction in momentum space. Hence, as soon as an electron-hole populations  $f_{\mathbf{k}+\mathbf{q}_e}^e f_{\mathbf{k}-\mathbf{q}_h}^h$  are present in the system, spontaneous emission at the excitonic resonances  $E_{\lambda}$  is observed.

At the first glance, this result might appear counterintuitive. In a simple one-particle picture one would expect only the emission from the plasma continuum to determine the PL spectrum in the absence of excitons. However, we should keep in mind that the single-particle states do not represent the real eigenstates of the interacting many-body system. When the Coulomb-coupling is present, every wave-function of a single particle contains contributions from the Coulomb-correlated many-particle states, e.g. excitons. Moreover, the light-matter interaction strength is orders of magnitude higher for the excitonic transitions compared to the band-to-band recombination in the continuum. Thus, the "excitonic" part of the single-particle wave-function gives a major contribution to the spontaneous emission. An alternative picture would be the quasi-instantaneous Coulomb-scattering of electrons and holes to the excitonic states prior to radiative recombination. The excess energy is then distributed among the remaining carriers, leading to a small temperature increase of the whole system.

Exemplary PL spectra, calculated using the expression (2.28), are plotted in Fig. 2.2 (a) and (b). A corresponding absorption spectrum in the vicinity of the band gap is shown schematically in Fig. 2.2 (c). The latter is strongly influenced by Coulomb-effects. The



## 2.1 Intrinsic photoluminescence properties of direct-gap semiconductors

dominant signature is the Lorentzian peak at  $E_{1s}$ , corresponding to the ground state of the exciton. It is accompanied by a series of transitions from higher excitonic states with  $\lambda = 2s, 3s, \dots$ , which merge into the ionization continuum at  $E_\infty$ . The absorption spectrum due to the non-interacting free carriers is shown by the dotted line for comparison. It is significantly lower than the Coulomb-enhanced contributions. Fig. 2.2 (a) shows the sample emission when only plasma and no excitons are present in the system, i.e.,  $\Delta N_\lambda^{exc}(\mathbf{q}) = 0$  for all  $\lambda$  and  $\mathbf{q}$ . Nevertheless, the PL emerges from the 1s-exciton peak according to (2.28). The luminescence from higher excitonic transitions as well as from the plasma continuum is much less pronounced. Furthermore, if only 10 % of the charge-carriers are bound to excitons, the 1s-emission increases drastically in comparison to the continuum-PL, see Fig. 2.2 (b). Again, the reason is the especially strong light-matter coupling for spatially correlated electrons and holes forming an exciton. Thus, regardless of the actual population of excitons, the excitonic resonances are always present in the PL spectra due to the Coulomb-interaction.

### 2.1.2 Photoluminescence of an ideal quantum-well structure

In this subsection, an ideal, defect-free semiconductor system is used for the illustration of the fundamental processes, involved in a typical PL experiment. Following the brief introduction in the beginning of the chapter 2, the processes are subdivided into three regimes, regarding photoexcitation, relaxation, and recombination of the charge-carriers. The discussion is based on the results and predictions of the previously outlined microscopic theory (2.1.1), as well as on the Refs. [9, 31].

#### Photoexcitation

An exemplary QW band structure is shown on the left-hand side of the Fig. 2.3.  $E_{barr}$  and  $E_{QW}$  denote the band gaps of the barrier and the QW, respectively. The single-particle levels of the electrons ( $e_1, e_2$ ) and holes ( $h_1, h_2$ ) confined in the QW are shown with their corresponding wavefunctions. A schematic linear absorption spectrum of the structure is plotted on the right-hand side of the Fig. 2.3. The spectrum shows the excitonic resonances of the first ( $e_1h_1$ ) and the second QW subbands ( $e_2h_2$ ), as well as the absorption from the corresponding continuum states and from the barrier.

In a time-resolved PL experiment, the QW structure is excited by a short laser pulse, with the typical temporal width in the range of 100 fs. Continuous-wave PL is briefly discussed in the end of the section. In general, three different excitation conditions are distinguished: resonant, quasi-resonant, and non-resonant. For the resonant excitation, the central energy of the laser pulse  $E_p$  corresponds to the excitonic ground-state of the QW, i.e.,  $e_1h_1$  transition. In this case, only a negligible amount of the excess energy

## 2 Photoluminescence spectroscopy

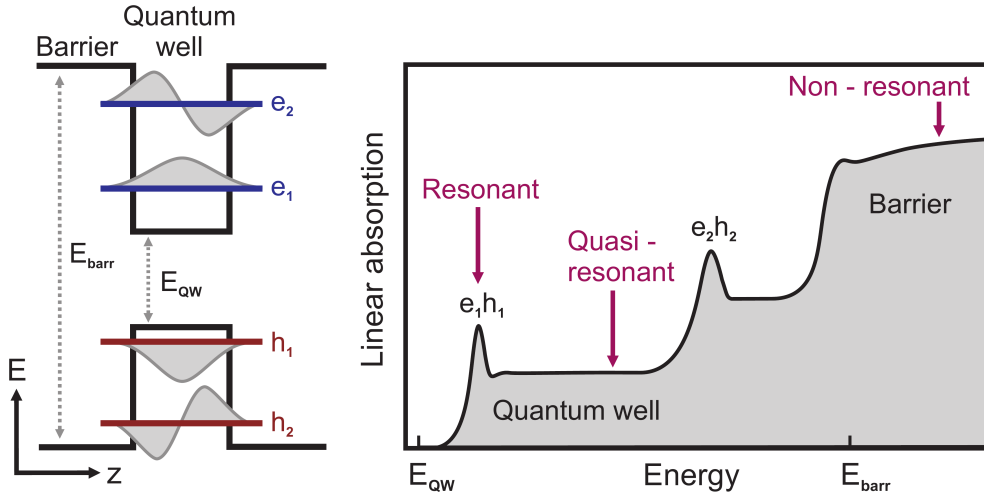


Figure 2.3: A schematic band alignment with the single-particle energy levels of an exemplary QW structure are shown on the left-hand side. The corresponding linear absorption spectrum is illustrated in the right figure. The three different excitation regimes are marked by the arrows.

above  $E_{e_1h_1}$  is transferred to the carrier system. Thus, the kinetic energies of the electrons and holes are rather small, and the carrier temperatures remain in the range of the lattice temperature. Also, during the decay of the laser-induced polarization, coherent processes contribute to the spontaneous emission of the QW [25]. In addition, excitons are created directly after the polarization decay.

Under the quasi-resonant conditions, the energy of the laser pulse is higher than the QW ground state, but still below the barrier absorption edge. Here, as an example, the continuum of the first subband is excited. In comparison to the resonant excitation, the decay of the polarization is extremely fast, in the range of several tens of fs. Thus, any coherent contributions to the QW emission are negligible. Also, due to a finite excess energy ( $E_p - E_{e_1h_1}$ ), the initial temperature of the carrier system is significantly higher than the lattice temperature. Finally, only the electron-hole plasma is initially created. It is then followed by the formation of excitons.

In case of the non-resonant excitation, the structure is excited into the barrier, i.e., the energy of the laser pulse is higher than  $E_{barr}$ . Thus, in contrast to the quasi-resonant conditions, the initial carrier distribution in the QW strongly depends on the carrier scattering between the barrier and the QW. On the other hand, a fast polarization decay, as well as comparably slow exciton formation and high carrier temperatures resemble the quasi-resonant scenario. For these reasons, the term "non-resonant" is often used for both quasi- and non-resonant excitation. Also, these conditions are often applied in the experiments, rather than the resonant excitation. In the latter case, the detection of the PL is more challenging due to the contributions from the laser stray-light and the resonant Rayleigh-

## 2.1 Intrinsic photoluminescence properties of direct-gap semiconductors

scattering. Hence, quasi-resonant excitation is assumed for the following discussion in the rest of this section. Being a typical experimental scenario, quasi-resonant conditions also allow for an easier illustration of the fundamental relaxation and recombination processes.

### Relaxation

Figure 2.4 (a) illustrates the temporal evolution of the polarization and carrier densities after the excitation of the QW with a short laser pulse in the electron-hole continuum. Initially, the laser light induces coherent polarization in the sample, i.e., in a simple picture, transitions between electron and hole states oscillating with the laser frequency and a fixed phase. Due to the ultra-fast Coulomb- as well as phonon-scattering the polarization decays fast, typically on a sub-100 fs time-scale [32]. According to the SBE, the dephasing of the polarization leads to creation of electron and hole populations in the conduction and valence bands, respectively. The lifetime of the carrier population is rather long, limited by radiative and non-radiative, i.e., Auger, recombination. During this lifetime, a fraction of electrons and holes form excitons. The formation rate depends on the experimental conditions such as lattice temperature, excitation density, as well as on the general material parameters, e.g., the strength of the Coulomb-interaction. The characteristic time-scales are in the range of 100's of ps in GaAs [33] and appear to be much shorter in wide-gap semiconductors [34]. However, this topic is still under discussion, mainly due to the challenges in finding direct experimental evidence for the exciton formation.

The thermalization of the carrier system is schematically shown in Fig. 2.4 (b)-(f). Here, the occupation probability of the single-particle states is plotted as function of momentum. Direct after the excitation and the quasi-instantaneous decay of the polarization, the carrier distribution is mainly determined by the spectral width of the laser pulse. The distribution is thus highly non-thermal and resembles a peak function, centered at a finite momentum  $\mathbf{k}_0$ . In the first 100's of fs, the carriers are scattered by phonons, as well as among each other via Coulomb-interaction. The latter becomes especially important at elevated carrier densities, often encountered in time-resolved PL experiments due to the comparably high pulse energies of the excitation sources. The carrier system thus thermalizes to the Fermi-Dirac distribution within the first ps. Finally, the carrier system cools down under the emission of phonons.

A typical evolution of the carrier temperature is illustrated in Fig. 2.4 (g). After the thermalization the initial temperature of the carrier distribution  $T_{init}$  roughly corresponds to the excess energy, divided by the Boltzmann constant  $k_B$ . In the first couple of picoseconds the carrier temperature decreases fast via emission of optical phonons. The cooling is especially efficient, since the energy of optical phonons is comparably high, e.g.,  $36 \text{ meV} = k_B \cdot 420 \text{ K}$  in GaAs [36]. In addition, the optical phonon dispersion is flat to a large extent, allowing for a wide range of scattering processes under energy and mo-

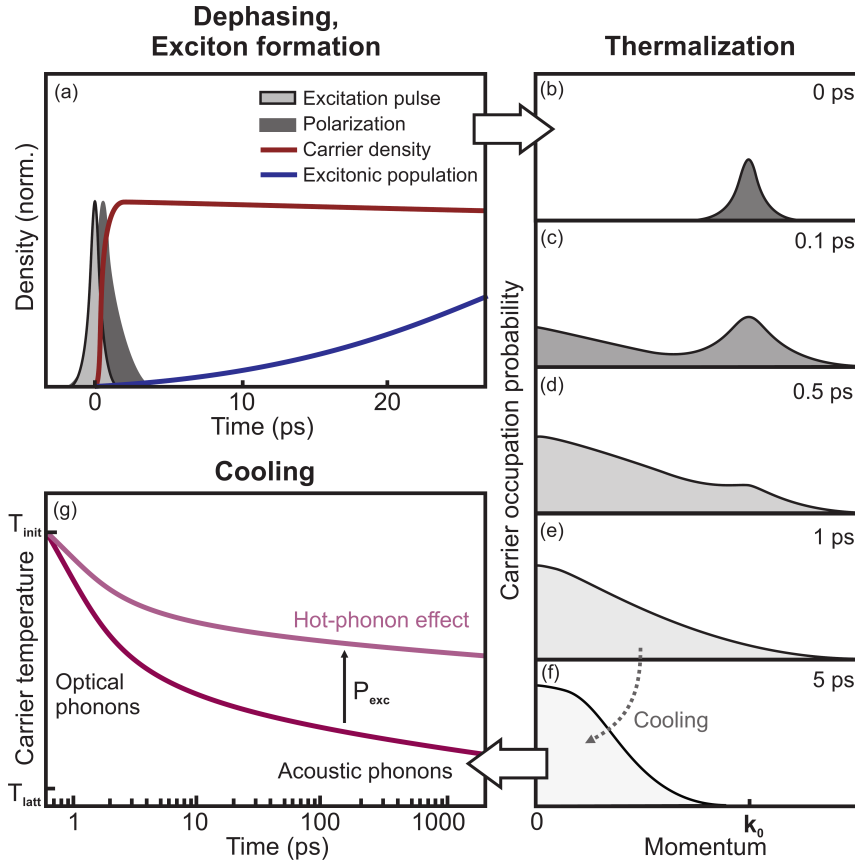


Figure 2.4: Schematic illustration of the relaxation processes after photoexcitation. (a) Temporal evolution of laser-induced polarization, carrier population, as well as exciton formation. (b)-(f) Occupation probability of the electronic single-particle states as function of momentum at various time-delays after the excitation. (g) Temperature of the carrier system as function of time for low and high excitation power  $P_{exc}$ . All figures are based on theoretical and experimental findings [24, 26, 29, 31, 35]. The quantitative information regarding time after the excitation provides an exemplary illustration of the typical time-scales.

momentum conservation. However, as soon as the carrier temperature decreases below the value corresponding to the optical phonon energy, the cooling by the emission of optical phonons becomes inefficient. In this regime, acoustic phonons dominate the relaxation. Due the small phonon energies, as well as the dispersion of acoustic phonons, the energy loss rate is significantly smaller in comparison to the cooling by optical phonons. Thus, the temperature decrease is rather slow beyond the first 10 ps. In general, several 100's of ps and even ns can be necessary to reach the lattice temperature  $T_{latt}$ , especially when the latter is low, in the range of several Kelvin [35, 37]. At elevated excitation densities, the carrier cooling is further inhibited by the so-called *hot-phonon effect* [38]. The relaxation of a large number of photoexcited hot carriers leads to a high generation rate of

## 2.1 Intrinsic photoluminescence properties of direct-gap semiconductors

optical phonons, exceeding the anharmonic decay rate into acoustic phonons. This creates a non-equilibrium "over-population" of optical phonons and thus causes an increased reabsorption of the latter by the charge-carriers. As a result, the cooling is significantly suppressed. Therefore, the temperature of the carrier system, obtained at a fixed time-delay after the excitation, increases with the pump power  $P_{exc}$ .

### Radiative recombination

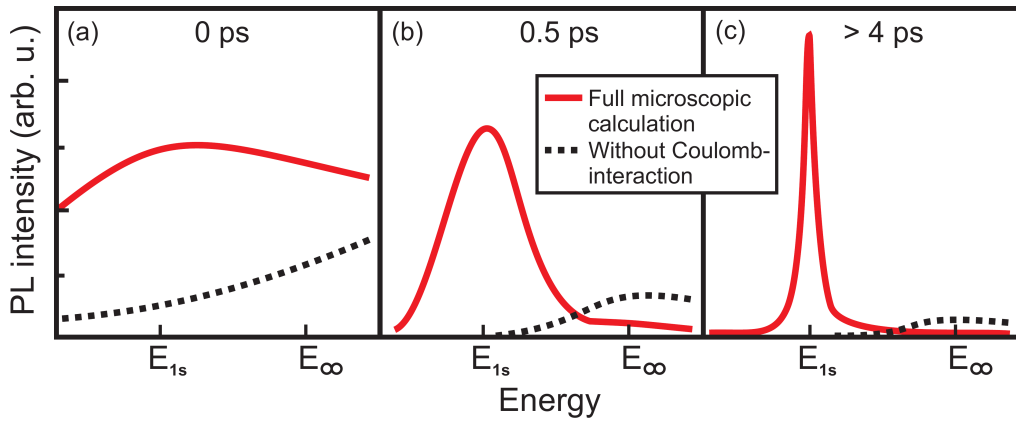


Figure 2.5: Calculated PL spectra of a QW at 0 ps (a), 0.5 ps (b), and  $> 4$  ps (c) after the pulsed, quasi-resonant excitation [24]. Corresponding spectra, calculated without Coulomb-interaction, are plotted by the dotted lines for comparison.

Calculated PL spectra [24] of an ideal QW structure are shown in Fig. 2.5. The lattice temperature is set to 4 K and the final carrier density to  $1.8 \cdot 10^{10} \text{ cm}^{-2}$ . Directly after the excitation, the emission is broadened significantly, yet still centered in the vicinity of the excitonic 1s-resonance. As the carrier distribution thermalizes and cools, the width of the PL peak decreases and the emission energy shifts to match the ground state of the exciton. After a couple of ps, the PL spectrum converges to the steady-state shape, characterized by the Elliott formula 2.28. For comparison, the calculation results omitting Coulomb-interaction are shown by the dotted lines in Fig. 2.5. In this case, the shape as well as the spectral position of the PL are defined by the distribution of electrons and holes in the corresponding bands, as it is expected for the single-particle approximation.

To illustrate the influence of the excitation power and lattice temperature, experimental PL results from high-quality (GaIn)As QWs are shown in Fig. 2.6. As already discussed, the QW emission is dominated by the excitonic ground state, i.e.,  $e_1hh_1$ , at low excitation densities. For high excitation densities, additional peaks from higher subband transitions  $e_1lh_1$  and  $e_2hh_2$  appear in the spectra due to the state-filling as well as possible heating effects. Also, the width of the main PL peak increases significantly with rising excitation power, see the inset of Fig. 2.6 (a). The reason is the so-called excitation-induced dephas-

## 2 Photoluminescence spectroscopy

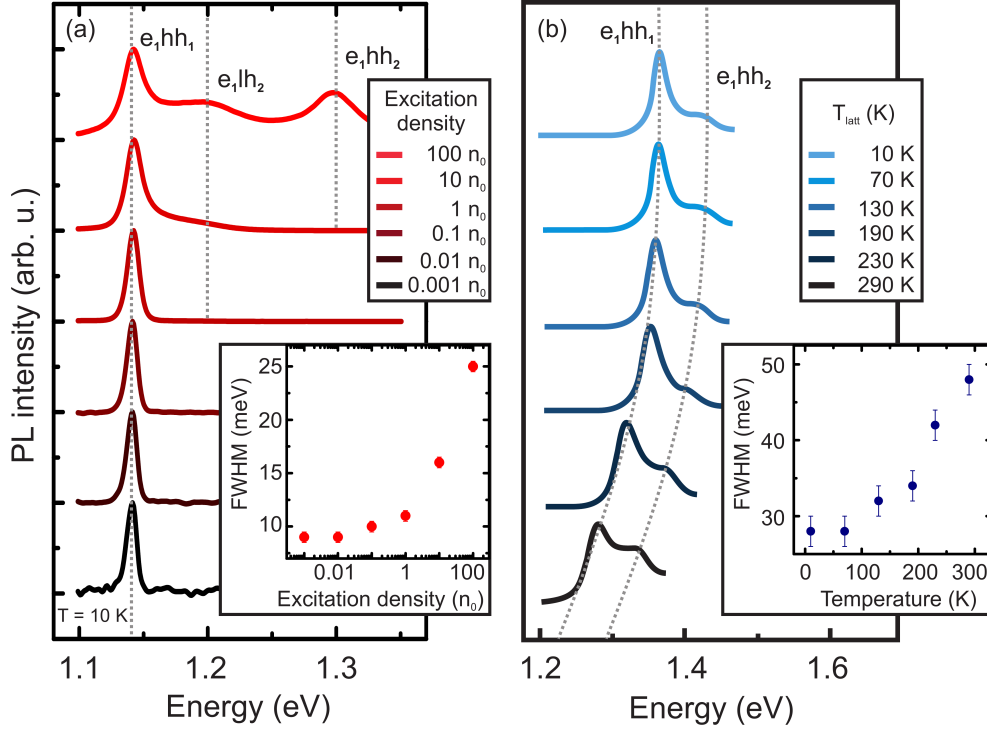


Figure 2.6: (a) PL spectra of a (GaIn)As QW sample at  $T=10$  K at various excitation densities, normalized to  $n_0=2 \cdot 10^{12} \text{ cm}^{-2}$  photons per pulse. (b) Temperature dependent (GaIn)As QW emission for the excitation density of about  $30 n_0$  [40]. The excitonic resonances are marked by the dotted lines. The FWHMs corresponding to the ground-state transitions are plotted in the insets.

ing [39]: at higher carrier densities, the Coulomb-scattering between the carriers becomes faster, thus leading to an increase of the homogeneous linewidth. In addition to broadening, the maximum of the main PL transition exhibits a small shift in energy, as the pump density increases, due to the Coulomb-renormalization and phase-filling [10].

Temperature-dependent PL spectra of a (GaIn)As QW are plotted in Fig. 2.6 (b). Due to the lower In content in this sample, the emission maximum is slightly higher in comparison to the sample from Fig. 2.6 (a). Otherwise, the overall quality as well as the structural and optical properties of the samples are nearly identical. At low temperatures, the PL spectra of the QW show the resonances from the first ( $e_1hh_1$ ) and the second subband ( $e_2hh_2$ ), the latter due to the comparably high excitation density of about  $30 n_0$ . As the temperature increases, the relative intensity of the second subband rises, according to the change in thermal distribution of carriers between the subbands. The full-width-at-half-maximum (FWHM) of the main peak also increases due to the increasing phonon population and therefore more efficient carrier-phonon scattering at higher lattice temperatures.

## 2.1 Intrinsic photoluminescence properties of direct-gap semiconductors

The corresponding phenomenological expression for the FWHM  $\Gamma$  is [41]:

$$\Gamma(T) = \Gamma_0 + \Gamma_{AC}T + \frac{\Gamma_{LO}}{e^{\frac{\hbar\omega_{LO}}{k_B T}} - 1}. \quad (2.30)$$

Here,  $\Gamma_0$  denotes the temperature-independent line-width due to the excitation-induced dephasing, impurity scattering and disorder-related broadening.  $\Gamma_{AC}$  and  $\Gamma_{LO}$  account for the coupling strength of carriers to acoustic and LO phonons, respectively.  $T$  is the lattice temperature,  $k_B$  - the Boltzmann constant, and  $\hbar\omega_{LO}$  - the LO phonon energy. According to this formula, the FWHM increases linearly with temperature due to the scattering of carriers with acoustic phonons. The scattering with optical phonons, on the other hand, is responsible for the non-linear increase of the FWHM, corresponding to the Bose-function in the last term in Eq. (2.30). In addition, an increase of the lattice temperature also leads to a shift of the PL maximum to lower energies. The sample emission follows the temperature-dependent shift of the material band-gap due to the anharmonicity of the potential between the lattice ions [42]. The temperature dependence of the band-gap energy  $E_g$  is often described by the semi-phenomenological Varshni formula [43]:

$$E_g(T) = E_0 - \frac{\alpha T^2}{T + \beta}. \quad (2.31)$$

Here,  $E_0$  is the band-gap energy at zero temperature,  $\alpha$  and  $\beta$  are material constants. The latter roughly corresponds to the Debye-temperature  $\frac{\hbar\omega_{LO}}{k_B}$ .

After discussing the spectral features of the QW PL, the focus is laid on the temporal dependence of the spontaneous emission. As already mentioned in previous sections, excitons and electron-hole plasma act both as sources for luminescence and are nearly indistinguishable in the spectral lineshape. However, they behave differently with respect to the emission dynamics. Fig. 2.7 shows the characteristic PL transients corresponding to the radiative recombination of excitons and plasma. For the uncorrelated electrons and holes, the probability of spontaneous emission  $I_{eh}$  is approximately proportional to the product of electron and hole populations,  $n \cdot p$ , see Eq. (2.29). This relation holds up to high excitation densities, near the lasing threshold, where this simple dependence fails [44]. Furthermore, the photoexcited electron and hole populations are equal in the ideal case of an undoped semiconductor, or, when the excitation density exceeds the doping concentration. Since the radiative recombination is the only source for the carrier decay, the time-dependent electron population  $n(t)$  obeys the following equation:

$$\dot{n}(t) \propto n^2(t) \quad (2.32)$$



## 2 Photoluminescence spectroscopy

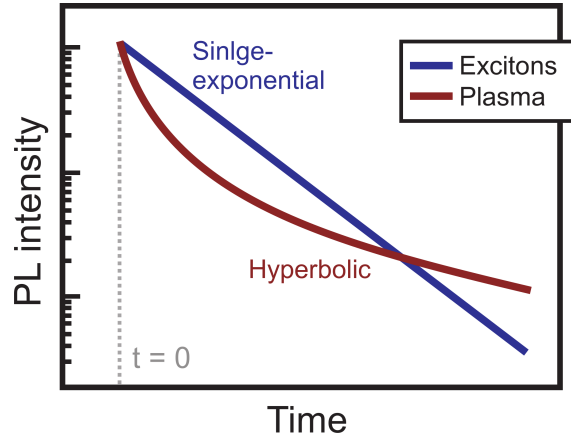


Figure 2.7: Characteristic transient PL from pure excitonic population and electron-hole plasma after a pulsed excitation at  $t = 0$ .

with the solution

$$n(t) = \frac{1}{\frac{t}{\tau_{eh}} + \frac{1}{n_0}}, \quad (2.33)$$

leading to

$$I_{eh}(t) \propto \frac{1}{\tau_{eh}} \left( \frac{1}{\frac{t}{\tau_{eh}} + \frac{1}{n_0}} \right)^2. \quad (2.34)$$

Here,  $n_0$  denotes the initial electron population and  $\tau_{eh}$  is the average recombination probability. The latter is approximately defined by the Fermi's golden rule, i.e., the dipole-overlap of the electron and hole wavefunctions. According to the expression (2.34), the PL from the electron-hole plasma exhibits hyperbolic behavior, see Fig. 2.7.

In contrast to plasma, the decay of excitonic PL is single-exponential, since the probability of the radiative recombination does not depend on the carrier density in case of excitons. The PL intensity  $I_X$  is thus simply proportional to the exciton population  $N_X$ . Hence, the dynamics of  $N_X(t)$  follow

$$\dot{N}_X(t) \propto -N_X(t), \quad (2.35)$$

solved by

$$N_X(t) = N_0 e^{-\frac{t}{\tau_X}}, \quad (2.36)$$



## 2.1 Intrinsic photoluminescence properties of direct-gap semiconductors

and yielding

$$I_X(t) \propto N_0 e^{-\frac{t}{\tau'_X}}. \quad (2.37)$$

$N_0$  is the initial population and  $\tau'_X$  denotes the effective radiative lifetime of excitons. In general,  $\tau'_X$  depends on the dipole-overlap of the wavefunctions of the exciton constituents [29] as well as on the temperature of the exciton gas [45].

The excitonic recombination is illustrated in more detail in Fig. 2.8. Here, the distribution of excitons is plotted as function of the center-of-mass momentum. In contrast to the electron-hole plasma, where carriers with an arbitrary momentum  $\mathbf{k}$  can recombine radiatively, the excitonic recombination is restricted by momentum-conservation. When an exciton recombines, the in-plane center-of-mass momentum  $\mathbf{Q}$  is transferred to the emitted photon and defines the angular direction of the PL [45]. Thus, radiative recombination is only allowed for excitons with momenta values smaller than the maximal photon momentum  $q = \omega_X/c$  with the photon frequency  $\omega_X$ , corresponding to the exciton ground state energy  $E_X = \hbar\omega_X$ . In the literature, the momentum-interval  $0 < \mathbf{Q} < \omega_X/c$  is often referred to as the *radiative cone*. Hence, only a fraction  $\alpha$  of the complete exciton population  $N_X$ , the so-called *bright* excitons, can directly recombine under the emission of photons. The dynamics of the exciton population  $N_X(t)$  thus obey:

$$\dot{N}_X(t) = \frac{1}{\tau_X} \alpha N_X(t). \quad (2.38)$$

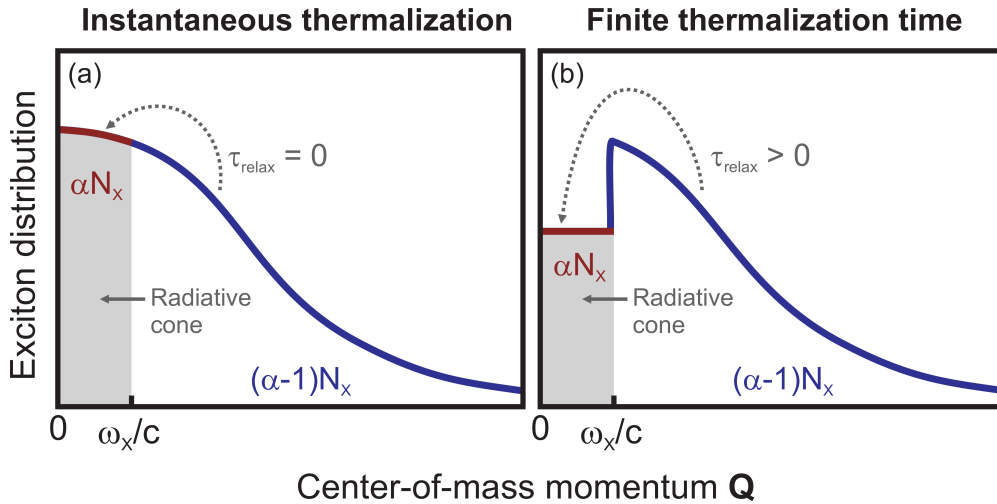


Figure 2.8: Exciton distribution as function of the center-of-mass momentum in case of instantaneous (a) and finite (b) thermalization rate. The gray area defines the range, where the radiative recombination of excitons is allowed by the momentum-conservation rules.

## 2 Photoluminescence spectroscopy

Corresponding to Eq.(2.36), the solution is a single-exponential function

$$N_X(t) = N_0 e^{-\frac{t}{\tau'_X}}, \quad (2.39)$$

with

$$\tau'_X = \frac{\tau_X}{\alpha}, \quad (2.40)$$

leading to

$$I_X(t) \propto \frac{1}{\tau_X} N_0 e^{-\frac{t\alpha}{\tau_X}}. \quad (2.41)$$

Again,  $N_0$  defines the initial population after the excitation and exciton formation.  $\tau_X$  is the radiative recombination time of excitons within the radiative cone. This recombination time is determined only by the dipole-overlap of the corresponding exciton wave-functions [29] and is usually in the range of 10 ps [46], depending on the material system. According to Eq.(2.40), the effective lifetime  $\tau'_X$  is significantly longer than  $\tau_X$ , even when the thermalization of excitons, i.e., relaxation to the radiative cone, is assumed to be instantaneous. Typically,  $\tau'_X$  is in the range of 100's of ps to several ns [9, 46, 47] due to the small bright exciton fraction  $\alpha$ , in the order of 0.01 - 0.1 [45]. In addition,  $\alpha$  decreases even more, when the carrier temperature increases and the exciton distribution changes in favor of higher center-of-mass momenta. In QWs, this leads to a linear dependence of the effective radiative recombination time  $\tau'_X$  on the lattice temperature [9, 45]. Also, the radiative recombination gets slower, when the excitation density is increased [48], resulting in an increase of the carrier temperature via hot-phonon effect. Interestingly, the PL itself leads to some heating of the carrier system, since only the excitons with small momenta are "removed" from the distribution by the emission of light.

In addition, the relaxation of excitons towards the radiative cone is not instantaneous in real material systems. The corresponding time constant  $\tau_{relax}$  is typically determined by exciton-phonon and exciton-exciton scattering [9]. This finite relaxation time leads to a non-thermal distribution of excitons - the so-called *kinetic-hole*, i.e., under-population of states within the radiative cone, see Fig. 2.8 (b). In this case, the fraction  $\alpha$  decreases, leading to an increase of the effective recombination time  $\tau_X$ . Hence, exciton recombination rate becomes dependent on the thermalization processes.

Finally, in analogy to the hydrogen atoms, excitons are found as triplets and singlets with parallel and anti-parallel spins of the constituents, respectively. Due to the spin conservation, only recombination of exciton singlets with spin quantum number 1 is dipole-allowed. Exciton triplets recombine either under the emission of two photons or after a spin-flip process, both leading to an extremely long lifetime. In the majority of cases,

## 2.1 Intrinsic photoluminescence properties of direct-gap semiconductors

the triplet fraction contributes in form of a weak long-living background signal or even decays non-radiatively and is thus completely neglected.

### Auger-recombination

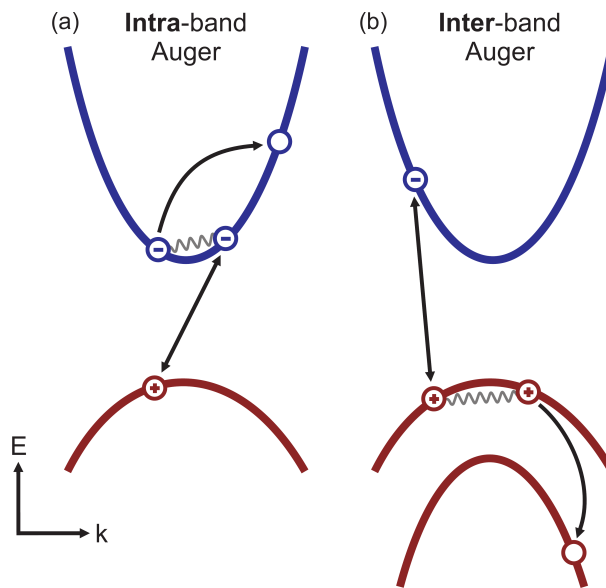


Figure 2.9: Schematic illustration of inter-(a) and intra-band (b) Auger-recombination in semiconductors.

The sole intrinsic non-radiative recombination in an ideal, defect-free semiconductor is the Auger-effect [49]. The mechanism is shown schematically in Fig. 2.9. An electron-hole pair recombines under energy and momentum transfer to another carrier via Coulomb-interaction. In case of the intra-band process, the additional carriers are excited within one band. For the inter-band Auger-recombination, carrier scattering between different bands or subbands is possible. These carriers, excited via Auger-interaction, subsequently relax to the corresponding band minima by phonon emission thus causing heating of the crystal lattice. Since three particles are involved in the Auger-recombination, the recombination probability is approximately proportional to the third power of the carrier density. In the analogy to the spontaneous emission from plasma, this simple relation is valid only for low and intermediate carrier densities, below the lasing threshold [44]. Also, the interaction matrix-elements for different Auger-processes depend strongly on material parameters, e.g. band alignment, effective masses, strain, etc. In a typical PL experiment, Auger recombination becomes relevant in the high-power excitation regime and, in the most cases, can be neglected at low excitation densities.

### Continuous-wave PL

The previous discussion of the PL properties is based on the scenario, when an ultra-short laser pulse is used for excitation. However, CW PL spectroscopy is often applied in experiments, mainly due to a broader availability of CW sources and detectors. Also, since the Heisenberg uncertainty relation does not restrict the spectral resolution in case of CW excitation and detection, it thus allows for high-precision measurements of the emission energies. In addition, the carrier density is usually much lower for CW in comparison to pulsed excitation. This becomes important when the non-linearities in the optical response should be avoided and the properties of an "undisturbed" system are of interest.

Finally, in case of CW excitation, all processes related to the excitation, relaxation, and recombination of carriers occur simultaneously. In a PL experiment, this leads to stable steady-state conditions, determined by the time-constants of the above-mentioned dynamics. Such a steady-state may include significant contributions from the coherent polarization, non-thermal carrier populations, as well as from hot carriers with high excess energies. Therefore, it becomes more challenging to achieve well-defined conditions in a CW PL experiment. Only if the characteristic time-constants for dephasing, thermalization and cooling are much shorter than for the recombination, one can approximately assume thermal distribution of relaxed carriers. The latter case then allows for an easier interpretation of the experimental results.

### 2.1.3 Influence of dimensionality

This subsection deals with the influence of the dimensionality on the PL properties. In principle, the majority of the processes, previously discussed in the subsection 2.1.2 for an exemplary two-dimensional structure, apply to the three-, one- and zero-dimensional cases as well. However, there are also characteristic effects, dependent on the specific dimensionality of the system. The discussion, based on the text-books [9] and [10], is focused on the most prominent phenomena, relevant for this thesis.

#### 3D: Bulk

Figure 2.10 shows a schematic absorption spectrum of a three-dimensional semiconductor structure, or *bulk*. The main difference to the QW absorption is the square-root-shaped contribution from the single-particle absorption in the plasma continuum. Also, the Coulomb-interaction is less effective in a three-dimensional system compared to the low-dimensional structures. As a direct result, a bulk crystal has the lowest exciton binding energy. However, the most important impact of the three-dimensional translation symmetry on the PL properties is the self-absorption [9]. When the light-matter coupling is strong enough, spontaneously emitted photons are quickly reabsorbed in the material,

## 2.1 Intrinsic photoluminescence properties of direct-gap semiconductors

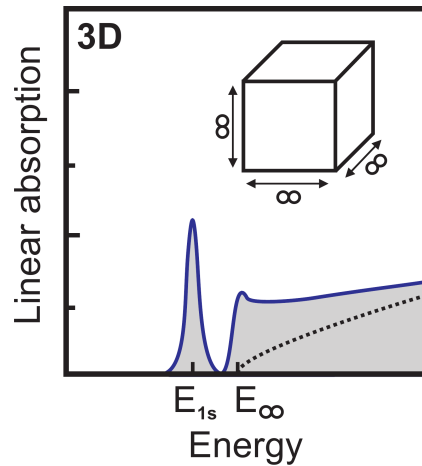


Figure 2.10: Schematic linear absorption of a three-dimensional bulk crystal. Single-particle contribution is shown by the dotted line.

leading to the formation of electron-hole pairs. The latter decay radiatively under the emission of photons which are again absorbed, and the scenario repeats. This effect is usually discussed along the concept of light-matter quasi-particles, the so-called polaritons [9, 10], illustrated in Fig. 2.11 in more detail. On the left-hand side, particle energies are plotted as function of their respective momenta. The dotted lines show the well-known linear dispersion of photons and the quadratic dispersion of excitons. A strong exciton-phonon coupling leads to the typical anti-crossing behavior of the corresponding energy bands. The photonic and excitonic properties are then mixed in a new quasi-particle, the polariton. The dispersion relation of the latter is thus composed of two bands, the so-called upper (UPB) and lower (LPB) polariton branches.

In a typical PL scenario, polaritons with high excess energies are created by the excitation pulse. They relax towards the saddle point of the LPB by emission of optical phonons. Then, a comparably slow acoustic phonon scattering becomes the dominant relaxation process, thus leading to the so-called *phonon bottle-neck* [9] in the polariton distribution. From this point on, the majority of polaritons (II) simply propagate through the crystal. Only a few (I) are scattered to the photonic-part of the LPB and can be "emitted" as photons when they reach the surface. The polariton propagation is schematically shown in Fig. 2.11 (b). The bottle-neck polaritons as well as polaritons with high momenta are scattered inside the crystal and are usually reflected at the surface since the momentum conservation inhibits the emission of photons. However, when the polariton momentum is small enough and the particle approaches the surface under an angle, smaller than the angle of total reflection, then it can be transmitted through the surface and thus be emitted as a photon, giving rise to the PL signal.

Under these restrictions and also by considering a finite polariton lifetime due to non-radiative recombination in real materials, the spontaneous emission of excitons is usually

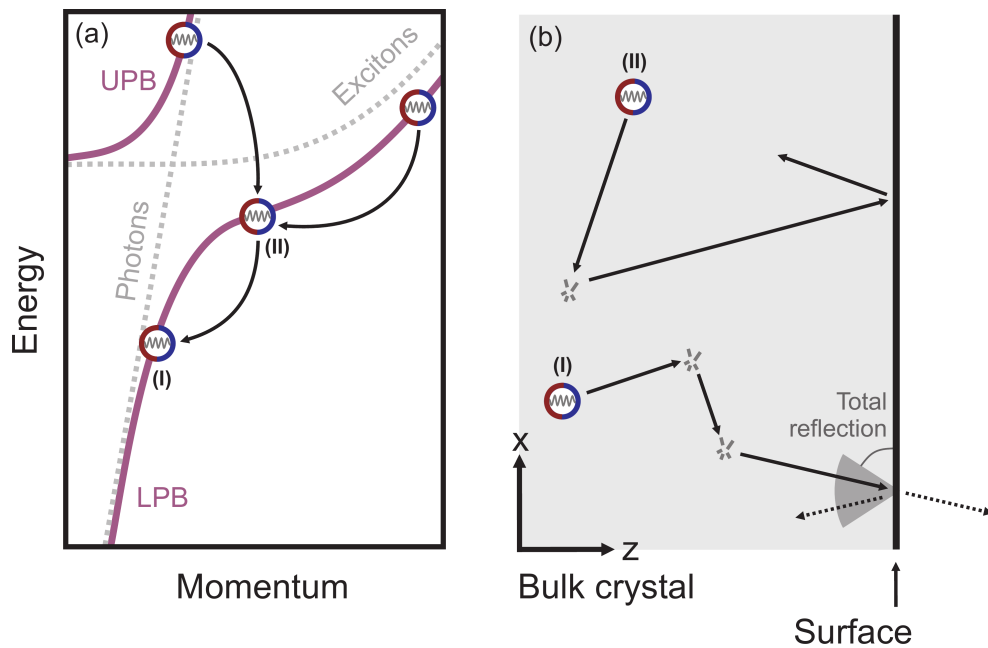


Figure 2.11: (a) Schematic dispersion relations of polaritons (solid lines), as well as photons and excitons (dotted lines). UPB and LPB mark the upper and lower polariton branches, respectively. Typical polariton relaxation processes are represented by arrows. (b) Exemplary propagation and surface recombination of polaritons in a bulk crystal.

strongly suppressed in bulk crystals. Thus, the polariton propagation effects make the interpretation of the luminescence intensities and, in particularly, of the carrier lifetimes especially challenging in case of a three-dimensional system. In addition, the influence of surface-related properties should be considered, when bulk PL is discussed. Fortunately, phonon-assisted (2.2) as well as defect-related (2.3) recombination are barely influenced by the self-absorption. Hence, these mechanisms can be used to probe bulk emission properties without significant contributions from the self-absorption.

## 2D: Quantum well

Since QW properties are discussed in-depth in section 2.1.2, this part is restricted to the direct comparison of two-dimensional to three-, one- and zero-dimensional systems. In contrast to bulk, the Coulomb-interaction is more efficient in a two-dimensional structure, leading to an increase of the exciton binding energy. Also, the light-matter coupling is stronger due to a higher dipole-overlap of the electron and hole wavefunctions, as a result of the carrier confinement. The linear absorption, shown in Fig. 2.12, exhibits the previously mentioned excitonic features as well as a spectrally flat plasma continuum. Furthermore, characteristic for all low-dimensional systems, subbands with discrete energy levels appear due to the carrier confinement (not shown here). The number of the

## 2.1 Intrinsic photoluminescence properties of direct-gap semiconductors

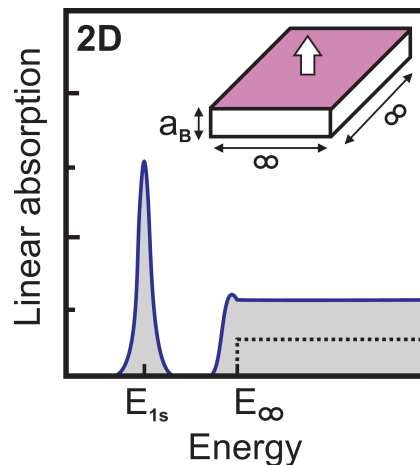


Figure 2.12: Schematic linear absorption of a two-dimensional QW. Single-particle contribution is shown by the dotted line. The direction of light emission is marked by the arrow in the sketch of the structure;  $a_B$  denotes the excitonic Bohr-radius.

subbands, as well as their specific spectral positions are determined by the depth and the shape of the confinement potential.

In a QW, the PL emission is generally not restricted by polariton propagation effects, since the translation symmetry and also momentum conservation are lifted in the  $z$ -direction, perpendicular to the QW plane. Photons are thus free to leave the material without reabsorption, as long as their  $z$ -momentum is non-zero. However, the in-plane light-matter coupling leads to the polariton formation and propagation parallel to the QW plane. Hence, the previously discussed bulk scenario applies, when the edge-PL from a QW is considered.

### 1D: Quantum wire

Quantum wires are one-dimensional systems with carriers confined in two dimensions. An illustration of the linear absorption is shown in Fig. 2.13. The Coulomb-correlations are especially strong in quantum wires and result in a further increase of the exciton binding energy in comparison to a QW. Interestingly, the Coulomb-enhancement of the continuum states is negative in one-dimension [10], leading to a decrease of the plasma absorption in comparison to the single-particle picture. The overall shape of the linear absorption thus becomes similar to that of a QW. In general, the PL properties of quantum wires also mimic the QW behavior. The PL emerges from the sides of the wire and the polariton propagation affects only the light emission along the respective length.

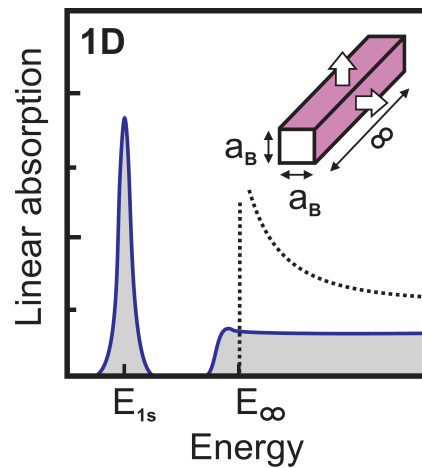


Figure 2.13: Schematic linear absorption of a one-dimensional quantum wire. Single-particle contribution is shown by the dotted line. The direction of light emission is marked by the arrows in the sketch of the structure;  $a_B$  denotes the excitonic Bohr-radius.

### 0D: Quantum dot

In quantum dots, carrier propagation is strongly limited in all three dimensions. This results in a discrete density of states (DOS), similar to atomic and molecular systems. Quantum dots are therefore often referred to as artificial atoms in the literature. A typical absorption spectrum in the vicinity of the excitonic ground state is shown in Fig. 2.14. In stark contrast to higher-dimensional systems, the spectrum is a series of Lorentzian peaks without continuum absorption. The absolute emission energy as well as the strength of the light-matter interaction, i.e., dipole-overlap of the electron-hole wavefunctions, are strongly dependent on the shape and the size of the quantum dot. In addition, the Coulomb-interaction is particularly strong for quantum dots and leads to a significant shift of the discrete transitions towards lower energies [11]. Furthermore, contributions from higher correlation effects, such as bi-excitons or even trions, significantly influence the emission spectra as well as the decay of the luminescence. These effects are most prominent for intermediate and high carrier densities. Also, due to the discrete energy levels and Pauli-blocking, the ground state of a quantum dot is saturated already at low excitation densities. Thus, the emission is often dominated by the PL from excited states and/or above-mentioned correlations. In addition, the luminescence properties are not influenced by polariton propagation, which is self-evident due to the structure's dimensions. Finally, in an ideal quantum dot, the PL is isotropic, i.e., is emitted in all spatial directions. However, real materials often show PL properties, deviating from the ideal behavior, due to the major challenges in growth and processing of zero-dimensional systems.



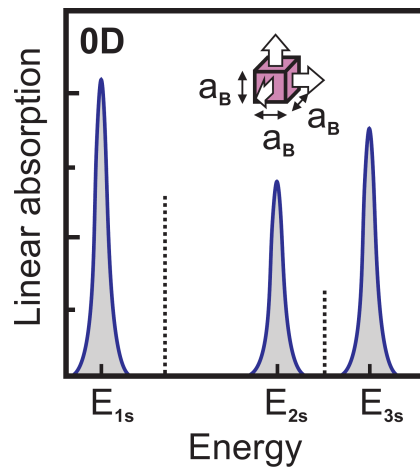


Figure 2.14: Schematic linear absorption of a zero-dimensional quantum dot. The single-particle contributions are shown by the dotted lines. The direction of light emission is marked by the arrows in the sketch of the structure;  $a_B$  denotes the excitonic Bohr-radius.

## 2.2 Role of phonons, internal fields, and the dielectric environment

Following the general discussion of the intrinsic PL properties of semiconductors, this section focuses on more specific phenomena: the first part deals with the phonon-assisted emission and, especially, with the influence of Coulomb-mediated many-body effects. Then, the impact of the internal electric fields on carrier dynamics and recombination processes in polar heterostructures is discussed. It is followed by the illustration of the PL from materials, embedded in a specific dielectric environment. Finally, the influence of the band-structure is briefly treated, focusing on the dipole selection rules and the radiative recombination in indirect semiconductors. The overall selection of topics reflects the background, essential for the interpretation of the experimental results, discussed in this thesis.

### 2.2.1 Phonon-assisted emission

In general, the interaction between electrons and lattice vibrations strongly influences the dynamics of charge-carriers in a semiconductor, and therefore the PL properties. The most prominent phenomena associated with the electron-phonon coupling are already discussed in sections 2.1.1 and 2.1.2. These include polarization dephasing, thermalization, as well as cooling of the carrier system via inelastic and elastic phonon scattering. The influence of the phonon-assisted dephasing, for example, is directly observable in the temperature dependence of the homogeneous PL linewidth, see Eq. (2.30). In addition, for

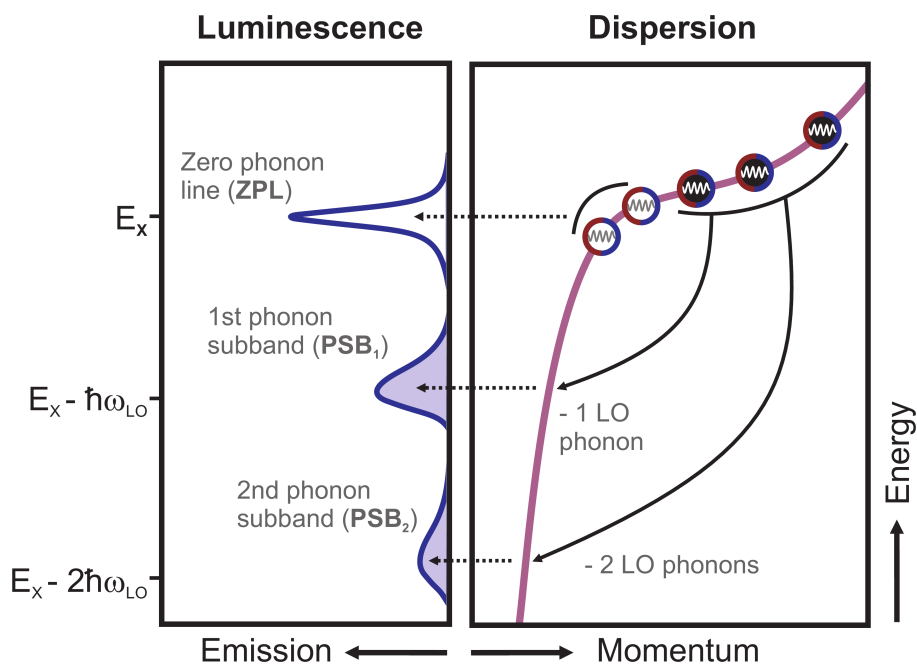


Figure 2.15: An illustration of the phonon-assisted luminescence process. The scattering of carriers on the LPB of the exciton-polariton dispersion under LO-phonon emission is shown on the right-hand side. The corresponding PL spectrum is plotted schematically on the left-hand side.

material systems with particularly strong carrier-phonon coupling, the carrier scattering with LO-phonons leads to the appearance of distinct spectral signatures in the emission spectra. These features, the so-called *phonon-sidebands* (PSBs) [9], emerge on the low-energy side of the main PL peak, and are roughly separated by multiple integers of the LO-phonon energy. An illustration of the PSB emission in a bulk crystal is schematically shown in Fig. 2.15 in polariton picture. Here, exciton-polaritons are thermally distributed on the LPB, resembling the typical scenario following the thermalization after pulsed, non-resonant excitation. As already discussed in the previous section 2.1.3, only the polaritons with sufficiently small momenta are emitted as photons at the crystal surface. These bright polaritons lead to the appearance of the main PL peak at the excitonic resonance  $E_X$ , the so-called zero-phonon-line (ZPL). Again, this transition is usually strongly suppressed in bulk crystals due to the polariton propagation effects, see discussion in 2.1.3. The rest of the polaritons with higher momenta values can not leave the crystal directly as photons and thus remain "dark". However, they can scatter to the photonic part of the LPB under the emission of LO-phonons. Then, they propagate freely through the crystal and are emitted as photons at the sample surface. This leads to the emergence of multiple PL peaks, i.e., PSBs, around  $E_X - n \cdot \hbar\omega_{LO}$ , depending on the number  $n$  of the emitted LO-phonons with the respective frequency  $\omega_{LO}$ . The spectral shape of the PSBs reflects the distribution of polaritons in momentum space and is thus asymmetric with a flat high-

## 2.2 Role of phonons, internal fields, and the dielectric environment

energy side, compared to the ZPL. The carrier-phonon coupling parameter is usually extracted from the PSB spectra by evaluating the so-called *Huang-Rhys* factor  $S$  [50]. This quantity corresponds to the average probability of the LO-phonon-emission during the radiative recombination of an electron-hole pair. The Huang-Rhys factor is obtained from the spectrally integrated photoluminescence intensities of the PSBs as follows [50, 51]:

$$S^n = \frac{I_{PSBn}}{I_{ZPL}} n! . \quad (2.42)$$

$I_{ZPL}$  and  $I_{PSBn}$  are the respective luminescence intensities of the ZPL and the n-th PSB with n as the number of LO-phonons participating in the scattering process.

Typically, PSBs are used to probe carrier-phonon interaction [52, 53] as well as various properties of the carrier system, e.g., a non-thermal distribution [34] or the temperature of thermalized carriers [54]. The traditional theoretical description of the phonon-assisted emission is based on the perturbative, quasi-single-particle approach [55]. Within this approach, the only source of the PSBs is the excitonic population, with excitons treated as purely bosonic quantities. However, the luminescence properties of the semiconductor are strongly influenced by the many-body interactions due to the Coulomb-scattering, see section 2.1.1. This is also predicted to be the case, when phonon-assisted emission is concerned. Here, the Coulomb-effects lead to a significant change in the interpretation of the PSB emission. Hence, the following discussion is based on the microscopic many-body theory, extended for the description of the PSB luminescence [11, 56, 57]. It starts with a brief illustration of the theoretical background, including phonon-assisted SLE and possible approximative approaches. The theoretical predictions are then subdivided into the discussion of the luminescence sources and the interaction mechanisms.

### Microscopic approach

The carrier-phonon coupling enters the SLE in the scattering term of the Eq. (2.23):

$$\begin{aligned} i\hbar \frac{\partial}{\partial t} \Delta \langle B_{qz, \mathbf{q}}^\dagger a_{v, \mathbf{k}-\mathbf{q}}^\dagger a_{c, \mathbf{k}} \rangle |_{scatt} &= \hbar \omega_{LO} \sum_{\mathbf{p}} [g_{c, \mathbf{p}} \Delta \langle B_{\mathbf{q}}^\dagger (D_{-\mathbf{p}} + D_{\mathbf{p}}^\dagger) a_{v, (\mathbf{k}+\mathbf{p})_h}^\dagger a_{c, (\mathbf{k}+\mathbf{p})_h - (\mathbf{q}+\mathbf{p})_e} \rangle \\ &\quad - g_{v, \mathbf{p}} \Delta \langle B_{\mathbf{q}}^\dagger (D_{-\mathbf{p}} + D_{\mathbf{p}}^\dagger) a_{v, (\mathbf{k}+\mathbf{p})_h}^\dagger a_{c, (\mathbf{k}-\mathbf{p})_e + (\mathbf{q}+\mathbf{p})_e} \rangle] \\ &\quad + i\hbar \frac{\partial}{\partial t} \Delta \langle B_{qz, \mathbf{q}}^\dagger a_{v, \mathbf{k}-\mathbf{q}}^\dagger a_{c, \mathbf{k}} \rangle |_{Coulomb} \end{aligned} \quad (2.43)$$

Here,  $g_{c, \mathbf{p}}$  and  $g_{v, \mathbf{p}}$  are the matrix elements for the LO-phonon interaction with electrons and holes, respectively. The coupling to the TO-phonons is negligible, since the lattice perturbation by charged carriers is mainly composed of longitudinal vibrations, see the discussion of polarons in Ref. [9] and the references within. Again,  $\hbar \omega_{LO}$  denotes the

## 2 Photoluminescence spectroscopy

LO-phonon energy. The renormalization of momenta is defined according to

$$\tilde{\mathbf{p}}_{e/h} = \frac{m_{e/h}}{m_e + m_h} \tilde{\mathbf{p}} \quad (2.44)$$

for an arbitrary momentum  $\tilde{\mathbf{p}}$  and the effective masses  $m_e$  and  $m_h$  of the electrons and holes, respectively. The first term on the right-hand side of the Eq. (2.43) accounts for the radiative recombination of carriers under the emission and absorption of phonons. The corresponding expectation values are the so-called phonon-photon-assisted polarizations  $\Delta\langle B^\dagger D^\dagger a^\dagger a \rangle$  and  $\Delta\langle B^\dagger D a^\dagger a \rangle$ . Since the typical LO-phonon energies are on the order of 30 meV to 100 meV [36], the phonon occupation number is negligible under the typical experimental conditions, especially at low lattice temperatures. Therefore, it is sufficient to consider only the processes involving phonon emission. The corresponding equation of motion for the polarization  $\Delta\langle B^\dagger D^\dagger a^\dagger a \rangle$  then reads:

$$\begin{aligned} i\hbar \frac{\partial}{\partial t} \Delta\langle B_{\mathbf{q}}^\dagger D_{\mathbf{p}}^\dagger a_{v,\mathbf{k}-(\mathbf{q}+\mathbf{p})_h}^\dagger a_{c,\mathbf{k}+(\mathbf{q}+\mathbf{p})_e} \rangle = & \\ & = [\tilde{\epsilon}_{\mathbf{k}}(\mathbf{q}) - \hbar\omega_{\mathbf{q}} - \hbar\omega_{LO}] \Delta\langle B_{\mathbf{q}}^\dagger D_{\mathbf{p}}^\dagger a_{v,\mathbf{k}-(\mathbf{q}+\mathbf{p})_h}^\dagger a_{c,\mathbf{k}+(\mathbf{q}+\mathbf{p})_e} \rangle \\ & + i\mathcal{F} [f_{\mathbf{k}-(\mathbf{q}+\mathbf{p})_h}^h \Delta\langle D_{\mathbf{p}}^\dagger a_{c,(\mathbf{k}+\mathbf{q})_e-\mathbf{p}_h}^\dagger a_{c,(\mathbf{k}+\mathbf{q})_e+\mathbf{p}_e} \rangle \\ & \quad - f_{\mathbf{k}+(\mathbf{q}+\mathbf{p})_e}^e \Delta\langle D_{\mathbf{p}}^\dagger a_{v,(\mathbf{k}-\mathbf{q})_h-\mathbf{p}_h}^\dagger a_{v,(\mathbf{k}-\mathbf{q})_h+\mathbf{p}_e} \rangle \\ & \quad + \sum_{\mathbf{k}'} \Delta\langle D_{\mathbf{p}}^\dagger a_{c,\mathbf{k}'+\mathbf{q}_e}^\dagger a_{v,\mathbf{k}-(\mathbf{q}+\mathbf{p})_h}^\dagger a_{c,\mathbf{k}+(\mathbf{q}+\mathbf{p})_e} a_{v,\mathbf{k}'-\mathbf{q}_h} \rangle] \\ & + \Theta_{stim} + \Theta_{Coul} + [\Theta_{num} + \Theta_0] + \Theta_{ph-corr}. \end{aligned} \quad (2.45)$$

In analogy to the Eq. 2.23 in the SLE, the first term on the right-hand side accounts for Coulomb-renormalization effects as well as for the excitonic correlations. The second term includes spontaneous emission terms due to the uncorrelated as well as the correlated electrons and holes. The stimulated emission,  $\Theta_{stim}$ , enters the first of the five scattering terms  $\Theta$  and is usually neglected under typical experimental conditions, when no cavity is applied. The next term,  $\Theta_{Coul}$ , describes Coulomb-scattering effects and is approximated by phenomenological damping for the analysis of the PSB emission. Higher-order correlations,  $\Theta_{num}$  and  $\Theta_0$ , depend on phonon occupation numbers and carrier densities in the third or even higher power, and are thus neglected for low lattice temperatures and excitation densities. Finally, the last contribution  $\Theta_{ph-corr}$  accounts for the coupling of the *one-phonon*-photon-assisted polarization  $\Delta\langle B^\dagger D^\dagger a^\dagger a \rangle$  to the *two-phonon*-photon-assisted polarizations, i.e.,  $\Delta\langle B^\dagger D^\dagger D^\dagger a^\dagger a \rangle$ . The Eqs. (2.43) and (2.45) extend the Eqs. (2.22), (2.23), (2.24), and (2.25) from the section 2.1.1 to the so-called *phonon-assisted SLE*.

In principle, the illustrated microscopic approach in electron-hole picture allows calculation of PSBs of arbitrary order. Due to the coupling of the n-th PSB to the (n+1)-th PSB,

## 2.2 Role of phonons, internal fields, and the dielectric environment

the necessary order of cluster expansion is  $(m+2)$  for the  $m$ -th PSB order. However, with all terms consistently included, the solution of the phonon-assisted SLE would exceed the resources of current supercomputers already for the computation of the second side-band [11]. Therefore, the theory has to be further simplified by additional approximations. One possibility is the calculation of the PSBs within the so-called *polaron*-picture [56]. Polaron is a quasi-particle composed of a charge carrier and a "phonon-cloud", surrounding it [9]. The polaron-picture is introduced via the unitary transformation of the Hamilton operator  $H = THT^\dagger$  with

$$T \equiv \exp \sum_{\mathbf{k}, \mathbf{p}} g_{\mathbf{p}} a_{\mathbf{k}-\mathbf{p}}^\dagger a_{\mathbf{k}} (D_{\mathbf{p}}^\dagger - D_{-\mathbf{p}}). \quad (2.46)$$

All details concerning the transformation and derivation of the equations of motion are given in Ref. [56]. The polaron approach simplifies the hierarchy of multi-phonon contributions and allows for the calculation of the PSBs with arbitrary order with a manageable numerical effort. The only disadvantage of this approximation is the underestimation of the polar carrier-phonon interaction. However, when the latter does not play a significant role, the predictions in the polaron-basis converge towards the exact results of the SLE solved in the initial electron-hole picture.

An alternative way to reduce the complexity is to apply the approximations, already introduced for the analytical solution of the SLE, i.e., the Elliott formula 2.28. The approximations assume a quasi-steady-state regime with constant thermal carrier distributions. Also, in analogy to the discussion in section 2.1.1, the regime of low densities and small broadening is considered. In addition, it is sufficient to consider only the excitonic  $1s$  ground state for the proper description of the PSBs. The phonon-assisted SLE are then solved in the exciton-basis [10]:

$$|X_{\nu, \mathbf{Q}}\rangle = \sum_{\mathbf{k}} \phi_{\nu}(\mathbf{k}) a_{c, \mathbf{k}+\mathbf{Q}}^\dagger a_{v, \mathbf{k}-\mathbf{Q}} |G\rangle. \quad (2.47)$$

Here,  $|G\rangle$  denotes the ground state of the semiconductor,  $\phi_{\nu}(\mathbf{k})$  the excitonic wavefunctions for the excited states  $\nu$ , i.e, the solutions of the so-called Wannier equation [9, 10], and  $\mathbf{Q}$  - the center-of-mass momentum. When plasma contributions are neglected, the results of the phonon-assisted SLE in the exciton-basis correspond to the perturbative treatment, illustrated in Ref. [55].

## 2 Photoluminescence spectroscopy

### Luminescence sources

For the discussion of the luminescence sources, we use the analytical solution of the phonon-assisted SLE in the exciton-basis [11]. The overall PL intensity is then given by:

$$I_{PL}(\omega_{\mathbf{q}}) = I_{PL}^{(0)}(\omega_{\mathbf{q}}) + I_{PL}^{(1)}(\omega_{\mathbf{q}}), \quad (2.48)$$

with the ZPL contribution

$$I_{PL}^{(0)}(\omega_{\mathbf{q}}) = \frac{2\mathcal{F}_q^2}{\hbar} |\phi_{1s}(r=0)|^2 \text{Im} \left[ \frac{\Delta N_{1s}^{exc}(\mathbf{q}) + N_{1s}^{eh}(\mathbf{q}) - N_{1s}^{PSB_1}}{E_{1s} - \hbar\omega_{\mathbf{q}} - i\gamma} \right], \quad (2.49)$$

and the intensity of the first PSB, under additional approximation of small exciton center-of-mass momenta  $\mathbf{Q}$ , i.e., low temperatures:

$$I_{PL}^{(1)}(\omega_{\mathbf{q}}) = \frac{2\mathcal{F}_q^2}{\hbar} |\phi_{1s}(r=0)|^2 \text{Im} \left[ \sum_{\mathbf{Q}} |\Delta g_{\mathbf{Q}}|^2 \frac{N_{1s}^{exc}(\mathbf{Q}) + N_{1s}^{eh}(\mathbf{Q})}{E_{1s} - \hbar\omega_{LO} - \hbar\omega_{\mathbf{q}} - i\gamma} \right]. \quad (2.50)$$

Again,  $\mathcal{F}_q$  denotes the light-matter coupling constant,  $\phi_{1s}$  the excitonic wavefunction,  $E_{1s}$  the absolute energy of the exciton ground state, and  $\gamma$  a phenomenological damping. The photon and LO-phonon energies are  $\hbar\omega_{\mathbf{q}}$  and  $\hbar\omega_{LO}$ , respectively.  $\Delta g_{\mathbf{Q}}$  accounts for the carrier-phonon coupling strength and is discussed in 2.2.1 in more detail. Equation (2.49) for the ZPL intensity basically resembles the Elliott formula from (2.28) for the  $1s$  luminescence. Excitons,  $N_{1s}^{exc}(\mathbf{q})$ , within the radiative cone as well as plasma,  $N_{1s}^{eh}(\mathbf{q})$ , both contribute to the spontaneous emission under the conservation of the momentum  $\mathbf{q}$ . The emission is centered at the excitonic transition  $E_{1s}$  and is homogeneously broadened with  $\gamma$ . A small deviation from the Eq. (2.28) is the renormalization of the overall ZPL intensity by  $N_{1s}^{PSB_1}$  due to the phonon-assisted recombination of electron-hole pairs. The spectrally integrated PL intensity is thus "distributed" among the ZPL and the PSBs.

The structure of the PSB contribution (2.50) is also similar to the original Elliott formula (2.28). However, in contrast to the ZPL luminescence, electron-hole pairs with arbitrary momenta  $\mathbf{Q}$  contribute to the PSB emission. Combined with the momentum dependence of the interaction matrix-element  $\Delta g_{\mathbf{Q}}$  this determines the asymmetric line-shape of the PSBs, i.e., pronounced high-energy flanks due to the distribution of carriers in momentum space. It also leads to the temperature dependence of the energy spacing between the PL maxima of the ZPL and PSB<sub>1</sub> peaks. According to the denominator in the Eq. (2.50), the PSB<sub>1</sub> maximum is shifted by the LO-phonon energy  $\hbar\omega_{LO}$  from the main excitonic transition  $E_{1s}$  at zero temperature. As the temperature increases, the maximum shifts linearly towards higher energies, following the broadening of the carrier distribution. Here,

## 2.2 Role of phonons, internal fields, and the dielectric environment

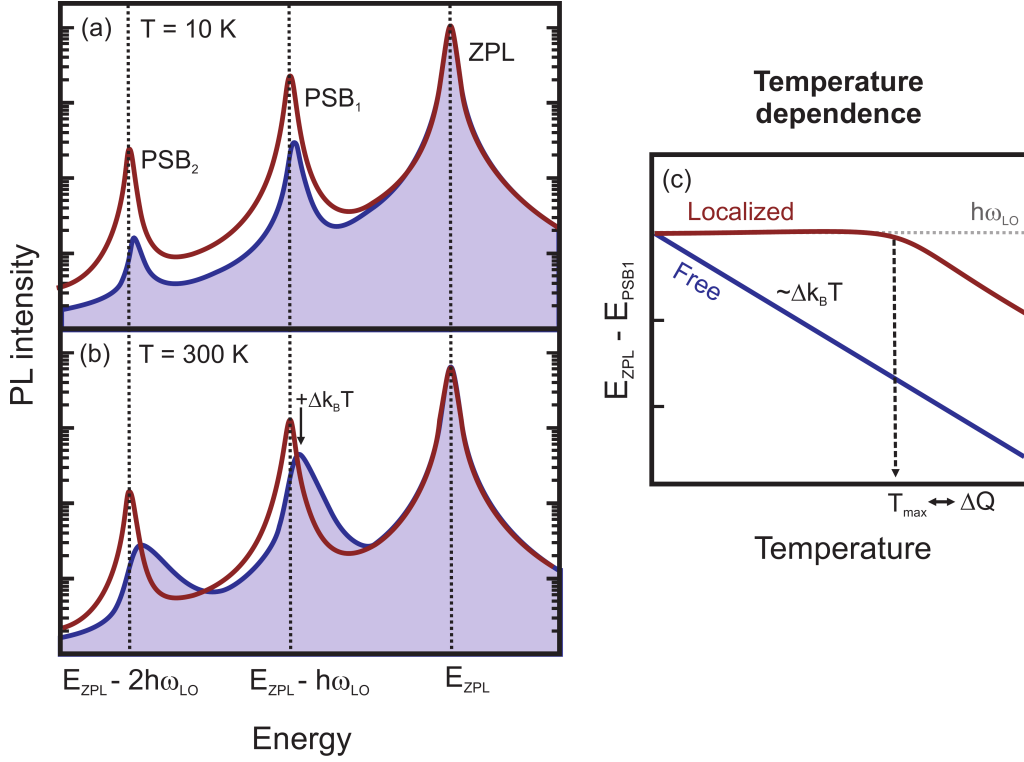


Figure 2.16: Calculated spectra of the ZPL and the first two PSBs from localized and free carriers, plotted in (a) and (b) for the lattice temperatures of 10 K and 300 K, respectively. The data is taken from the Ref. [11]. (c) Schematic illustration of the temperature dependence of the energy spacing between the ZPL and the first PSB.

the microscopic calculations qualitatively agree with the perturbative result [55]:

$$E_{PSB_1} = E_{ZPL} - \hbar\omega_{LO} + \Delta \cdot k_B T. \quad (2.51)$$

The factor  $\Delta = 3/2$  is given for the first PSB in the Ref. [55]. This temperature dependence of the ZPL-PSB<sub>1</sub> spacing can be used to characterize the PL sources in terms of spatial localization. Equation (2.51) holds for free, delocalized carriers and is based on the momentum conservation rule, applied for the ZPL luminescence. As it is already discussed in 2.1.2, the corresponding PL maximum is then defined by the radiative cone in the carrier distribution, i.e., exciton center-of-mass momentum  $\mathbf{Q} = \mathbf{q} \approx 0$ . In contrast to that, since the propagation of localized carriers is restricted to a length  $\Delta x$  in real-space, it leads to the relaxation of the momentum conservation rule according to the Heisenberg uncertainty relation

$$\Delta x \Delta Q \geq \frac{1}{2}. \quad (2.52)$$



## 2 Photoluminescence spectroscopy

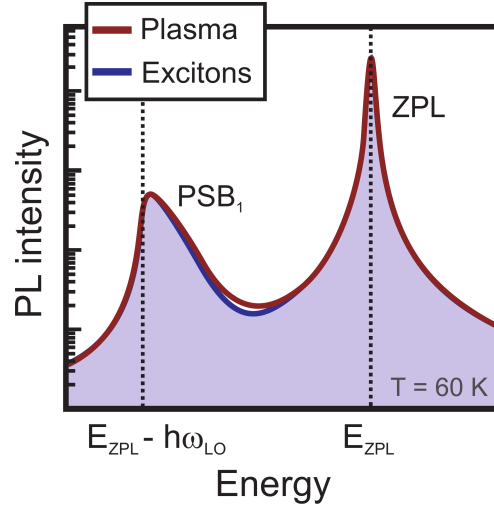


Figure 2.17: Direct comparison between the calculated PL spectra from Ref. [11] of phonon-assisted emission from excitons and plasma.

The excitonic ZPL luminescence for higher center-of-mass momenta  $\mathbf{Q} \geq 0$  thus becomes an equally possible process, compared to the  $PSB_1$  PL. In this case, the spacing between the ZPL and the first PSB,  $E_{ZPL} - E_{PSB_1}$ , is determined only by the LO-phonon energy and not by the carrier distribution. Therefore, it does not exhibit any pronounced temperature dependence.

Calculated PSB spectra from Ref. [11] for localized and free carriers are plotted in Fig. 2.16 (a) and (b) for the lattice temperatures of 10 K and 300 K, respectively, for direct comparison. The energy spacing between the ZPL and the first PSB is schematically shown in Fig. 2.16 (c) as function of temperature. In an experiment, this temperature dependence thus can be used as a characteristic signature for the emission from localized or free carriers. Furthermore, the maximum temperature  $T_{max}$  for the relaxed momentum conservation defines the uncertainty  $\Delta Q$ , when the band structure of the semiconductor is known. Hence, it allows for the estimation of the upper limit of the average localization length  $\Delta x$ , by simply using Eq. (2.52).

Aside from the effect of carrier localization, the intrinsic sources of the PSB luminescence appear in the numerator of the Eq. (2.50). These are fully correlated electron-hole pairs, i.e., excitons  $N_{1s}^{exc}$ , as well as electron-hole plasma  $N_{1s}^{eh}$ . Since both sources share the same denominator, i.e., basically the same energy dependence of the PL intensity, they cannot be distinguished directly in the emission spectra, as illustrated by the calculation results from [11], shown in Fig. 2.17. Hence, according to the microscopic theory, the appearance of the PSBs cannot be considered as an unambiguous signature for the excitonic population. The  $PSB_n$  PL from plasma at the excitonic resonances  $E_{1s} - n \cdot \hbar\omega_{LO}$  thus strongly contradicts the assumptions of the widely used perturbative treatment. The corresponding experimental proof is part of this thesis work and is given in chapter 4.1.



## Interaction mechanisms

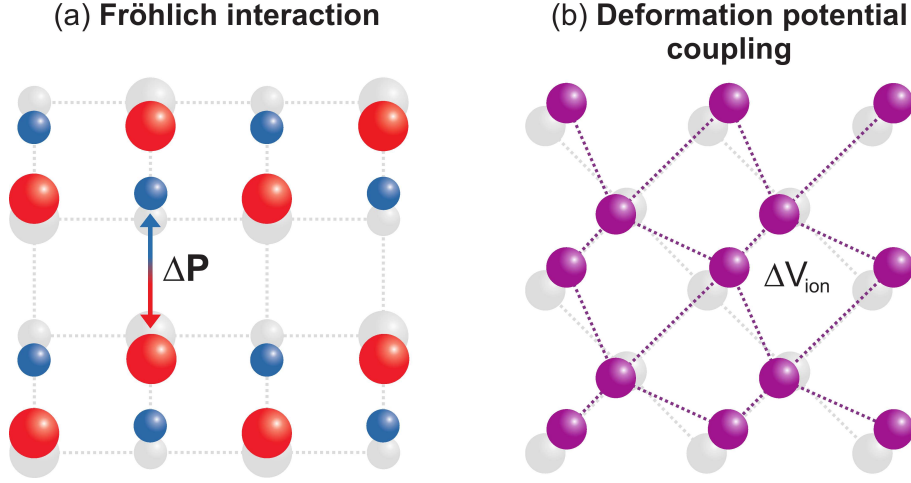


Figure 2.18: Schematic illustration of electron-phonon coupling mechanisms: polar Fröhlich interaction (a) and deformation potential scattering (b).

The inelastic scattering of charge carriers with optical phonons is commonly treated in terms of two different interactions. The first and, presumably, the most prominent mechanism is the so-called *Fröhlich-coupling* [58, 59, 60]. A schematic illustration is given in Fig. 2.18 (a). Here, an LO-phonon, i.e., the relative displacement of oppositely charged ions within the unit cells of a polar lattice, produces macroscopic polarization  $\Delta\mathbf{P}$ . Then, a single electron or hole couples directly to  $\Delta\mathbf{P}$  via Coulomb-interaction. The corresponding band-independent matrix elements for Fröhlich-scattering are [58]

$$\left|g_{c,\mathbf{p}}^{\text{Fröhlich}}\right|^2 = \left|g_{v,\mathbf{p}}^{\text{Fröhlich}}\right|^2 = \frac{e^2}{\epsilon_0 \mathcal{L}^3 2\hbar\omega_{LO}} \frac{1}{|\mathbf{p}|^2} \left[ \frac{1}{\epsilon(\infty)} - \frac{1}{\epsilon(0)} \right]. \quad (2.53)$$

Again,  $\mathbf{p}$  is the transferred momentum between a charge carrier and a phonon and  $\hbar\omega_{LO}$  - the LO-phonon energy. The expression further includes elementary charge  $e$ , vacuum dielectric constant  $\epsilon_0$ , as well as the three-dimensional normalization volume  $\mathcal{L}^3$ .  $\epsilon(\infty)$  and  $\epsilon(0)$  denote the dielectric constants for high- and low-frequencies, respectively. Since Fröhlich-interaction is mediated by the Coulomb-potential, it is long-ranged in real space and thus according to Fourier-transformation, short-ranged in momentum space. This is manifested in the reciprocal momentum dependence of the interaction strength, schematically plotted in Fig. 2.19. The interaction is thus most efficient at transferring small momenta between charge carriers and phonons.

The second carrier-phonon scattering mechanism is based on the deformation of the atomic lattice by a phonon, see Fig. 2.18 (b) for illustration. The variations of the bond lengths and angles locally change the electronic band energies. This leads to the indirect interaction of the phonon with a charge carrier via modulations of the periodic lattice

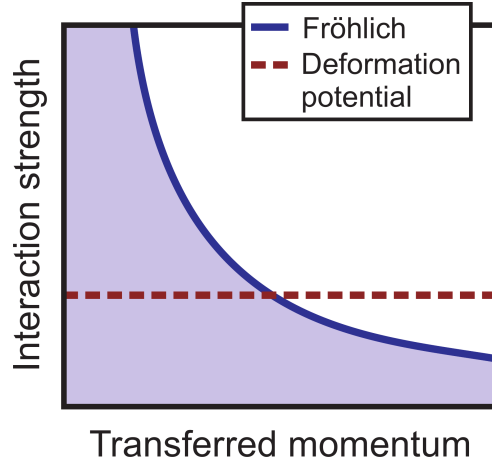


Figure 2.19: Carrier-phonon interaction strength, shown schematically as function of transferred momentum for Fröhlich interaction and deformation-potential coupling.

potential  $\Delta V$ . The process is known as *deformation potential scattering*. [9, 61, 62]. The interaction is strongly band-dependent, i.e., the corresponding matrix elements vanish in direct semiconductors for the scattering of conduction-band electrons with LO-phonons due to symmetry arguments [63, 64]. The coupling strength is given by

$$\left|g_{v,\mathbf{p}}^{Def.pot.}\right|^2 = \frac{1}{2\rho\mathcal{L}^3\hbar\omega_{LO}^3} \frac{(M_1 + M_2)^2}{2M_1M_2} \frac{|d_v|^2}{a^2}, \quad \left|g_{c,\mathbf{p}}^{Def.pot.}\right|^2 = 0, \quad (2.54)$$

where  $\rho$  is the density of the material,  $M_1$  and  $M_2$  - the masses of the two base atoms,  $\hbar\omega_{LO}$  - the LO-phonon energy, and  $\mathcal{L}^3$  - the three-dimensional normalization volume.  $\mathbf{p}$  denotes the optical deformation potential constant, and  $a$  is the lattice parameter. In contrast to the Fröhlich-coupling, the deformation potential scattering is a local interaction in real space and therefore does not depend on the transferred momentum  $\mathbf{p}$ , c.f. Fig. 2.19.

When the absolute interaction strengths of the two mechanisms are compared, Fröhlich-coupling is known to dominate carrier-phonon scattering in compound materials such as GaAs and GaP with polar contributions to atomic bonds [9, 64]. Also, it is particularly strong in wide-gap materials, like CdS, ZnO, and GaN. In addition, Fröhlich-interaction is commonly applied to describe surface-related phonon scattering [65], vibrational properties of low-dimensional systems [66], and coupling to polarons [67]. Deformation potential mechanism determines the carrier scattering with LO-phonons in non-polar materials like Si or Ge [64, 68]. It is usually neglected in polar semiconductors due to the rather weak interaction strength in comparison to the Fröhlich-coupling.

However, the many-body effects due to the carrier-carrier Coulomb-scattering introduce significant modifications to the relative contributions of the carrier-phonon interaction mechanisms. Fig. 2.20 illustrates the influence of Coulomb-effects on Fröhlich-

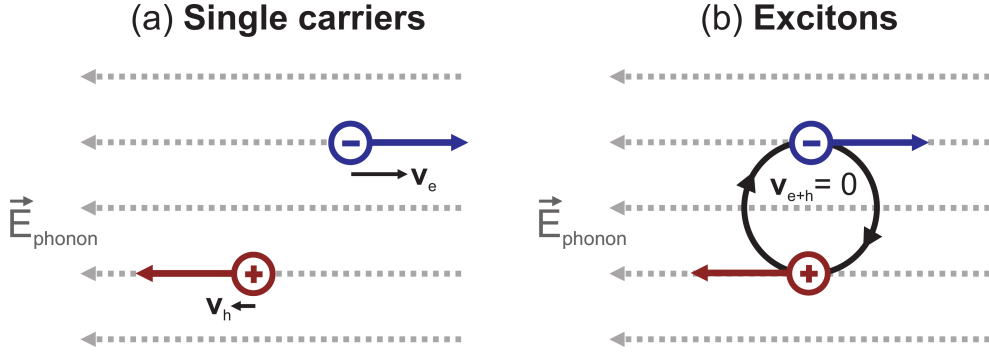


Figure 2.20: Illustration of Fröhlich-scattering mechanism in the presence of carrier-carrier Coulomb-interaction. Uncorrelated charge carriers (a) as well as excitons (b) couple to the electric field of a LO-phonon.

interaction. Even when the coupling to the electric field of a LO-phonon is strong for the uncorrelated carriers (Fig. 2.20 (a)), it becomes ineffective when electrons and holes are bound to excitons (Fig. 2.20 (b)). In the latter case, the Coulomb-forces, acting on the exciton constituents, should compensate each other due to the opposite charges of electrons and holes. Thus, polar interaction with LO-phonons should be strongly suppressed, when excitons are considered. Within the framework of the microscopic approach, this behavior is reflected in the structure of the carrier-phonon interaction matrix elements  $G_{\mathbf{p}}$ , written in the exciton-basis:

$$G_{\mathbf{p}} = \hbar\omega_{LO} \sum_{\mathbf{Q}} \phi(\mathbf{Q} + \mathbf{p}_e) [g_{c,\mathbf{p}} \phi(\mathbf{Q} + \mathbf{p}) - g_{v,\mathbf{p}} \phi(\mathbf{Q})]^*. \quad (2.55)$$

According to the previously used notation,  $\phi$  is the exciton wavefunction in momentum space,  $\mathbf{p}$  the transferred momentum,  $\hbar\omega_{LO}$  the LO-phonon energy, and  $\mathbf{Q}$  the center-of-mass momentum. The expression (2.55) easily shows that one observes only a weak Fröhlich contribution of the phonon interaction in case of band-independent single-particle matrix elements  $g_{c,\mathbf{p}} = g_{v,\mathbf{p}}$ . In particular, the interaction strength is strongly suppressed for small phonon momenta  $\mathbf{p}$ , i.e., when  $\phi(\mathbf{Q} + \mathbf{p}) \approx \phi(\mathbf{Q})$ . Notably, the absolute strength of Fröhlich interaction  $g_{c/v,\mathbf{p}}$  can be still rather high for the same specific conditions,  $\mathbf{p} \approx \mathbf{0}$ . This fact renders the polar scattering mechanism being strong but ineffective in case of excitons. In contrary, since the deformation potential scattering is a non-polar coupling, it is only marginally changed for excitons or other correlated many-body states compared with the individual carrier interaction. Hence, it should be possible to observe deformation potential-dominated PSB emission even in polar semiconductors with strong Fröhlich-coupling. The corresponding experimental evidence is part of this thesis work and is given in chapter 4.2.

The contributions of the two interaction mechanisms are distinguished by the specific

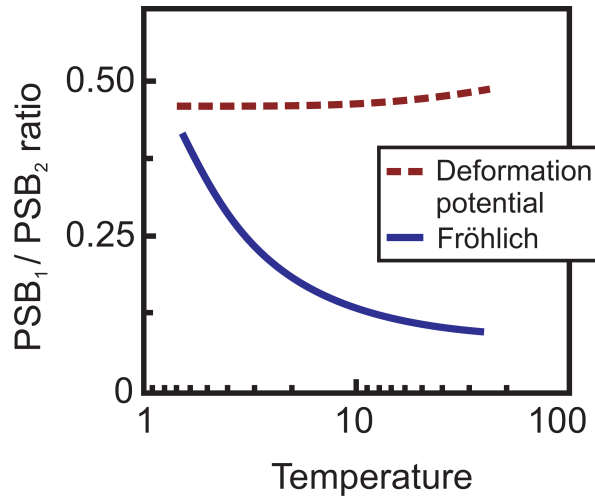


Figure 2.21: Exemplary, calculated  $PSB_2/PSB_1$  ratios as function of temperature for the two different carrier-phonon interaction mechanisms. The data is taken from Ref. [11].

temperature dependence of the PSB intensity ratios, exploiting the characteristic momentum dependencies of the respective interaction matrix elements. According to the phonon-assisted SLE, the intensities of the first two replica,  $PSB_1$  and  $PSB_2$ , depend on the phonon-matrix elements  $G$  in the second and fourth power, respectively [11]. Thus, the ratio between the  $PSB_2$  and  $PSB_1$  is roughly proportional to  $G^2$ . In general, it is determined by the distribution of carriers in momentum space, i.e., the carrier temperature, and by the dependence of  $G$  on the transferred momentum. As the temperature increases, excitonic states with higher momenta are populated. For the momentum-dependent Fröhlich interaction, the corresponding phonon-matrix elements  $G$  decrease for increasing momenta, c.f. Fig. 2.19. Thus, one expects the  $PSB_2/PSB_1$  ratio to decrease with increasing temperature when polar exciton-phonon coupling dominates the scattering processes. In case of the momentum-free deformation-potential, however, the phonon-matrix elements become constant factors in the PSB intensities. Hence, the ratio  $PSB_2/PSB_1$  does not depend on the transferred momenta and therefore on the carrier temperature. As a result, the carrier temperature dependence of the PSB-emission ratios, schematically illustrated in Fig. 2.21, offers an experimentally accessible method to identify the nature of the exciton-phonon interaction. Also, as an additional advantage, the ZPL intensity can be neglected in this analysis thus allowing for accurate PL studies of bulk semiconductor crystals.

### 2.2.2 Internal electric fields

Possible influence of static electric fields should always be considered when optical properties of semiconductor heterostructures are studied. The electric fields are either applied

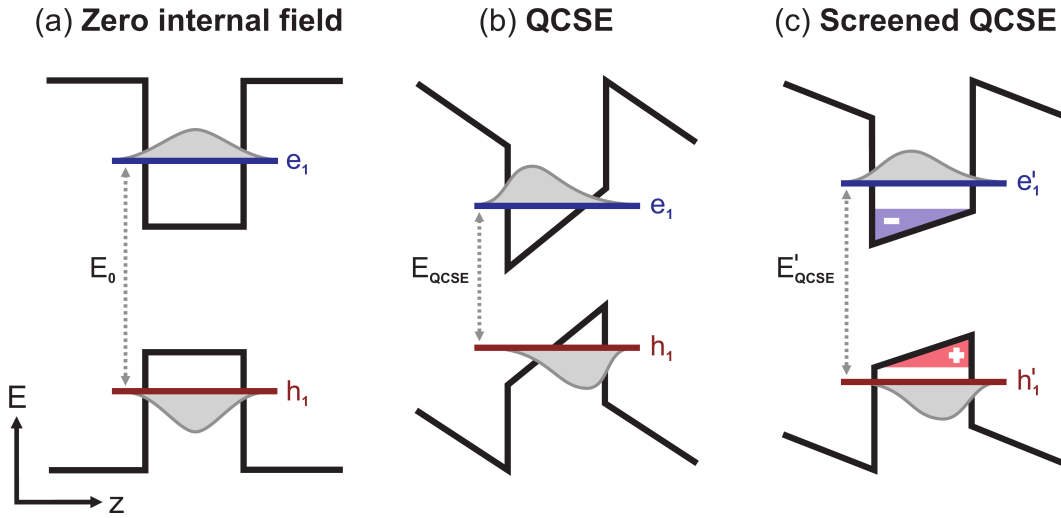


Figure 2.22: Influence of the QCSE on the energy levels and wavefunctions of carriers, confined in a QW. Zero field scenario, the effect of QCSE, as well as of partially screened QCSE are shown in (a), (b), and (c), respectively.

externally or they are intrinsically present due to the specific properties of the respective material. Here, the discussion is focused on the internal fields, relevant for the analysis of the experimental studies within the framework of this thesis. These fields result from spontaneous polarizations or from the piezoelectric effect [69]. The former occurs in polar semiconductors with a characteristic asymmetry in their crystal structure, resulting in a finite dipole moment for every unit cell. Most prominent example of such materials are wurtzites like ZnO or GaN [70]. In case of the bulk crystals, the microscopic polarization contributions compensate each other. However, they become important in structures of reduced dimensionality. Then, the effective interface-charges lead to a finite macroscopic polarization and thus to an effective electric field. The piezoelectric effect, on the other hand, describes the appearance of electric fields due the lattice distortion. In heterostructures, the latter is typically caused by strain, when materials with different lattice constants are grown on top of each other.

Figure 2.22 illustrates the influence of the electric field on the carrier energies and wavefunctions in an exemplary QW structure. The initial QW structure without an internal field is shown in (a). Confined electron and hole states are labeled by  $e_1$  and  $h_1$ , respectively. The energy of the ground state transition is denoted by  $E_0$ . When a static electric field is introduced, see Fig. 2.22 (b), the carrier energy levels shift, and the wavefunctions become asymmetric due to the altered potential profile. In analogy to the well-known Stark effect in atomic systems, this phenomenon is commonly labeled as *quantum-confined Stark effect* (QCSE) [71, 9]. The shift of the energy levels leads directly to the decrease of the band-gap  $E_{QCSE}$  and thus of the PL energy. Since the strength of the internal fields can reach considerable magnitudes up to several MV/cm [72], the PL maximum of a QW can

## 2 Photoluminescence spectroscopy

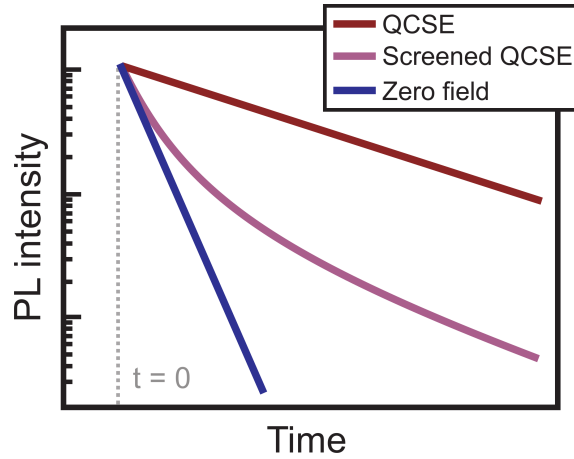


Figure 2.23: PL transients of a QW emission after pulsed excitation in case of the zero-field scenario, QCSE, as well as of screened QCSE.

easily shift below the bulk value due to the QCSE. In addition, the decrease of the dipole-overlap of the electron and hole wavefunctions leads to a lower coupling strength of the QW to the light-field, i.e., to slower radiative recombination. Also, the exciton binding energy decreases due to the spatial separation of carriers. In general, the overall strength of the QCSE-related effects increases with the magnitude of the internal field as well as with the width of the QW.

In a PL experiment, the influence of QCSE on the emission properties is most prominent at low carrier densities. However, as the density of the photoexcited carriers increases, the static electric field is successively screened by charged electrons and holes [10, 73]. The characteristic time scale  $\tau_S$  for the build-up of screening roughly corresponds to the inverse plasma frequency  $\omega_{pl}$  [9, 74]:

$$\tau_S \approx \omega_{pl}^{-1} = \left( \frac{e^2 n}{m^* \epsilon_0 \epsilon} \right)^{-1/2} \quad (2.56)$$

Here,  $e$  is the elementary charge,  $n$  - the carrier density,  $m^*$  - carrier effective mass,  $\epsilon_0$  - vacuum dielectricity, and  $\epsilon$  - the dielectric constant of the semiconductor. As a result of the screening, the effective electric field is reduced and the QCSE-phenomena are weakened, see Fig. 2.22 (c). The carrier ground states shift to higher energies and the spatial separation of the electrons and holes decreases. Hence, the light-matter coupling becomes stronger and the radiative recombination rate increases.

The impact of QCSE on carrier dynamics is illustrated in Fig. 2.23. Characteristic PL transients after a pulsed excitation are shown for the three cases of the zero-field scenario, the QCSE, as well as of the screened QCSE. A single-exponential decay of excitons is assumed for the unperturbed QW. In case of the QCSE, the decay is significantly longer due

to the weaker dipole-coupling, yet the dynamics still remain single-exponential. However, when the QCSE is screened, the carrier recombination becomes again fast, but only short after the excitation. At the later times, the carrier density and thus the amount of screening decrease. Then, the decay rate approaches low-density conditions of an unscreened QCSE, leading to a non-exponential PL transient.

### 2.2.3 Influence of the dielectric environment

In most PL experiments, the dielectric environment is basically the interface between the material under study with the refraction index  $n$ , higher than 1, and the air or vacuum with  $n \approx 1$ . Aside from reflection (see Fig. 2.11), the influence of this interface on the PL properties is rather weak, especially for low-dimensional structures. However, there are specific cases when the dielectric surroundings of the sample can not be neglected. In particular, active materials, processed for the integration in an optical device, e.g., in a laser, are often embedded in a complex dielectric structure. The latter strongly affects the emission properties [75, 76] and should always be considered to avoid possible misinterpretations of the experimental data.

In this subsection, the influence of the dielectric environment is discussed for an exemplary case of a QW inside a Fabry-Perot resonator [77]. The PL from a free-standing QW is schematically plotted in Fig. 2.24 (a). The asymmetric broadening of the sample emission represents the case of high carrier densities [24, 39], corresponding to the typical excitation conditions of a laser device. The dielectric structure of the Fabry-Perot cavity is represented by the reflection spectrum, shown in Fig. 2.24 (b). In contrast to vacuum, there are allowed and forbidden modes of the electric-field, i.e., photon states, inside the resonator. Here, the mode structure is determined by the Fabry-Perot conditions [77]. The photon states within the cavity are quantized; the respective energies correspond to the minima in the reflection spectrum. Hence, only these photons are allowed to enter the resonator, the rest is simply reflected. In addition, according to the Heisenberg uncertainty principle, the transmission peaks are homogeneously broadened due to the finite lifetime of the photons, determined by losses inside the cavity. In analogy to the reflection, the emission of photons within the resonator is only allowed when their energies match the cavity-modes. Thus, the initial PL spectrum is modified according to the dielectric structure. As shown in Fig. 2.24 (c), the QW emission now exhibits a series of peaks, centered at the reflection minima of the resonator. The relative amplitudes of the peaks are determined by the original spectral shape of the PL, c.f. Fig. 2.24 (a).

Within the framework of the microscopic many-body theory, the dielectric surroundings of a semiconductor determine the photon dispersion  $\hbar\omega_{\mathbf{q}}$  from Eq. (2.4) in section 2.1.1. The resulting higher-order effects, such as the coupling between the cavity-modes and the active material are beyond the scope of the phenomena studied in this thesis and



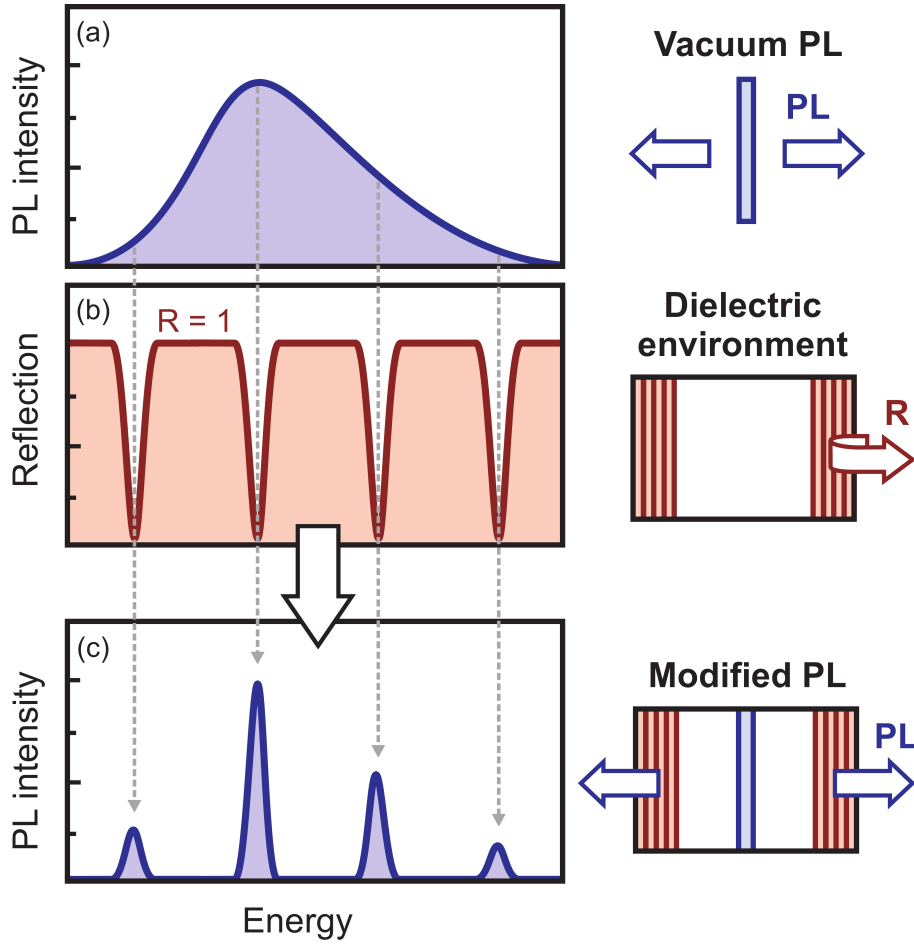


Figure 2.24: Schematic illustration of the influence of the dielectric environment on the PL emission for the exemplary case of a QW inside a Fabry-Perot resonator: (a) PL spectrum of the free-standing QW, (b) reflection spectrum of the dielectric structure, (c) emission of the QW, modified by the cavity. Allowed resonator modes are shown by the dashed arrows.

are thus omitted. The reader is referred to [25] for further details. Approximately, the impact of the specific mode-structure on the PL emission is treated by multiplying the PL intensity  $I_{PL}$  by the so-called filter function  $F_{\mathbf{q}}$ , see Ref. [78]:

$$I_{PL}^{diel.}(\omega_{\mathbf{q}}) = F_{\mathbf{q}} \left[ \frac{\partial}{\partial t} \Delta \langle B_{\mathbf{q}}^{\dagger} B_{\mathbf{q}} \rangle \right]. \quad (2.57)$$

As in the Eq. (2.21),  $B_{\mathbf{q}}^{\dagger}$  and  $B_{\mathbf{q}}$  are creation and annihilation operators of photons with momenta  $\mathbf{q}$ , respectively.  $F_{\mathbf{q}}$  is computed by evaluating the reflection and transmission of light in the dielectric environment.



### 2.2.4 Impact of the band structure

The subsection briefly summarizes the influence of the specific band structures on the PL properties. Since the corresponding scientific field is rather broad [9], the discussion is focused on the topics, relevant for this thesis: dipole selection rules and the luminescence in indirect-gap semiconductors.

#### Selection rules

In general, the dipole selection rules define the conditions, when the radiative dipole matrix element  $\mathcal{F}_{\mathbf{q}}$ , see Eq. (2.7) is non-zero. They are mainly based on symmetry arguments but also incorporate momentum conservation, e.g., the well-known relation for the change of the magnetic quantum-number [42]:  $\Delta m = \pm 1$ . The selection rules determine the transitions, directly accesible in absorption and emission of single photons. In QWs, for example, the conservation of the quantization number allows only the excitation and recombination of electrons and holes within the subbands  $e_n$  and  $h_n$  with equal indices  $n$ , c.f. Fig. 2.3. In addition, dipole rules may also imply a specific polarization of the incident and emitted electric field. This last point is most important for the experiments discussed in chapters 4 and 5.

A schematic illustration of the dipole-allowed transitions is shown in Fig. 2.25 for the two, presumably most-prominent, direct-gap semiconductor crystal structures: *zinc-blende* (e.g. GaAs, AlAs, InAs) and *wurtzite* (e.g. GaN, CdS, ZnO) [27]. In case of the zinc-blende crystals (a), the interband transitions couple to the circularly polarized ( $\sigma$ ) photon eigenstates, according to the conservation rule  $\Delta m = \pm 1$ . The exact rotating direction of the electric field only defines the electron and hole population with specific spin quantum-numbers [79]. However, aside from the spin populations, transitions from all valence bands, i.e., the heavy-hole (hh), the light-hole (lh), and the split-off (so) to the conduction band can be excited with arbitrary polarized light due to the cubic symmetry of the crystal structure [36].

The hexagonal wurtzite lattice exhibits an intrinsic asymmetry in one spatial direction, the so-called *c-axis* [27]. This leads to the splitting of the two top-most valence bands, degenerated in case of a symmetric zinc-blende structure. The valence bands are usually labeled from top to bottom by A, B, and C [36]. The asymmetry also implies specific selection rules for the polarization of the absorbed and emitted light with respect to the *c-axis*. For all valence bands, the optical transitions require linearly polarized ( $\pi$ ) light. The A-band couples only to the electric-field  $\mathbf{E}$ , perpendicular to the *c-axis*. In contrast to that, the excitation of the C-band holes requires light, which is polarized co-linearly with the *c-axis*. The B-band is accessed with both polarizations with equal transition probabilities. A small deviation from these selection rules, typical to the standard wurtzite semiconductors

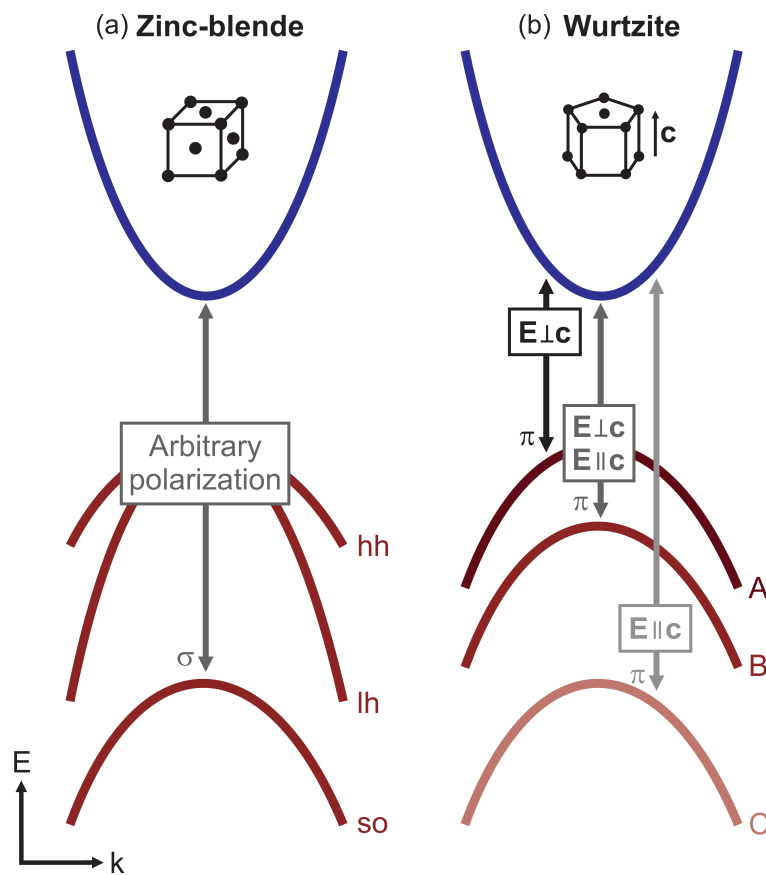


Figure 2.25: Simplified illustration of zinc-blende (a) and wurtzite (b) band structures in momentum space. The arrows show the dipole-allowed transitions with the corresponding selection rules for the polarization of the light field  $\mathbf{E}$ . Circular polarization is represented by  $\sigma$  and linear polarization by  $\pi$ . "hh", "lh" and "so" denote the heavy-hole, light hole, and split-off bands, respectively. The valence bands in the wurtzite structure are typically labeled "A", "B" and "C".

like GaN or CdS [80], occurs in case of the ZnO. Here, the B-band couples only to the perpendicularly polarized light with respect to the c-axis [81, 82], in analogy to the A-band. This issue was partly responsible for the controversial discussions of the valence band symmetries in ZnO [81, 83, 84].

### Indirect-gap semiconductors

The discussion in the previous sections is based on the properties of direct-gap semiconductors. Here, the influence of an indirect band-gap on the light emission and carrier dynamics is briefly discussed. A generic band structure for an indirect material is shown in Fig. 2.26 in momentum space. Naturally, as the main feature in the band alignment, the absolute minimum of the conduction band is not at the center of the Brillouin zone,

## 2.2 Role of phonons, internal fields, and the dielectric environment

i.e., the  $\Gamma$  point [27]. However, a local conduction band minimum is deliberately placed at  $\Gamma$ , typical for the band structure of Ge-based materials [36], investigated in this work. In an experiment, when electrons are excited within this quasi-direct valley, they either recombine radiatively or scatter and relax towards the indirect gap; the corresponding characteristic times are  $\tau_{direct}$  and  $\tau_{relax}$ , respectively. Since typical inter-valley scattering processes are extremely fast, i.e., on a sub-ps timescale [85], the relation  $\tau_{relax} \ll \tau_{direct}$  holds true in the most cases. In addition to the radiative recombination at  $\Gamma$ , indirect luminescence is also possible. In the latter case, however, in stark contrast of the emission from electrons in holes at the quasi-direct gap with nearly equal momentum values, i.e.,  $\Delta\mathbf{k} \approx 0$ , the conservation rules require a transfer of considerable momentum difference  $\Delta\mathbf{k} \gg 0$ . Hence, the radiative indirect-gap recombination is usually assisted by phonons and is thus much slower, than the  $\Gamma$ -emission, i.e.,  $\tau_{indirect} \gg \tau_{direct}$  [86]. Only in systems of reduced dimensionality, momentum transfer by scattering at the interfaces [87] and/or localization of carriers due to the interface fluctuations [88], i.e., delocalization in momentum-space, provide a finite probability for the zero-phonon transitions.

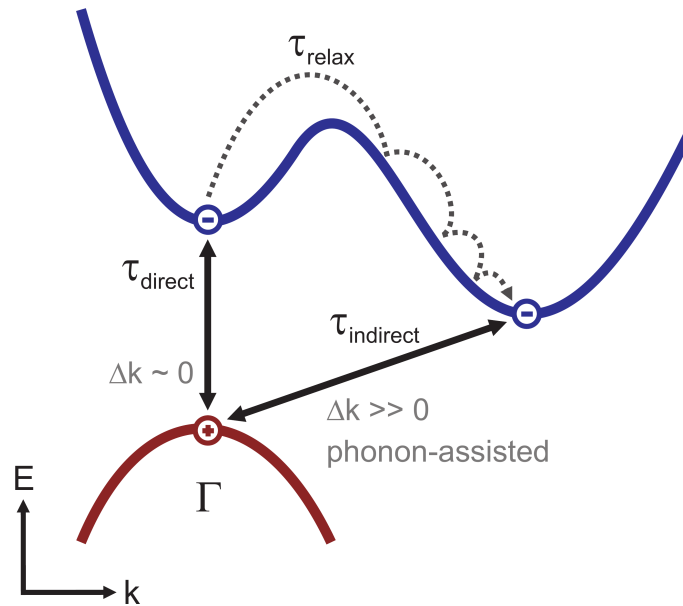


Figure 2.26: Schematic band structure of an indirect material in momentum space, with an illustration of the main carrier relaxation and recombination processes.

## 2.3 Extrinsic photoluminescence properties: defects and disorder

This section illustrates the influence of defects and disorder on the emission properties of a semiconductor. In the previous two sections 2.1 and 2.2, ideal, defect-free crystals were assumed. However, the lattice of real materials deviates more or less from the ideal, strictly mathematical ordering of atoms. To some extent, semiconductors always incorporate defects, impurities, as well as spatial fluctuations of the band structure parameters, i.e., disorder. Since all materials are grown at finite temperatures significantly higher than absolute zero, imperfections are inevitably introduced to the crystal lattices simply due to the elementary thermodynamics, i.e., the interplay between energy and entropy in the system. In addition, the quality of real semiconductors is further degraded by growth imperfections. Naturally, in well-established material systems like Si or GaAs, the defect concentrations are extremely low due to the optimized growth conditions, systematically developed over decades. However, in less established, novel semiconductor structures, defects and disorder can still play a significant role with respect to the energy structure as well as carrier dynamics. Also, a controlled introduction of impurities to the semiconductor crystals, i.e., doping [9], is often used for selective altering of the specific electro-optical properties. Thus, understanding the role of material imperfections is crucial for the proper analysis of the experimental findings.

The first part of this section starts with a brief description of defects and their influence on PL spectra and carrier dynamics. The discussion in this subsection is mainly based on the textbooks on semiconductor physics [4, 9]. In the second part, the disorder-related properties of semiconductors are discussed and a quantitative analysis scheme is presented.

### 2.3.1 Defects

#### Types of defects

The defects in semiconductors are typically classified in *structural defects* and *chemical impurities*. They are further subdivided according to their respective dimensionality. Here, we focus on the zero-dimensional defects, the so-called *point-defects*, since this type is the most abundant in real materials. In addition, the influence of point-defects on the PL properties is very similar to the impact of defects with higher dimensionality. For more detailed discussion of the latter, the reader is referred to the standard textbooks, e.g., Ref. [4].

An overview of typical point-defects is given in Fig. 2.27 for an exemplary case of a polar cubic lattice. The typical structural defects are various misplacements of the two

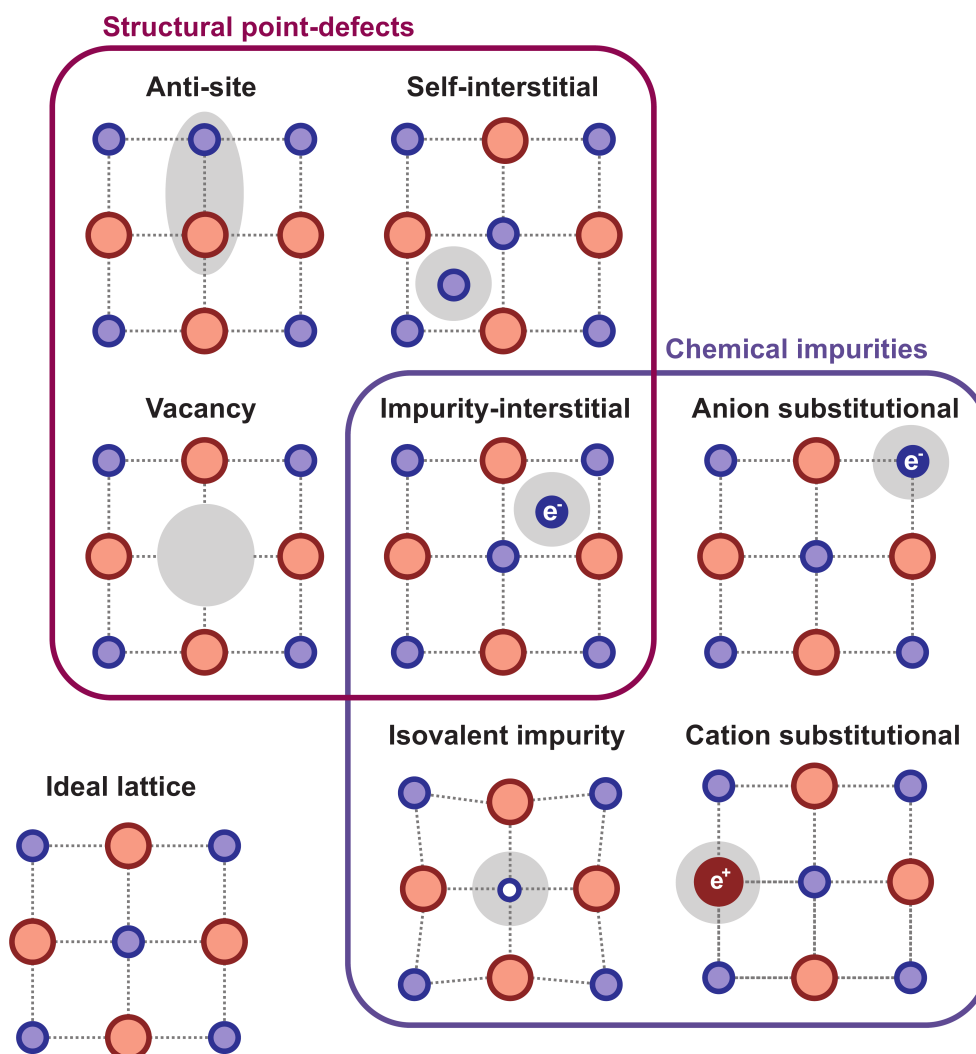


Figure 2.27: A schematic overview of the different point-defect types in a polar lattice.

original atoms in contrast to the ideal crystal structure. These are the *anti-sites*, *self-interstitials*, as well as *vacancies*. In general, the structural defects may also involve changes of the bond lengths and angles. The chemical impurities are various extrinsic atoms incorporated in the original crystal during growth, e.g., as sub-products of gas-epitaxy or desorbed from the chamber walls in molecular-beam epitaxy like hydrogen and carbon. Depending on their respective chemical group, these atoms are typically *anion-* or *cation-substitutionals*. However, the chemical impurities can also be found as interstitials, combining their specific chemical nature with the properties of a structural defect. An additional special case are the so-called *isovalent impurities*. These are the atoms within the same chemical groups as the intrinsic crystal constituents. When the isovalent impurities significantly differ in size and electronegativity from the latter, they strongly perturb the lattice thus acting almost like structural defects.

In general, the electronic structure of the defects is an atom-like sequence of quantized

## 2 Photoluminescence spectroscopy

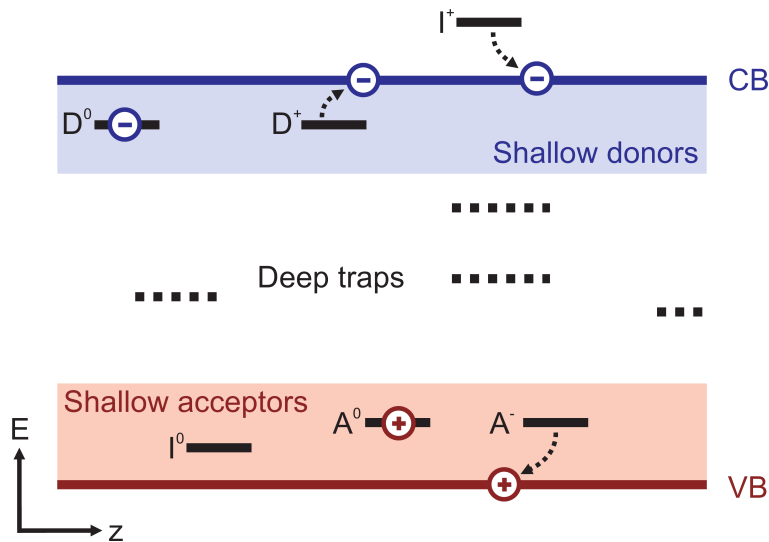


Figure 2.28: Representative scheme of energy levels of point-defects in a semiconductor band structure.

states. The important states determining the optical properties are those with energies inside the band gap of the host material. Typical energy levels of the point-defects are shown in Fig. 2.28 in the real-space semiconductor band structure. The defects, both structural as well as chemical, are subdivided in *shallow* and *deep*, according to the position of the corresponding energies relative to the band edges. Shallow defects are categorized in donors ( $D$ ) and acceptors ( $A$ ), lying close to the conduction and valence bands, respectively. These defects are responsible for the doping of the semiconductor and are thus in neutral or ionized states, depending on the lattice temperature, i.e.,  $D^0$  and  $D^+$  in case of donors, and  $A^0$  and  $A^-$  for acceptors. Isovalent impurities ( $I$ ) can be found either within the band gap or above (below) the conduction (valence) band [89, 90]. Finally, the defect states close to the middle of the band gap are conveniently labeled as the *deep traps*.

### Influence of defects on the photoluminescence

The influence of defects and impurities on the emission properties is illustrated in Fig. 2.29: a typical PL spectrum of a semiconductor with comparably high defect density is shown. The inset of Fig. 2.29 gives a brief illustration of the corresponding carrier dynamics. Here, we assume that the charge carriers are already bound to excitons which is a highly probable scenario for the wide-gap materials studied in this thesis. According to the previous discussion, the radiative recombination of the so-called *free* excitons (FX), provides dominant contribution to the luminescence at the excitonic resonance. Apart from the direct emission, the excitons can be trapped, i.e., localized, by shallow and deep defects. In case of the shallow donors ( $D$ ) and acceptors ( $A$ ), this leads to pronounced luminescence peaks just below the FX-transition; the emission of the ionized defects is slightly shifted

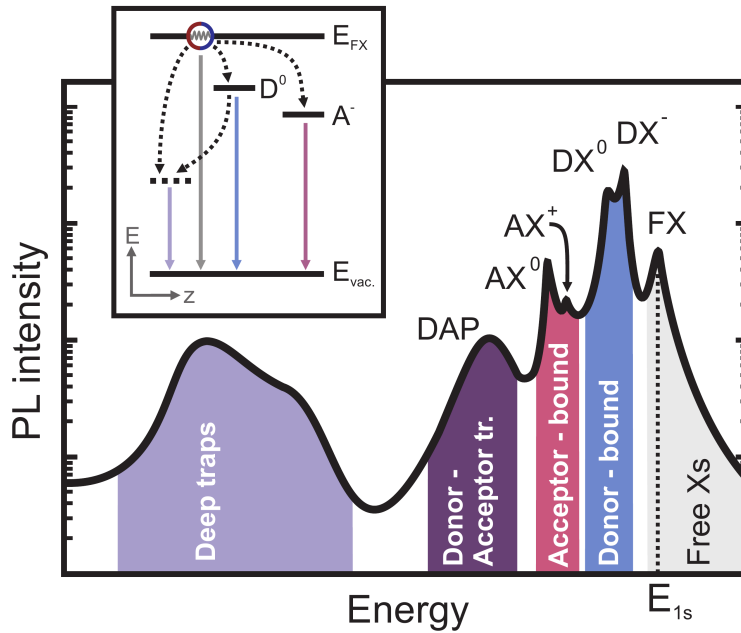


Figure 2.29: A typical spectrum of a semiconductor material with significant contributions from defects and impurities. Possible emission peaks due to the scattering with LO-phonons are omitted for clarity. The inset shows a schematic illustration of the corresponding carrier dynamics in the exciton picture. The ground state of the free excitons and the vacuum level are labeled by  $E_{FX}$  and  $E_{vac.}$ , respectively.

to higher energies in comparison to the neutral ones. According to the so-called *Haynes-rule* [91], the binding energy of excitons to the neutral impurities, e.g., to donors  $E_{DX^0}^B$ , is proportional to the ionization energy  $E_{D^0}$  of the respective defect state. The emission energy  $E_{DX^0}$  thus obeys:

$$E_{DX^0} = E_{FX} - E_{DX^0}^B = E_{FX} - m \cdot E_{D^0}, \quad (2.58)$$

with the material parameter  $m$  between 0 and 1. The corresponding recombination dynamics generally depend on the dipole-overlap of the bound exciton wavefunctions as well as on the local environment of the defect state, e.g., the presence of additional traps. Hence, the PL decay is typically single-exponential for isolated impurities, but can exhibit arbitrary behavior, when an ensemble of defects with different surroundings is considered. Also, the luminescence peaks from bound excitons are usually present in the PL spectra only at low temperatures. As the temperature increases, bound excitons are eventually ionized and the FX luminescence with the corresponding PSBs dominate the PL, e.g., see Ref. [92, 93].

At sufficiently high concentrations of shallow impurities, additional PL signatures, the

## 2 Photoluminescence spectroscopy

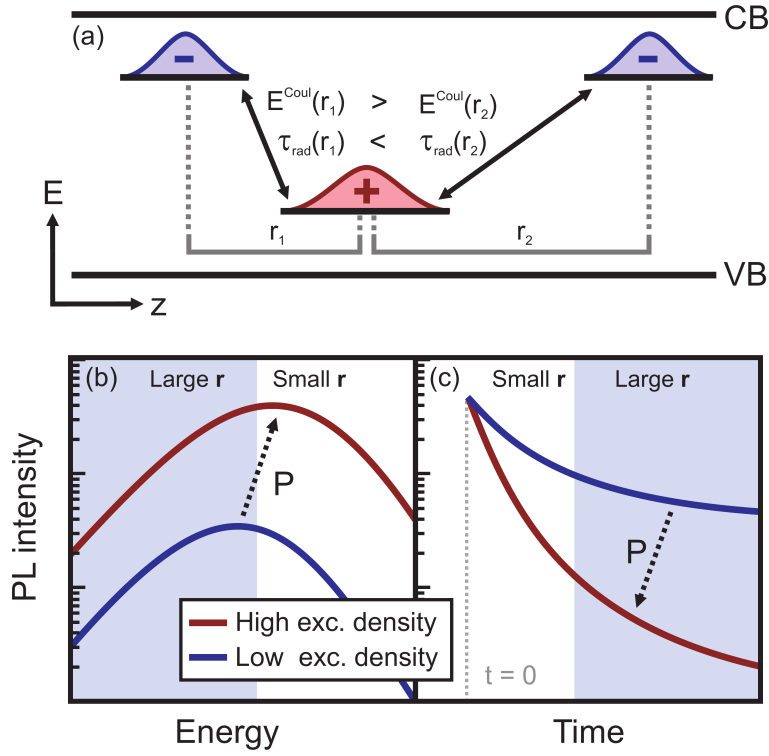


Figure 2.30: Illustration of the DAP recombination process (a) with the corresponding density dependencies of the PL spectra (b) and emission dynamics (c).

so-called *donor-acceptor-transitions* (DAPs) [9], appear in the emission spectra. They result from the radiative recombination of single electrons and holes, bound to donors and acceptors, respectively. The recombination process is schematically illustrated in Fig 2.30 (a). The emission energy of the DAP transition depends on the carrier binding energies  $E_{D^0}$  and  $E_{A^0}$  as well as on the Coulomb-interaction between the two carriers with the opposite charges [94]:

$$E_{DAP} = E_{FX} - E_{D^0} - E_{A^0} + E^{Coul}(r); \quad E^{Coul}(r) = \frac{e^2}{4\pi\epsilon_0 r^2}. \quad (2.59)$$

Here,  $e$  denotes the elementary charge and  $\epsilon_0$  - the vacuum dielectric constant. The signature of the DAP recombination is the reciprocal quadric dependence of the Coulomb-term on the distance  $r$  between the corresponding donor and acceptor. This mainly determines the characteristic signatures of the DAPs in the emission spectra and transients, shown in Fig. 2.30 (b) and (c), respectively. In a PL experiment, carriers are randomly distributed among donors and acceptors after the excitation, resulting in an ensemble of DAPs with different spacings  $r$  and therefore different emission energies, according to Eq. (2.59). Hence, the DAP luminescence peak is rather broad in comparison to the bound exciton PL from the isolated impurities, c.f. Fig. 2.29. Also, the radiative recombination time



### 2.3 Extrinsic photoluminescence properties: defects and disorder

$\tau_{rec}(r)$  of a pair-transition increases with the decreasing distance  $r$  due to a higher dipole-overlap of the corresponding electron and hole wavefunctions, leading to a characteristic non-exponential decay of the DAP luminescence, see Fig. 2.30 (c). Naturally, as the excitation power is increased a higher number of impurity states is populated. This results in an increased probability of finding an electron on a donor site close to an acceptor-bound hole and vice versa. Thus, the mean distance of the populated DAPs decreases and the PL energy as well as the decay rate both increase. This characteristic dependence of the PL properties on the excitation density is a strong indication for the DAP-related emission.

In addition to the localization at shallow impurities, carriers can be efficiently captured by the deep traps. The relaxation is followed by the recombination of electrons and holes via interaction with phonons and/or photon emission. The resulting PL is often strongly broadened due to the fluctuations of the local environment of the defect states as well as being a result of the carrier-phonon scattering. The emission peak is also shifted to lower energies with respect to the band gap, usually by many 100's of meV, see, e.g., Refs. [95, 96]. Thus, the PL from the deep traps is typically not observed in a standard PL experiment which often focuses on the study of the near-band gap luminescence. On the contrary, the carrier-capture processes by various deep impurities are considered as extrinsic non-radiative recombination channels for the band-edge PL. Depending on the defect concentration, these processes can strongly affect or even limit carrier lifetimes, leading to a fast PL decay as well as to low quantum efficiencies [9]. The latter is defined as the ratio between the radiative and the full recombination rates.

In an experiment, only a simultaneous measurement of the absolute PL intensity and the decay time allows to separate the non-radiative from the radiative recombination and thus to determine the corresponding time-constants. Unfortunately, in the most cases, the absolute PL data is not available. However, strong contributions from the non-radiative recombination channels are often identified by the characteristic features in the power and temperature dependencies of the PL intensity and decay time, see Fig. 2.31. Typically, the lifetime of carriers trapped in the deep states is much longer than both relaxation and radiative recombination times of the free carriers [97, 98]. Hence, when the excitation density is high enough, i.e., it approaches or even exceeds the density of the traps, the latter become more and more saturated. As a result, due to the Pauli-blocking, the non-radiative recombination time and thus the PL decay time both increase, c.f. Fig. 2.31 (a). The resulting rise of the quantum efficiency leads to a superlinear dependence of the relative PL intensity  $I_{PL}$  on the excitation density  $I_{exc}$ , shown in Fig. 2.31 (b), c.f. Ref. [99].

Aside from the excitation density, the rate of the non-radiative recombination is strongly influenced by the lattice temperature. Since the thermal velocity of the photo-excited carriers increases with temperature, both electrons and holes get a higher probability to reach randomly distributed traps and thus recombine non-radiatively. According to the

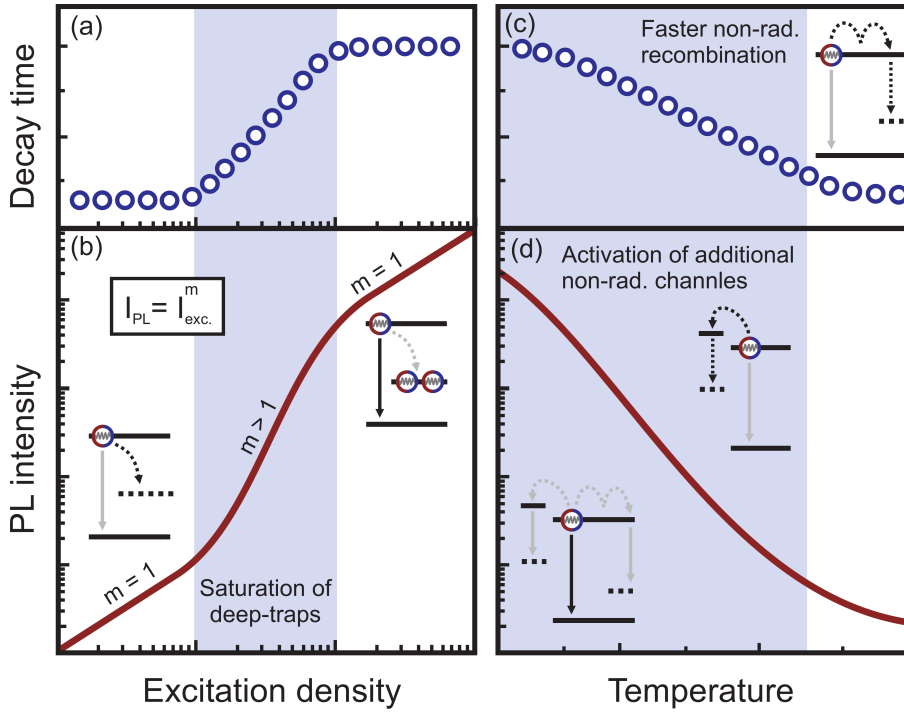


Figure 2.31: Influence of the excitation power (a,b) and lattice temperature (c,d) on the decay time and relative intensity of the PL emission is illustrated for the case of major contributions from non-radiative recombination channels to the carrier dynamics. The grey and black arrows in the included schematics denote relaxation processes with low and high probabilities, respectively.

*Shockley-Read-Hall* (SRH) model [4, 100], the capture rate is proportional to the square root of the lattice temperature. Also, additional non-radiative channels, e.g., surface states, are activated as the temperature increases [101, 102]. For the quantitative analysis, a phenomenological thermal activation model is used [101]. Within the framework of this model, the basic expression for the PL intensity  $I_{PL}$  reads:

$$I_{PL} \propto \left( 1 + A e^{-\frac{E_a}{k_b T}} \right)^{-1}. \quad (2.60)$$

Here,  $A$  denotes the relative increase of the non-radiative capture probability for a state with an activation energy  $E_a$ , compared with the recombination rate at  $T=0$  K. Hence, both SRH and thermal activation effects lead to a decrease of the PL decay time, and also to a strong quenching of the PL intensity for increasing temperatures, see Fig. 2.31 (c) and (d), respectively. On the other hand, an increase of the carrier lifetime with temperature under constant PL intensity is usually considered as an indication for suppressed non-radiative capture processes and thus dominating radiative recombination [9], see the discussion in section 2.1.2.

In general, one should always keep in mind that non-radiative processes are often the

### 2.3 Extrinsic photoluminescence properties: defects and disorder

most effective recombination channels, especially, at low excitation densities and elevated lattice temperatures. However, it depends on the aim of the experimental study, whether the influence of the non-radiative recombination affects the interpretation of the findings or not.

#### 2.3.2 Disorder

*Disorder* in semiconductor structures is commonly understood as spatial fluctuations of material parameters, leading to the fluctuations of carrier energy levels, see Ref. [9] and the references therein. The reasons for the fluctuations are manifold: (i) inhomogeneities in chemical composition, (ii) spatial variations of the size of low-dimensional structures, e.g., widths of QWs, (iii) fluctuations of strain and/or internal fields. The influence of disorder on the carrier DOS and thus on the optical response of the semiconductor is illustrated in Fig. 2.32. On the left-hand side, the linear absorption and PL spectra of an ideal semiconductor with perfectly aligned conduction and valence bands are shown. The absorption spectrum exhibits pronounced excitonic resonances and the luminescence peak is centered at the ground state transition, see the discussion in section 2.1. The right-hand side of the Fig. 2.32 illustrates the optical response of a disordered system. Here, the band structure exhibits spatial variations of the conduction and valence band edges, resulting in the fluctuations of the gap energy, with a characteristic energy scale  $\epsilon_0$ . In an experiment, the investigated area of the sample is typically much larger than the characteristic scale of the fluctuations. The latter thus lead to *inhomogeneous* broadening of the absorption and emission spectra. In addition, when the charge carriers are able to move within the disordered band potential, the PL peak is shifted to lower energies, towards the so-called *band-tail*, the low-energy flank of the DOS [9]. A finite energy spacing between the absorption

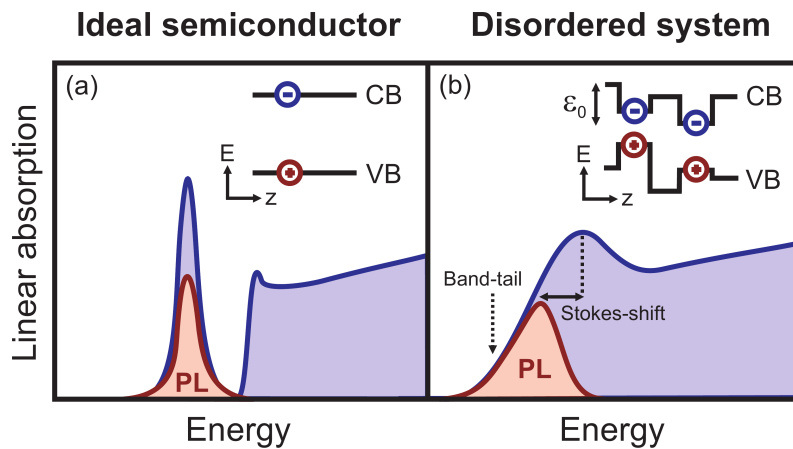


Figure 2.32: Schematic linear absorption of an ideal semiconductor (a) and disordered system (b) with the corresponding emission spectra as well as the respective band structures in real space coordinates.

## 2 Photoluminescence spectroscopy

and emission maxima is commonly labeled as the *Stokes-shift* [23, 9]. Also, the DOS within the band-tail often corresponds to Gaussian or exponential distributions [23]. For simplicity and consistency reasons, the latter is assumed for the rest of the discussion in this section. In contrast to that, there are specific material structures with pronounced disorder, yet extremely high potential barriers and/or large separations between the potential minima compared to carrier diffusion lengths, as illustrated in Fig. 2.33 (a). Typical example for such a system is a quantum dot ensemble with varying dot sizes [9, 103]. In this case, the disorder-induced Stokes-shift is again zero, see Fig. 2.33 (b), and the PL properties are not affected by carrier relaxation among spatially separated, localized states, c.f. following discussion in 2.3.2. However, for the majority of disordered semiconductors, the emission dynamics are indeed strongly influenced by the potential fluctuations.

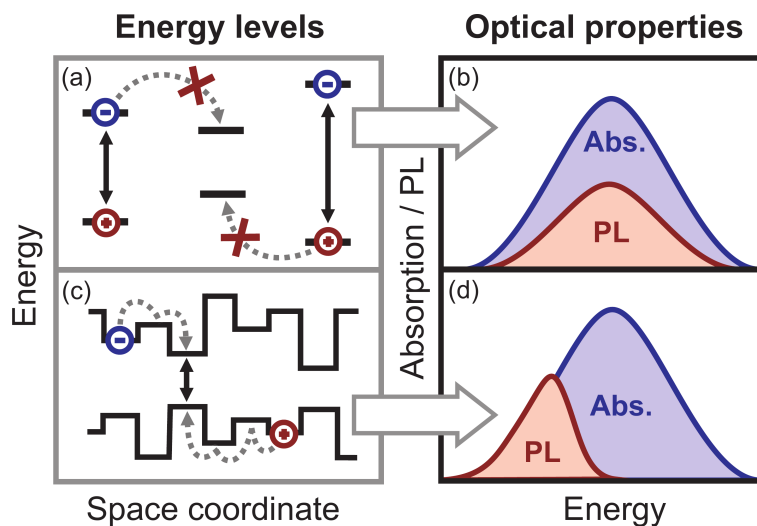


Figure 2.33: Schematic illustration of a material system with spatially fluctuating energy levels (a), yet without carrier relaxation processes between the potential minima. Despite the pronounced inhomogeneous broadening, no energy shift between the absorption and the PL is observed (b). Corresponding scenario including the relaxation is shown in (c) and (d) for comparison.

### Characteristic signatures of disorder in the photoluminescence

For the discussion of the disorder-related PL phenomena, the exciton picture is chosen for clarity reasons, though the introduced fundamental concepts also apply to the luminescence of uncorrelated electrons and holes. A typical PL spectrum of a semiconductor with pronounced disorder is shown in Fig. 2.34, in the regime of low excitation densities and low temperatures. For these experimental conditions, an asymmetric spectral shape of the PL is a clear hallmark of a disordered system [104, 105]. Here, the low-energy slope basically represents the distribution of the band-tail states, whereas the much

### 2.3 Extrinsic photoluminescence properties: defects and disorder

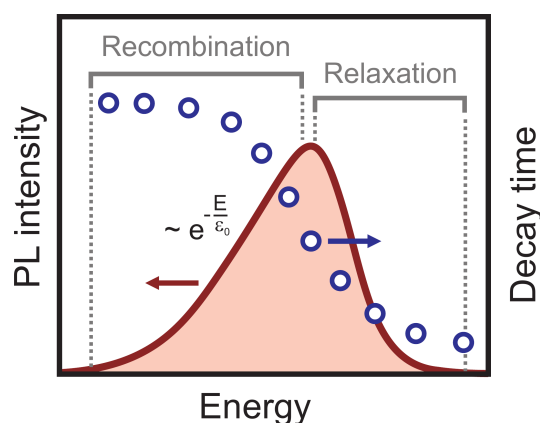


Figure 2.34: Influence of disorder on the PL spectrum and decay times of a semiconductor at low temperatures and excitation densities.

steeper high-energy side of the spectrum is related to carrier temperature and the homogeneous broadening of the optical transitions. The emission dynamics are subdivided into two different regimes. Carriers, typically excited in the continuum, relax towards locally available potential minima, resulting in fast luminescence decay on the high-energy flank of the spectrum. On the other hand, localized states on the low-energy flank exhibit much longer carrier lifetimes, since no further relaxation channels are available. Thus, the decay time strongly depends on the spectral position, increasing orders of magnitude for decreasing emission energy [106, 107]. This characteristic spectral dependence of carrier lifetime can be already used for the estimation of the energy scale  $\epsilon_0$  of potential fluctuations [106, 108].

The influence of the excitation power on the PL properties of a disordered semiconductor is illustrated in Fig. 2.35. In (a), the band-tail DOS is represented by a distribution of the localized states below the "band-edge". In case of the disordered system, the latter is typically defined as the onset of the DOS region with high carrier mobility [9], roughly corresponding to the maximum of the broadened excitonic ground-state in the absorption spectrum, c.f. Fig 2.32 (b). Also, defects states, i.e., deep traps, are introduced to the real-space band-structure, mimicking realistic scenario. At low excitation densities, carriers relax to the local potential minima, leading to the previously discussed shift of the PL maximum to lower energies with respect to the band-edge. Also, most of these carriers do not reach any of the deep traps due to the spatial localization. As the excitation density increases, the energy minima of the disordered potential are more and more filled by carriers. The average energy of the carrier distribution increases thus leading to an increase of the PL maximum as function of the excitation density, as shown in Fig. 2.35 (b). In addition, carriers become more delocalized due to the occupation of higher-lying states or even the band-edge, both leading to an increase of carrier mobility. Hence, the probability of carrier capture by the deep traps, i.e., non-radiative recombination rate, increases. As a

## 2 Photoluminescence spectroscopy

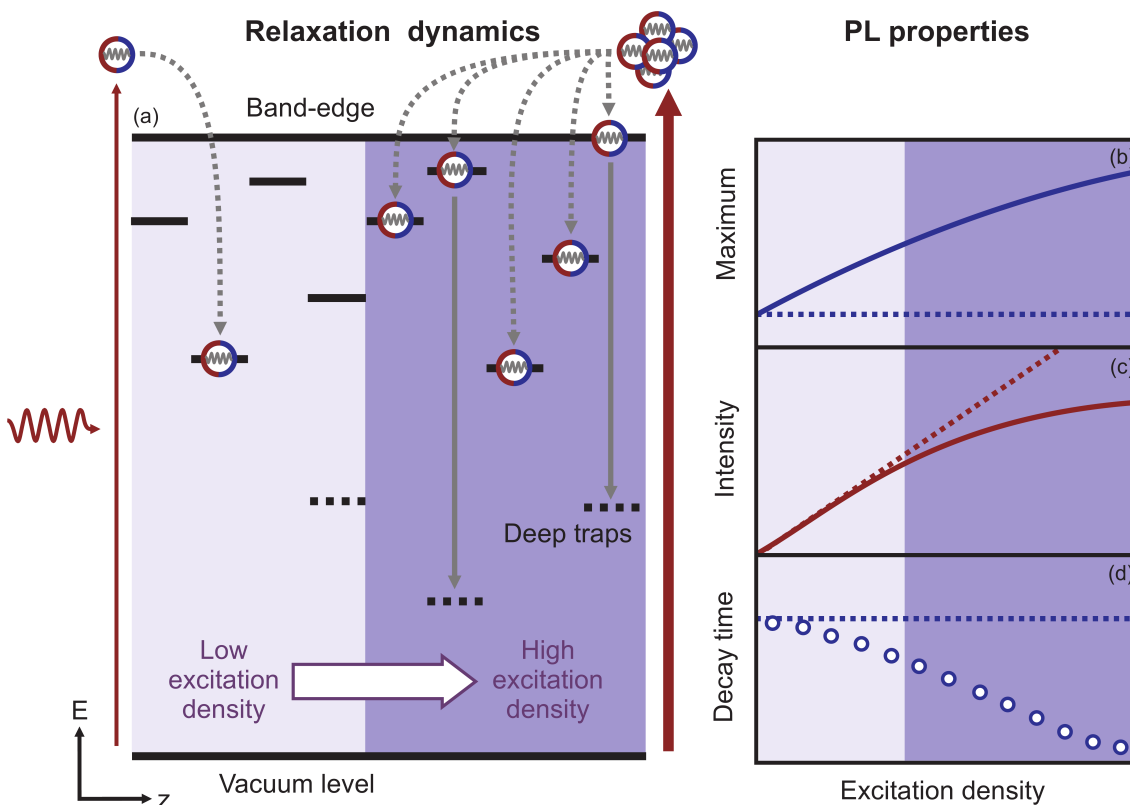


Figure 2.35: (a) Carrier relaxation dynamics in the excitonic picture for low and high excitation power at low lattice temperatures. Corresponding PL energy maximum, emission intensity, as well as the decay time of the luminescence are exemplary plotted in figures (b), (c) and (d), respectively, as function of the excitation density. The respective dependencies in case of an ideal semiconductor are shown by the dotted lines for comparison.

result, the emission intensity exhibits a sublinear behavior as function of the exciton density, and the decay time decreases, see Fig. 2.35 (c) and (d), respectively. In an experiment, all these dependencies of the PL properties on the excitation power are characteristic for a disordered system, in stark contrast to the optical response of an ideal semiconductor, shown by the dotted lines in Fig. 2.35 (b), (c), and (d), for direct comparison.

Aside from the power dependence, the most prominent impact of carrier localization is observed in temperature-dependent PL spectra and transients. Figure 2.35 (a) illustrates the carrier relaxation dynamics as well as their influence on the energy of the PL maximum (a), the FWHM (b), the intensity of the sample emission (c), and the evolution of the decay times (d) as function of the lattice temperature, low excitation density assumed. As the temperature is low, carrier scatter to the lowest locally available potential minima. Again, the emitted PL is shifted to lower energies with respect to the band-edge and the non-radiative recombination is partially suppressed due to the strong carrier localization. At elevated lattice temperatures, carriers are able leave local potential minima by

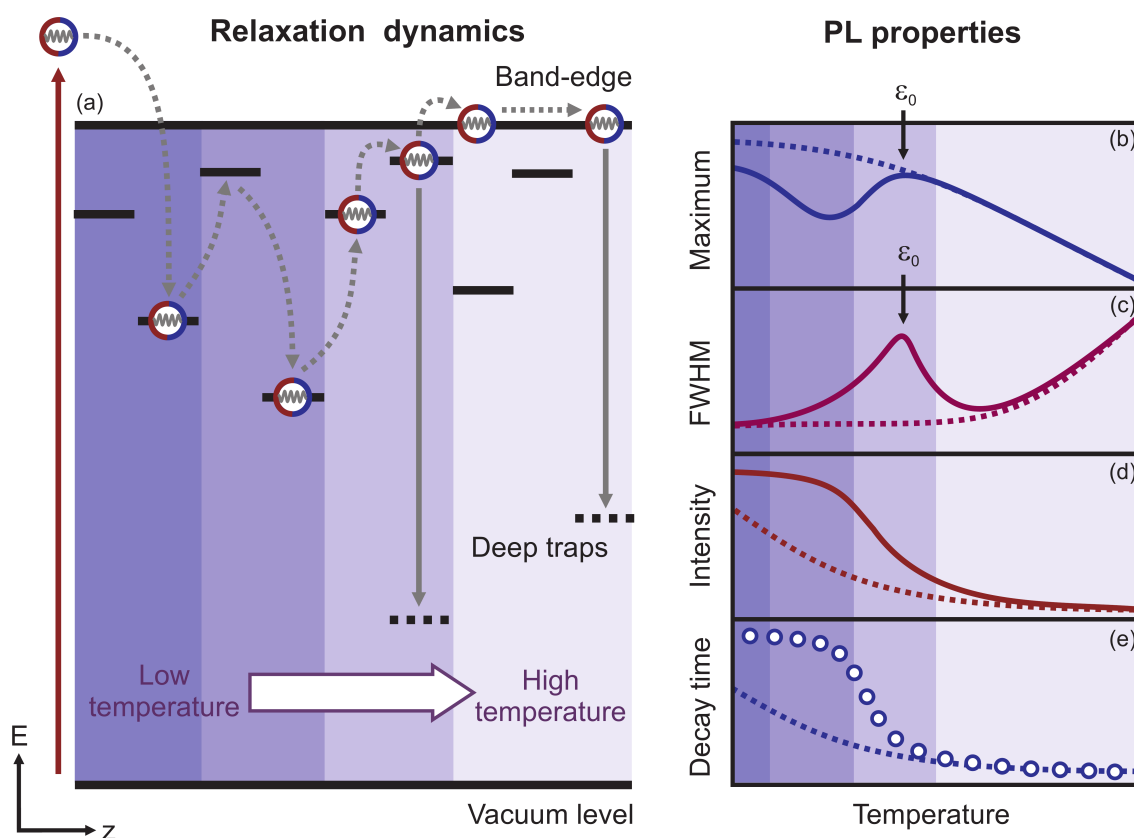


Figure 2.36: (a) Carrier relaxation dynamics in the excitonic picture for low, intermediate and high lattice temperatures for low excitation densities. Corresponding PL energy maximum, FWHM, emission intensity, as well as the decay time of the luminescence are exemplary plotted in (b), (c), (d), and (e), respectively, as function of the lattice temperature. For comparison, the corresponding dependencies in case of an ideal semiconductor are shown by the dotted lines.

phonon-assisted hopping into even more favorable states at lower energies. This causes the frequently observed shift of the PL peak position to lower energies, which is a part of the so-called *S-shape* behavior [23, 109, 110]. Also, the FWHM of the emission peak increases since carriers occupy a higher number of localized sites, then recombine radiatively thus leading to a broader distribution of possible photon energies. However, the decay time and the PL intensity remain virtually unchanged due to the still low carrier mobility and therefore suppressed non-radiative recombination. As the temperature is increased further, the carriers are thermally activated to higher-lying states. The PL maximum is blue shifted, completing the above-mentioned S-shape, and the FWHM reaches a local maximum, at least for the exponential band-tail DOS. The emission intensity as well as the decay time both decrease due to the higher mobility and therefore an increased capture probability by the deep impurities. At even higher temperatures, the carriers are completely delocalized and the PL energy corresponds to the energy of the band-gap, i.e.,



## 2 Photoluminescence spectroscopy

zero Stokes-shift is observed. The FWHM is reduced to the value given by the phonon-induced broadening, see Eq. (2.30) in section 2.1.2. Also, the non-radiative recombination probability corresponds to the rate, determined by the impurity density and thermal velocity of carriers, c.f. Eq. (2.60) and Ref. [100]. In general, the disorder-related parameters, such as characteristic energy scale, relative density of the local potential minima as well as the concentration of the deep traps can be extracted from the temperature dependence of the PL spectra by using the results of kinetic Monte-Carlo-simulations [23, 111]. An example for the most direct estimation of the energy scale  $\varepsilon_0$  from the experimental spectra is the multiplication of the Boltzmann factor with the temperature value corresponding to the FWHM maximum or to the final "turn" of PL maximum within the S-shape, see Fig. 2.35 (b) and (c).

### Theoretical treatment: Monte-Carlo-simulations

In this last section, a phenomenological approach to the evaluation of the PL data from disordered semiconductors is briefly discussed. This approach is based on the Monte-Carlo simulations of carrier relaxation and recombination within spatially fluctuating potentials [23, 111]. The starting point is the assumption of energy distribution for the localized band-tail states with the average spatial density  $N$ . In the most cases, this choice is based on the experimental findings, e.g., the shape of absorption or emission spectra. Carriers, either excitons or uncorrelated electrons and holes, are randomly distributed among the available states, mimicking the ultra-fast carrier thermalization after a pulsed excitation at low pump densities. Now, these carriers can either perform phonon-assisted hopping transitions between different localized states, or recombine either radiatively or non-radiatively. The two latter processes are summarized in the effective recombination rate  $\tau_{rec}$ . The corresponding rate  $v_{ij}$  for a transition between the state  $i$  with energy  $E_i$  and the state  $j$  with energy  $E_j$  is given by the so-called *Miller-Abrahams expression* [112, 113]

$$v_{ij} = v_0 \exp\left(-\frac{2r_{ij}}{\alpha} - \frac{E_j - E_i + |E_j - E_i|}{2k_B T}\right). \quad (2.61)$$

Here,  $v_0$  is the attempt-to-escape frequency,  $\alpha$  - the localization radius,  $r_{ij}$  - the distance between the two states,  $k_B$  - the Boltzmann-factor, and  $T$  - the lattice temperature. Hopping processes are thus most probable between close-lying potential minima and also strongly dependent on the mean kinetic energy of the charge carriers. The total decay rate  $v_i$  of the state  $i$  is computed by the sum of all possible hopping rates, corresponding to the effective relaxation time  $\tau_{relax}$  and the inverse recombination time:

$$v_i = \tau_{rec}^{-1} + \sum_j v_0 \exp\left(-\frac{2r_{ij}}{\alpha} - \frac{E_j - E_i + |E_j - E_i|}{2k_B T}\right). \quad (2.62)$$



### *2.3 Extrinsic photoluminescence properties: defects and disorder*

The simulation is iterated for several 10's of thousands carrier pairs to ensure statistically significant results. Further details concerning the algorithm and the numerical realization are given in Refs. [40, 114]. Since both the emission energy and the time delay after the excitation are recorded for every recombination event, PL spectra as well as the energy-dependent transients are obtained from these simulations. Then, a comparison of the theoretical results to the spectrally and temporally resolved PL data at various temperatures, allows for the extraction of the complete set of the simulation parameters thus characterizing the disorder in the studied structures.



# 3 Experimentals

This chapter illustrates the experimental realization of the spectroscopic studies carried out within the framework of my thesis. In the first part the time-resolved photoluminescence setup is presented. Here, the excitation source, non-linear frequency mixing, as well as the operation of the streak camera are discussed in detail. The second part deals with the linear spectroscopy setup used for CW PL and absorption measurements.

## 3.1 Time-resolved photoluminescence

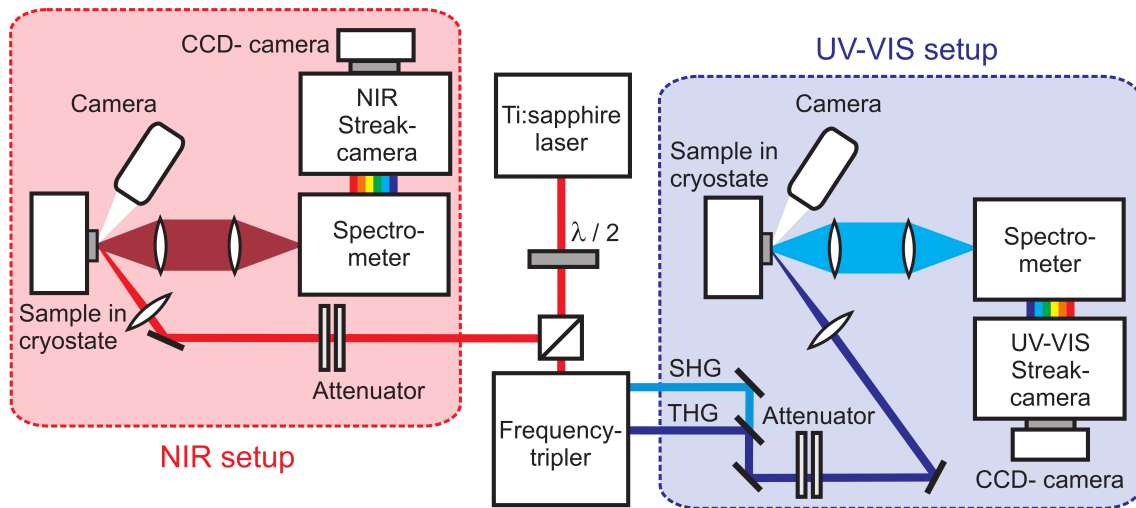


Figure 3.1: TRPL setup for the NIR and UV-VIS spectral range

The setup for the TRPL measurements is schematically shown in Fig. 3.1. A pulsed titanium-sapphire (Ti:Sa) laser<sup>1</sup> is used as an excitation source. The Ti:Sa is pumped by an intra-cavity frequency-doubled neodymium doped yttrium-aluminum-garnet (Nd:YAG) laser<sup>2</sup> with the central emission wavelength of 532 nm and a maximum output power of 11 W. A slightly lower pump power of 9.5 W is typically used in the experiments to provide higher long-term stability of the setup. In the pulsed regime the Ti:Sa is passively mode-locked by the self-focusing effect due the Kerr-non-linearity inside the sapphire crystal. The dispersion of the spectrally broad pulses is compensated by a series

<sup>1</sup>"Tsunami", Spectra-Physics

<sup>2</sup>"Millenia", Spectra-Physics

### 3 Experimentals

of prisms inside the cavity. This leads to a typical pulse width of approximately 100 fs at a repetition rate of  $(80 \pm 0.5)$  MHz, corresponding to a separation of 12.5 ns between the pulses. This sets the upper limit for the directly accessible time range in the TRPL experiments. Also, when desired, the operating mode can be changed to the CW by a minor detuning of the laser cavity. The Ti:Sa operates in the TEM<sub>00</sub> mode with linearly polarized emission. A broad-band mirror set is used for the laser cavity, taking advantage of the spectrally broad gain of the Ti:Sa crystal. Thus, emission wavelengths between  $\lambda_{em} = 690$  nm and  $\lambda_{em} = 1010$  nm are achieved, corresponding to photon energies  $E_{em} = 1.80$  eV and  $E_{em} = 1.23$  eV. For  $\lambda_{em} > 930$  nm, the laser is purged with nitrogen gas to minimize intra-cavity water absorption. The average output power ranges from 0.6 W for  $\lambda_{em} > 950$  nm and up to 2.3 W around  $\lambda_{em} = 800$  nm.

The initially accessible wavelengths are further extended into the visible and the UV spectral range by taking advantage of the non-linear frequency-mixing. It is especially efficient for the high electric field strengths associated with the ultra-short Ti:Sa pulses. For this purpose the so-called frequency-tripler<sup>3</sup> is integrated into the experimental setup. The basic layout of the tripler is shown in Fig.3.2 Pulses from the fundamental laser mode centered at the frequency  $\omega$  enter the tripler and are focused on a lithium triborate crystal (LBO). LBO exhibits a particularly strong second-order non-linearity in the optical

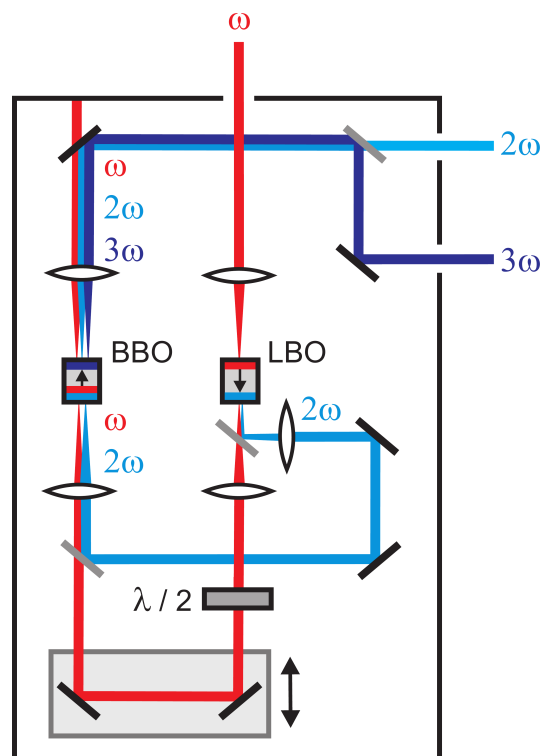


Figure 3.2: Schematic layout of the frequency tripler

<sup>3</sup>"SuperTripler 8315", CSK Optronics

### 3.1 Time-resolved photoluminescence

response to the incident EM-wave, i.e., polarization with the frequency  $2\omega$  is induced inside the crystal. According to the Maxwell's equations the  $2\omega$ -polarization wave is naturally associated with an EM-wave, the so-called second-harmonic (SH). When the phase velocities of the  $\omega$ - and  $2\omega$ -waves are matched by adjusting the relative angle of the LBO, both waves interfere constructively. Thus, the amplitude of the SH pulse increases while the  $\omega$ -pulse propagates through the crystal. Under such phase-matched conditions about 25 % of the incident power are converted to the SH emission. The later emerges from the LBO crystal collinearly to the fundamental mode, yet perpendicularly polarized.

The fundamental and the SH beams are spatially separated by a dichroic mirror plate and then focused on a bismuth triborate crystal (BBO). Inside the crystal the second-order non-linearity leads to a partial conversion of  $\omega$ - and  $2\omega$ -radiation to an EM-wave with the tripled initial frequency and about 1 % of the Ti:Sa power, the so-called third-harmonic (TH). Again, the phase-match is adjusted by fine-tuning the angle of the BBO as well as the  $90^\circ$  rotation of the linear polarization of the fundamental mode. In addition, both incident beams overlap spatially and temporally. The temporal overlap is achieved by altering the length of the fundamental beam path using a delay stage. After passing the BBO crystal the three beams are spatially separated by wavelength-selective mirrors and the fundamental mode is guided to a beam dump. In the TRPL measurements both SH and TH pulses are used for excitation, depending on the experimental requirements. The initial wavelength range of the Ti:Sa is thus expanded to 345 nm - 505 nm (SH) and 230 nm - 337 nm (TH), corresponding to the photon energies of 3.59 eV - 2.46 eV and 5.39 eV - 3.68 eV, respectively.

In the experiment the Ti:Sa emission is separated by a polarizing beam-splitter cube before entering the tripler (Fig. 3.1). A  $\lambda/2$  wavelength-plate is applied to adjust the distribution of the laser power between two different TRPL setups, optimized for NIR and UV-VIS detection, respectively. Aside from the differences in excitation wavelengths, both setups share the same design. First, the power of the incident laser beam is attenuated by using reflective neutral-density filters to avoid thermal lensing. Then, the laser is focused on a sample with the pump spot FWHM of  $30\ \mu\text{m}$  -  $40\ \mu\text{m}$  in the NIR and  $20\ \mu\text{m}$  -  $25\ \mu\text{m}$  in the UV-VIS setup, respectively. The FWHM are measured by a CCD-based beam-profiler<sup>4</sup>. The laser profile as well as the position of the excitation spot on the sample are monitored during the measurement by a digital camera<sup>5</sup>. The camera allows for spatial resolution down to  $5\ \mu\text{m}$  at a working distance of about 10 cm. For the measurements at the temperatures down to 5 K the sample is held in a He-flow cryostat<sup>6</sup>. The PL from the sample is imaged to the entrance slit of a spectrometer<sup>7</sup> under numerical-

<sup>4</sup>Standard web-camera with removed imaging optics

<sup>5</sup>"FINEPIX S100FS", Fujifilm, upgraded with additional optics

<sup>6</sup>Micro-cryostat, CryoVac

<sup>7</sup>"25015", Bruker

### 3 Experimentals

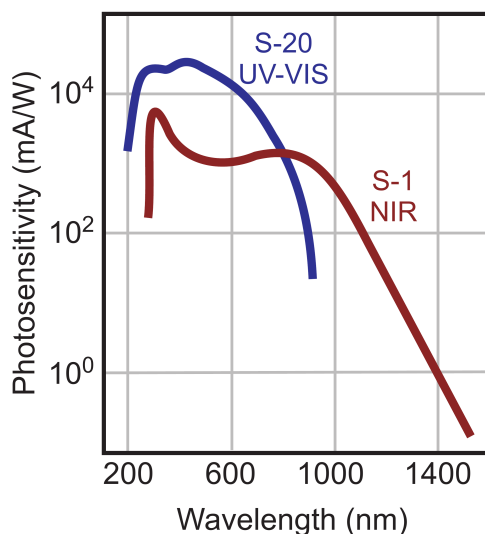


Figure 3.3: Sensitivity of the streak camera cathodes as function of detection wavelength

aperture (NA)-matching conditions. Polarization and/or wavelength-selective filters are placed in front of the spectrometer according to experimental requirements. In addition, the magnification of the image and the spectrometer slit-width are chosen such that only the emission within the FWHM of the pump spot enters the detector. Thus, the photon flux at the sample surface in the area of interest is determined only by the pump power and the FWHM of the laser spot. A script for "Mathematica" given in appendix (1) is used to calculate the The maximal spectral resolution of the measured PL signal in both NIR and UV-VIS setups is about 0.1 nm; it depends on the chosen grating and the slit widths of the spectrometer.

After passing the spectrometer, the PL signal is temporally resolved in a streak camera<sup>8</sup>. The streak-camera as well as the spectrometers are operated using the "HPDTA 8.1" software from Hamamatsu. The spectral response of the employed cameras is shown in the Fig. 3.3. Effective detection windows are 200 nm - 800 nm and 300 nm - 1300 nm for the NIR and UV-VIS setups, respectively. Also, the UV-enhanced streak camera provides over an order of magnitude higher sensitivity in comparison to the NIR device and a lower noise level.

Figure 3.4 illustrates the operation principle of a streak camera in detail. In the realized TRPL setup the PL signal that enters the streak camera is already spatially dispersed by the spectrometer. Thus, in a simplified picture, several photons distributed in horizontal direction according to their respective energies reach the detector. Also, some time-delay between the photons is introduced. These photons pass a variable vertical slit and hit the photosensitive screen of the streak camera tube. With some finite probability, each impinging photon leads to an emission of an electron due to the photoelectric effect. The

<sup>8</sup>NIR setup: "M5675(S-1)", Hamamatsu; UV-VIS setup: "M6860(S-20)", Hamamatsu

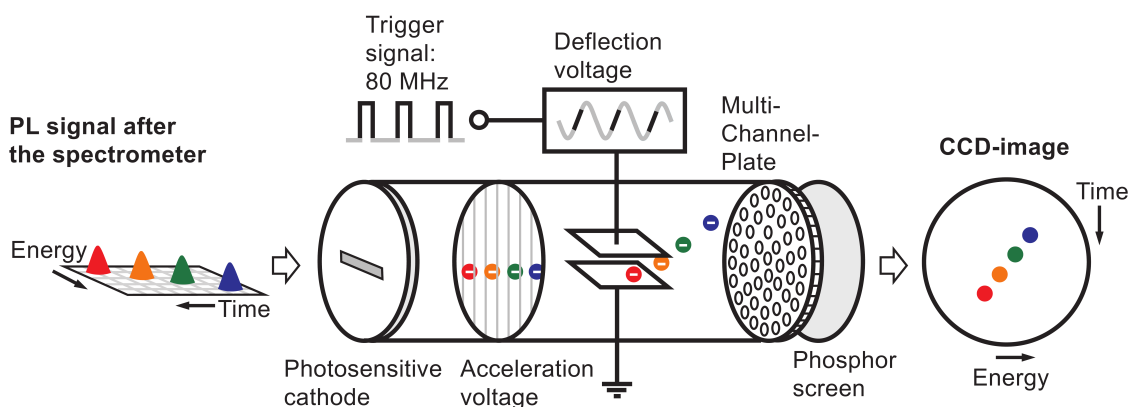


Figure 3.4: Operation principle of a streak camera

quasi-instantaneous nature of the photo-effect conserves the spatial and temporal order of the emitted electrons with respect to the initial photon distribution. The electrons are accelerated along the evacuated tube and pass a pair of horizontally aligned capacitor plates. In the so-called "synchro-scan" mode used in all TRPL experiments for this work the streak camera is a sinusoidal deflection voltage is applied to those plates. The oscillation frequency is locked to the repetition rate of the pump laser. Also, the streak camera is triggered such that the voltage increases linearly as the electrons pass the capacitor plates. Thus, the electrons are deflected in the vertical direction according to their arrival time. Subsequently, the vertically and horizontally spread electron beam is amplified in a multi-channel plate and hits the fluorescent phosphorous screen at the end of the streak camera tube. Then, the image of the screen is acquired with a CCD-camera. In this way, the initial temporal distribution of PL photons is converted to a spatially resolved signal.

The temporal resolution of a streak camera mainly depends on the width of the vertical entrance slit and the deflection voltage amplitude. However, the resolution is limited due to the electron beam broadening as well as the thermal and mechanical jitter of the detection system and the excitation source. The ultimate limit is given by the Heisenberg uncertainty principle due to the initial spectral dispersion of the measured PL signal. The maximal temporal resolutions of the employed streak-cameras are 1.5 ps and 0.5 ps for the NIR and UV-VIS setup, respectively. The acquisition window ranges from 50 ps to 2 ns.

An exemplary PL image taken by the NIR streak camera is shown in Fig. 3.5. The signal is plotted as function of photon energy and time on a false-color intensity scale. The PL spectra are extracted from the 3D-image by the integration over a time interval. In the same way the time-dependent PL traces, or transients, are obtained by spectral integration. The upper boundary of the measured PL signal on top of the image defines the time-zero, i.e., the arrival of the excitation pulse. A weak signal at negatives times is a common artifact in the applied detection mode, the so-called *back-sweep*. The origin

### 3 Experimentals

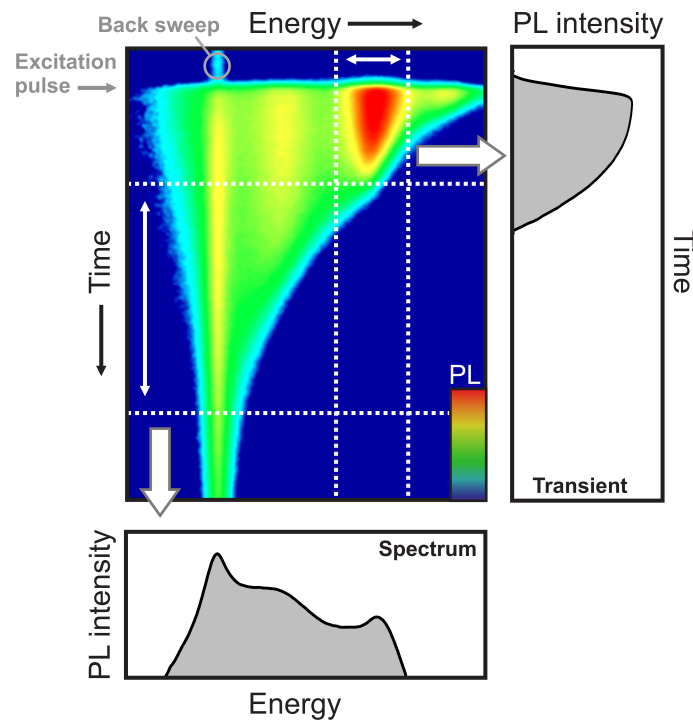


Figure 3.5: Exemplary PL image taken by a streak camera in series with a spectrometer. The sample is a (GaIn)As multi-quantum well stack at the lattice temperature of 10 K. The PL spectra and transients are extracted from the 3D-image by the integration of temporal and spectral intervals, respectively.

of the back-sweep is illustrated in Fig. 3.6. The top part of the graph shows a typical PL signal from a sample excited by a train of short laser pulses with a repetition rate of 80 MHz. The PL rises with the excitation pulse and then decays slowly with time. When the average decay time is in the same order of magnitude or even longer than the time-interval of 12.5 ns between two excitation pulses, the PL exhibits a finite offset due to the pile-up effect. The deflection voltage of the streak camera, synchronized with the repetition rate of the laser, is shown in the bottom graph. The shaded area corresponds to the detection window of the CCD-camera. Thus, the measured signal is an overlap of two contributions: pile-up background from the preceding PL trace followed by the rise and the initial decay of the sample emission (red line) as well as the PL delayed by 6.3 ns (blue line). The later is deflected in the opposite spatial direction with respect to the initial signal due to the sinusoidal voltage profile. The contribution from the "delayed" PL and the pile-up background give rise to the back-sweep artifact. When the back-sweep fraction of the total measured signal is significant, i.e., more than 20 %, the PL transients can not be analyzed directly, e.g., by fitting with exponential decay functions. In this case, the average decay time is extracted from the back-sweep-to-maximum ratio applying a numerical algorithm to deconvolute different contributions. This routine deduces decay times up to 100 ns with reasonable accuracy. The corresponding script for "Mathematica"



### 3.2 Linear absorption and continuous-wave photoluminescence

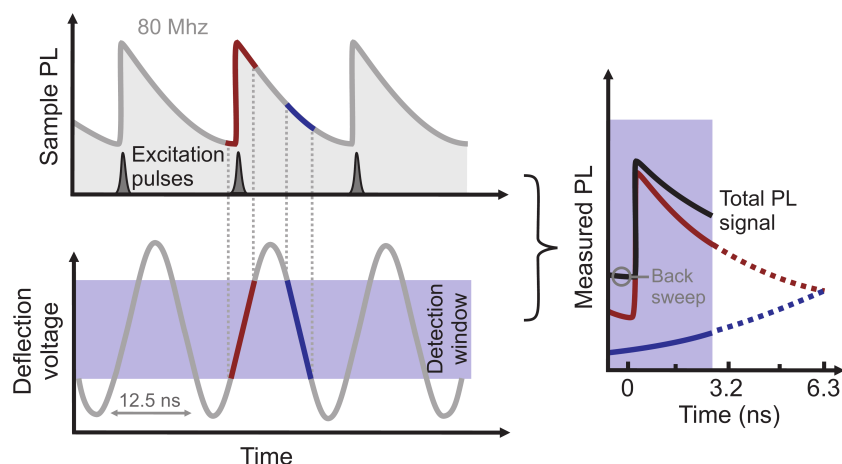


Figure 3.6: Formation of a PL time-trace in a streak camera working in a synchro-scan mode. The graph on top shows the periodic PL emission from the sample. The voltage between the deflection plates of the streak camera is plotted in the bottom graph. On the right-hand side the evolution of the measured signal is illustrated.

is given in appendix (2). For the majority of the studied samples, however, the PL decay is significantly shorter than 12.5 ns. Therefore, the contributions from the pile-up and the emission at 6.3 ns are negligible in most cases. They are treated as a constant offset and thus subtracted from the measured signal. In addition, the so-called *blanking unit* can be used to apply an additional horizontal voltage inside the camera-tube thus separating the back-sweep from the initial signal. The drawback of this technique is the rather challenging extraction of the spectral information, especially, for large temporal detection windows. All images obtained in the streak camera setup are processed using a "LabView 8.0" code. The contributions from the background radiation are subtracted and the data is corrected for the spectral response of the detector system and spatially varying sensitivity of the phosphorous screen as well as the CCD-camera. Finally, "Origin 9.0" software is used for the quantitative analysis of the PL data.

## 3.2 Linear absorption and continuous-wave photoluminescence

The experimental setup for absorption and CW-PL measurements is shown in Fig 3.7. The Ti:Sa laser used in the TRPL setup and a helium-neon (He:Ne) laser operating at 632.8 nm are employed as excitation sources for the CW-PL experiments. The incident laser beam is focused on the sample, held in a He-flow cryostat. PL emission is imaged

### 3 Experimentals

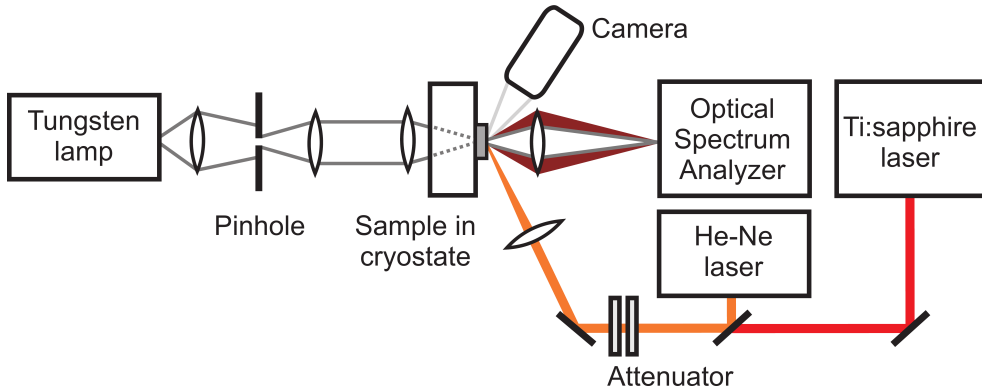


Figure 3.7: Experimental setup for measurements of linear absorption and continuous-wave photoluminescence.

on the entrance slit of the optical spectrum analyzer (OSA)<sup>10</sup>. The OSA is a spectrometer with integrated detector and data processing unit. The sensitivity of the OSA ranges from 330 nm to 1700 nm with a maximal spectral resolution of 0.05 nm.

A tungsten lamp is used as a white-light source for linear absorption measurements. The lamp provides a broad thermal spectrum with the central wavelength of about 1000 nm. This yields an effective spectral range from 400 nm to 1700 nm, limited by the light-source and the sensitivity of the detector. The strongly diverging light from the lamp is first focused on a pinhole with the diameter of 50  $\mu\text{m}$ . The pinhole is then imaged on the sample. The light, transmitted through the sample, is focused on the OSA entrance slit applying the same optics as for the CW-PL measurements. A digital-camera is used to monitor the overlap of the PL excitation spot with the focus of the white-light. Linear absorption spectra are obtained from the initial and transmitted light intensities  $I_0$  and  $I_T$ , respectively, after the subtraction of the background according to the Beer's law:

$$\frac{I_T}{I_0} = e^{-\alpha L}. \quad (3.1)$$

Here,  $\alpha$  is the absorption coefficient and  $L$  is the thickness of the sample. For the absorption of quasi-two-dimensional structures only the product  $\alpha L$  is evaluated.

<sup>10</sup>"AQ-6315A", Ando

## 4 Role of the Coulomb-interaction in phonon-assisted emission

This chapter covers the experimental studies of many-body effects in phonon-assisted emission of semiconductors due to the carrier-carrier Coulomb-interaction. The corresponding theoretical background is discussed in section 2.2.1. The following investigations are focused on the two main questions: (i) does Coulomb-correlated electron-hole plasma contributes to the PSB emission, and (ii) how strong is the impact of exciton formation on the carrier-phonon interaction. These topics are treated in the following two sections. All calculations involved are performed by Christoph N. Böttge and Dr. Thomas Feldtmann in the group of Profs. Stephan W. Koch and Mackillo Kira at the Philipps Universität Marburg.

### 4.1 Luminescence sources: plasma contributions

The section deals with the experimental evidence for the two different sources of PSB emission, excitons and electron-hole plasma. Since the excitonic PSBs are considered common knowledge [55, 115, 116, 117, 51], the evidence of plasma contributions remains the main goal of the conducted studies. The discussion starts with the presentation of the material systems used for the experiments as well as their brief characterization. The next two subsections are dedicated to PL investigations at carefully chosen, specific excitation conditions, known to favor or to inhibit exciton or plasma formation.

#### 4.1.1 Material systems

The proposed investigations of plasma-related radiative recombination via phonon-assisted transitions impose rather demanding requirements on the investigated materials. The exciton binding energy  $E_B$  of the semiconductor under study should be not too high, since phase-transition from the exciton- to the plasma-dominated regime should be reached with reasonable carrier densities, i.e., pump power, avoiding radiative damage of the sample. On the other hand,  $E_B$  should be not too low to facilitate efficient exciton formation.

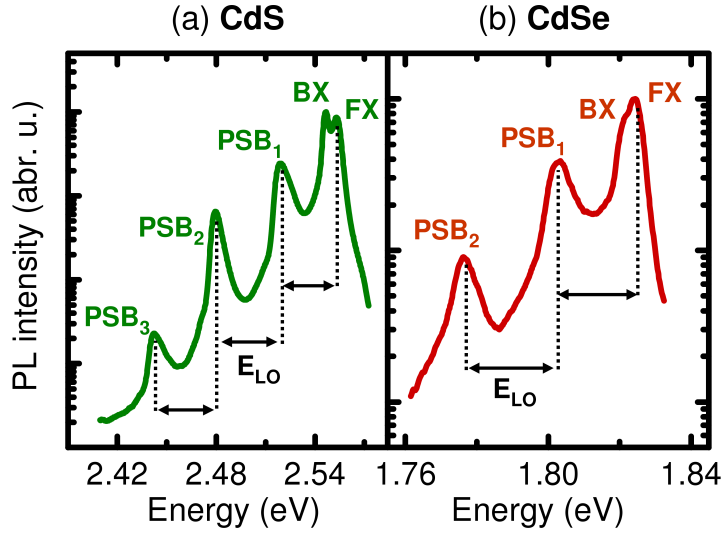


Figure 4.1: PL spectra of CdS (a) and CdSe (b) for low excitation density and non-resonant excitation conditions at the lattice temperature of 10 K. Signatures of bound and free excitons as well as the corresponding PSBs are marked by BX, FX, and PSB<sub>*n*</sub>, respectively.

In addition, strong carrier-phonon coupling is required for the observation and quantitative analysis of the PSB emission. Finally, the studied materials should be high-quality in terms of defect- and impurity-concentrations as well as not being subject to disorder. Otherwise, the emission spectra as well as the carrier dynamics are influenced by the extrinsic phenomena, see section 2.3, and any study of the intrinsic properties is thus inhibited.

Based on these requirements, chemically synthesized CdS and CdSe bulk crystal flakes with several  $\mu\text{m}$  thickness are chosen for the experiments. Both materials are well-studied, direct semiconductors exhibiting pronounced PSB luminescence [118, 119, 120, 9]. The exciton binding energies of CdS and CdSe are 27 meV and 15 meV [36], respectively. These energies are in the intermediate range between easily ionized excitons in GaAs [33, 30] with  $E_B^{\text{GaAs}} = 4$  meV and rather stable excitons in ZnO [9] with  $E_B^{\text{ZnO}} = 60$  meV.

As an overview, Fig. 4.1 shows the PL spectra of the CdS (a) and the CdSe (b) samples, time-integrated over a 2 ns-range after the excitation for a lattice temperature of  $T = 10$  K. The data is taken for the non-resonant excitation at 2.85 eV and low pump density of about  $10^{11}$  cm<sup>-2</sup> photons per pulse. Spectral and temporal resolutions are 0.4 nm and 20 ps, respectively. The dominant emission signatures at 2.547 eV and 2.553 eV for CdS, as well as 1.821 eV and 1.825 eV for CdSe are attributed to the well-known ZPLs of the bound (BX) and free A-excitons (FX), respectively [121, 122, 36]. Despite the suppression of the FX emission due to the polariton propagation effects in bulk crystals, c.f. section 2.1.3, the rather strong FX PL compared to the BX emission is already an

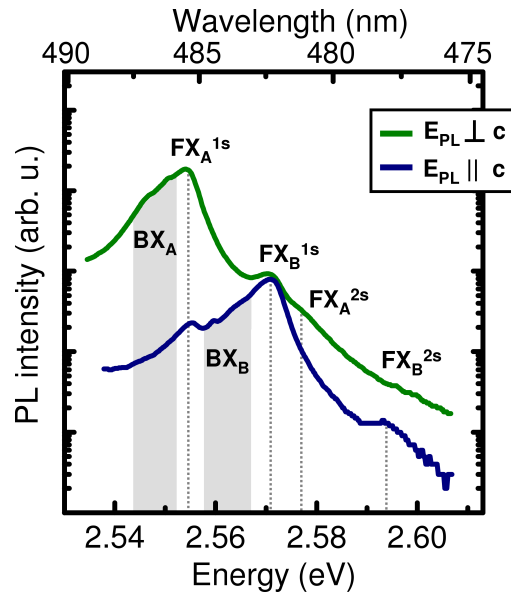


Figure 4.2: PL spectra over first 10 ps after the excitation of the CdS sample for two different linear polarization of the detected emission at  $T = 10$  K and for low excitation density of about  $10^{11}$   $\text{cm}^{-2}$  photons per pulse. The polarization of the incident laser beam is tilted by  $45^\circ$  with respect to the  $c$ -axis.

indication for a high material quality of the two samples. In addition to the BX and FX transitions, several pronounced luminescence peaks are observed at the low-energy side of the spectrum. The respective intensities decrease with decreasing peak energy. The peaks are nearly equidistantly spaced with a separation of about 38 meV for CdS and 27 meV for CdSe, as are the separations between the first peak and the FX line. These energies correspond to the energies of the LO-phonons in these materials [122, 36]. Therefore, the peaks are unambiguously identified as the PSBs of the FX emission. As already discussed in section 2.2.1 the PSB luminescence is only weakly affected by polariton effects and thus originates from the entire excited bulk volume, in contrast to the surface-related FX PL.

Also, both CdS and CdSe samples adopt wurtzite crystal structure and are grown with the  $c$ -axis parallel to the sample surface. Therefore, the selection rules become important for the excitation as well as for the PL detection, c.f. section 2.2.4. Since the emission from the ground state, i.e., A-exciton, is of interest for this study, the proper experimental conditions are first identified by polarization-resolved measurements. Exemplary low-temperature spectra of the CdS sample are shown in Fig. 4.2 for two different linear polarizations of the detected PL, perpendicular and parallel to the  $c$ -axis. The polarization of the incident laser beam with the average photon energy of 2.85 eV is tilted by  $45^\circ$  with respect to the latter, leading to the photoexcitation of holes in both A- and B-valence bands. Altogether, the PL spectra show the typical resonances from the ground and the

#### 4 Role of the Coulomb-interaction in phonon-assisted emission

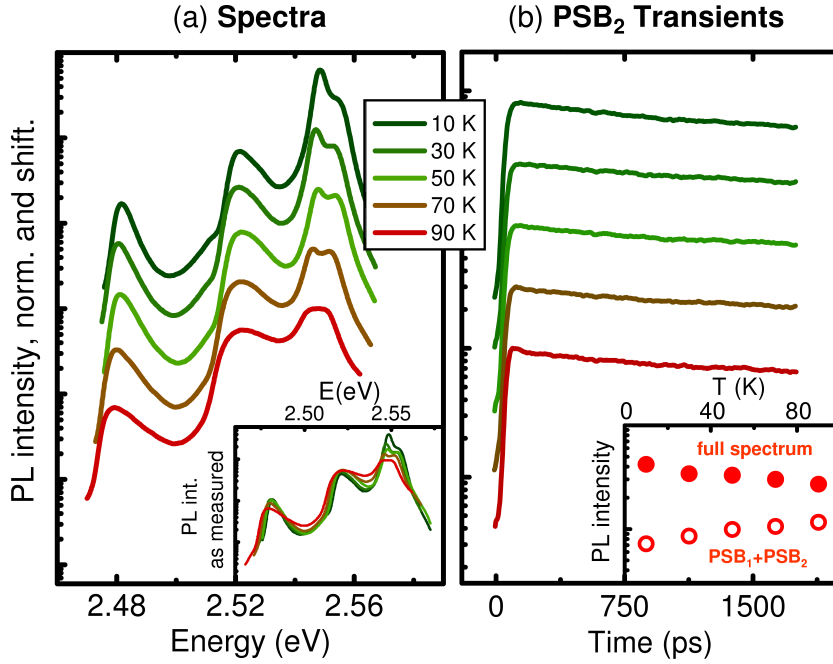


Figure 4.3: Temperature-dependent PL spectra (a) and PSB<sub>2</sub> transients (b) at low excitation density of about  $10^{11} \text{ cm}^{-2}$  photons per pulse. The data is normalized and shifted for clarity. As-measured emission spectra and PL intensities are plotted in the respective insets .

first-excited excitonic states in CdS [80] as well as the weak signatures of the corresponding BX transitions. As expected for a wurtzite semiconductor, only the B-excitons appear in the luminescence when the detected electric field  $E_{PL}$  is linearly polarized parallel to the symmetry axis. In contrast to that, both A- and B-excitons are observed in case of the perpendicular polarization, according to the selection rules. The latter configuration is thus chosen for the following experiments.

Finally, temperature-dependent PL studies are performed to ensure that non-radiative recombination plays only a minor role for the recombination dynamics in both samples. Again, representative results from the CdS sample are plotted in Fig. 4.3. As the temperature increases, the spectra show a typical shift of the PL maximum towards lower energies as well as a quenching of the BX transition due to the ionization, see sections 2.1.2 and 2.3; no disorder-related S-shape is observed. Also, due to increasing phonon population and thus more efficient scattering processes, the spectra broaden and the PSBs become more pronounced. To analyze the dynamics of the FX emission, the PSB<sub>2</sub> transients are evaluated, as they are less distorted by possible impurity contributions at the PL energy of the latter and suppressed polariton propagation effects. The PL decay, see Fig. 4.3 (b), is nearly unchanged as the temperature is increased from 10 K to 90 K. In addition, the spectrally integrated luminescence intensity decreases only slightly, and the intensity of the PSBs even increases, both consistent with the ionization of the BX. All

these findings are clear hallmarks of the sample emission being dominated by radiative recombination and intrinsic effects like scattering with optical and acoustic phonons, c.f. 2.1.2 and 2.3.1. Non-radiative capture processes are slow and/or negligible, resulting in only a slight decrease of the absolute decay rate of the PL signal. Together with the weak BX luminescence (Fig. 4.1) and the observation of higher excitonic transitions (Fig. 4.2), the temperature-dependent results confirm high material quality, required for the following studies.

#### 4.1.2 Resonant vs. non-resonant excitation

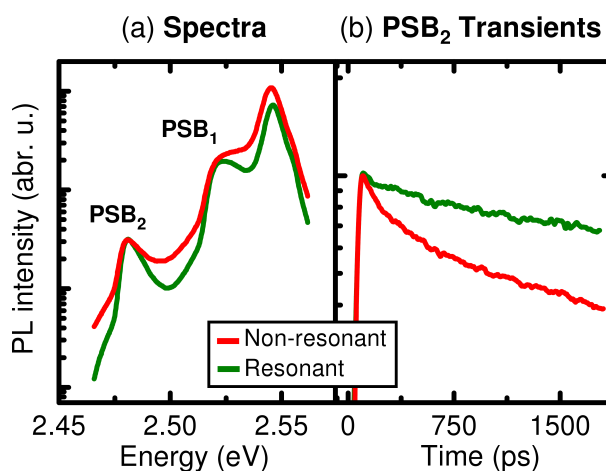


Figure 4.4: (a) PL spectra of CdS at high excitation density for the resonant and non-resonant excitation energies of 2.54 eV, and 2.85 eV, respectively. (b) Normalized transients of the second PSB. The lattice temperature is set to 10 K.

The first and the most direct way to create excitonic population in a PL experiment is the resonant excitation at the ground state transition, i.e. 1s exciton-resonance. In contrary, when continuum states are excited, electron-hole plasma is always created directly after the absorption of the incident pulse, see the discussion in section 2.1.2. In the latter case, however, the excitation density should also be high enough to observe plasma-dominated luminescence due to the density-dependent radiative recombination rate of the uncorrelated electrons and holes. The pump density is thus set to  $10^{14} \text{ cm}^{-2}$  photons per pulse. Low excitation results are always recovered after the application of high pump densities to ensure that the material is not damaged during the experiment. For this study, the CdS sample is chosen, since the exciton ground state of the CdSe at 1.82 eV is beyond the spectral range accessible with a Ti:Sa laser. Hence, the photon energy is set to 2.85 eV and 2.54 eV for the non-resonant and resonant excitation of CdS, respectively. In the latter case, the pump energy is slightly detuned towards lower energies with respect to the exci-



#### 4 Role of the Coulomb-interaction in phonon-assisted emission

ton transition to ensure that no continuum states are excited by the spectrally broad 100 fs pulses. Also, the pump power is increased to balance the resulting decrease in absorption. PL spectra of CdS are plotted in Fig. 4.4 (a) for the two different excitation conditions and the lattice temperature of 10 K with pronounced PSBs found in both cases. Remarkably, the shape and the relative intensities of the sidebands are nearly independent of the excitation energy. Only a slight broadening due to the higher carrier temperature is observed for the non-resonant scenario. However, in stark contrast to the similar spectral line shapes, differences in the luminescence dynamics are significant. Normalized PL time traces at the energy of the second PSB are shown in Fig. 4.4 (b). The signal decays mono-exponentially in case of the resonant excitation, as commonly expected for the exciton-related PL. On the other hand, for non-resonant excitation conditions, the PL exhibits a more complicated non-exponential behavior with fast initial decay and slower recombination at later times. As already discussed in section 2.1.2, these temporal signatures are a clear hallmark of plasma recombination due to the characteristic dependence of the decay rate on carrier density.

##### 4.1.3 Excitation power dependence: the Mott-transition

The second possibility to obtain exciton- or plasma-dominated dynamics is the variation of the excitation power. For non-resonant excitation, it is well-known that exciton populations are typically formed at low carrier densities, yet electron-hole plasma is easily obtained in the high-density regime [9, 10]. The case of intermediate densities, when the exciton population starts to decrease in favor of the electron-hole plasma, is the so-called *Mott-transition*, in analogy to the semiconductor-metal phase-transition in the band-structures of solids [27]. The main reason for this behavior is the increasingly efficient screening of the Coulomb-interaction at sufficiently high carrier densities. In a simple picture, the Mott-transition occurs when the inverse density of carriers  $n^{-1}$  approaches the value of the "exciton volume", approximately defined as the volume of a sphere with the excitonic Bohr-radius  $a_B$  [9], i.e.,

$$n \approx \frac{3}{4\pi a_B^3}. \quad (4.1)$$

This relation can be used to estimate the critical density of carriers for the exciton-plasma transition. As a qualitative result, the Mott-transition typically occurs at higher carrier densities when the Bohr-radius is small and the exciton binding energy is high. However, though the picture of clearly distinguishable phases is tempting, the boundary between the exciton- and plasma-dominated regimes is rather a continuous transition than a discrete step due to the complexity of the many-body interactions.

Based on these considerations, excitation densities between  $n_0 = 10^{11} \text{ cm}^{-2}$  photons per



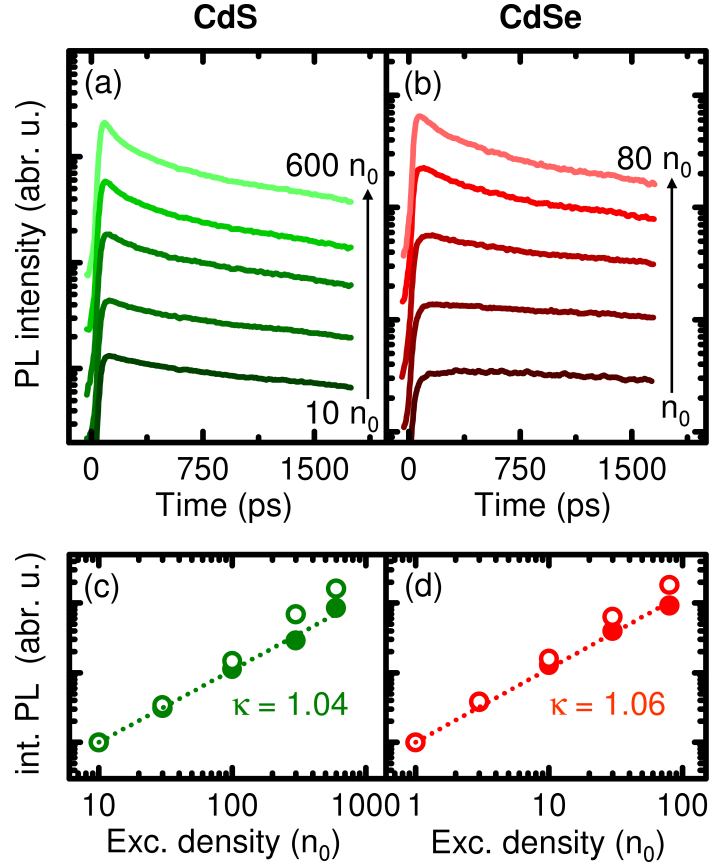


Figure 4.5: Time-resolved PSB<sub>2</sub> emission of CdS (a) and CdSe (b) as function of excitation power for a lattice temperature of  $T=10$  K. The lowest excitation density is  $n_0 = 10^{11}$  cm<sup>-2</sup> photons per pulse. The corresponding absolute PL intensities (full circles) and the PL amplitudes directly after the excitation (empty circles) of the second PSB are shown in (c) and (d) for CdS and CdSe, respectively. The dotted lines are fits with the power law  $I_{PL} \propto I_{pump}^\kappa$ .

pulse and  $600 n_0$  are chosen for the experiment. The values correspond to average carrier densities up to several  $10^{18}$  cm<sup>-3</sup>, estimated from the absorption coefficients of CdS and CdSe [36]. These densities, evaluated using the approximative Eq. (4.1), are in the range of the Mott-transitions at about  $10^{19}$  cm<sup>-3</sup> and  $10^{18}$  cm<sup>-3</sup> for CdS and CdSe, respectively. Again, to identify excitonic emission and plasma recombination, PL transients of CdS (a) and CdSe (b) are plotted in Fig. 4.5 as function of the excitation density at the spectral position of the PSB<sub>2</sub>. For both samples, we observe a single-exponential decay at low pump densities, similar to the PL dynamics under the resonant excitation. As the pump power is increased, the PL dynamics show a pronounced non-exponential behavior. To confirm the observed increase in the radiative recombination rate at higher excitation densities, the PL amplitudes and relative intensities are evaluated. Figures 4.5 (c) and (d) show the spectrally- and temporally-integrated PL intensity (full circles) as well as the PL intensity direct after the excitation (empty circles) as function of the pump density for

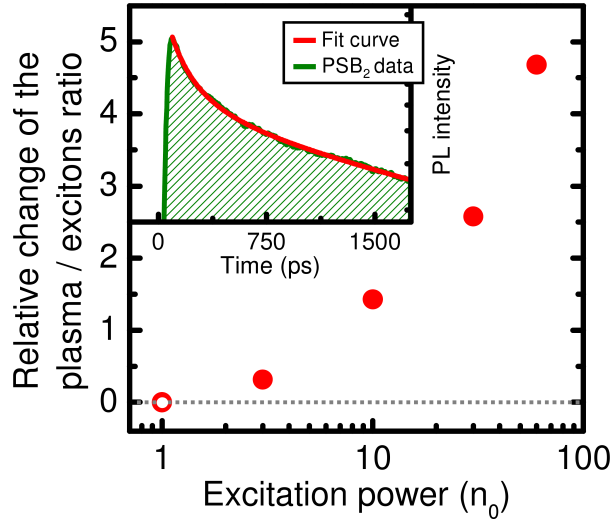


Figure 4.6: Relative change of the ratio between plasma density and exciton population, obtained from the fit parameters  $A_1$  and  $n_{eh}$ . The inset shows an exemplary PSB<sub>2</sub> transient of CdS at the excitation density of  $600 n_0$ , fitted by the equation (4.2).

CdS and CdSe, respectively. The absolute intensity of the PL is directly proportional to the excitation density, while the initial PL intensity exhibits a pronounced superlinear increase. The latter is a clear hallmark of an increased radiative decay rate, since the initial emission intensity is proportional to the inverse radiative lifetime and carrier density only, see Eq. (2.41) and (2.34). In addition, non-radiative recombination via defects, Auger processes, or stimulated emission parallel to the sample surface would always lead to a pronounced sublinear behavior of the PL intensity which is not observed in the experimental data. Also, any saturation of impurity-related non-radiative channels at higher pump densities, i.e. SRH recombination, is excluded due to the linear increase of the absolute PL intensity and shorter carrier lifetimes. Thus, the enhancement of the decay rate for the increasing excitation power is unambiguously attributed to faster radiative recombination. Based on the characteristic PL dynamics, the recombination processes are dominated by excitons at low and electron-hole plasma at high carrier densities. Interestingly, the transition between the two regimes occurs at about one order of magnitude lower excitation density in CdSe compared to CdS, matching the difference in the previously estimated Mott-thresholds.

Further support for the proposed interpretation of the experimental findings is given by quantitative line-shape analysis of the transient data. When both excitons and plasma contribute to the luminescence decay, the PL dynamics should obey following expression,

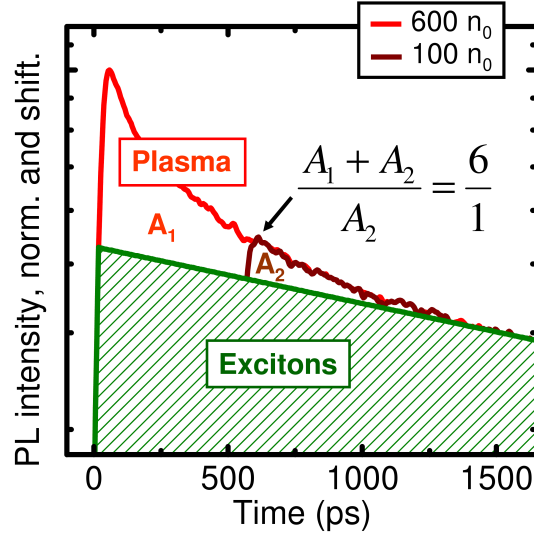


Figure 4.7: PL transients of the CdS sample for the excitation densities of 100  $n_0$  and 600  $n_0$ . The data are normalized to the intensity of the excitonic emission at time delays > 1500 ps. The emission trace for the lower power is shifted on the time-axis for better comparison.

resulting from the sum of the Eq. (2.41) and (2.34):

$$I_{PL}(t) = \left( A_1 e^{-\frac{t}{\tau_X}} \right) + \left( \frac{A_2}{\frac{t}{\tau_{eh}} + \frac{1}{n_{eh}}} \right). \quad (4.2)$$

Here, the excitonic population is proportional to  $A_1$  and the electron-hole plasma density is given by  $n_{eh}$ . Characteristic radiative decay times are given by  $\tau_X$  and  $\tau_{eh}$  for excitons and plasma, respectively. An exemplary fit of the transient PL from the CdS sample is shown in the inset of Fig. 4.6 for the maximal excitation density of 600  $n_0$ . The theoretical line-shape, predicted by the Eq. (4.2), agrees well with the experimental data. Thus, it is reasonable to extract parameters from the proposed decay model, and the PSB<sub>2</sub> density-dependent transients of CdS are, hence, fitted with the Eq. (4.2). All fit curves are in excellent agreement with the measured transients for the constant decay rates  $\tau_X = 3.1$  ns and  $\tau_{eh} = 0.6$  ns. This result is reasonable, since recombination constants are not expected to change with carrier density. The analysis also yields the relative change of the ratio between the plasma density and excitonic population, shown in Fig. 4.6. Here, the low-density result is artificially set to zero, since the corresponding plasma density parameter is below the "detection" range of the fitting procedure due to the experimental noise. The relative increase of the plasma population with excitation power is clearly superlinear and thus consistent with the expected phase-transition-like behavior in the region of the Mott-density.

Finally, the characteristic superlinear scalability of the plasma emission with carrier den-

#### 4 Role of the Coulomb-interaction in phonon-assisted emission

sity is verified. PL transients of the CdS sample are plotted in Fig. 4.7 for the excitation densities of  $100 n_0$  and  $600 n_0$ . The emission trace for the lower power is shifted on the time-axis for better comparison. In both cases, the luminescence from excitons with a long decay time is considered as background for the plasma-related PL. The two transients are thus normalized to the intensity of the excitonic emission at time delays  $> 1500$  ps. At high excitation density, the carriers decay fast until the carrier density reaches the value corresponding to the low excitation conditions. The comparison of the respective integrated PL intensities ( $A_1 + A_2$ ) and  $A_2$  yields the ratio 6:1, perfectly matching the difference in the pump densities. This result illustrates that the same density conditions are reached when the excitation power is decreased by a constant factor or when the carrier density decays to the same amount. Thus, the dynamics of the plasma emission are governed by the carrier density only, fully corresponding to the proposed intrinsic behavior of plasma-related luminescence.

In summary, unambiguous experimental evidence for phonon-assisted plasma emission is presented, clearly confirming the predictions of the many-body theory, c.f. section 2.2.1. The experimental results are further supported by the quantitative analysis of the PL dynamics, characteristic for exciton and/or plasma luminescence. Hence, due to the carrier-carrier Coulomb-interaction the emission at the excitonic PSB resonances can definitely not be considered as an evidence of the exciton population. The PL from electron-hole plasma can, indeed, strongly contribute or even dominate the PSBs. The experiments show that both exciton- and plasma-dominated regimes are accessible by the specific choice of the excitation conditions.

## 4.2 Interaction mechanisms: Fröhlich vs. deformation potential scattering

In this section, the influence of Coulomb-correlations between electrons and holes on carrier scattering with optical phonons is studied. Phonon-assisted emission is used to quantify the contributions from the two distinctive carrier-phonon interaction mechanisms, previously discussed in the section 2.2.1. The investigations are focused on finding the evidence for possible suppression of Fröhlich interaction in case of the quasi-neutral excitons. The aim is to show that even in polar semiconductors with naturally strong, polar carrier-phonon coupling, the interaction via deformation potential can contribute or even dominate the scattering of excitons with LO-phonons. The first part of the section deals with the characterization of the semiconductor materials, used for the conducted studies. In the second part, the analysis of the experimental data is presented and the results are compared with the theoretical predictions from many-body calculations. The samples are

## 4.2 Interaction mechanisms: Fröhlich vs. deformation potential scattering

provided by the groups of Profs. Martin Eickhoff and Bruno Meyer at the Justus-Liebig University Giessen (Germany).

### 4.2.1 Material systems

Three different bulk materials with the sample thickness between  $0.3\ \mu\text{m}$  and  $10\ \mu\text{m}$  are chosen for the proposed investigations: ZnO, ZnS, and CdS. These are typical representatives for polar wide-gap semiconductors exhibiting strong electron-phonon and Coulomb-interaction effects [55, 64, 9]. The exciton binding energies are in the range of several  $10^2$ 's of meV, large enough to ensure efficient exciton formation, allowing measurements in the excitonic regime below the Mott-transition. For this purpose, the studies presented in the previous subsection are used to identify the required excitation conditions, c.f. 4.1. According to the theoretical considerations, outlined in the section 2.2.1, e.g., Fig. 2.21, the analysis of the experimental data involves an evaluation of spectrally and temporally integrated PSB intensities. Hence, the material quality should be high enough to clearly resolve the first two sidebands in a reasonable temperature range for accurate comparison with the theoretical calculations.

Figure 4.8 shows the PL spectra of the ZnO (a), ZnS (b), and CdS (c) samples, time-integrated over the 2 ns-window after the excitation as function of the lattice temperature ranging between  $T = 10\ \text{K}$  and  $T = 90\ \text{K}$ . For these measurements, the spectral and temporal resolutions of the TRPL setup are 0.4 nm and 5 ps, respectively. The excitation density is set to  $n_0 = 10^{11}\ \text{cm}^{-2}$  photons per pulse. Taking into account the pump geometry and the absorption coefficients [9, 36] this corresponds to initially injected carrier densities of several  $10^{15}\ \text{cm}^{-3}$  in all three samples. All values are well below the respective estimated Mott-densities thus favoring the formation of excitons, confirmed by the analysis of the emission dynamics, discussed in section 4.1. All spectra show the well-known PL signatures from free (FX) and bound (BX) excitons [36], as well as the corresponding PSB peaks. The latter are separated by 72 meV (ZnO), 48 meV (ZnS), and 38 meV (CdS), matching the respective LO-phonon energies [36]. Based on the energy spacings between the  $\text{PSB}_1$  and the FX peak, as well as the temperature stability of the sideband emission, the strong phonon-assisted luminescence is unambiguously attributed to the FX-related transitions in all three samples. As illustrated in section 2.3.1, the BX-related PSBs, on the other hand, appear as small peaks on the low-energy side of the FX sidebands, decreasing fast in intensity with the rising temperature due to the BX ionization. The observation of pronounced PSB emission over one order of magnitude of lattice temperature as well as the weak BX contributions to the phonon-assisted PL both render the samples as highly suitable for the analysis of the sideband ratios.

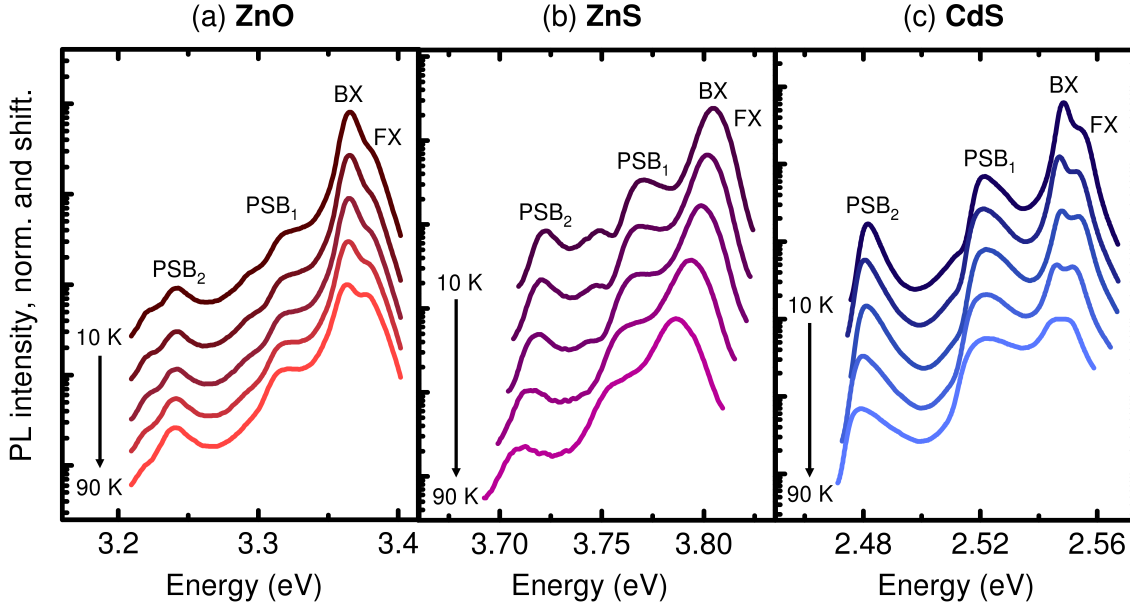


Figure 4.8: PL spectra of ZnO (a) ZnS (b), and CdS (c) samples at low excitation densities and non-resonant excitation conditions as function of lattice temperature. The latter is varied between 10 K and 90 K in discrete steps of  $\Delta T = 20$  K. Signatures of bound and free excitons as well as the PSBs, corresponding to the latter, are marked by BX, FX, and  $PSB_n$ , respectively.

#### 4.2.2 Analysis of phonon-sideband ratios

As a qualitative overview, time-integrated PL spectra of the CdS and the ZnO samples are shown in Fig. 4.9 (a) and (b), respectively, at two different lattice temperatures of  $T = 10$  K and  $T = 90$  K, in the spectral range of the first two PSBs. The spectra are normalized to the respective PL maxima of the second PSB, and the energy scale is chosen relative to the ZPL peak for better comparison. Time resolved PL traces of the  $PSB_2$  emission are plotted in the corresponding insets. In both samples, the luminescence dynamics are almost single-exponential and do not change significantly with rising temperature. The data thus confirms exciton-related PL, see section 4.1, and also excludes thermal activation of additional recombination channels, c.f. 2.3.1. The most important observation, however, is the strong decrease of the ratio between the second and the first PSB in CdS and almost constant relative PSB intensities in case of the ZnO when the lattice temperature is increased from 10 K to 90 K.

To quantify these differences, temperature-dependent relative areas of the first two PSBs are evaluated. To ensure that no extrinsic contributions from the BX luminescence, c.f. Fig. 4.8, affect the analysis, the BX peaks are fitted with Lorentzians and subtracted from the measured spectra. Exemplary results of this procedure are shown in Fig. 4.10 (a) and (b) at a lattice temperature of 10 K for CdS and ZnO, respectively. After the subtrac-

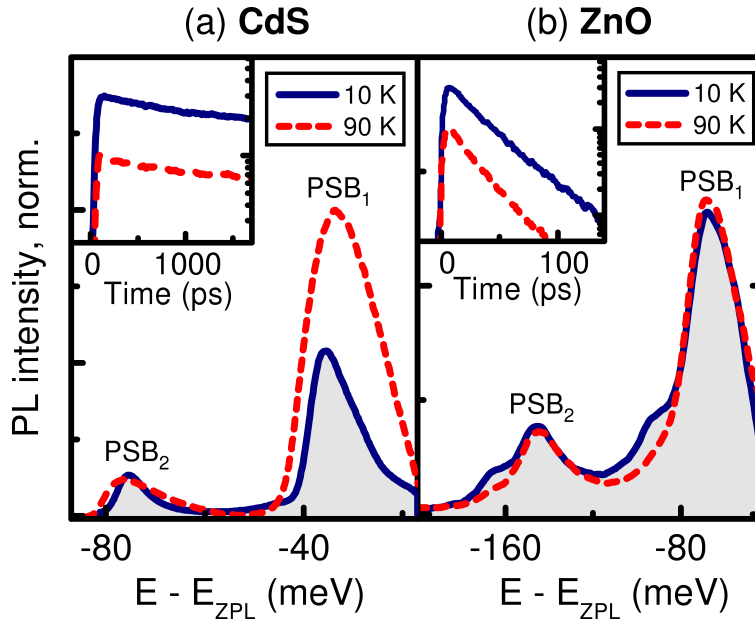


Figure 4.9: Time-integrated PL spectra of the first and the second PSB in CdS (a) and ZnO (b) at lattice temperatures of  $T = 10$  K and  $T = 90$  K and the excitation density of  $10^{11}$  photons/cm<sup>2</sup> per pulse. The spectra are normalized to the PSB<sub>2</sub> maximum for clarity. The inset shows the emission dynamics of the second PSB.

tion of the BX contributions, the typical, intrinsic spectral shape of the PSBs is revealed, with a steep low-energy slope and a pronounced flank at higher energies. Especially in case of the ZnO sample, the difference between the measured spectrum with the broad BX emission and the pure PSB luminescence is significant. Therefore, the ZnO data is used to estimate the effect of the fitting procedure on the extracted subband ratio PSB<sub>2</sub>/PSB<sub>1</sub>. The comparison of different evaluation schemes is shown in Fig. 4.10 (c). In addition to the BX subtraction, results of the integration over the PSB peaks as well as the simple ratio of the sideband intensity maxima are included. Interestingly, though the different approaches yield slightly deviating PSB ratios, the overall temperature-dependent PSB<sub>2</sub>/PSB<sub>1</sub> value remains constant at about  $(0.24 \pm 0.03)$ . Also, the data from a second ZnO bulk sample, used for the confirmation of the experimental findings, reproduces the results of the original sample. As a result, to ensure consistent analysis, the BX subtraction scheme is applied for the evaluation of the PSB ratios from all three samples. The error bars are then given by the standard deviation in the range of 0.03 due to the uncertainties in the fitting procedure.

The temperature dependence of the experimentally obtained PSB<sub>2</sub>/PSB<sub>1</sub> intensity ratios for ZnO, ZnS and CdS samples is plotted in Fig. 4.11 (a). The ratio strongly decreases for CdS, exhibit a less pronounced change for the ZnS, and remains constant in case of the ZnO within the experimental error. The corresponding theoretical results from many-body



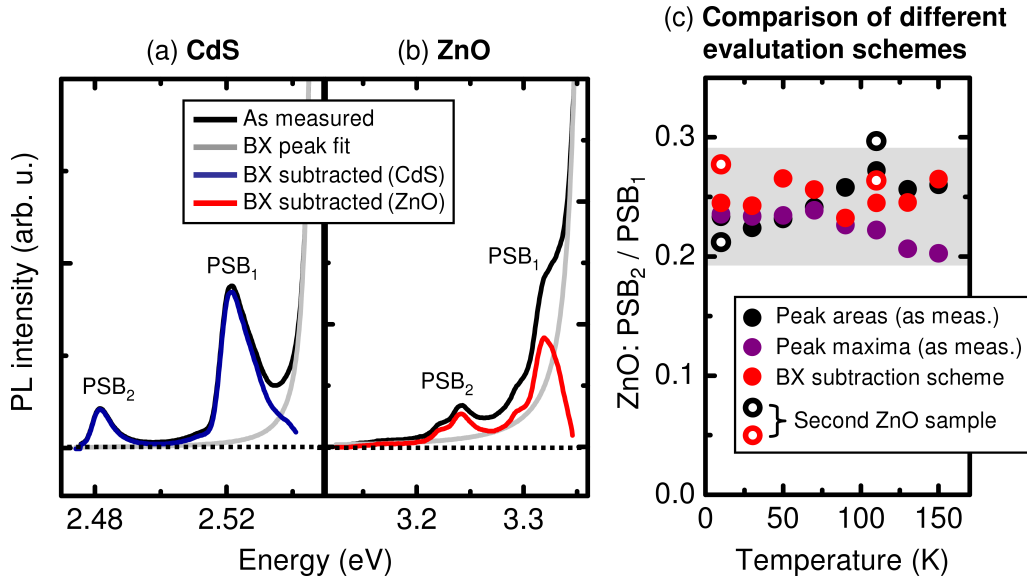


Figure 4.10: As measured PL spectra, corresponding BX fits, as well as the resulting spectra after BX subtraction are exemplary plotted for CdS (a) and ZnO (b) at  $T = 10$  K in the energy range of the first two PSBs. Comparison of different evaluation schemes for the relative subband intensities is shown in Fig. (c). Open circles denote data from a second ZnO sample, included for additional verification of the experimental observations.

calculations are shown in Fig. 4.11 (c). The ratios are obtained by calculating the contributions of Fröhlich and deformation-potential coupling using material parameters and interaction constants from the literature [58, 123, 36, 124]. No fitting to the experimental data is applied. The calculations can thus be considered as fundamental theoretical predictions for the material behavior. The more astonishing is the perfect match of the experimental results to the calculated PSB ratios regarding the characteristic temperature dependence and also the absolute values. According to the previous discussion in section 2.2.1 and as a result of the respective calculations, the dominant exciton-phonon interaction mechanisms are clearly assigned to Fröhlich interaction for CdS and to deformation-potential coupling for ZnO, with ZnS as an intermediate case.

These findings are further corroborated by the pump power dependence of the PSB luminescence. Since the carrier temperature rises for increasing excitation densities due to the hot-phonon effect [38], this approach provides an alternative way to alter the exciton distribution in favor of higher  $\mathbf{k}$ -values, i.e., momenta. However, the carrier density should be kept below the Mott-transition to ensure dominant excitonic contributions to the PL signal. Figure 4.12 (a) shows the  $PSB_2/PSB_1$  intensity ratios for ZnO and CdS at  $T = 10$  K as a function of the excitation power. Again,  $n_0$  corresponds to the photon flux of  $10^{11}$  photons/cm<sup>2</sup> per pulse. The approximate density region of the Mott-transition is marked by the gray area for CdS, based on the results of previous investigations, see sec-



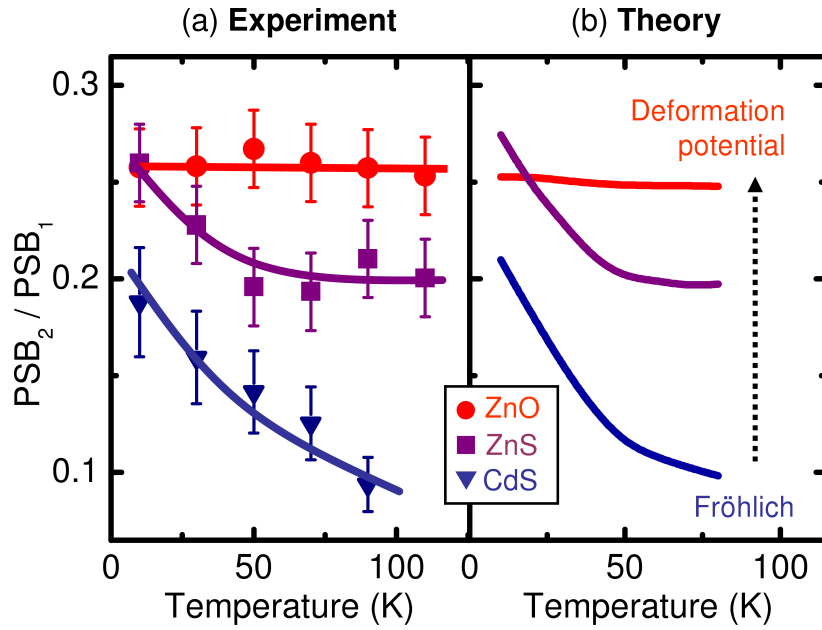


Figure 4.11: (a) Ratios of the second and first phonon sidebands as function of lattice temperature for ZnO (circles), ZnS (squares), and CdS (triangles, top to bottom) for an excitation density of  $10^{11}$  photons/cm<sup>2</sup> per pulse. The solid lines are given as guides to the eye. The corresponding results obtained from the fully-microscopic calculations are shown in (b).

tion 4.1. In case of the ZnO, this region is beyond the CdS value due to the smaller exciton Bohr radius and is thus not reached by the highest pump power. When the carrier density is increased, the  $PSB_2/PSB_1$  ratio remains nearly constant and even increases slightly for ZnO. At the same time, the relative intensity of the second sideband decreases almost by a factor of two in case of CdS. These results are fully consistent with temperature-dependent measurements, showing the expected behavior for Fröhlich interaction for the PSB emission in CdS and deformation potential scattering as the dominant mechanism in ZnO. Interestingly, the pronounced density dependence of the PSB ratio also influences the relative PL dynamics, plotted in Fig. 4.12 (b) and (c) for ZnO and CdS as direct comparison. The decay rates of the first and the second PSB are equal for the ZnO sample, as commonly expected, yet they deviate from each other in case of CdS due to the significant change in the PSB ratio for decreasing carrier density, c.f. Fig. 4.12 (a).

In summary, exciton-phonon interaction mechanisms in polar semiconductors are studied. The experimental data is analyzed by evaluating the relative ratios of the excitonic PSBs as function of lattice temperature and excitation density, both used to alter the carrier distribution in momentum space, c.f. discussion in section 2.1.2. The findings are compared to the calculations via microscopic many-body approach to identify the dominant scattering processes. Fröhlich coupling governs the exciton-phonon interaction in

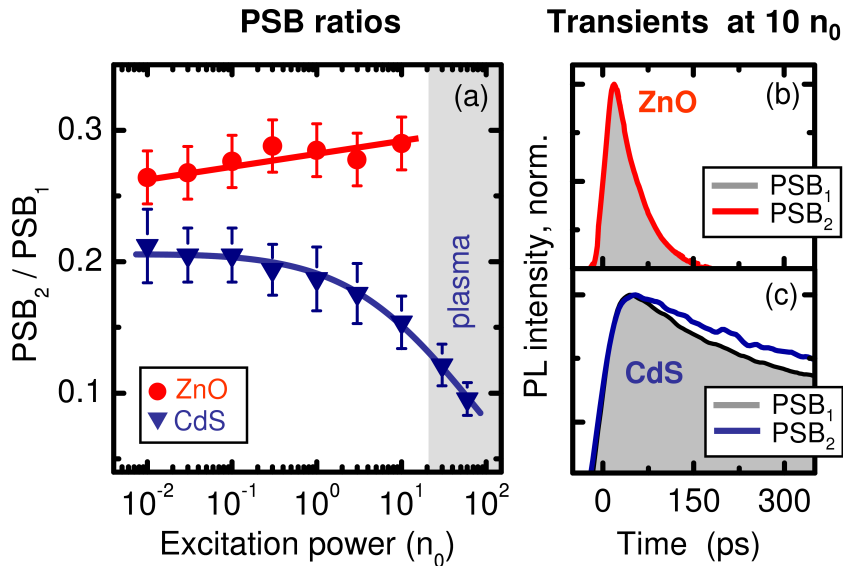


Figure 4.12: (a) Ratio of the second and first phonon sidebands as a function of excitation density at  $T = 10$  K for ZnO and CdS. Solid lines are guides to the eye.  $n_0$  corresponds to the photon flux of  $10^{11}$  photons/cm<sup>2</sup> per pulse. Normalized transients for ZnO (b) and CdS (c) of the first and the second PSB are shown by solid lines and gray areas, respectively.

CdS while deformation potential scattering turns out to be the dominant mechanism in ZnO, and both processes contribute about equally in ZnS. It is important to notice that the scattering between *single electrons* and optical phonons are dominated by the Fröhlich interaction in all studied cases due to the strong polarity of the respective materials. However, particularly for ZnO, these contributions are suppressed by the strong Coulomb-coupling of electrons and holes in *excitons* rendering deformation potential scattering the overall dominant mechanism responsible for the sideband emission.

# 5 Ultra-fast luminescence studies of novel semiconductor material systems

The experiments presented this chapter are focused on the characterization measurements of recently synthesized material systems: ZnO/(ZnMg)O heterostructures, GaN quantum wires (QWires), as well as the (GaAs)Bi quantum wells (QWs). The former two materials are designed for potential electro-optical applications in the UV spectral range [12, 13]. The TRPL spectroscopy is applied to gain insight as well as a better understanding of the respective carrier relaxation and recombination processes, both crucial for the device operation. The latter material system, Ga(AsBi), is a possible candidate for light-emitting devices in the NIR, at the telecom wavelengths of 1.3  $\mu\text{m}$  and 1.55  $\mu\text{m}$  [14]. The main hallmark of this semiconductor is the giant band gap reduction with Bi content [22], unusually large for the more typical materials [36]. The aim of the studies is the systematic investigation of carrier dynamics. The measurements are supported by kinetic Monte-Carlo simulations [23], providing a quantitative analysis of carrier localization effects.

## 5.1 Carrier dynamics in ZnO/(ZnMg)O heterostructures

This section deals with time-resolved spectroscopy studies of ZnO-based heterostructures. ZnO is a direct-gap II-VI semiconductor with the band-gap in the UV spectral range at about 3.4 eV, adopting the hexagonal wurtzite crystal structure. The material is known for its comparably large exciton binding energy of 60 meV as well as for strong electron-phonon coupling, both exploited for the investigations discussed in the previous chapter, see 4.2. A comprehensive review of the material properties is given in Refs. [125, 12, 126]. The studies conducted within the framework of my thesis are focused on the investigation of the ZnO quantum wells with (ZnMg)O barriers, recently available due to the improved growth methods [127, 128, 129]. This system is proposed for the application of ZnO in electro-optical devices as photo-detectors, light-emitting diodes and, above all, lasers in the UV spectral range, attracting much interest in the scientific community [130, 131, 132, 133]. All these applications have in common that, in general, their

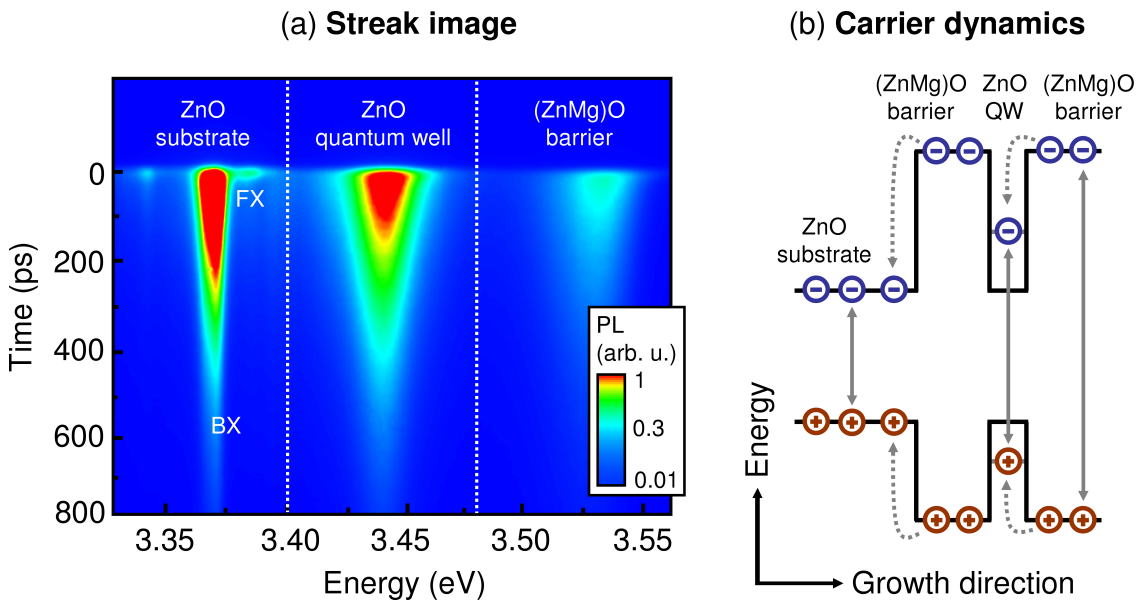


Figure 5.1: (a) Exemplary TRPL intensity plot of a ZnO/(ZnMg)O heterostructure as function of emission energy and time after non-resonant, pulsed excitation. The lattice temperature is set to 10 K and the excitation density - to  $4 \cdot 10^{10}$  photons/cm<sup>2</sup> per pulse. Free- and bound-exciton emission of the ZnO substrate is marked by FX and BX, respectively. (b) Schematic illustration of the corresponding carrier relaxation and recombination dynamics.

performance is highly sensitive to the carrier dynamics. Hence, the detailed knowledge of the latter remains a crucial task for the optimal design as well as the effective operation of the ZnO-based devices. Here, time-resolved PL spectroscopy is applied to gain insight as well as a better understanding of the respective carrier relaxation and recombination processes in ZnO/(ZnMgO) heterostructures. All samples studied in the following investigations are grown in the group of Prof. Martin Eickhoff by Bernhard Laumer and Dr. Thomas Wassner using plasma-assisted molecular beam epitaxy[127]; details are found in Ref. [134, 135].

As an overview, an exemplary streak-camera image of the measured low temperature TRPL from a ZnO/(Zn<sub>0.9</sub>Mg<sub>0.1</sub>)O sample is shown in Fig. 5.1 (a) for low excitation density. The sample consists of an about 300 nm thick ZnO buffer on a sapphire substrate, followed by a 2 nm ZnO QW embedded between two (Zn<sub>0.9</sub>Mg<sub>0.1</sub>)O barriers of about 20 nm each. The carriers are non-resonantly excited into the barriers at  $E_{exc} = 4.3$  eV, corresponding to the typical excitation conditions for an optically pumped laser. The ratio of photons absorbed in the (ZnMg)O layers is estimated to about 50 %, using the absorption coefficient of ZnO from Ref. [136] as an approximation. The emission peaks of the ZnO QW, the (ZnMg)O layers, as well as from the ZnO substrate are clearly observed and identified by their respective spectral positions. The QW and substrate PL both dominate the spectrum. Also, in all three cases, the signal rises quasi-instantaneously with

## 5.1 Carrier dynamics in ZnO/(ZnMg)O heterostructures

the resolution of the experiment of about 30 ps. Based on these first observations, a basic, general scheme for the carrier dynamics is proposed, illustrated in Fig. 5.1 (b). Most carriers are directly excited either in the (ZnMg)O barriers or in the ZnO substrate since the contribution of the single QW to the overall absorption is negligible. The carriers in Zn(MgO) layers are captured into the QW on a sub-30 ps time-scale, leading to a strong QW emission. However, some of the carriers are still localized in the barrier layers since a pronounced, long-living PL signal from the (ZnMg)O is observed. In addition, relaxation of carriers from the lower barrier towards the ZnO substrate can not be excluded. These findings lead to a number of questions, relevant for possible applications of ZnO-heterostructures as emitting devices:

- What is the reason for carrier localization in the barrier layers?
- How fast are the carriers captured into the QW?
- Are QW carriers free to move in two dimensions or are they localized in the in-plane direction?
- Does radiative or non-radiative recombination dominates carrier lifetime in the QW?

The aim of the following studies is finding answers to these questions. The discussion is organized as follows: first, carrier localization in (ZnMg)O epi-layers is investigated, excluding any contributions from fast relaxation processes towards QW. Then, carrier-density-dependent screening of internal electric field is used as a probe for carrier population in the ZnO QWs, allowing to monitor carrier capture from the barriers. Finally, radiative and non-radiative contributions to the carrier lifetime are studied for different growth conditions of the QWs. In the latter two subsections, an additional emphasis is laid on the quantification of the in-plane carrier localization. For this purpose, the analysis of the phonon-assisted emission, previously discussed in sections 2.2.1 and 4.2, is applied.

### 5.1.1 Carrier localization in (ZnMg)O layers

The investigations in this subsection are focused on the study of carrier relaxation dynamics in ternary  $(\text{Zn}_{1-x}\text{Mg}_x)\text{O}$  alloys. The samples are single epitaxial layers grown on a sapphire substrate with an average layer thickness of  $0.3\ \mu\text{m}$  and Mg concentrations of  $x = 0$ ,  $x = 0.04$ ,  $x = 0.06$  and  $x = 0.21$ , respectively. The Mg concentrations are estimated by comparing the measured PL emission energies with literature values [129, 134, 137, 138] and are also confirmed by the x-ray diffraction measurements in the group of Prof. Martin Eickhoff. The absence of the QW and only a thin ZnO buffer of several 10's of nm are

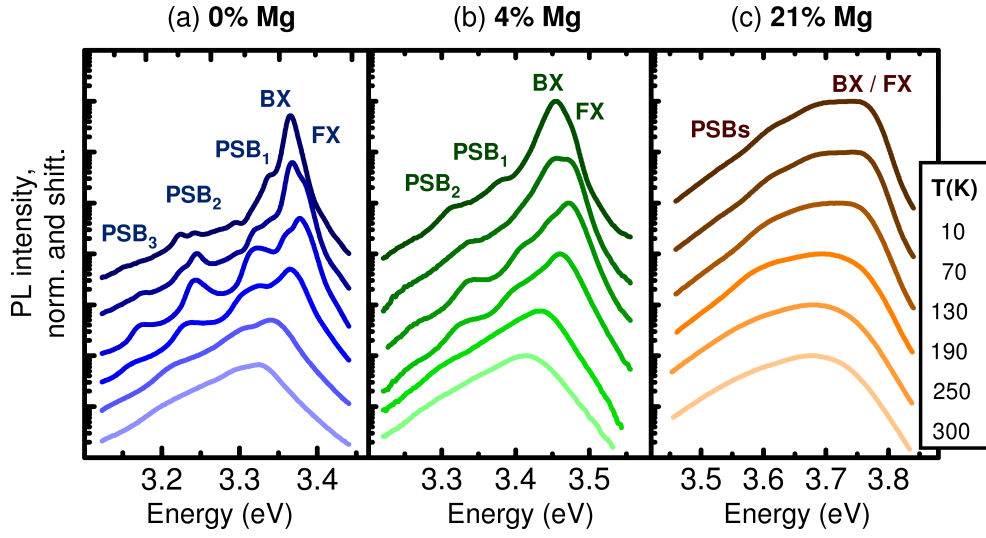


Figure 5.2: TRPL spectra of  $(\text{Zn}_{1-x}\text{Mg}_x)\text{O}$  samples with Mg concentrations of  $x=0$  (a)  $x=0.04$  (b), and  $x=0.21$  (c). The lattice temperature is varied between 10 K and 290 K. The excitation energy and incident photon density are held constant at 4.3 eV and  $10^{11}$  photons/cm<sup>2</sup>, respectively.

chosen to avoid any significant contributions of fast carrier capture processes, typically present in more complex heterostructures. All samples are excited non-resonantly with a photon energy of 4.3 eV, far above the absorption edge in all samples, and a pump flux of  $10^{11}$  photons/cm<sup>2</sup> per pulse to ensure comparable experimental conditions. The temporal resolution is varied between 4 ps and 30 ps, corresponding to detection windows of 200 ps and 2 ns, respectively.

PL spectra for three exemplary  $(\text{Zn}_{1-x}\text{Mg}_x)\text{O}$  samples are shown in Fig. 5.2 in the temperature range between 10 K and 290 K. The experimental data are time-integrated over the complete detection window, normalized, and vertically shifted for clarity. The sample with  $x=0$  shows the well-known spectral signatures of ZnO, i.e., bound (BX) and free (FX) excitons, as well as the corresponding LO-phonon sidebands [9, 139]. Aside from an increased broadening and a frequency shift, the spectra of the  $(\text{Zn}_{1-x}\text{Mg}_x)\text{O}$  sample with a Mg concentration of  $x=0.04$  exhibit spectral characteristics similar to those of the ZnO reference sample. As shown in Fig. 5.2 (c), the broadening and the spectral shift are even more pronounced for higher Mg concentration [137]. The concentration-dependent broadening of PL spectra is a common feature in ternary alloys. It is generally attributed to spatial fluctuations of the alloy composition, such as the Mg content in the  $(\text{Zn}_{1-x}\text{Mg}_x)\text{O}$  material system [9]. The influence of such fluctuations on the absorption and PL spectra of  $(\text{Zn}_{1-x}\text{Mg}_x)\text{O}$  has been reported in a number of experiments [127, 134, 138, 140]. The alloy disorder results in the formation of localized states below the band edge, i.e., additional broadening of the so-called Urbach tail [9, 141]. As already discussed in section 2.3.2, the presence of these states strongly affects both the emission spectrum and the

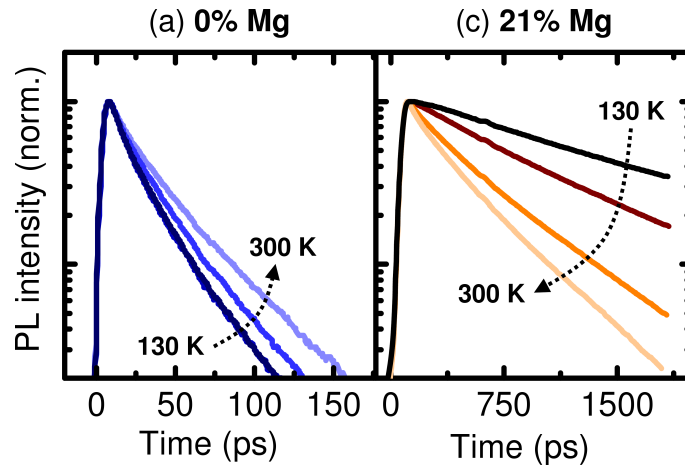


Figure 5.3: Transients of the  $(\text{Zn}_{1-x}\text{Mg}_x)\text{O}$  samples with  $x=0$  and  $x=0.21$  in the temperature range between 130 K and 290 K.

dynamics of the excited carrier system, leading, e.g., to a pronounced S-shape of the PL maximum. Here, though the PL spectra from the samples clearly exhibit an S-shape, c.f. Fig. 5.2 (b), the deconvolution between the impact of alloy-disorder and the contributions from the BX ionization is rather challenging due to the spectrally broad emission. In addition, the S-shape-related shift of the PL maximum to higher energies with rising temperature starts only at about 300 K for the sample with the Mg concentration of 21 %. At these temperatures a quantitative approach is also limited by phonon-induced broadening. Therefore, the analysis of the time-resolved data is applied.

For direct comparison, the PL intensities of the ZnO reference with 0% Mg and the 21 % Mg sample are plotted in Fig. 5.3 (a) and (b), respectively. The temperature range is chosen from 130 K to 290 K to minimize contributions from bound excitons. The ZnO signal shows a fast decay on a 30 ps time-scale and only a weak temperature dependence. Here, the lifetime of the excited carriers is governed by the interplay of radiative carrier recombination and the carrier capture by the deep traps. In contrast to the ZnO reference, the PL decay time decreases by almost one order of magnitude for the sample with  $x=0.21$  as the temperature is raised from 130 K to 290 K. At the same time, the absolute carrier lifetimes are significantly longer than in the pure ZnO sample, excluding a trivial explanation by faster non-radiative recombination rates in the  $(\text{Zn}_{0.79}\text{Mg}_{0.21})\text{O}$  sample.

An overview of the temperature-dependent  $1/e$  decay times for all  $(\text{ZnMg})\text{O}$  samples is shown in Fig. 5.4. The  $1/e$  time is defined as the time when the signal intensity decays to the  $1/e$ -th of the peak value, and is used here for consistency. The decay time strongly increases with increasing Mg concentration by up to two orders of magnitude. In addition, the temperature variation of the carrier lifetime is much more pronounced for Mg-rich samples. The inset of the Fig. 5.4 shows the integrated PL intensity and the recombination rate, i.e. the inverse lifetime, of the 21 % Mg sample as function of temperature.



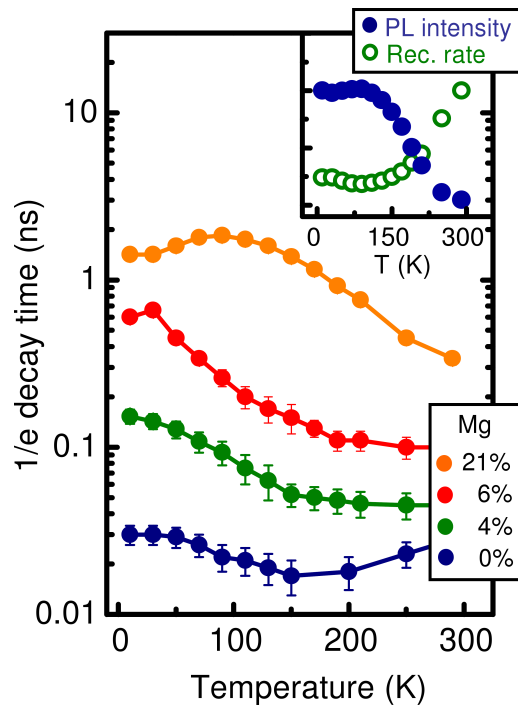


Figure 5.4: Temperature-dependent  $1/e$  decay times of the  $(\text{ZnMg})\text{O}$  samples with varying Mg concentrations. Integrated PL intensity and carrier recombination rate of the 21 % Mg sample are shown in the inset.

The decrease of the PL amplitude follows the increase of the carrier recombination rate. Thus, the faster PL decay at elevated temperatures is clearly attributed to an increased non-radiative recombination rate. These results strongly suggest that localization and disorder effects dominate the emission properties and carrier dynamics with increasing Mg concentration, see the discussion in section 2.3.2.

At low temperatures and high Mg concentrations, most carriers are trapped in randomly distributed local potential minima generated by alloy fluctuations. As a consequence, the carrier mobility is low and the carrier lifetime is high compared to that of mobile carriers. The potential fluctuations become more pronounced with increasing Mg-content, i.e., increasing alloy disorder, as one can also deduce from the absorption spectra by the broader band-tail state distribution [127, 134]. The carriers are thus stronger localized with a further-reduced non-radiative recombination probability and therefore exhibit a longer PL decay. At elevated lattice temperatures, photo-generated carriers can leave local potential minima by hopping into more favorable states at lower energies. This causes the frequently observed red shift of the PL peak position which is a part of the S-shape. As the temperature is increased further, the carriers are thermally activated to higher states. The PL maximum exhibits a blue shift and the decay time becomes shorter, c.f. Fig. 5.4, due to the faster carrier diffusion and therefore an increased capture probability by the deep impurities. At even higher temperatures, the carriers are completely delocalized with an



even larger non-radiative recombination probability.

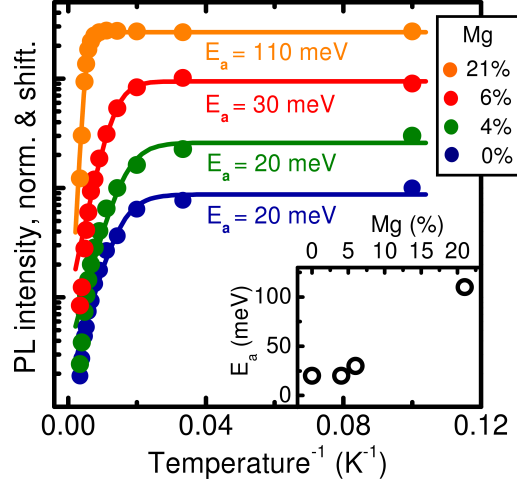


Figure 5.5: Spectrally and temporally integrated PL intensities of the  $(\text{Zn}_{1-x}\text{Mg}_x)\text{O}$  samples as function of the lattice temperature along with the corresponding fit curves. The inset shows the extracted activation energies for the different Mg concentrations.

This interpretation is strongly corroborated by the analysis of the spectrally and temporally integrated PL intensity as a function of temperature, shown in an Arrhenius plot in Fig. 5.5 for all four samples. For quantitative description of the experimental data, the standard thermal activation model is used:

$$I_{PL} \propto \left( 1 + A e^{-\frac{E_a}{k_b T}} \right)^{-1}, \quad (5.1)$$

see section 2.3.1 and Ref. [101]. Here, the most important parameter is the activation energy  $E_a$  of the luminescence quenching process. For the pure ZnO sample, the fit yields  $E_a$  in the range of 20 meV, corresponding to the binding energy of donor bound excitons. The activation energy strongly increases for an increasing Mg concentrations up to  $(110 \pm 10)$  meV for  $x = 0.21$ . This value is the first estimation of the mean localization energy and therefore the characteristic disorder scale.

The influence of alloy disorder is also observed in the characteristic energy dependence of the PL decay time. The  $1/e$  decay times are shown as function of the emission energy for the ZnO and the  $(\text{Zn}_{0.79}\text{Mg}_{0.21})\text{O}$  samples in Fig. 5.6 (a) and (b), respectively. The PL lifetime show no dependence on the emission energy within the resolution of our experimental setup in the ZnO reference, as expected. In contrast to that, significant variations are found for the  $(\text{Zn}_{0.79}\text{Mg}_{0.21})\text{O}$  sample. Here, the  $1/e$  time is nearly constant on the low-energy side of the PL spectra, drops slightly below the maximum of the PL peak and show a pronounced decrease on the high-energy side. The remaining Mg-containing

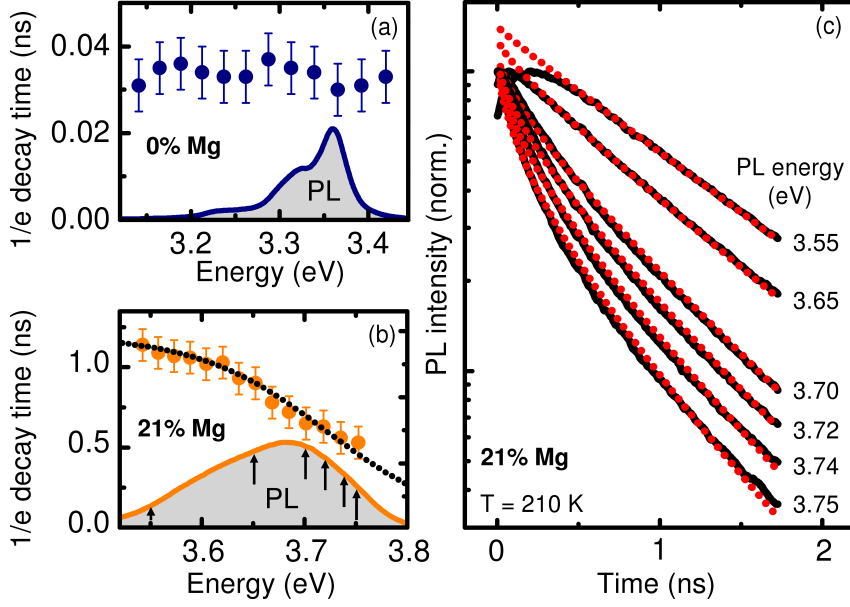


Figure 5.6:  $1/e$  decay times for the (ZnMg)O samples with Mg concentration of  $x=0$  (a) and  $x=0.21$  (b) at 500 ps after the excitation as function of the emission energy. Respective PL spectra are shown by filled areas for comparison. Time resolved transients for the  $x=0.21$  sample at  $T=210$  K are plotted in (c) for different emission energies between 3.55 eV and 3.75 eV; the energies are marked by arrows in (b). The theoretical fits in (b) and (c) are shown as dotted lines.

structures exhibit comparable behaviors. The energy dependence of the carrier lifetime results from the interplay between the relaxation and recombination processes [142]: fast relaxation into low-lying states dominates the carrier dynamics on the high-energy flank of the state distribution whereas the much slower recombination is the main decay channel for the localized carriers on the low-energy side. For a quantitative analysis, the theoretical model [106] for the energy-dependent PL decay rate is used

$$\tau^{-1}(E, t) = \tau_0^{-1} + \frac{\pi}{2t} N_0 \alpha^3 \ln^2 \left( \frac{tV_0}{\ln 2} \right) e^{\frac{E-E_{me}}{E_0}} \quad (5.2)$$

and

$$I(E, t) \propto \exp \left[ -\frac{1}{\tau_0} - \frac{\pi}{6} N_0 \alpha^3 \ln^3 \left( \frac{tV_0}{\ln 2} \right) e^{\frac{E-E_{me}}{E_0}} \right], \quad (5.3)$$

for the transient PL intensity.

As can be seen in Fig. 5.4 (b) and (c), this phenomenological model yields an excellent agreement with the experimental data thus allowing for a reasonable extraction of the fit parameters. The best fit is obtained for the characteristic energy scale for the exponential distribution of the localized states of  $E_0 = (60 \pm 15)$  meV with a relative density of the localization sites of  $N_0 \alpha^3 = (0.08 \pm 0.02)$ . The characteristic energy  $E_0$  matches well

## 5.1 Carrier dynamics in ZnO/(ZnMg)O heterostructures

to the magnitude of the thermal activation energy of the PL quenching and the energy-scale of the absorption tail, measured in Ref. [134]. It also explains the observation of the S-shape at rather high temperatures in the  $(\text{Zn}_{0.79}\text{Mg}_{0.21})\text{O}$  sample, see Fig. 5.2 (c). One further obtains  $E_{me} = (3.90 \pm 0.1) \text{ eV}$  for the mobility edge which agrees with the absorption edge of the sample with comparable Mg concentration [134]. The remaining parameters are the effective lifetime  $\tau_0 = (1000 \pm 50) \text{ ps}$  and the attempt-to-escape-frequency  $\nu_0 = (7 \pm 1) \cdot 10^{13} \text{ s}^{-1}$ .

In summary, the characteristic temperature dependence of the carrier lifetimes as well as the emission intensities in  $(\text{Zn}_{1-x}\text{Mg}_x)\text{O}$  alloys clearly show that carrier localization dominates the emission dynamics. These effects become increasingly important for higher Mg content and are present even at room temperature in the sample with 22 % Mg. The localization phenomena are thus clearly attributed to the alloy disorder due to Mg concentration fluctuations. In addition, characteristic disorder scale of  $(60 \pm 15) \text{ meV}$  is identified for the sample with the highest Mg concentration of  $x = 0.21$  by a quantitative analysis of the time-resolved data. Hence, in case of a ZnO/(ZnMg)O heterostructure, the alloy disorder in (ZnMg)O should lead to emission from localized states within the barriers, c.f. Fig 5.1, and also might have an impact on localization and/or carrier capture in ZnO QWs. The latter phenomena are further clarified in the following sections.

### 5.1.2 Screening of the internal-fields as a probe for carrier populations

The final aim of the experiments discussed in this subsection is the direct observation of carrier relaxation from (ZnMg)O barriers into the ZnO QW. Unfortunately, emission spectroscopy usually does not allow for a direct measurement of the carrier populations, especially, in systems with translational symmetry. In general, the rise of the PL signal is determined by both carrier density and carrier temperature since radiative recombination rates are much slower in case of hot carrier distributions, see the discussion in section 2.1.2. Therefore, an experimental procedure is developed to circumvent this issue. One of the major hallmarks of wurtzite crystals are the built-in electric fields, typically present in structures of reduced dimensionality. These fields strongly influence the optical properties of the material system, leading to the previously introduced QCSE 2.2.2. The influence of the latter, however, is rather sensitive to the carrier density in the system due to the Coulomb-mediated screening of the internal fields. Hence, it should be possible to exploit the screening phenomena for the direct observation of carrier population inside a QW. In addition, the build-up of screening is expected to occur on an ultra-fast time-scale of sub 1 ps [74]. This allows to take full advantage of the time-resolution of the streak-camera setup.

The discussion of the experimental studies is organized as follows: first, specifically designed ZnO/(ZnMg)O heterostructures are characterized by TRPL measurements. The emphasis of these preliminary investigations is laid on the evidence for a pronounced QCSE, required for the screening studies, but also on carrier localization in the QWs. In the second part, the effect of screening of the internal field on the PL properties is quantified. Finally, the verification for the concept of monitoring QW carrier population by exploiting screening phenomena is given and the results are discussed.

### Characterization of QCSE in ZnO quantum wells

The samples used for the screening studies are ZnO/(ZnMg)O heterostructures with varying QW widths between  $d=0.8$  nm and  $d=9$  nm, grown in the group of Prof. Martin Eickhoff. The Mg concentration, chosen as high as 20%, should lead to significant strain due to the large lattice-mismatch thus yielding considerable piezo-fields in the QWs [124, 143]. The samples are characterized in the TRPL setup at the lattice temperature of  $T=10$  K. Low-power excitation into the (ZnMg)O barriers is applied, with a photon energy of 4.3 eV and the average photon flux of about  $10^{12}$   $\text{cm}^{-2}$  per pulse. The temporal and spectral resolution of the TRPL setup are 30 ps and 0.5 nm, respectively.

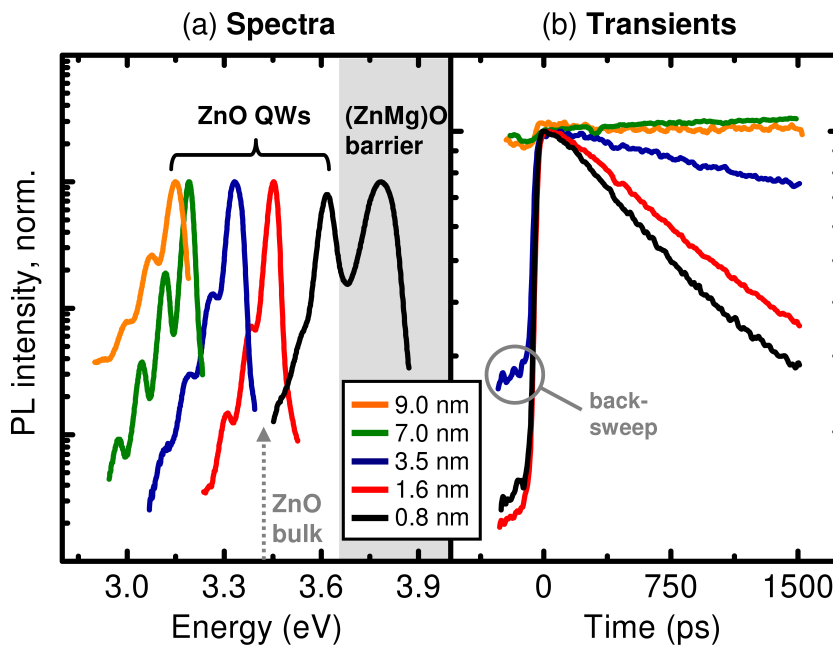


Figure 5.7: Spectra (a) and transients (b) of the ZnO/(Zn<sub>0.8</sub>Mg<sub>0.2</sub>)O samples with QW widths between  $d=0.8$  nm and  $d=9$  nm for non-resonant excitation into the barrier at 4.3 eV. The lattice temperature is set to 10 K and the excitation density - to  $10^{12}$   $\text{cm}^{-2}$  photons per pulse. Energy of the ZnO bulk PL is shown by the dotted arrow in (a) for comparison.

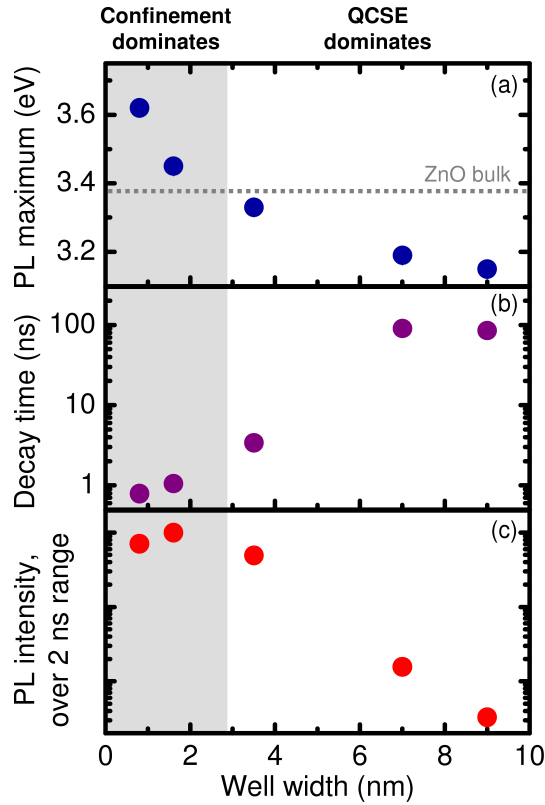


Figure 5.8: Shift of the PL maximum (a), evolution of the decay time (b) as well as the spectrally integrated PL intensity over 2 ns time-range (c) as function of the QW width of ZnO/(Zn<sub>0.8</sub>Mg<sub>0.2</sub>)O samples.

PL spectra, integrated over 2 ns after the excitation and normalized for better comparison, are plotted in Fig. 5.7 (a) for the QW series. Pronounced QW emission is observed in all five samples along with the respective phonon-assisted transitions. As the QW width increases, the PL maximum shifts to lower energies, well below the ZnO bulk emission energy for the QWs with  $d \geq 3.5$  nm. Simultaneously, the corresponding PL transients, shown in Fig. 5.7 (b), exhibit a strong increase of the decay time, leading to pronounced a "back-sweep" artifact in the data of the 3.5 nm, 7 nm and 9 nm QWs due to the long carrier lifetimes. Furthermore, the barrier PL, emerging on the high-energy side of the  $d = 0.8$  nm spectrum at about 3.8 eV, confirms high Mg content of about 20 %, c.f. Fig 5.2. The dependencies on the QW width of the PL maximum, decay time, and intensity are summarized in Fig. 5.8 (a), (b), and (c), respectively. The decay times are extracted by the fitting procedure discussed in section 3.1 and given in appendix (2). The PL intensity is integrated over the respective QW spectra and the temporal detection window of the streak-camera of 2 ns. All findings are characteristic for the presence of a strong internal electric field inside the QWs, parallel to the growth direction. While the emission of the two QWs with the smallest width is still governed by carrier confinement, the PL of the remaining three samples shows pronounced QCSE contributions. The decrease

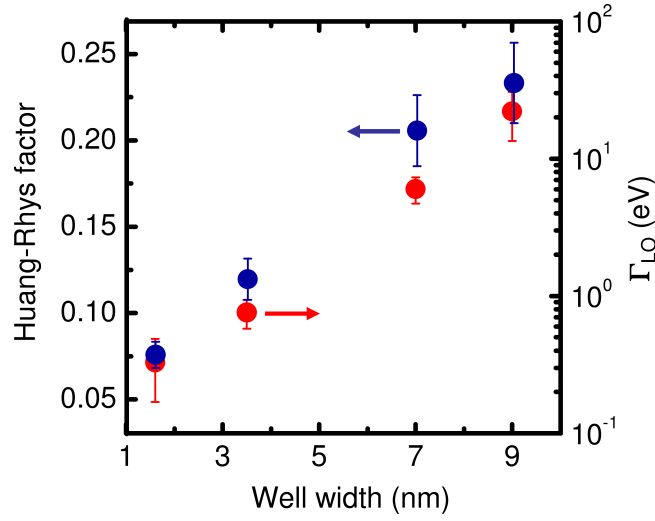


Figure 5.9: Huang-Rhys factor, extracted from the  $PSB_1/ZPL$  ratio, and optical phonon scattering coefficient from the temperature-dependent FWHMs as function of the QW width

of the PL maximum is accompanied by the increase of carrier lifetimes as well as the decrease of the PL intensity, both by more than two orders of magnitude. The latter occurs since the temporal detection range becomes much smaller than the recombination time of the spatially separated electrons and holes for increasing well widths. The data from Fig. 5.8 (a) also allow for an approximative estimation of the electric field strength  $F$ . The slope of the PL maximum as function of the well width for the three samples with  $d \geq 3.5$  nm gives  $F \approx 34$  meV/nm = 0.3 MV/cm, matching the magnitude of the electric fields expected for comparable systems [129, 143].

Interestingly, such a high built-in electric field and the resulting carrier separation with increasing QW width also strongly influences the carrier-phonon coupling. The evaluation of the Huang-Rhys factor from the relative intensities of the first PSB and the ZPL (s. Eq. (2.42) in 2.2.1) as well as the  $\Gamma_{LO}$  parameter for the scattering strength with optical phonons from temperature-dependent FWHMs (s. Eq. (2.30) in 2.1.2) both clearly demonstrate this fact, see Fig. 5.9. Indications for this behavior are observed in a couple of experiments [144, 143]. However, neither the hypothesis from the Ref. [144] applies for the studied samples, nor any additional contributions from the Fröhlich scattering due to the spatial separation of exciton constituents are observed. Possible influence of the latter is evaluated applying the temperature-dependent PSB analysis from section 4.2. Hence, the origin of the experimentally found enhancement of the carrier-phonon coupling with rising QW width in the presence of a strong internal field is still unclear. Additional experimental and, above all, theoretical studies aimed to clarify this question are beyond the scope of this work, opening opportunities for further investigations.

In conclusion, the preliminary characterization of the  $ZnO/(Zn_{0.8}Mg_{0.2})O$  samples clearly

## 5.1 Carrier dynamics in ZnO/(ZnMg)O heterostructures

shows that strong electric field in order of 0.3 MV/cm is present in the heterostructures. The influence of the QCSE on the emission properties is significant, especially for the samples with large well widths. Based on these observations, the QW with  $d=7$  nm is chosen for the following investigations, offering a good trade-off between pronounced QCSE and comparably high emission intensity thus providing reasonable signal-to-noise ratios.

### Carrier localization effects

After clarifying the influence of QCSE in the samples under study, the focus of the investigations is laid on the characterization of carrier localization, aimed to answer the third initially raised question, see 5.1. For this purpose, temperature-dependent TRPL measurements on the QW sample with  $d=7$  nm are discussed. The sample is excited non-resonantly with a photon energy of 4.3 eV and a photon flux of  $10^{12}$  cm<sup>-2</sup> photons per pulse. Figure 5.10 shows the experimental data for the PL maximum, decay time and the integrated PL intensity as function of the lattice temperature. The characteristic S-shape is clearly observed in the energy shift of the emission maximum, typical for disordered systems with effective carrier localization, c.f. section 2.3.2. As already discussed, the average localization energy  $E_{loc}$  of about 11 meV marks the critical temperature for the delocalization of carriers, trapped in potential minima at lower temperatures. Also, the decay time as well as the overall emission intensity both decrease, indicating faster non-radiative recombination due to increased carrier diffusion and thus capture probability into the deep traps. There are several possible reasons in the ZnO QW systems for carrier localization. Excitons can be bound to chemical impurities, already present in the bulk crystals. Also, the energy levels are affected by the fluctuations of barrier heights due to the alloy disorder in the (ZnMg)O layers, studied in section 5.1.1. The latter should also influence the local strain and thus the magnitude of the internal field, leading to varying QCSE contributions. The precise contributions of the different origins for potential fluctuations are rather challenging to estimate due to the broad FWHMs of the sample PL. However, an additional analysis of the PSBs provides a convenient way to estimate the maximal localization length. As previously discussed in section 2.2.1, Fig. 2.16, localized and free carriers lead to different characteristic dependencies of the energy spacing  $\Delta E_{ZPL-PSB1}$  between the ZPL and the first PSB on temperature. In case of carrier localization, the relaxation of the momentum conservation rule leads to a constant  $\Delta E_{ZPL-PSB1}$ , equal to the LO-phonon energy  $E_{LO}$ . In contrast to that, this energy difference is always lower than  $E_{LO}$  for freely moving carriers, even at low temperatures. Furthermore, as the temperature is increased,  $\Delta E_{ZPL-PSB1}$  exhibits a monotonous decrease. The spectral interval between  $PSB_1$  and  $PSB_2$ , on the other hand, always remains in the range of the phonon energy for both free and localized electron-hole-pairs. Figure 5.11 shows the cor-



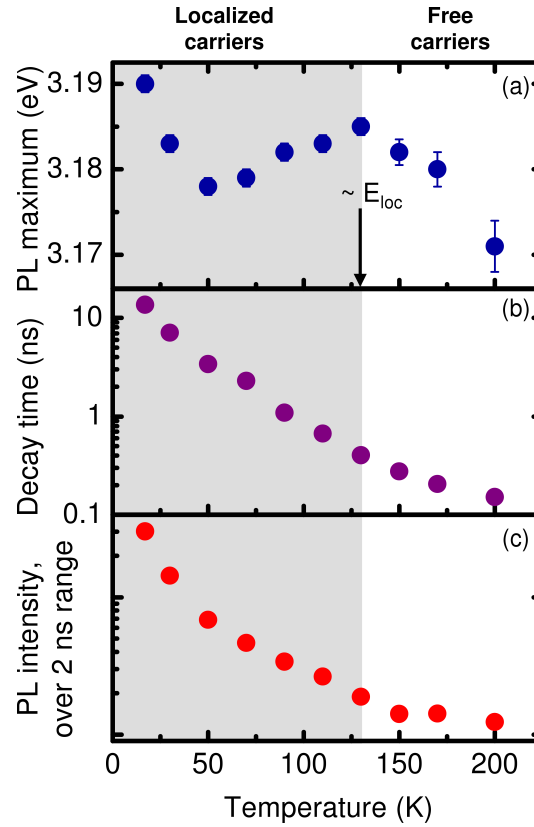


Figure 5.10: PL energy maximum (a),  $1/e$  decay time (b) and the integrated intensity (c) of the ZnO/(Zn<sub>0.8</sub>Mg<sub>0.2</sub>)O QW with  $d = 7$  nm as function of the lattice temperature for the excitation density of  $10^{12}$  cm<sup>-2</sup> photons per pulse

responding plots of the  $\Delta E_{ZPL-PSB1}$  and  $\Delta E_{PSB1-PSB2}$  for the ZnO/(Zn<sub>0.8</sub>Mg<sub>0.2</sub>)O QW (a) and a ZnO bulk layer (b) for comparison. In the latter case, the evolution of the respective energy intervals with the rising lattice temperature confirms the theoretical predictions for free (FX) and bound (BX), i.e., localized, excitons. Clear support for the previous results, shown in Fig. 5.10, is found in the ZnO QW data. A constant energy spacing between the ZPL and the PSB<sub>1</sub> peak of about  $E_{LO}$  is a characteristic hallmark of the emission from localized states. Here, the highest temperature for the measured, constant  $\Delta E_{ZPL-PSB1}$  value is 150 K, limited by the overlap between the ZPL and the PSB peaks due to the spectral broadening of the sample emission. This temperature corresponds to the energy of  $\Delta E = 13$  meV, indicating that momentum relaxation rule is softened at least for the carrier momenta lower than  $\Delta k = 6 \cdot 10^6$  cm<sup>-1</sup>. The value is obtained from  $\Delta E$ , approximating the band structure with parabolic bands and taking into account the effective masses of electrons and holes in ZnO [36]. According to the uncertainty relation, the corresponding length  $\Delta x$  is about 5 nm, marking the upper limit of the spatial scale for carrier localization.



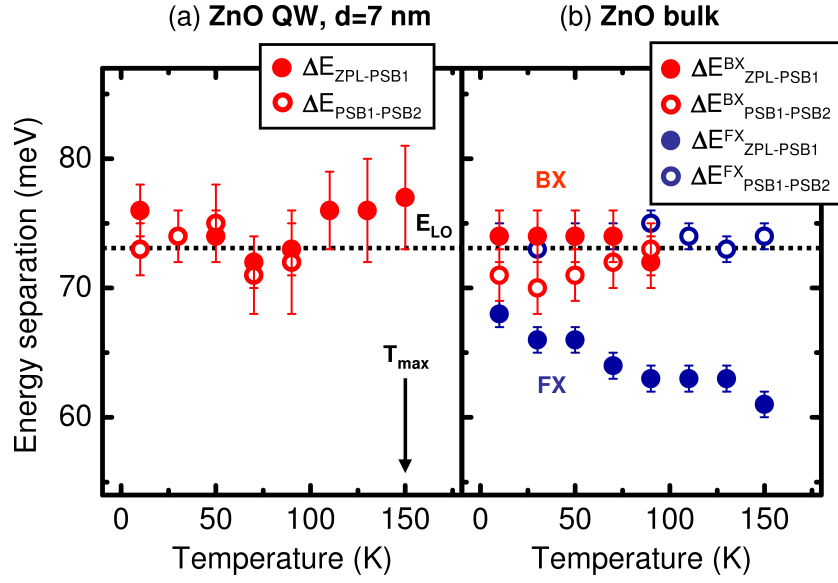


Figure 5.11: Respective energy intervals between the ZPL,  $PSB_1$  and  $PSB_2$  for ZnO/(Zn<sub>0.8</sub>Mg<sub>0.2</sub>)O QW (a) and bulk (b) samples as function of the lattice temperature.  $E_{LO}$  denotes the LO-phonon energy and  $T_{max}$  the highest temperature for the measured, constant  $\Delta E_{ZPL-PSB1}$  value.

### Screening of the QCSE

In this last part of the section, the screening of the internal electric fields is studied. Again, the sample with a well width of  $d = 7$  nm is used for the investigations. The lattice temperature is set to 10 K to avoid any additional homogeneous broadening thus allowing most precise measurements of the PL energy shifts. Since the final aim of the experiments is the analysis of carrier capture from the barrier states into the QW, the sample is excited non-resonantly in the (ZnMg)O layer with a photon energy of 4.3 eV. These excitation conditions also allow for better comparison with the previously discussed experiments.

Figures 5.12 (a) and (b) show several exemplary emission spectra from the ZnO QW for various time-delays after excitation for low and high excitation density of  $3 \cdot 10^{12} \text{ cm}^{-2}$  and  $1.4 \cdot 10^{13} \text{ cm}^{-2}$  photons per pulse, respectively. All spectra show pronounced QW PL with the low-energy dominated by the phonon-assisted emission peaks as well as some contributions from the back-sweep artefact for the spectra in Fig. (b). At low pump power, the PL maximum remains constant over the complete temporal window of about 1.5 ns. Merely a slight excitation-induced broadening is observed at early times. In stark contrast to that, the PL exhibits an initial shift to higher energies of about 90 meV for the high-power conditions. At longer times, the emission maximum shifts back to lower energies. The pronounced energy shift observed at high pump densities is characteristic for the Coulomb-mediated screening discussed in more detail in section 2.2.2. The carriers within the QW screen the internal field thus weakening the impact of the QCSE, leading

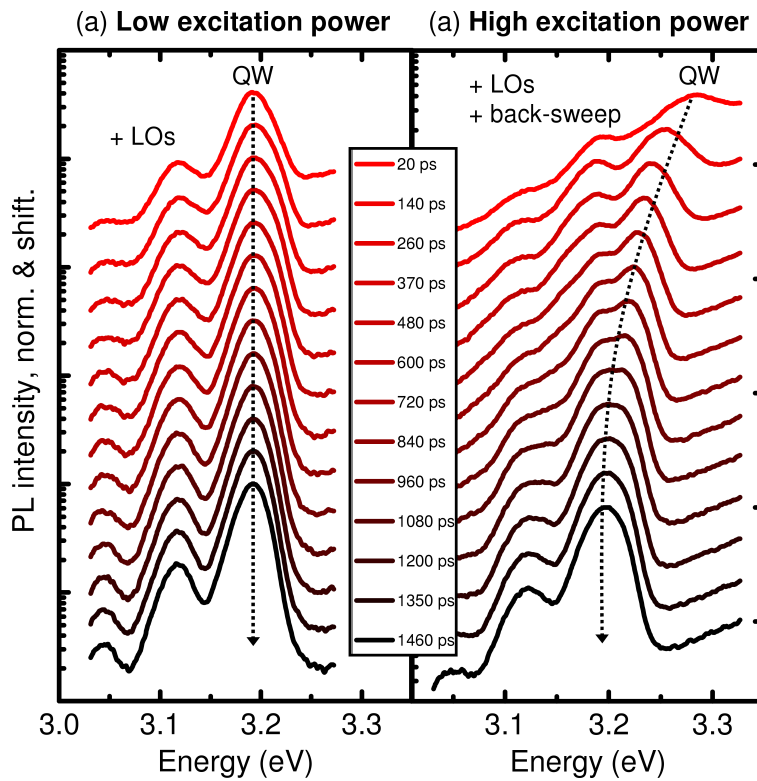


Figure 5.12: PL spectra of a ZnO/(Zn<sub>0.8</sub>Mg<sub>0.2</sub>)O QW with  $d=7$  nm for two different pump densities of  $3 \cdot 10^{12} \text{ cm}^{-2}$  and  $1.4 \cdot 10^{13} \text{ cm}^{-2}$  photons per pulse for various time-delays after the excitation. All spectra are integrated over a time window of 120 ps. The data are normalized and shifted for clarity. The lattice temperature is set to 10 K.

to faster radiative recombination as well as to a pronounced shift of the PL energy. As the carriers recombine, the effect of screening also decreases, following the decrease of the carrier density. Hence, at longer time-delays after the excitation, the emission maximum returns to the initial position in energy.

The influence of carrier density-dependent screening on the emission properties of the QW is summarized in Fig. 5.13. The emission maximum is extracted from the PL spectra, integrated over a 50 ps temporal window directly after the excitation. As the pump density increases, the PL energy strongly shifts towards higher energies. This behavior is accompanied by a decrease of the decay time of about two orders of magnitude. A super-linear dependence of the emitted intensity on the pump power quantified by the exponent  $\kappa=1.4$ , attributes the decrease of the carrier lifetime to faster radiative recombination. Hence, possible alternative interpretation of the experimental findings as saturation of the localized states is clearly excluded. In the latter case, the PL intensity dependence on the excitation density would show a linear or even a sublinear behavior. According to the PL data, the density-dependent screening of the QCSE is a strongly non-linear process thus allowing to sub-divide the excitation regimes in regions of an un-screened and screened

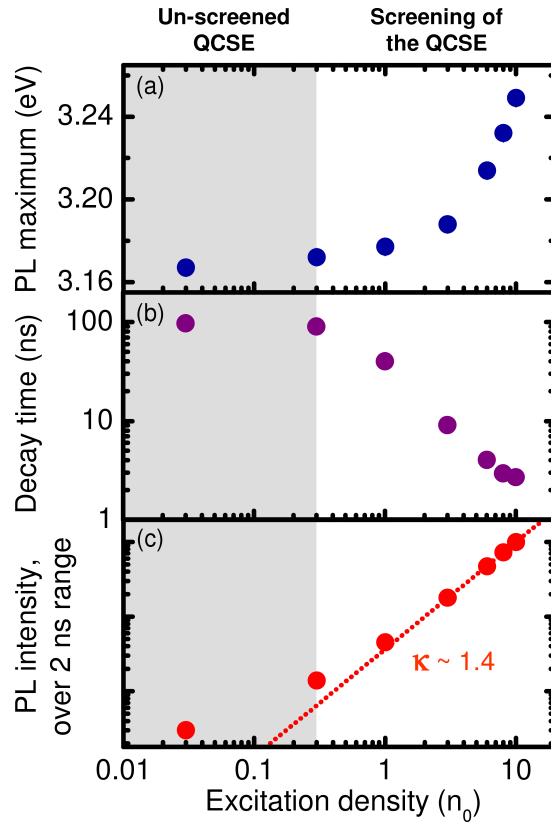


Figure 5.13: PL energy maximum (a),  $1/e$  decay time (b) and the integrated intensity (c) of the ZnO/(Zn<sub>0.8</sub>Mg<sub>0.2</sub>)O QW with  $d=7$  nm as function of the excitation density for the lattice temperature of 10 K. The excitation density is normalized to the photon flux of  $n_0 = 10^{12}$  cm<sup>-2</sup> per pulse.  $\kappa$  denotes the exponent extracted from the dependence of the PL intensity  $I_{PL}$  on the pump power:  $I_{PL} = I_{pump}^\kappa$ .

QCSE. Here, it should be noted, that since the PL maximum is always below the energy of the ZnO bulk transition, corresponding to a fully screened electric field, the term "screened QCSE" should be understood as a substitute for "*partially* screened QCSE".

Based on the results shown in Fig. 5.13 the excitation density of  $6n_0$  is chosen for the study of the screening formation. The temporal detection window is set to 50 ps instead of 2 ns, corresponding to the effective time resolution of about 3 ps. In addition, the streak-camera is operated with an active blanking unit to avoid back-sweep contributions. Transient PL spectra, integrated over an interval of 2 ps, are plotted in Fig. 5.14 (a) as function of the time-delay after the excitation. The corresponding streak-image with the PL intensity plotted as function of the emission energy and time is shown in Fig. 5.14 (b). The PL signal at negative times results from the remaining carrier population in the QW, created by the previous laser pulse. At  $t=0$  ps, as the excitation pulse arrives, the emission peak, attributed to the screened QCSE, appears instantaneously at the high-energy flank of the "un-screened" PL. At later delay times, the intensity of the "screened" luminescence

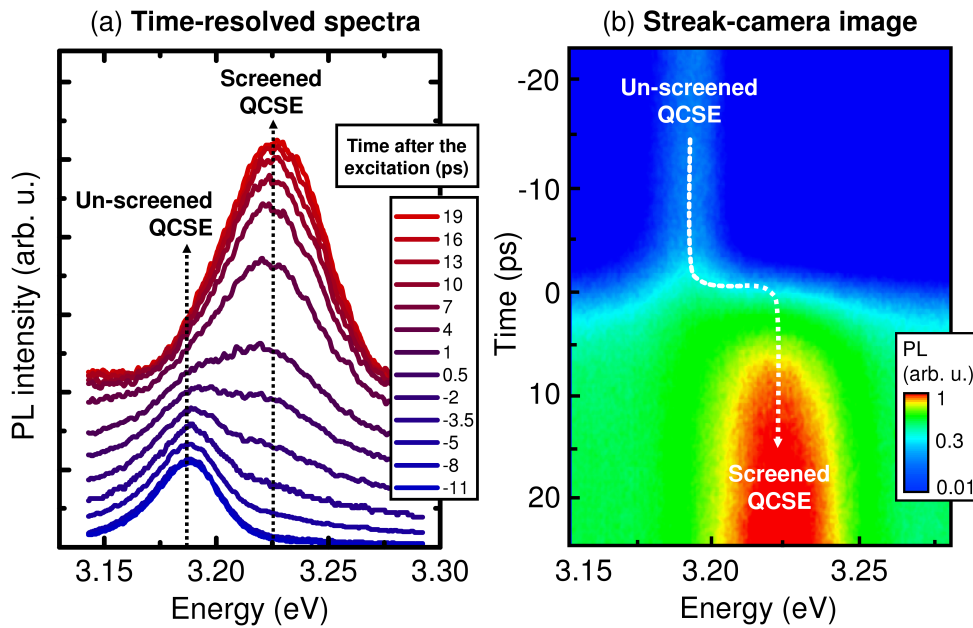


Figure 5.14: (a) Transient PL spectra of the ZnO/(Zn<sub>0.8</sub>Mg<sub>0.2</sub>)O QW with  $d = 7$  nm for the excitation density of  $6 n_0 = 10^{12}$  cm<sup>-2</sup> per pulse and the lattice temperature of 10 K. (b) Corresponding image of the streak-camera with the PL intensity plotted as function of emission energy and time-delay after the excitation.

increases, yet the energy of the peak does not exhibit any additional shift. The overlap between the two peaks is due to the convolution of the signals with a Gaussian with FWHM of 3 ps, corresponding to the temporal resolution of the setup. Hence, the build-up of the "screened" PL is instantaneous within the experimental uncertainty. In general, the corresponding time-scale is determined by the faster of the two following processes: the rise of the carrier population and the build-up of screening. It should be noted, however, that the estimated time-scale for the latter is in the range of 100 fs, corresponding to the length of the excitation pulse, see Ref. [74]. The time constant is roughly estimated from the inverse plasma frequency in the excited electron-hole system [9], using ZnO material parameters [36] and approximate carrier densities for the applied excitation conditions. Figure 5.15 summarizes the dependence of the PL maximum as well as the integrated PL intensity on the delay-time after the excitation. In addition, the corresponding carrier densities are shown, estimated from the PL energies using the data from Fig. 5.13 (a). The QW carrier population increases almost instantaneously at  $t = 0$  ps, i.e., within the experimental resolution of 3 ps, in stark contrast to the slowly rising luminescence intensity. The increase of the PL on the time-scale of several 10's of ps is thus clearly attributed to carrier relaxation, i.e., cooling processes, inside the QW. Hence, as a main result, the capture of carriers, excited in the (ZnMg)O barriers, into the QW occurs within the first 3 ps.

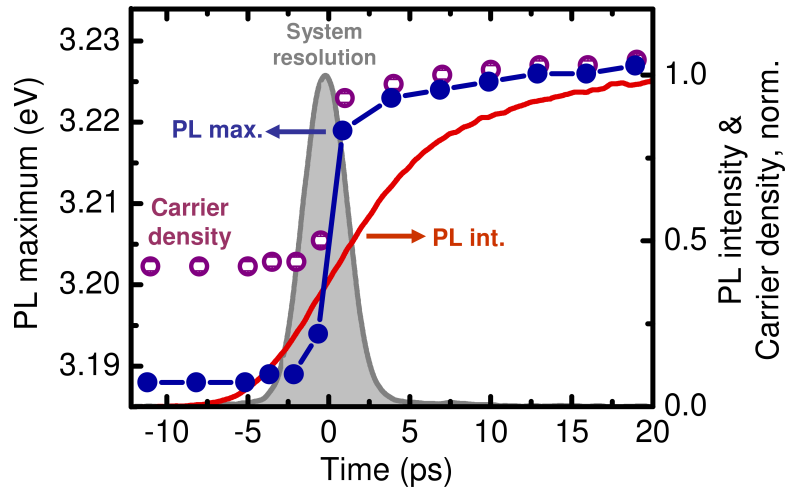


Figure 5.15: PL maximum, resulting carrier population as well as the integrated emission intensity of the ZnO/(Zn<sub>0.8</sub>Mg<sub>0.2</sub>)O QW with  $d = 7$  nm as function of time-delay after the excitation. The excitation density is set to  $6n_0 = 10^{12}$  cm<sup>-2</sup> per pulse and the lattice temperature is 10 K. The system resolution is shown by the gray area for comparison.

In summary, the TRPL measurements of ZnO/(Zn<sub>0.8</sub>Mg<sub>0.2</sub>)O heterostructures with varying well widths reveal the presence of a strong electric field of about 0.3 MV/cm inside the QWs. This field leads to a pronounced QCSE, influencing and even dominating the emission properties of the QWs, especially, for the well widths above 3.5 nm. It also significantly enhances the carrier-phonon coupling. In addition, carriers inside the QWs are found to be localized in all three dimensions at temperatures below  $T = 150$  K. Upper limit of the localization length is estimated by the analysis of the PSB emission to 5 nm. Furthermore, the effect of screening of the internal field is shown to influence the PL energies as well as the carrier lifetimes. Finally, the concept of monitoring the QW carrier population by exploiting screening phenomena is verified. As a result, the capture of carriers from the barriers into the QW is found to occur on an ultra-fast time-scale below 3 ps, limited by the experimental resolution. This fast relaxation is observed despite rather high Mg concentration in the (ZnMg)O layers, which leads to pronounced potential fluctuations and carrier localization, see section 5.1. Hence, the carrier capture into the QW occurs on the same or an even faster time-scale than the carrier-trapping processes within the barriers. Such a behavior should be a significant benefit for the operation of optical devices, e.g., lasers, based on ZnO-heterostructures.

### 5.1.3 Recombination processes in ZnO quantum wells

This subsection is focused on the carrier dynamics in ZnO/(ZnMgO) QWs with small internal fields and negligible QCSE. These materials are typically proposed for the realization of opto-electronic devices due to the strong light-matter coupling in the absence of the charge carrier separation. In the first part, carrier localization is studied by applying a temperature-dependent analysis of the spectral features as well as the phonon-assisted luminescence from a QW sample. The second part deals with the recombination mechanisms in homo- and heteroepitaxially grown ZnO QWs. These different growth conditions are chosen as a parameter, determining the material quality and thus the relative contributions of radiative and non-radiative recombination channels to the PL dynamics.

#### Carrier localization effects

The sample used for the study of carrier localization is a 2.5 nm thick ZnO QW, embedded within two (Zn<sub>0.9</sub>Mg<sub>0.1</sub>)O layers of about 25 nm width, grown on a ZnO substrate in the group of Prof. Martin Eickhoff. The choice of a small Mg concentration in the barriers and a narrow QW both ensure negligible electric field in the growth direction of the heterostructure [145]. Thus, possible contributions from the QCSE to the carrier dynamics are clearly excluded [143].

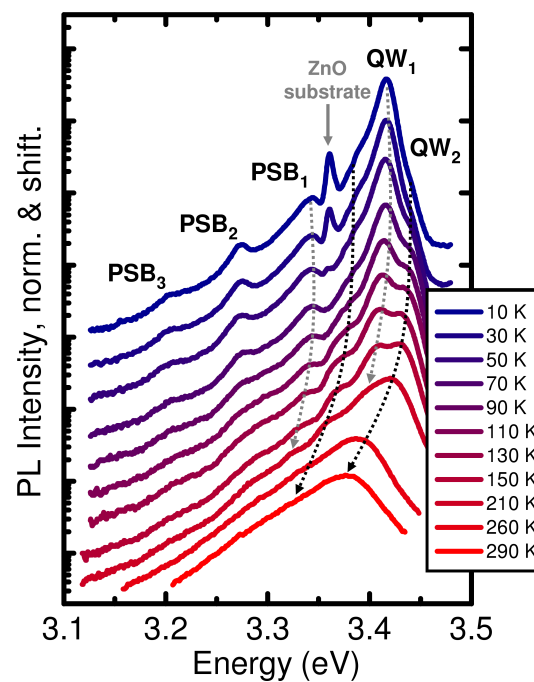


Figure 5.16: Temperature-dependent PL spectra of the ZnO/(Zn<sub>0.9</sub>Mg<sub>0.1</sub>)O sample with QW width of 2.5 nm. The excitation density is set to  $2 \cdot 10^{11}$  photons  $\text{cm}^{-2}$  per pulse. The data is normalized and shifted for clarity.



## 5.1 Carrier dynamics in ZnO/(ZnMg)O heterostructures

In analogy to the experiments in the previous studies, see 5.1.1 and 5.1.2, localization effects are investigated by evaluating temperature-dependent TRPL data. For these measurements, the sample is excited non-resonantly with the photon energy of 4.3 eV and an average density of about  $2 \cdot 10^{11}$  photons  $\text{cm}^{-2}$  per pulse. Time-integrated PL spectra are plotted in Fig. 5.16, normalized and shifted for clarity. The spectra are dominated by two distinct emission peaks, labeled QW<sub>1</sub> and QW<sub>2</sub>, both attributed to the QW luminescence due to the energy shift, caused by the quantum confinement effect. The energy spacing between the two QW signatures is  $(27 \pm 1)$  meV. These peaks are further accompanied by the PSB signatures on the low-energy side. In addition, a weak PL signal from the ZnO substrate contributes to the sample luminescence at low temperatures. As the temperature is increased, the relative intensity of the QW<sub>2</sub> emission strongly increases, whereas the QW<sub>1</sub> peak quenches and is completely suppressed in the room-temperature spectrum. This fact clearly excludes possible explanation of the QW<sub>2</sub> luminescence as the emission from the second confined state of the QW. Otherwise, due to the approximately equal density of states and comparable light-matter coupling strength of the first and the second subbands, the PL of the latter is not supposed to dominate the sample emission, especially at low excitation densities, see Fig. 2.6 in section 2.1.2 for comparison. Hence, the experimental findings strongly suggest the attribution of the QW<sub>1</sub> PL to the recombination of carriers from the localized states inside the QW. For increased temperatures, these carriers become delocalized, leading to a luminescence signal at higher energies, i.e., at the QW<sub>2</sub> resonance.

As previously shown in sections 2.2.1 and 5.1.2, the analysis of the energy spacing  $\Delta E_{ZPL-PSB1}$  between the first PSB and the ZPL allows to distinguish the PL from localized and free carriers. Figure 5.17 shows the corresponding results for  $\Delta E_{ZPL-PSB1}$ , extracted from the experimental data plotted in Fig. 5.16. Supporting the above interpretation, the QW<sub>1</sub> emission is clearly attributed to the PL from localized carriers, since the energy separation between the PSB<sub>1</sub> and the ZPL remains constant up to  $T_{max} = 200$  K at the value of the LO-phonon energy of 72 meV. In contrast to that, the  $\Delta E_{ZPL-PSB1}$  decreases with increasing temperature for the QW<sub>2</sub> peak, as expected for the free carrier luminescence. Also, the temperature  $T_{max}$  allows the estimation of the upper limit for the carrier localization length to about 5 nm, c.f. sections 2.2.1 and 5.1.2. Again, there are several reasons for the carrier localization, excluding QCSE-related local potential fluctuations due to the inhomogeneity of the internal electric field: chemical impurities [139] and well-width fluctuations [53]. Since both lead to the comparable carrier behavior observed in a TRPL experiment, the precise origin of the localization should be determined by additional studies, e.g., magneto- or micro-PL in combination with transmission electron-microscopy.

In conclusion, charge carriers are found to be localized in the ZnO/(Zn<sub>0.9</sub>Mg<sub>0.1</sub>)O QW at low temperatures, even in the absence of the QCSE. The corresponding localization

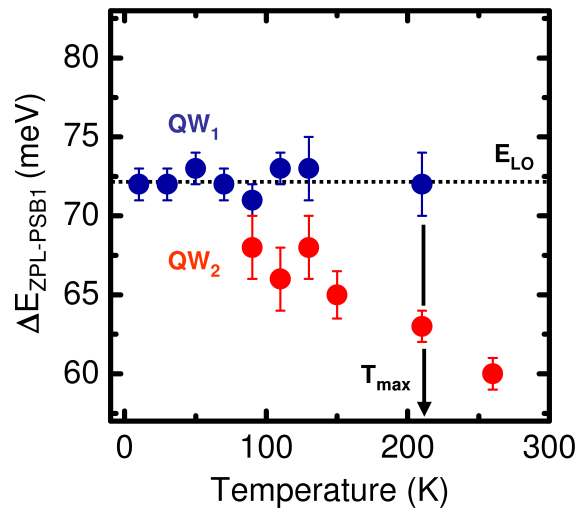


Figure 5.17: Energy spacing between the first PSB and the ZPL of the ZnO/(Zn<sub>0.9</sub>Mg<sub>0.1</sub>)O QW sample as function of the lattice temperature. The data is extracted for the PL spectra, shown in Fig. 5.16.

energy is in the range of 30 meV and the maximal localization length is estimated to 5 nm. However, confirmed by the analysis of the PSB emission, free carrier luminescence is shown to dominate the PL spectra at lattice temperatures above 200 K.

### Recombination mechanisms

For the study of the carrier recombination mechanisms two ZnO/(Zn<sub>0.9</sub>Mg<sub>0.1</sub>)O heterostructures with the QW widths of 1.5 nm are chosen. The samples are homo- and heteroepitaxially grown in the group of Prof. Martin Eickhoff on ZnO and sapphire substrates, respectively. Growth details as well as a comprehensive structural and optical study of these structures are found in Ref. [135]. As an overview, low-temperature TRPL data is shown in Fig. 5.18 for different excitation densities between 10<sup>9</sup> cm<sup>-2</sup> and 10<sup>13</sup> cm<sup>-2</sup> photons per pulse. Similar emission signatures are observed in the time-integrated luminescence spectra of the two samples, plotted in Fig. 5.18 (a): narrow PL from the ZnO buffer layer at 3.36 eV, inhomogeneously broadened ZnO QW luminescence between 3.40 eV and 3.43 eV and a peak attributed to the (ZnMg)O barriers in the range of (3.48 ± 0.01) eV. The QW emission of the homoepitaxial sample is slightly shifted to lower energies in comparison to the PL from the heteroepitaxial QW. Most obvious reason is the lower Mg content in the respective barrier layers, confirmed by the difference in the (ZnMg)O PL peak energies, leading to a decrease of the confinement energy. As the excitation is increased by four orders of magnitude, the QW emission broadens due to excitation-induced increase of the homogeneous linewidth, yet the spectral positions of the PL peaks remain constant. Also, the luminescence dynamics, shown in Fig. 5.18 (b) do not change with increasing carrier density, exhibiting single-exponential



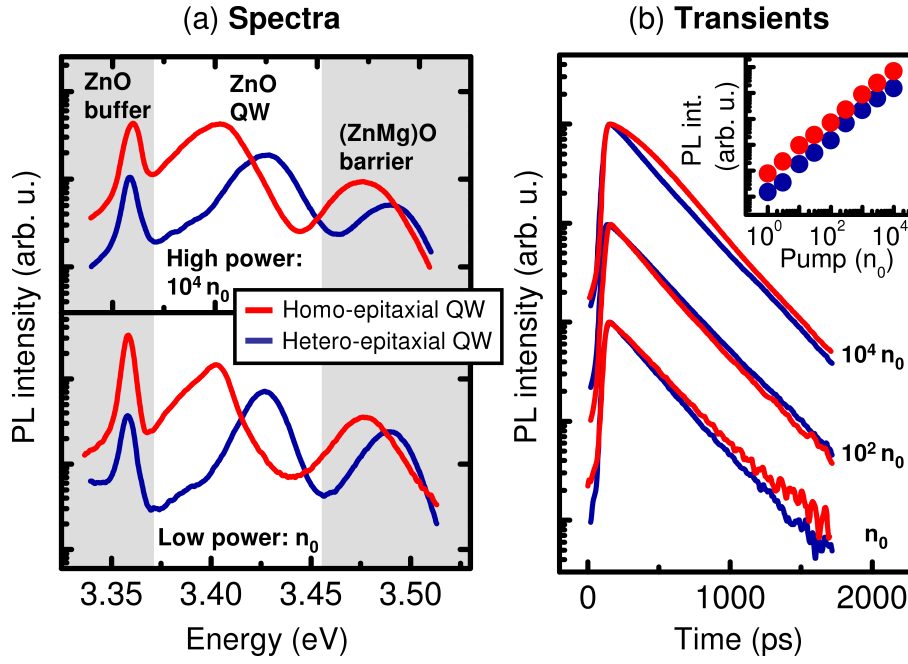


Figure 5.18: (a) Time-integrated PL spectra for homo- and heteroepitaxial ZnO/(Zn<sub>0.9</sub>Mg<sub>0.1</sub>)O samples at the lattice temperature of 10 K and low and high excitation densities of  $n_0 = 10^9 \text{ cm}^{-2}$  and  $10^4 n_0 = 10^{13} \text{ cm}^{-2}$  photons per pulse, respectively. (b) Corresponding PL transients of the QW emission for the excitation densities of  $n_0$ ,  $10^2 n_0$ , and  $10^4 n_0$ . The inset shows the spectrally and temporally integrated PL intensities of the two QWs as function of the pump density.

decay with a time constant of  $(300(\pm 20))$  ps. In addition, the overall PL intensity increases linearly with the pump power, see the inset of Fig. 5.18 (b). Thus, the relative ratio of the non-radiative and radiative recombination rates remains constant for all applied excitation conditions. Hence, despite initial inhomogeneous broadening, no disorder-related delocalization of carriers, trapped in local potential minima is observed when the carrier density is increased by a factor of  $10^4$ , c.f. 5.1.3. The density of the localization sites is thus comparably high, on the order of  $10^{-18} \text{ cm}^{-3}$ . This value is estimated from the approximative maximal carrier density in the QWs achieved in the TRPL measurements, renormalized to the three-dimensional bulk concentration. The carrier density is computed by taking into account the applied excitation density, the respective layer widths of the ZnO QW and the (ZnMg)O barriers, and the absorption coefficient of the ZnO [36].

The temperature-dependent PL maxima, corresponding to the emission from the low-temperature peak,  $1/e$  decay times of the luminescence signal as well as the overall PL intensities are shown in Fig. 5.19 (a), (b), and (c), respectively. The energy of the PL peaks decreases monotonously as function of temperature, following the typical behavior of the band-gap, see section 2.1.2. Thus, aside from the carrier trapping with a discrete

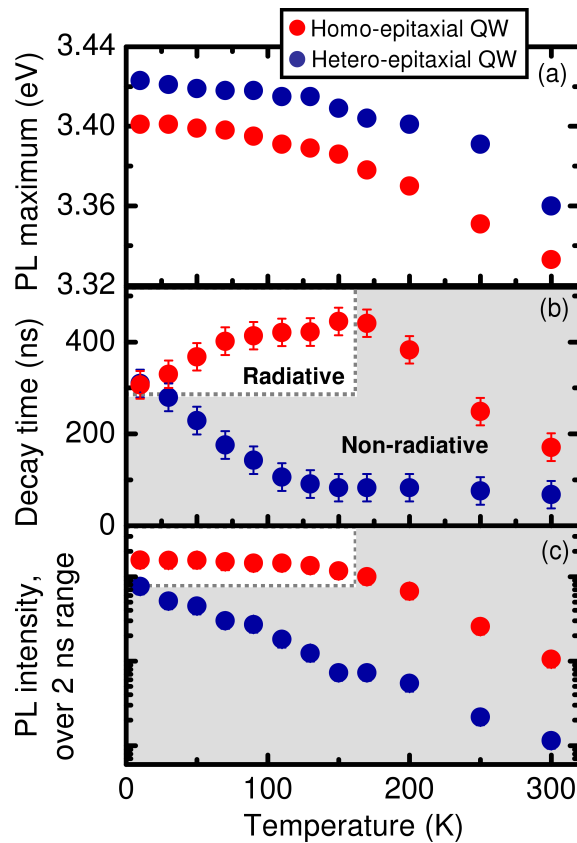


Figure 5.19: PL maximum (a), corresponding to the emission from the low-temperature peak,  $1/e$  decay time of the luminescence signal (b) as well as the overall PL intensity (c) of the homo- and heteroepitaxial ZnO/(Zn<sub>0.9</sub>Mg<sub>0.1</sub>)O QWs as function of the lattice temperature. The excitation density is set to  $0.3 \cdot 10^{12} \text{ cm}^{-2}$  photons per pulse.

binding energy of the corresponding localized state in the range of 30 meV, c.f. Fig. 5.16, no additional disorder-related features, e.g., an S-shape, are observed. For the heteroepitaxial sample, the decay time as well as the PL intensity both decrease as the temperature is increased from 10 K to 300 K. This result is a clear hallmark of non-radiative recombination dominating carrier dynamics. The non-radiative channel becomes increasingly important at higher temperatures due to the faster carrier diffusion and thus efficient trapping of electrons and holes into the deep states, c.f. discussion in section 2.3.1. In stark contrast to that, the PL intensity of the homoepitaxially grown QW remains nearly constant and the decay time even increases in the temperature range from 10 K to 150 K. Hence, radiative recombination mainly determines carrier dynamics of the QW sample at these temperatures. In fact, in an ideal QW structure, the radiative recombination time is expected to increase linearly with temperature [9]. The experimental findings perfectly match the expected behavior for the homoepitaxial QW, even when the PL dynamics are evaluated not only for free but also for the localized carriers, due to the spectral overlap of

## 5.1 Carrier dynamics in ZnO/(ZnMg)O heterostructures

the two contributions. As the temperature is increased further than 150 K, the decay time decreases, accompanied by a quenching of the emission intensity thus indicating dominant non-radiative recombination in the homoepitaxial sample for these temperatures.

In conclusion, the recombination dynamics of carriers of ZnO/(Zn<sub>0.9</sub>Mg<sub>0.1</sub>)O QWs are studied as function of the excitation density and lattice temperature. Both radiative and non-radiative channels are found to contribute to the carrier dynamics. Depending on the growth conditions, i.e., on the sample quality, radiative processes dominate the recombination at low and intermediate temperatures below 150 K. However, for higher defect concentrations as well as temperatures, the carrier lifetimes become strongly limited by carrier capture into the deep traps. In addition, the experimental results indicate carrier localization at low temperatures at spatially localized states with a discrete binding energy of about 30 meV. However, no disorder-related features related, e.g., to the alloy-disorder in the barrier layers, are observed.

To summarize the TRPL studies of the ZnO-based heterostructures, performed within the framework of this thesis, the answers to the initially raised questions are given:

- *What is the reason for carrier localization in the barrier layers?*

Alloy disorder due to the spatial fluctuations Mg concentration is found to cause localization of electrons and holes within the (ZnMg)O layers. The influence of disorder becomes increasingly important for higher Mg content and is observed even at room temperature in the sample with the highest Mg concentration of 22 %. In addition, for the latter sample, characteristic disorder scale of  $(60 \pm 15)$  meV is identified.

- *How fast are the carriers captured into the QW?*

The experimental results show that the capture of carriers from the barriers into the QW occurs on an ultra-fast time-scale below 3 ps, this value being limited by the experimental resolution. This result is obtained by exploiting the build-up of screening of the internal electric field for direct observation of carrier population inside a QW. Thus, carrier capture into the QW occurs on the same or even faster time-scale than the carrier-trapping processes within the barriers.

- *Are QW carriers free to move in two dimensions or are they localized in the in-plane direction?*

In all samples under study, carriers are found to be localized in growth and also in the in-plane dimension at low temperatures, regardless of the presence or absence of a strong internal field. The upper limit for the localization length is estimated to be around 5 nm. However, the depth of the potential minima is comparably

small, in the range of 10 meV - 30 meV, depending on the exact sample parameters. These values are usually lower than the average localization energy in the (ZnMg)O layers. At temperatures higher than 200 K, the QW emission is dominated by free, delocalized carriers.

- *Does radiative or non-radiative recombination dominates carrier lifetime in the QWs?*

Radiative recombination dominates the PL dynamics at low temperatures in the homoepitaxially grown ZnO/(Zn<sub>0.9</sub>Mg<sub>0.1</sub>)O QW sample without the QCSE as well as in the ZnO/(Zn<sub>0.8</sub>Mg<sub>0.2</sub>)O QW samples with strong QCSE contributions. At higher temperatures and also in the sample with a higher defect density, i.e., heteroepitaxially grown QW, non-radiative carrier capture determines the temporal behavior of the PL signal.

## 5.2 Ga(AsBi): carrier localization and phonon-coupling

In this section, the emission properties of Bi-containing GaAs alloys are studied. The Ga(AsBi) material system is a possible candidate for light-emitting devices in the near-infrared spectral range, at the telecom wavelengths of 1.3  $\mu\text{m}$  and 1.55  $\mu\text{m}$  on GaAs substrates [14]. The main hallmark of this semiconductor is the giant band gap reduction by as much as 60 - 80 meV per percent Bi [22, 146, 147, 148]. The latter is almost an order of magnitude higher compared to more typical GaAs-based alloys, e.g., (GaIn)As with about 15 meV band gap decrease per percent In [15]. The reason for this unusual behavior is the strong perturbation of the GaAs host lattice by the Bi atoms, incorporated as isovalent impurities due to their electronegativity and ionization energy being significantly lower than those of As. These impurities lead to the formation of a dispersionless Bi band below the valence band edge which strongly couples to the valence bands of GaAs yielding mixed states, typically described by a band anticrossing model [149]. Hence, these alloys allow for independent valence band engineering since mostly the hole states are affected [150]. In addition, despite the metallic character of GaBi and the high lattice mismatch between GaAs and GaBi [151], it is possible to grow high-quality Ga(AsBi) crystals containing up to 10 % Bi [152].

As already discussed in sections 2.3.2 and 5.1, spatial fluctuations of chemical concentration are always present in compound materials due to the fundamental thermodynamics [153]. In case of Ga(AsBi), these fluctuations are expected to be particularly strong due to the large impact of Bi on the GaAs band structure. The resulting disorder of the lattice potential influences the carrier dynamics and typically leads to carrier localization, significantly influencing the optical response of the material. In general, the understand-

## 5.2 Ga(AsBi): carrier localization and phonon-coupling

ing of the latter is crucial for the interpretation of the experimental data, optimization of the growth conditions, as well as for the proper design of Ga(AsBi)-based devices. Hence, the aim of the experimental studies discussed in the first part of this section is the systematic investigation of carrier localization effects in Ga(AsBi). For this purpose, TRPL measurements supported by kinetic Monte-Carlo simulations, provide a quantitative analysis of the disorder. The simulations are performed by Sebastian Imhof and Christian Wagner in the group of Prof. Angela Thrähnhardt at University of Technology, Chemnitz (Germany). In addition, since Bi strongly perturbs the local lattice potential, the expected influence of Bi incorporation on carrier-phonon coupling is investigated and discussed in the second part of the section. The Ga(AsBi) samples are grown by molecular-beam epitaxy by Xianfeng Lu and Dan A. Beaton in the groups of Prof. Thomas Tiedje at the University of Victoria (Canada) and Dr. Shane R. Johnson at the Arizona State University (USA).

### 5.2.1 Carrier localization

The sample used for the study of carrier localization is a 30 nm thick layer of Ga(AsBi) with a Bi concentration of about 4-5 %, grown on a GaAs substrate. The growth details are given in Ref. [152]. For the TRPL experiments, quasi-resonant excitation conditions are applied with the pump energy set to 1.38 eV, well below the absorption edge of the GaAs substrate. The PL spectra are acquired using the time-integrated mode of the streak camera with the spectral resolution of about 1 nm.

As an overview, the linear absorption and an emission spectrum of the sample are plotted in Fig. 5.20(a) for the lattice temperature of  $T=10$  K and the excitation density of  $4 \cdot 10^{12} \text{ cm}^{-2}$  photons per pulse. One clearly observes a strongly broadened exciton signature at 1.19 eV with a pronounced Gaussian band tail at low energies. The spectral position of the sample PL, shifted by 360 meV to lower energies in comparison to the GaAs band edge confirms the large band gap reduction in Ga(AsBi), since only 4-5 % Bi are incorporated in the respective layer. In addition, the broad band tail of the absorption is a clear hallmark of disorder present in the sample. This observation is further supported by a large Stokes shift in the PL emission, strongly indicating carrier localization, c.f. discussion in section 2.3.2. The carriers, which are initially excited in the continuum above the band edge, first relax towards the states with lower energy and then recombine radiatively. The corresponding PL energy is thus significantly lower than the inhomogeneously broadened exciton peak at 1.19 eV.

The influence of the disorder is also observed in the temperature-dependent data. Figure 5.20 shows the PL peak position as function of the lattice temperature at various excitation densities between  $n_0$  and  $100 n_0$ . Here,  $n_0$  corresponds to the excitation density of  $1.5 \cdot 10^{12} \text{ cm}^{-2}$  photons per pulse. The PL exhibits a pronounced S-shape behavior at

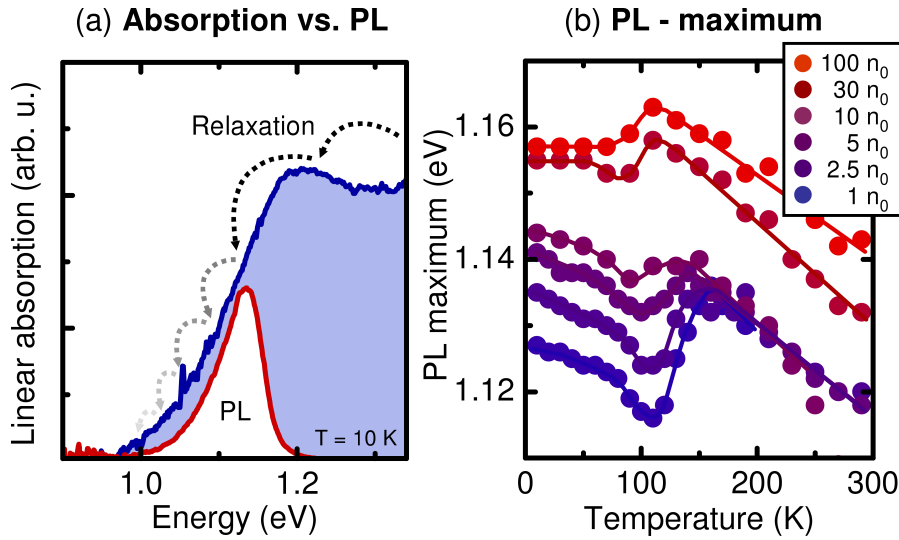


Figure 5.20: (a) Linear absorption at  $T = 10 \text{ K}$  and the PL spectrum for the excitation density of about  $4 \cdot 10^{12} \text{ cm}^{-2}$  photons per pulse. (b) Experimental results for the temperature-dependent PL peak position at various pump intensities.  $n_0$  corresponds to the excitation density of  $1.5 \cdot 10^{12} \text{ cm}^{-2}$  photons per pulse.

low pump intensities, corresponding to the characteristic localization energy in the range of  $\epsilon_0 = 10 \text{ meV}$ . As the excitation density increases, the band tail states become saturated and the S-shape is suppressed. However, even at room temperature, the increase of the pump power still leads to a strong shift of the PL maximum towards higher energies, also observed in comparable samples [152]. This behavior is not expected for a rather small disorder scale of  $10 \text{ meV}$ . In addition, the broad band tail of about  $100 \text{ meV}$  FWHM in the absorption spectra is not compatible with the above estimation for  $\epsilon_0$  [23].

Hence, the experimental findings lead to the following conclusions: (i) disorder effects seem to play a major role in the optical response of the material, (ii) a simple picture of carrier localization on a single energy scale does not apply. Thus, for a consistent description of carrier dynamics in the Ga(AsBi) sample a more complex two-scale picture is proposed. Also, a phenomenological theoretical approach based on kinetic Monte-Carlo simulations is applied, allowing for a quantitative analysis of the disorder parameters.

### Two-scale model

The concept of the two-scale model [154, 155] is motivated by the fact that in addition to the typical alloy disorder, few-atom Bi clusters are likely to exist in the Ga(AsBi) material system [156], acting as localization sites for the carriers. The proposed energy distribution of the energy levels is shown schematically in Fig. 5.21. Potential fluctuations caused by the varying Bi concentration are represented by the randomly-distributed sites with a large localization length. The corresponding DOS is described by a Gaussian in good

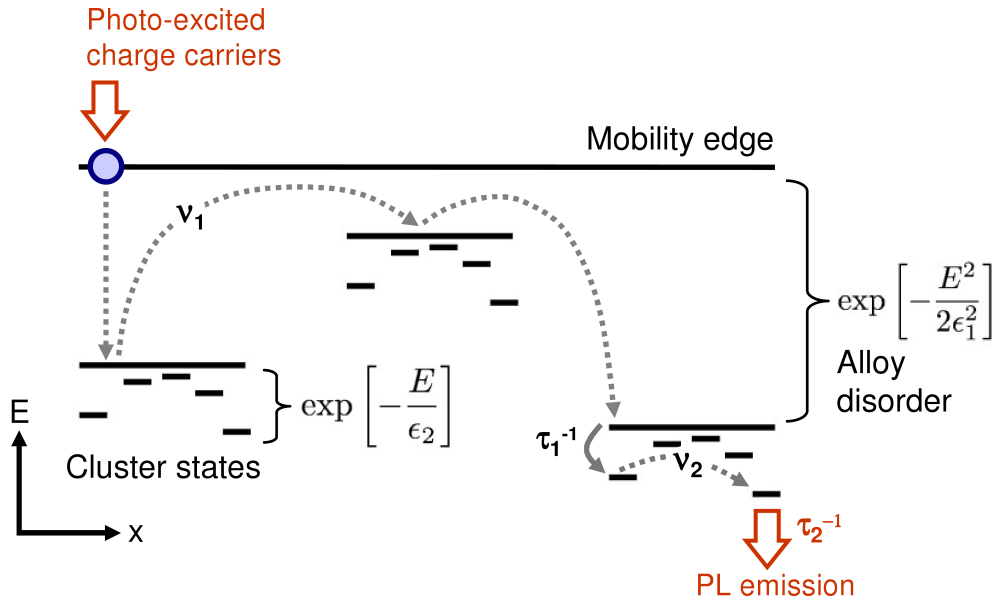


Figure 5.21: Schematic illustration of carrier hopping on two energy scales. The first scale is given by a Gaussian distribution with the characteristic energy scale  $\epsilon_1$  and the second scale - by an exponential distribution with energy scale  $\epsilon_2$ , representing alloy disorder and cluster localization, respectively.

agreement with the linear absorption data. The model parameters are  $N_1\alpha_1^2$ ,  $v_1$ ,  $\tau_1$  and the energy scale  $\epsilon_1$ , representing the alloy disorder. Here,  $N_1$  is the spatial density of the localization sites with the average radius  $\alpha_1$ . The parameter  $N_1\alpha_1^2$  is used as an approximation to describe the excitation power dependence of the experiment. The potential minima are occupied by carriers for higher excitation powers, leading to the decrease of the effective number of free sites  $N_1$  thus reducing possible hopping transitions due to the restriction of only one carrier per site. Also, for every spatially large site, additional smaller sites are included, lower in energy and, again, randomly distributed. These sites represent the Bi clusters. The DOS of the second scale is assumed to be exponential and is characterized by  $N_2\alpha_2^2$ ,  $v_2$ ,  $\tau_2$  and  $\epsilon_2$ . The average hopping rates within the first and the second energy scales are given by  $v_1$  and  $v_2$ , respectively. The time constant  $\tau_1$  corresponds to the carrier capture time from the sites of the first energy scale towards the Bi clusters.  $\tau_2$  denotes the effective recombination time of the carriers localized on the second energy scale. According to the simulations, only the products  $v_j\tau_j$  influence the spectral features in the time-integrated PL data. Time-resolved measurements, on the other hand, allow to determine the complete set of parameters  $v_1$ ,  $v_2$ ,  $\tau_1$ , and  $\tau_2$  thus giving a full description of the carrier dynamics.



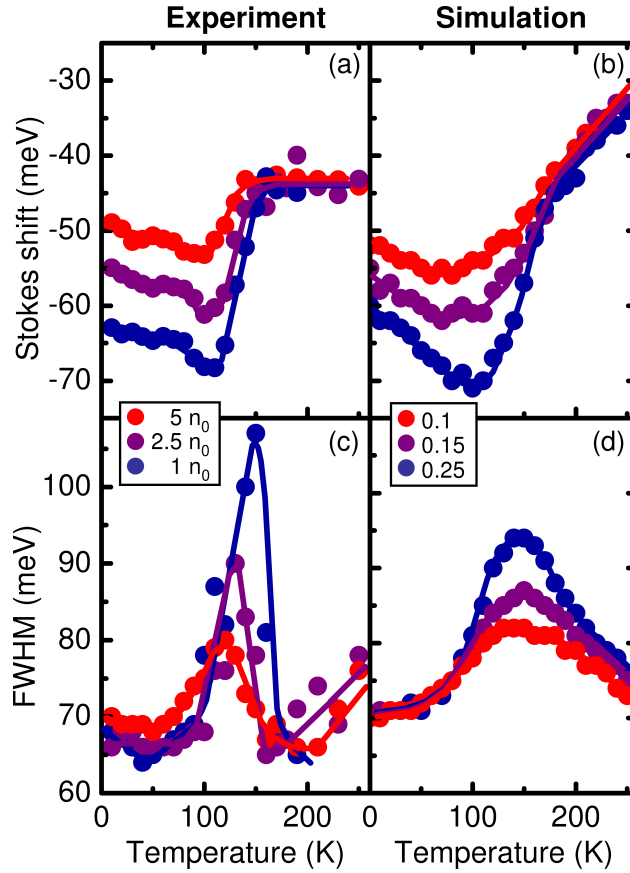


Figure 5.22: Experimental Stokes shift (a) and FWHM (c), extracted from the temperature-dependent PL spectra of the Ga(AsBi) sample, for varying excitation densities. Calculated Stokes shift (b) and FWHM (d) for varying  $N_2\alpha_2^2$  between 0.1 and 0.25 using the kinetic Monte-Carlo simulations with the two-scale model.

### Luminescence spectra

First, the two-scale model is used to fit the time-integrated spectral features. Figures 5.22(a) and (c) show the Stokes shift and the FWHM of the PL emission as function of the lattice temperature, respectively. Three exemplary excitation densities of  $n_0$ ,  $2.5n_0$  and  $5n_0$  are chosen due to the observation of a pronounced S-shape behavior accompanied by the maximum of the FWHM in the corresponding luminescence spectra. The Stokes shift is deduced from the PL peak position as follows: the zero-temperature band gap of 1.19 eV is given by the linear absorption spectrum. The temperature dependence of the band gap for  $T > 150$  K is assumed to follow Varshni's law [43] with  $\alpha = 0.274$  meV/K and  $\beta = 468$  K as fit to the experiment. The latter two values are reasonable parameters for a GaAs-based system, compared to the temperature-dependent band gap shift of the host material [36]. The non-vanishing Stokes shift at higher temperatures is due to the presence of disorder-related effects at the room temperature.



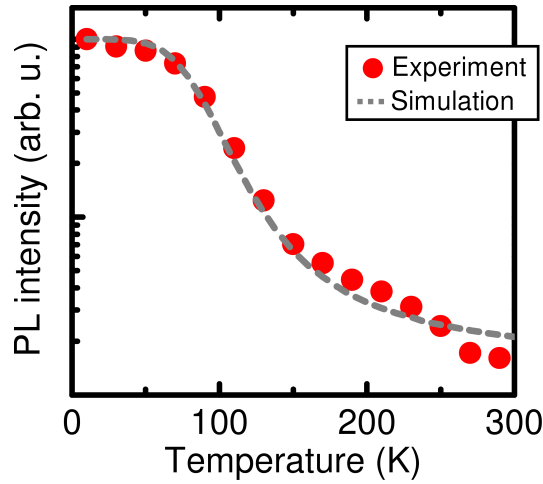


Figure 5.23: Experimental and simulated PL intensity of the Ga(AsBi) sample as function of lattice temperature for the excitation density of  $5 n_0$ .

The corresponding results of the kinetic Monte-Carlo simulations using the two-scale model are shown in Fig 5.22 (b) and (d) for the Stokes shift and the FWHM of the emission peak, respectively. A very good agreement with the experimental data is obtained, with the main characteristics of the temperature- and density-dependent PL spectra being correctly reproduced, c.f. Fig 5.22 (a) and (c). To obtain this agreement, the parameters  $N_1 \alpha_1^2 = 0.01$ ,  $\nu_1 \tau_1 = 10^5$ ,  $\epsilon_1 = 45$  meV,  $\nu_2 \tau_2 = 10^4$  and  $\epsilon_2 = 11$  meV are used. The minor differences between theory and experiment are mainly attributed to uncertainties in the temperature dependence of the Ga(AsBi) band gap and the precise distribution of the Bi cluster states.

The kinetic Monte-Carlo algorithm also explains the characteristic temperature dependence of the PL intensity, often observed in disordered semiconductor materials [111], c.f. section 2.3.2. Two parameters are important: The DOS, where the exponential distribution with the characteristic energy scale  $\epsilon_2$  is used and the relative density of non-radiative sites given by  $N_{nr}/(N_r+N_{nr})$ . It is assumed that the carriers, weakly localized on the first energy scale, can easily reach the non-radiative recombination centers due to the spatially large extension of the corresponding sites. Thus, the energy scale  $\epsilon_2 = 11$  meV is sufficient in order to explain the PL intensity. Figure 5.23 shows the measured and simulated temperature dependence of the normalized PL intensity for the excitation density of  $5 n_0$ . Again, a good agreement between the experiment and the simulation is obtained, allowing for the extraction of the parameter  $N_{nr}/(N_r+N_{nr}) = 0.012$ .

Altogether, the comparison of the experimental PL data with the results of the Monte-Carlo simulations clearly shows that disorder effects in the Ga(AsBi) sample are strongly influenced by carrier localization on two different energy scales. The S-shape, the relative maximum of the FWHM, and the temperature dependence of the PL intensity are

mainly determined by the presence of Bi clusters with the average carrier binding energy of 11 meV. The broad linewidth of the sample emission and absorption spectra at low temperatures as well as the non-vanishing Stokes shift of the PL energy at higher temperatures are due to the alloy disorder. The latter is characterized by the energy scale of 45 meV and spatially extended localization sites.

### Carrier dynamics

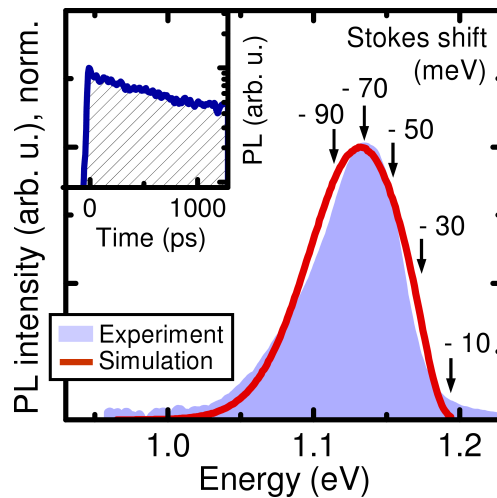


Figure 5.24: Measured and simulated time-integrated PL spectra of the Ga(AsBi) sample at  $T = 10$  K. The inset shows the decay of the measured spectrally-integrated PL intensity. The spectral positions of the extracted PL transients, shown in Fig. 5.25 are marked by arrows with the corresponding Stokes shift values.

The carrier relaxation and recombination dynamics are investigated by temporally resolved PL measurements performed on the same sample. The excitation conditions correspond to the experimental parameters for the time-integrated study to ensure consistent results. The streak camera is operated in the time-resolved mode with the temporal resolution of 20 ps. The lattice temperature is set to  $T = 10$  K and the excitation density is  $4 \cdot 10^{12} \text{ cm}^{-2}$  photons per pulse.

For direct comparison, a time-integrated measured PL spectrum as well as the result of the simulation are shown in Fig. 5.24. The PL peak position, the PL line width, and the overall spectral shape are correctly reproduced by the Monte-Carlo approach. The corresponding measured and calculated TRPL data are plotted in Fig. 5.25 (a) and (b), respectively, as function of emission energy and time after the excitation. Again, an excellent agreement between the simulation and the experiment is obtained in for all emission energies and time delays. For detailed analysis of the carrier dynamics, the PL intensities are integrated across  $\pm 10$  meV for different emission energies. The resulting transients are plotted in Fig. 5.25 (c). The central spectral positions are indicated by the arrows in

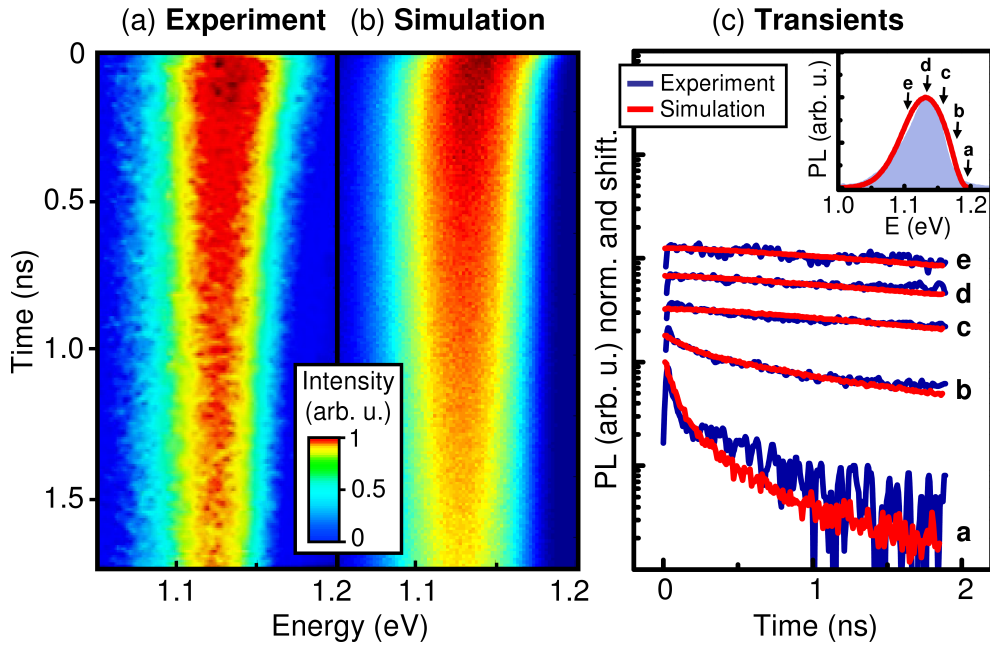


Figure 5.25: Measured (a) and simulated (b) PL intensity of the Ga(AsBi) sample at  $T = 10$  K as function of the emission energy and time after the excitation. (c) Corresponding PL transients at  $T = 10$  K for Stokes shift energies  $E_{\text{PL}} - E_{\text{gap}}$  of  $-10$ ,  $-30$ ,  $-50$ ,  $-70$ , and  $-90$  meV from bottom to top, c.f. Fig. 5.24

Fig. 5.24 together with the corresponding Stokes shift. The data show a fast PL decay on the high-energy side and comparably slow dynamics for low energies, typical for disorder-dominated emission at low temperatures, c.f. section 2.3.2. The dynamics of carriers at the high-energy flank are dominated by hopping to states with lower energy. The carriers on the low-energy side, however, are trapped in localized states and decay slowly with  $\tau_2$ . Additionally, localized low-energy states get filled by carriers from energetically higher sites resulting in a further reduction of the effective decay rate on the low-energy tail of the PL.

The overall excellent agreement between the experimentally obtained and the modeled data allows for the extraction of the disorder parameters. Energy scales of  $\epsilon_1 = 45$  meV and  $\epsilon_2 = 11$  meV are found for the alloy disorder with Gaussian and for the cluster sites with exponentially distributed DOS, respectively. The product  $N_1 \alpha_1^2$  is, again, correlated to the excitation power in the experiment and thus set to 0.15 for the photon flux of  $4 \cdot 10^{12} \text{ cm}^{-2} \text{ s}^{-1}$ . All these parameters are completely consistent with the analysis of the previously discussed time-integrated PL. The additional information, available by monitoring the PL dynamics, allows to determine the parameters  $\tau$  and  $\nu$  individually. The attempt-to-escape frequency for the alloy-disorder scale  $\nu_1 = 10^{14} \text{ s}^{-1}$ , a relaxation time to the cluster scale of  $\tau_1 = 5$  ps, as well as  $\nu_2 = 2.5 \cdot 10^{12} \text{ s}^{-1}$  and  $\tau_2 = 4$  ns for the effective carrier lifetime are obtained. Thus, the hopping rates are generally faster for the first

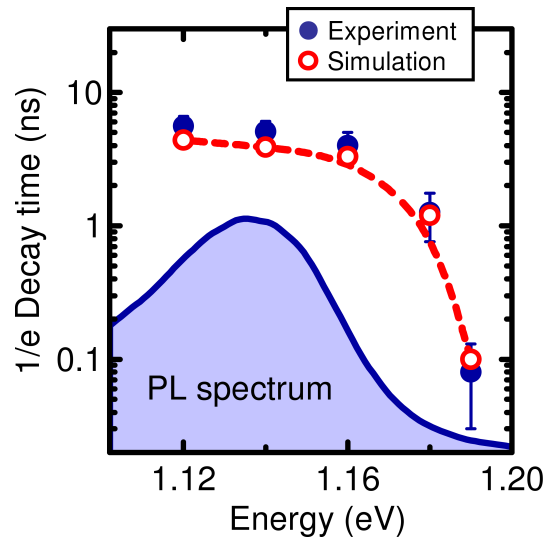


Figure 5.26: Measured and simulated 1/e-decay times, extracted for the corresponding PL transients. The time-integrated measured PL spectrum is given by the shaded area as a reference.

disorder scale attributed to the alloy fluctuations than for the transitions between the individual cluster sites. Also, the average capture time to a Bi cluster  $\tau_1$  of 5 ps is significantly smaller than the effective recombination time  $\tau_2$  in the ns range. In addition, as an alternative evaluation scheme, the deduced 1/e-decay times of the measured and calculated PL transients are plotted as function of the emission energy in Fig. 5.26. Consistently, the decay-times at higher energies are much shorter than the lifetime  $\tau_2$  while the values on the low-energy side are slightly above  $\tau_2$ , indicating additional filling effects.

In summary, the carrier localization dynamics in the Ga(AsBi) sample are experimentally studied and compared to the results of the kinetic Monte-Carlo simulations applying the two-scale approach. In general, typical disorder-induced effects appear in the TRPL, a fast decay on the high-energy side of the luminescence spectrum and much longer decay at lower energies, attributed to the relaxation- and recombination-dominated dynamics, respectively. The comparison of the measured data with the simulations yields a complete set of the individual disorder parameters. Faster carrier hopping among localized sites with fluctuating alloy compositions is found, compared to much slower carrier diffusion between the Bi clusters. In addition, carrier capture into the clusters occurs on an ultra-fast time-scale of about 5 ps.

### 5.2.2 Carrier-phonon coupling

This subsection deals with the study of carrier-phonon coupling in Ga(AsBi). For this purpose, two samples containing 12 nm thick GaAs<sub>1-x</sub>Bi<sub>x</sub> single QWs with Bi-concentrations of  $x = 0.011$  and  $x = 0.055$  placed between GaAs barriers are chosen. The emission prop-

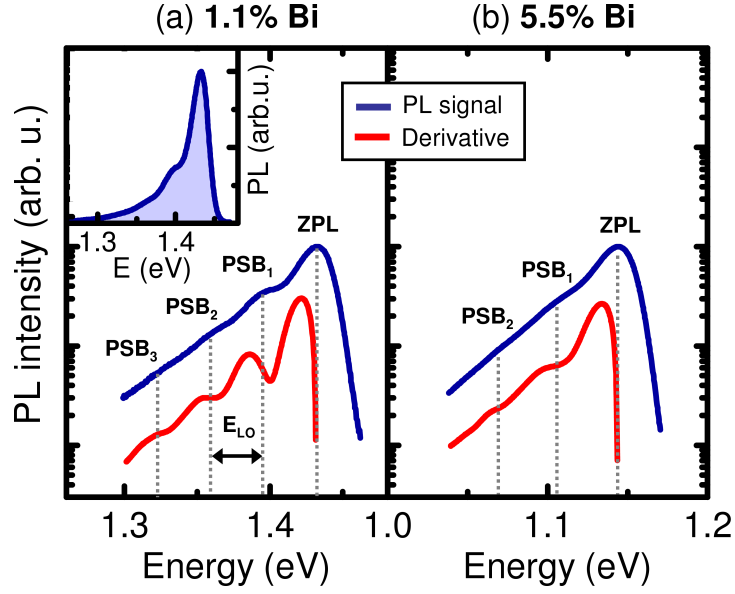


Figure 5.27: Measured and simulated  $1/e$ -decay times, extracted for the corresponding PL transients. The time-integrated measured PL spectrum is given by the shaded area as a reference.

erties of the both samples exhibit pronounced localization effects, closely mimicking the behavior of the Ga(AsBi) layer investigated in the previous subsection 5.2.1. Again, the main feature strongly influencing the optical response is the presence of Bi clusters with a characteristic localization energy in the range of 10 meV. The PL measurements are performed in the CW-PL setup with the He-Ne laser as the excitation source. An OSA is used for the detection of sample luminescence, yielding a spectral resolution of 1 nm.

Figures 5.27 (a) and (b) show the PL spectra of the two GaAs<sub>1-x</sub>Bi<sub>x</sub> QW samples for a lattice temperature of  $T = 10$  K. The excitation density is set to  $80 \text{ mW/cm}^2$ . For a better quantitative analysis the numerical derivatives are plotted as dotted lines below the corresponding spectra. Several pronounced luminescence peaks are observed on the low-energy side of the main emission in both samples. The peaks are equidistantly spaced, separated by about 37 meV, corresponding to the LO-phonon energy in diluted GaAs<sub>1-x</sub>Bi<sub>x</sub> [157]. Thus, the additional emission signatures are unambiguously identified as LO-phonon-sidebands.

To quantify the carrier-phonon coupling-strength, the Huang-Rhys factor  $S$  is used [50]. This quantity corresponds to the average probability of the LO-phonon-emission during the radiative recombination of an electron-hole pair, c.f. discussion in section 2.2.1. The Huang-Rhys factor is obtained from the spectrally integrated PL intensities of the PSBs as follows [50, 51]:

$$S^n = \frac{I_n}{I_0} n!. \quad (5.4)$$

The luminescence intensity of the ZPL is denoted by  $I_0$  and the the emission strength

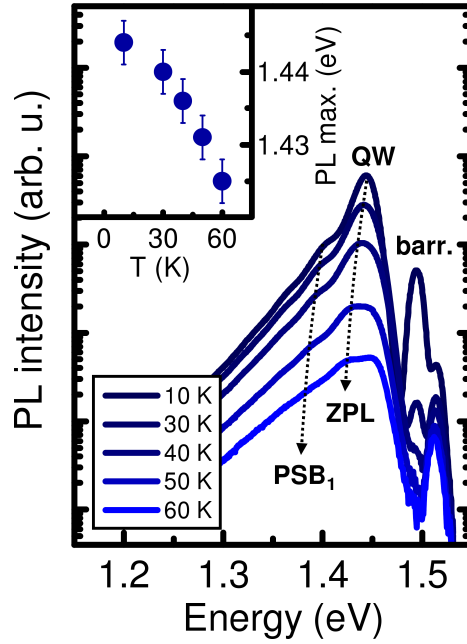


Figure 5.28: PL spectra of the  $\text{GaAs}_{1-x}\text{Bi}_x$  quantum well with Bi-concentration of  $x = 0.011$  for the lattice temperatures between  $T = 10$  K and  $T = 60$  K. The energy of the ZPL maximum is plotted in the inset as function of temperature.

of the  $n$ -th PSB by  $I_n$ , where  $n$  is the number of LO-phonons participating in the scattering process. The relative intensities of the PSBs and the ZPL are obtained applying a line-shape fitting procedure of the PL spectra where the disorder-related exponential low-energy flanks of the emission peaks are taken into account according to [158, 155]:

$$I_n = \Theta(1 - E_n) A_n^e e^{\frac{E-E_n}{\varepsilon_0}} + \Theta(E_n) A_n^g e^{-2\frac{(E-E_n)^2}{w_g^2}} \quad (5.5)$$

Here,  $\varepsilon_0$  and  $w_g$  are the characteristic energy scale of the disorder and the inhomogeneous broadening of the  $n$ -th PSB peak, respectively.  $A_n^e$  and  $A_n^g$  are the corresponding amplitudes,  $E_n$  is the spectral position of the peak maximum, and  $\Theta$  is a step-function. An exemplary fit of the measured PL spectrum is plotted in the inset of Fig. 5.27 (a). Huang-Rhys factors of  $S = (0.20 \pm 0.05)$  for the  $x = 0.011$  sample and  $S = (0.16 \pm 0.05)$  for the  $x = 0.055$  sample are obtained; the precision is limited by the fitting procedure. Thus, the values are comparable within the margin of error, even when the PSBs are less pronounced in the spectrum for  $x = 0.055$  sample due to higher broadening, see Fig. 5.27 (b). The obtained Huang-Rhys factors are more than one order of magnitude larger than extracted from the PSB ratios reported for free and bound excitons in GaAs, [159, 160] indicating unusually strong carrier-phonon coupling for a GaAs-based material.

Next, the temperature dependence of the sample emission and thus of the Huang-Rhys factor is investigated. The PL spectra of the QW with a Bi content  $x = 0.011$  are plotted

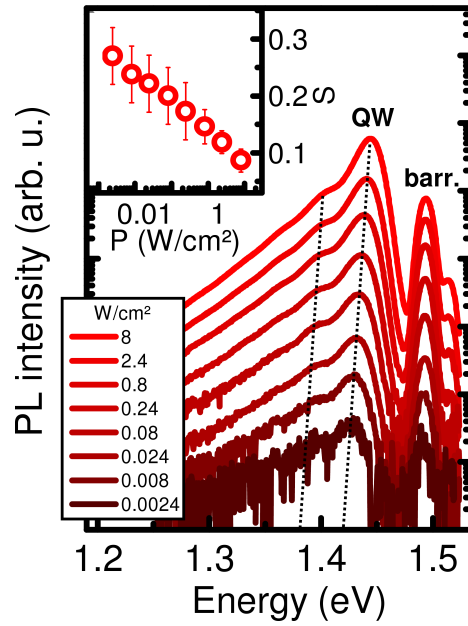


Figure 5.29: PL spectra as function of the excitation density at  $T=10$  K for the  $\text{GaAs}_{1-x}\text{Bi}_x$  sample with  $x=0.011$ . The inset shows the corresponding Huang-Rhys factor  $S$ .

in Fig. 5.28 for the lattice temperatures between  $T=10$  K and  $T=60$  K. The luminescence peaks on the high-energy side at 1.494 eV and 1.514 eV are related to the shallow impurities in GaAs barriers and substrate [36]. The ZPL and the corresponding PSBs in the investigated  $\text{GaAs}_{1-x}\text{Bi}_x$  sample exhibit a strong shift to lower energies of more than 20 meV, as the temperature is increased from 10 K to 60 K. For higher lattice temperatures an additional feature appears on the high-energy side of the ZPL at about 1.45 eV, dominating the spectrum at  $T=60$  K. Both observations clearly indicate that the ZPL and the PSBs originate from bound states. The corresponding PL shows a typical disorder-related red-shift of the emission maximum for increasing temperature in the low-temperature regime, discussed in the previous subsection 5.2.1. Eventually, the bound states are ionized for sufficiently high lattice temperatures.

Previous studies have shown that Bi tends to form clusters when alloyed with GaAs, giving rise to a number of shallow localized states below the band-gap. The estimated ionization energy in the range of 10 meV for the ZPL matches the average localization energy of the Bi-clusters [156, 161], c.f. the discussion in 5.2.1. In addition, a strong electron-phonon-coupling is typical for an isoelectronic impurity such as Bi as already observed for the Ga(AsBi) bulk samples [156]. The reason is the strong local deformation of the lattice by the impurity cluster. In addition, the strength of the deformation is significantly altered by the presence of carriers, bound to the impurities. This dependence enhances the efficiency of the deformation potential scattering between carriers and



phonons, previously discussed in sections 2.2.1 and 4.2. Therefore, the phonon-assisted PL in the studied  $\text{GaAs}_{1-x}\text{Bi}_x$  QW is clearly attributed to the emission from carriers bound to Bi-clusters.

To investigate the effect of saturation of localized states, the excitation density dependence of the PSB emission is studied at  $T = 10$  K for the QW sample with  $x = 0.011$ . The PL spectra for the excitation densities between  $2.4 \text{ mW/cm}^2$  and  $8.0 \text{ mW/cm}^2$  are plotted in Fig. 5.29. The emission spectrum shifts to higher energies as the pump power is increased. Also, the carrier-phonon-coupling strength decreases as shown in the inset. Both findings support the previous interpretation of phonon-assisted PL originating from Bi-clusters. The cluster states become saturated for higher excitation densities leading to a typical blue-shift of the luminescence spectra [155, 162], c.f. discussion in section 2.3.2. Under these conditions the carriers are less localized and thus have a lower probability of scattering with LO-phonons.

In summary, the phonon-assisted luminescence from  $\text{GaAs}_{1-x}\text{Bi}_x$  QW samples is studied by CW PL as function of lattice temperature and excitation density. Pronounced PSBs are observed in all emission spectra of the samples. The LO-phonon-coupling strength is unusually strong for a GaAs-based material; it is quantified by the Huang-Rhys factor  $S$  ranging between 0.1 and 0.3. Carriers bound to isoelectronic impurities, i.e., Bi-clusters, are identified as the origin of the intense phonon-assisted emission. The intensity of the PSBs decreases as the cluster states are ionized at elevated lattice temperatures.

### **5.3 GaN quantum wires: confinement in a quasi 1D-system**

In this section, the emission properties of GaN quantum wires (QWires) are studied. GaN is a III-V wide-gap semiconductor with the band gap energy in the UV spectral range, at 3.5 eV. In analogy to the previously discussed ZnO, the exciton binding energy as well as the carrier-phonon coupling are rather strong in GaN compared to the typical III-V systems, e.g. GaAs. In general, the GaN material properties are well studied [36, 163] and GaN-based devices, as LEDs and diode-lasers, are already widely used for the light-emitting applications [164, 13]. Furthermore, GaN-nanostructures became available due to the improved growth techniques, providing additional insight into the physics of weakly confined carriers as well as being candidates for potential applications as light emitters on a sub-wavelength scale. Typically, in these systems, the confinement length is in the order of several 10's of nm, larger than the exciton Bohr radius in GaN [36]. However, only few reports on the properties of "real" 1D GaN quantum structures with strong carrier confinement are found in the literature [165, 166].



### 5.3 GaN quantum wires: confinement in a quasi 1D-system

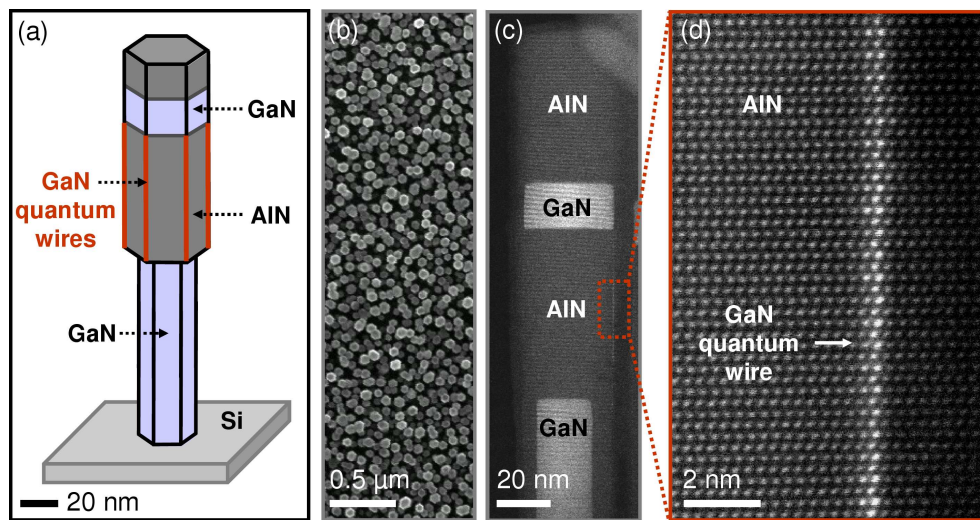


Figure 5.30: (a) Schematic illustration of the studied GaN quantum wire structures. (b) Typical TEM image of the GaN/AlN nanowire ensemble, measured in the growth direction. (c) TEM image of a single GaN/AlN nanowire with GaN quantum wires located at the facet edges. (d) Scanning TEM image of the GaN quantum wire, located on surface of the GaN/AlN nano-wire, measured with sub-nm spatial resolution.

The studies conducted within the framework of this thesis are focused on such 1D GaN systems. The QWires are grown in the group of Prof. Martin Eickhoff and are characterized by TEM measurements in the group of Prof. Jordi Arbiol at the Institut de Ciència de Materials de Barcelona (Spain). The typical structure of the GaN QWire samples, based on the results of the TEM studies, is schematically illustrated in Fig. 5.30 (a). The corresponding, exemplary TEM images are shown in Fig. 5.30 (b), (c), and (d) on a 0.5 μm, 20 nm and 2 nm scale, respectively. The samples consist of ensembles of hexagonally shaped GaN nanowires with the diameters of about 20 nm and lengths in the range of a μm, grown on silicon substrates. The nanowires are covered with 50 nm of AlN, then overgrown with a thin GaN QW-like layer of several nm up to 20 nm thickness. At this growth step, GaN QWires are formed at the facet edges of the nanowires. In addition, in a fraction of the investigated samples an AlN capping layer of 50 nm width is deposited on top of the structure. The presence of the AlN cap also results in a thin AlN shell of several nm thickness covering the GaN QWires, c.f. Fig. 5.30 (d).

The main aim of the TRPL experiments is finding the evidence for the luminescence activity in the GaN QWires as well as the confirmation of the quantum confinement effect, expected to be especially large in these material system. In addition, possible influence of the QCSE, carrier localization as well as the overall temperature stability of the PL are studied. Finally, the impact of the growth parameters is discussed.

### 5.3.1 Carrier confinement

The samples used for the initial investigations are capped with the additional AlN layer on top of the nanowires. The excitation energy is set to 4.43 eV taking into account the potentially large confinement energy, i.e., the absorption edge, of the QWires. The spectral and temporal resolutions in the experiment are 0.2 nm and 10 ps, respectively. The PL intensity of the sample is plotted in Fig. 5.31 as function of the emission energy and time-delay after the excitation. The lattice temperature is set to 10 K and the excitation energy to  $1.4 \cdot 10^{12} \text{ cm}^{-2}$  photons per pulse. A time-integrated luminescence spectrum and the transient intensity of the PL peak at 4.1 eV are shown at the bottom and on the right-hand side of the graph, respectively. The temporal interval is chosen between 50 ps and 750 ps. As expected for the low-temperature spectrum of the bulk-like emission from GaN nanowires [36, 167, 168], a pronounced peak from the bound excitons appears at about 3.5 eV. A broad shoulder on the low-energy side with considerably longer PL decay is attributed to the luminescence of the thin GaN layer, significantly influenced by the QCSE, see Refs. [169, 170] and the discussion below. In addition, a distinct PL peak appears at 4.1 eV. This emission signature is present in all studied samples and is not ob-

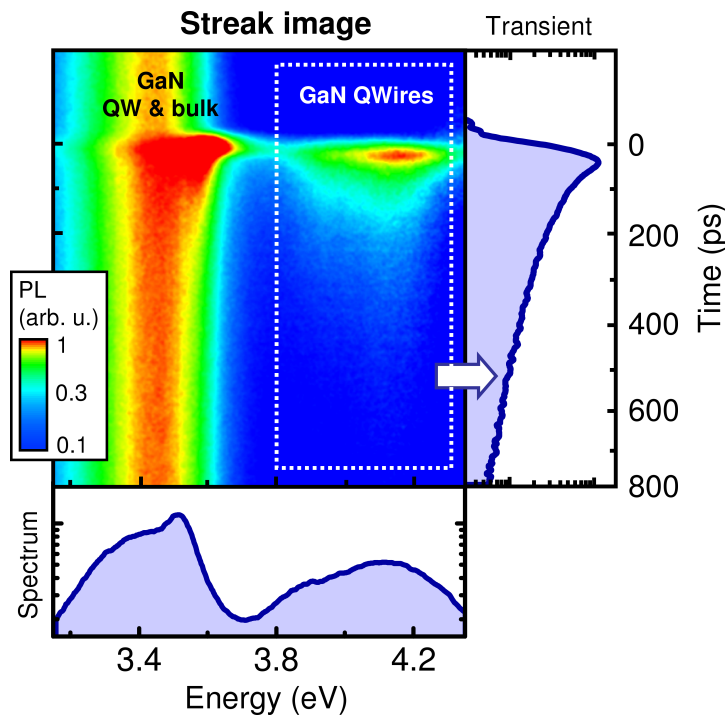


Figure 5.31: PL intensity of a GaN QWires sample as function of emission energy and time-delay after the excitation for the lattice temperature of 10 K and the excitation energy of  $1.4 \cdot 10^{12} \text{ cm}^{-2}$  photons per pulse. Time-integrated PL spectrum and the transient intensity of the luminescence peak at 4.1 eV are shown at the bottom and on the right-hand side, respectively.

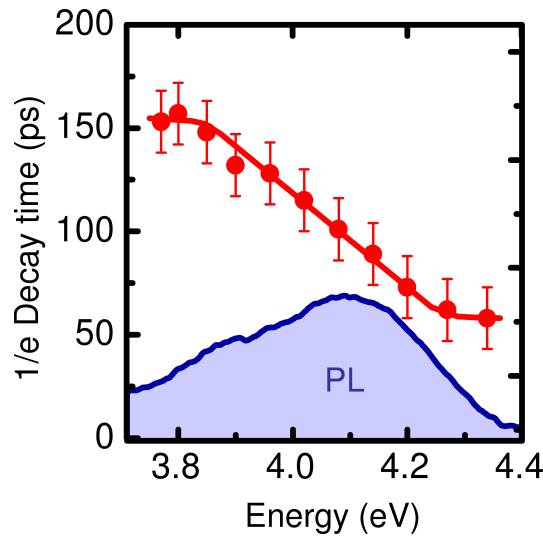


Figure 5.32: Decay time of the GaN QWires PL as function of the emission energy for the lattice temperature of 10 K and the excitation energy of  $1.4 \cdot 10^{12} \text{ cm}^{-2}$  photons per pulse. The solid line is a guide to the eye. Corresponding PL spectrum is shown in the same plot for comparison.

served in the spectra of comparable structures without the QWire growth [171]. Also, the energy shift of about 0.6 eV with respect to the GaN bulk luminescence is a clear evidence of a considerable confinement effect. Thus, the 4.1 eV peak is unambiguously attributed to the emission from the GaN QWires. The diameter of the QWires, estimated from the confinement energy of  $E_{conf} \geq 0.6 \text{ eV}$  by basic particle-in-a-box calculations [28] using the effective masses of electrons and holes in GaN [36], is in the range of 3 nm or even smaller. This value matches well the QWire thickness, obtained from the TEM measurements. The PL is also inhomogeneously broadened with the FWHM of about 300 meV, indicating width fluctuations within single and/or between different, spatially separated QWires. Furthermore, the luminescence signal exhibits a non-exponential decay on the 100 ps time-scale. Thus, any ultra-fast carrier capture processes from the QWires into the GaN layers are excluded.

For an additional analysis of the non-exponential luminescence dynamics, the extracted 1/e decay time is plotted in Fig. 5.32 as function of the emission energy. The PL spectrum is shown in the same graph for comparison. The average decay time varies between 50 ps and 150 ps on the high- and low-energy side, respectively. This variation alone already causes the non-exponential PL decay of spectrally integrated emission. In general, for an ensemble of QWires, the dependence of the decay time on the PL energy is either due to the disorder-related hopping processes within a single QWire, c.f. section 2.3.2, or due to the different recombination rates from spatially separated QWires with varying widths.

### 5.3.2 Influence of the excitation density and the lattice temperature

Following the identification of the PL signature of the GaN QWires, additional characterization measurements are performed on the same sample, focused on the study of possible QCSE contributions as well as the temperature stability of the PL. Figure 5.33 (a) shows the time-integrated PL spectra at  $T = 10$  K as function of the excitation density. Here,  $n_0$  corresponds to the photon flux of  $1.4 \cdot 10^{12} \text{ cm}^{-2}$  photons per pulse. As the excitation density is increased, the energy of the GaN nanowire PL remains constant, whereas the emission maximum from the QW-like GaN layer shifts towards higher energies. This shift is expected due to the screening of a strong internal piezo-electric field within the GaN QW in the growth direction induced by the strain between GaN and AlN [169, 170]. In contrast to that, no screening is observed in case of the GaN QWires, indicating a negligible influence of the QCSE, i.e., the absence of an internal field. In addition, the PL intensity exhibits a slightly superlinear behavior accompanied by a small increase of the decay time thus suggesting only insignificant contributions from the saturation of non-radiative decay channels, c.f. section 2.3.1. Also, these observations further confirm negligible influence of the QCSE. Otherwise the carrier lifetime is expected to decrease with increasing excitation density due to the screening of the internal field, see the discussion in section 2.2.2. This finding is reasonable since the QWires are grown on the non-polar plane of the AlN.

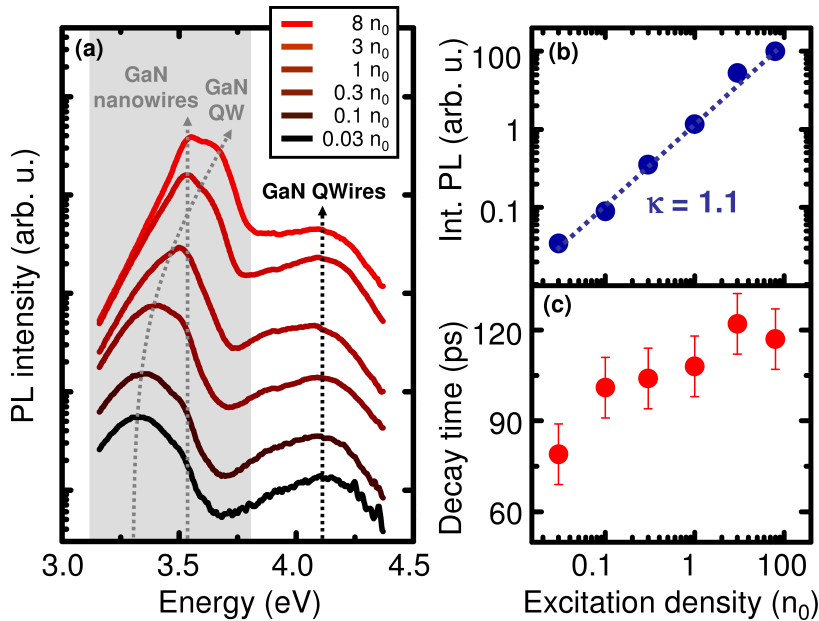


Figure 5.33: Time-integrated PL spectra of the GaN QWires (a) the corresponding spectrally integrated intensity (b), and the 1/e decay time (c) as function of the excitation density for  $T = 10$  K.  $\kappa$  denotes the exponential parameter obtained by fitting the PL intensity  $I_{PL}$  as function of the excitation power  $I_{exc}$  with the power law  $I_{PL} = I_{exc}^{\kappa}$ .

### 5.3 GaN quantum wires: confinement in a quasi 1D-system

Temperature-dependent data are shown in Fig. 5.34 for the pump density of  $1.4 \cdot 10^{12} \text{ cm}^{-2}$  photons per pulse. All GaN-related peaks shift towards lower energies as the temperature is increased. However, the energy difference between  $T = 10 \text{ K}$  and  $T = 300 \text{ K}$  emission maxima of about 20 meV is much lower than the typical shift of more than 50 meV in GaN [172], indicating significant influence of strain and/or carrier localization on the PL energy. Also, the integrated PL intensity of the GaN QWires emission, plotted in Fig. 5.34 (b), remains nearly constant for  $T \leq 150 \text{ K}$ . In the same temperature range, the decay time exhibits a small increase from 90 ps to 120 ps, suggesting the strong suppression of non-radiative decay channels. As the temperature is increased beyond  $T = 150 \text{ K}$  towards the room temperature, the luminescence intensity decreases by a factor of three. The intensity decrease is accompanied by a decrease of the carrier lifetime, indicating faster non-radiative recombination rates at higher temperatures, c.f. section 2.3.1. Altogether, the emission of the QWires shows much higher temperature stability, compared to the PL from the nanowires and the QW. The PL intensity of the two latter peaks decreases over an order of magnitude in the temperature range between  $T = 10 \text{ K}$  and  $T = 300 \text{ K}$ .

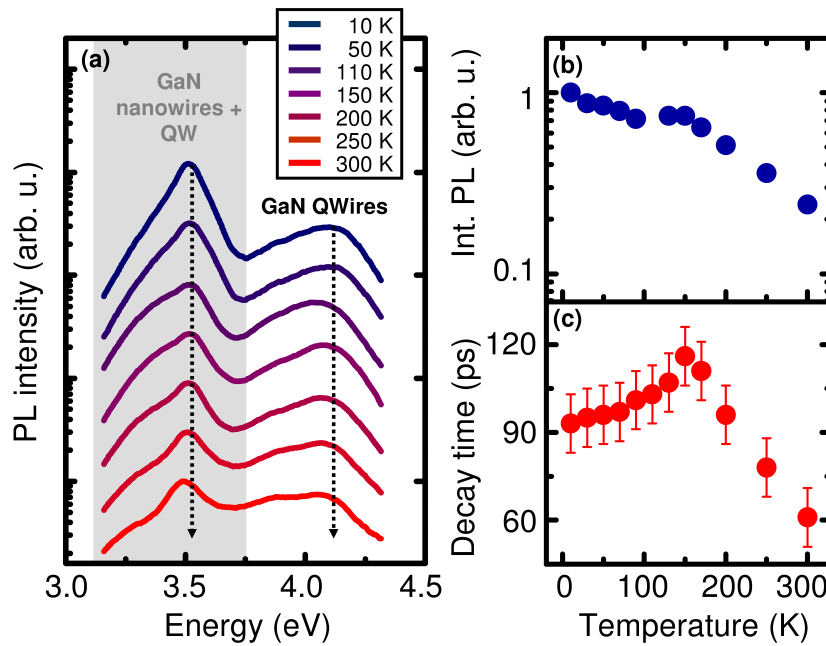


Figure 5.34: Time-integrated PL spectra of the GaN QWires (a), the corresponding spectrally integrated intensity (b), and the  $1/e$  decay time (c) as function of the lattice temperature. The excitation density is set to  $1.4 \cdot 10^{12} \text{ cm}^{-2}$  photons per pulse.

### 5.3.3 Impact of the growth temperature

In this last subsection, the PL properties from a series of the QWires grown under different temperatures between  $T_g = 1000^\circ\text{C}$  and  $T_g = 1055^\circ\text{C}$  are studied. The TEM results show that as the growth temperature increases, the amount of the deposited GaN increases leading to higher diameters of the QWires. In this series, the AlN capping layer is omitted, leaving only a thin GaN layer on top of the nanowires and no AlN shell around the QWires. The TRPL measurements are performed at the lattice temperature of 10 K with the excitation density of  $1.4 \cdot 10^{12} \text{ cm}^{-2}$  photons per pulse. Time-integrated PL spectra of the samples are shown in Fig. 5.35. On the low-energy side, only the emission from the nanowires is observed. The peak from the thin GaN layer is missing, indicating damage of the latter due to the absence of the AlN capping. However, pronounced PL peaks from the QWires are found in all four samples. This growth configuration thus provides an advantage over AlN capping since the QW emission does not influence the PL spectra, whereas the QWires remain optically active. For higher growth temperatures, the PL intensity of the QWires strongly decreases. The carrier lifetimes, on the other hand, remain nearly constant around  $(60 \pm 20)$  ps. These observations show that no additional loss channels are introduced for the  $T_g = 1033^\circ\text{C}$  and  $T_g = 1055^\circ\text{C}$  samples, indicating either lower number of photoexcited QWires or lower absorption coefficients.

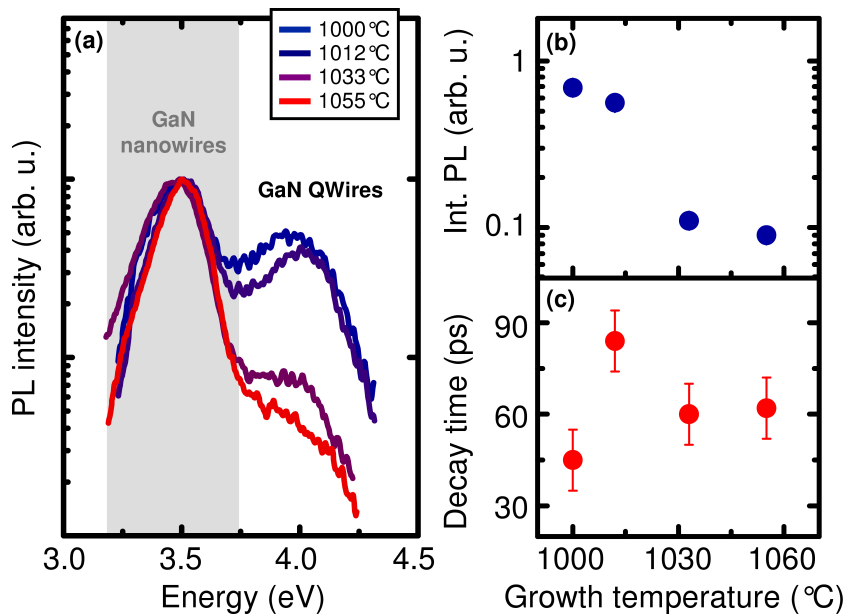


Figure 5.35: Time-integrated PL spectra of the GaN QWires (a), the corresponding spectrally integrated intensity (b), and the  $1/e$  decay time (c) as function of the growth temperature of the QWires. The lattice temperature is set to 10 K and excitation density - to  $1.4 \cdot 10^{12} \text{ cm}^{-2}$  photons per pulse.



### 5.3 GaN quantum wires: confinement in a quasi 1D-system

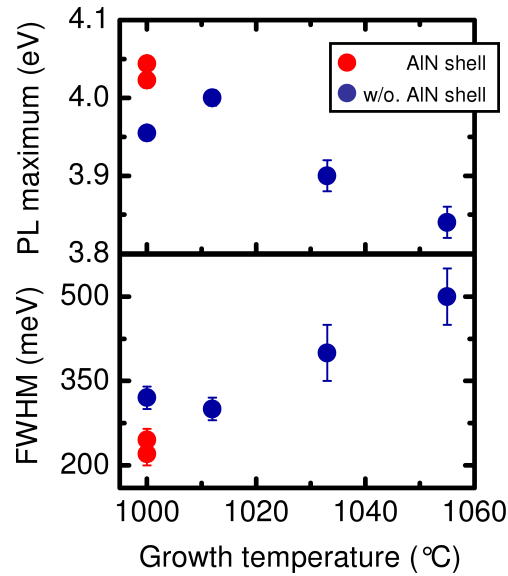


Figure 5.36: Emission maximum (a) and the FWHM (b) of the GaN QWires series (w/o. AlN shell) as function of the growth temperature. Samples with AlN shell are shown for comparison in the same plot. The lattice temperature is set to 10 K and excitation density - to  $1.4 \cdot 10^{12} \text{ cm}^{-2}$  photons per pulse.

For a more detailed analysis of the spectral features, the PL peaks of the nanowires and the QWires are fitted with Gaussians. The fit parameters for the QWires, i.e., the peak energies and FWHMs, are shown in Fig. 5.36. As the growth temperature is increased, the PL peak shifts towards lower energies. This result is consistent with the higher widths for the QWires grown at increased  $T_g$ , observed in the TEM data. A larger wire diameter leads to a weaker confinement and thus to the decrease of the emission energy. In addition, the FWHM of the PL peak increases with  $T_g$ , indicating a higher inhomogeneous broadening related to the energy scale of the disorder. The latter would also contribute to the shift of the PL maximum if carrier hopping between potential minima would occur, i.e. the broadening is due to the width fluctuations in each individual QWire. Finally, the presence of the AlN shell seem to have only a small impact on the PL maximum and FWHM, c.f. Fig. 5.36. The observed differences are attributed to a slightly different confinement energy, strain, and possible width fluctuations between the samples.

In summary, PL emission from 1D GaN QWires is clearly identified. The findings are supported by the evidence of a significant confinement effect, leading to the energy shift of the band gap more than  $\geq 0.6 \text{ eV}$ . The estimated QWires diameter of several nm is in a good agreement to TEM data. Also, the optical response of the QWires shows no indications of the QCSE, i.e., the absence of strong internal fields perpendicular to the length of the QWires. Finally, the PL intensity as well as the carrier lifetimes are found to be rather stable as function of the lattice temperature, especially in comparison to the GaN nanowires.





## 6 Vertical-external-cavity surface-emitting lasers for NIR applications

This chapter deals with the characterization and optimization studies of semiconductor lasers designed for NIR applications based on the well-studied (GaIn)As material system [173, 174, 175, 176, 177]. The device under investigation is the so-called *vertical-external-cavity surface-emitting laser* (VECSEL) developed in the late 90's [16, 178]. This particular type of a laser perfectly combines the excellent beam quality of surface emitters and the high output power of semiconductor edge-emitting diode-lasers [16]. In addition, solid-state on-chip fabrication, small packaging dimensions and the spectral tunability are all maintained as the main advantages of a semiconductor device. VECSELs are available in a broad spectral range [18, 179, 17, 180, 181]. They offer efficient intra-cavity frequency mixing [182, 19, 183, 184, 185] combined with frequency stabilization [20], and are able to operate in a pulsed regime, emitting sub-500 fs pulses [186, 187, 21, 188]. For the majority of the applications, however, high output power of the device remains crucial.

The performance of the VECSEL is generally limited by overheating. This leads to the so-called thermal rollover - a rapid decrease of the output power even when the pump power is increased. The excess heat is generated inside of the VECSEL chip due to the intrinsic properties of the active structure and off-resonant pumping conditions required for laser operation [189, 190]. Therefore, efficient cooling concepts are inevitable for the high-power operation. Fortunately, VECSEL chips offer a potentially large active area and are therefore proposed to achieve higher output power by simply increasing the size of the pump spot [191, 17, 192, 193]. However, this power-scalability is questioned in several reports, at least for specific pumping conditions [194, 195, 196]. Possible reasons for this behavior are an inhomogeneous loss-channel distribution due to the growth and processing imperfections or a substantial importance of three-dimensional heat transfer in the structure [194, 196].

The experiments discussed in this chapter focus on the study of the thermal properties of a high-power VECSEL. The VECSEL setup as well as the semiconductor chip structure are discussed in the first section. The second section addresses the distribution and removal of the excess heat as well as the optimization of the device for increased performance via different heat-spreading and heat-transfer approaches. Based on these investigations, the possibility for power-scaling is evaluated and the underlying restrictions are analyzed in the third section. The latter investigations are performed applying spatially resolved PL measurements. An experimental setup is implemented for monitoring the spatial distribution of heat in the semiconductor structure during laser operation. The investigated VECSEL chips are grown and processed in the group of Dr. Wolfgang Stolz at the Material Sciences Center in Marburg, in close cooperation with the groups of Profs. Yushi Kaneda and Jerome V. Moloney at the University of Arizona (USA).

## 6.1 VECSEL Setup

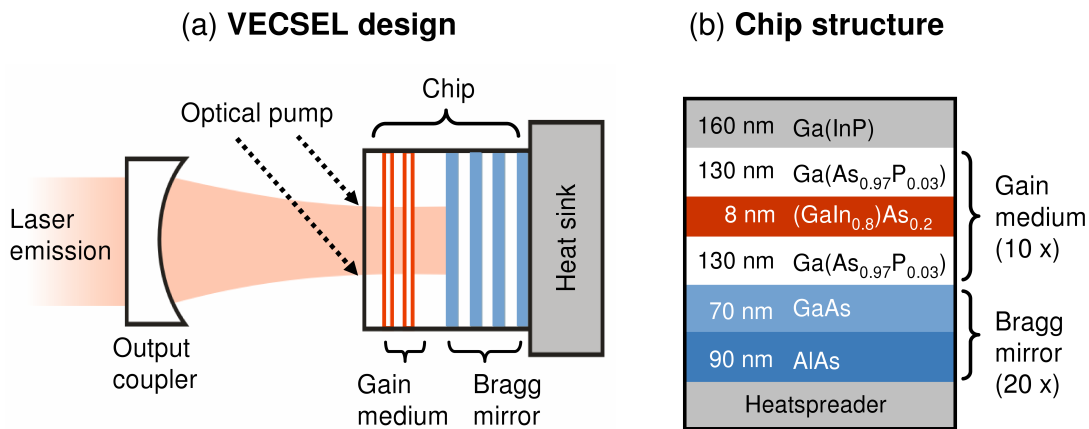


Figure 6.1: (a) Basic design of a VECSEL with a standard linear cavity. (b) Schematic illustration of the chip structure used for the investigations within the framework of this thesis.

Figure 6.1 (a) and (b) illustrate the basic design of the VECSEL device, and the structure of the semiconductor chip used for the investigations within the framework of this thesis. The chip is designed for the operation in the near-infrared spectral range at about 1040 nm. The semiconductor structure is grown using metal-organic vapor phase epitaxy (MOVPE) and the so-called "upside-down" approach. First, an (GaIn)P window layer of about 150 nm thickness is deposited on a 650- $\mu\text{m}$ -thick GaAs wafer. The active region consists of 10 (GaIn)As QWs placed between GaAs buffer layers (not shown here) and Ga(AsP) barriers for pump-absorption and strain-compensation, respectively. The quantum wells are arranged in a resonant-periodic-gain configuration, i.e. their spatial posi-

## 6.2 Device characterization: cooling concepts and high power operation

tions overlap with the field maxima of the lasing mode. A high-reflectivity distributed Bragg reflector (DBR) with 20 pairs of GaAs/AlAs is grown on top of the structure. For efficient heat transfer, the device is soldered to a heat-spreader using an indium layer (not shown here) of several microns thickness. Afterwards, the GaAs substrate is removed by selective chemical etching. No anti-reflective coating is applied to fully exploit the enhanced coupling of the material gain to the cavity mode for optimal high-power performance [190, 197, 198]. Further details on the chip structure and growth parameters are given in [196].

The chip is placed inside an external linear cavity of 6 cm length using an output coupler with 10 cm radius of curvature and a transmission of 5 %. This configuration supports higher transversal modes, allowing spatially extended pump spots and thus high output power [189]. A fiber-coupled diode laser emitting a maximum output power of 400 W at 808 nm is used as a pump source. The angle of incidence is set below  $30^\circ$  to obtain an only slightly elliptical pump spot. A charge-coupled-device-based beam-profiler and an external high-resolution digital camera are used to control the size and shape of the tailored pump profiles, obtained by appropriate pump optics. The output power is detected by a power meter capable of measuring up to 200 W. The laser emission is spectrally resolved by an optical spectrum analyzer.

## 6.2 Device characterization: cooling concepts and high power operation

### 6.2.1 Heat spread

Efficient cooling of the device strongly relies on heat spreading, i.e., the efficient distribution of heat generated in the small area excited by the pump spot. Two properties are crucial for an optimal heat-spreader: high thermal conductivity and low surface roughness, providing a smooth interface with the semiconductor device. In this subsection, two different materials are studied to optimize the heat-spreading properties of the structure for the pump spot width of  $300\ \mu\text{m}$ . Chemically-grown diamond and high-purity copper are both obvious choices for distributing the heat due to their large thermal conductivities. For the experiments,  $5 \times 5\ \text{mm}^2$  large diamond and copper plates are bonded to VECSEL chips from the same wafer. The advantage of diamond is the extremely high thermal conductivity of  $1800\ \text{W m}^{-1}\ \text{K}^{-1}$  compared to about  $400\ \text{W m}^{-1}\ \text{K}^{-1}$  in copper. On the other hand, the lower cost and easier processing favor the use of copper as a heat-sink material. To evaluate the advantages of different heat-spreaders, the thermal resistances and the output curves of the two devices are measured. While the input/output characteristics are easily obtained by power measurements, the study of the thermal properties in the

6 Vertical-external-cavity surface-emitting lasers for NIR applications

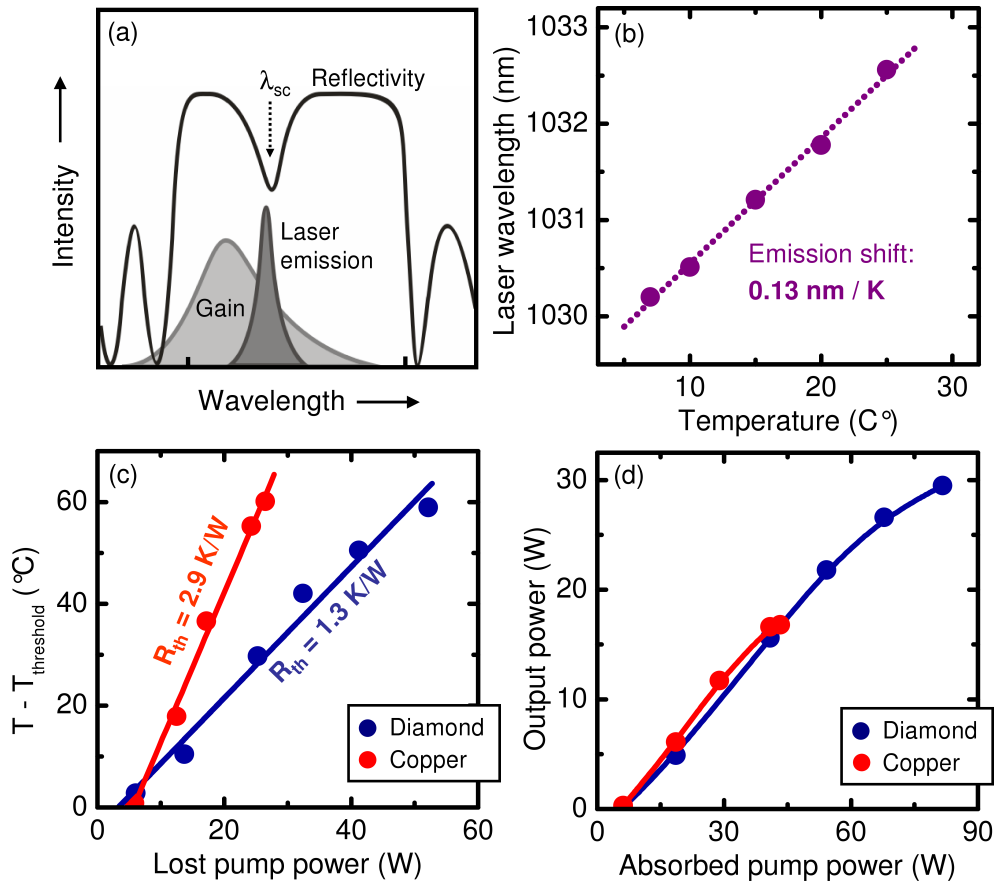


Figure 6.2: (a) Schematic plots of the device reflectivity, representing the underlying dielectric structure, material gain and laser emission. (b) Central wavelength of the laser emission for different heat-sink temperatures. The pump power is set slightly above threshold. (c) Relative temperature increase with respect to the threshold for a copper and a diamond heat-spreader as function of the dissipated pump power, i.e., the difference between absorbed pump and output of the device. (d) Output power characteristic for copper- and diamond-bonded chips.

high power regime requires a less direct approach. The spectral position of the emission during laser operation provides a convenient access to the temperature increase across the active area. Generally, the laser spectrum is determined by the optical modes of the surrounding dielectric environment [16, 197]. Figure 6.2(a) schematically shows the cavity mode-structure, represented by the reflectivity spectrum. A broad stop-band around the lasing wavelength and some smaller features on the sides are due to the DBR. The dip in the middle of the stop-band is the so-called sub-cavity resonance, a Fabry-Perot mode resulting from multiple reflections between the chip-to-air surface and the DBR. The spectral position of the sub-cavity resonance in the investigated device is  $\lambda_{sc} = 1032$  nm at the temperature of 20 °C. The laser emission is determined by the overlap between the broad gain spectrum of the active material and the narrow sub-cavity resonance.

## 6.2 Device characterization: cooling concepts and high power operation

The absolute spectral positions of the material gain and the dielectric-structure are both temperature-dependent, shifting  $0.4 \text{ nm K}^{-1}$  and  $0.1 \text{ nm K}^{-1}$ , respectively. The VECSEL is designed with an initial detuning between the gain maximum at threshold and the sub-cavity mode. As the pump power is increased, the gain shifts faster with temperature and reaches an optimal overlap with the sub-cavity mode in the high power regime. The detuning thus strongly affects the lasing threshold, the maximum power, and the relative slope efficiency. The central wavelength of the laser emission is plotted in Fig. 6.2 (b) as function of the heat-sink temperature. The pump power is set at about  $1.3 \times$  lasing threshold power to avoid any additional heating. A linear increase of the wavelength with a temperature-induced shift of  $\delta\lambda/\delta T = 0.13 \text{ nm K}^{-1}$  is clearly observed. The value in the range of  $0.1 \text{ nm K}^{-1}$  confirms the spectral position of the laser emission being governed by the sub-cavity resonance. Now, the temperature increase is extracted from the spectral shift of the laser wavelength by evaluating:  $T - T_0 = (\delta\lambda/\delta T)^{-1} \Delta\lambda$ . The initial value  $T_0$  is the device temperature in the low pump regime, i.e., around lasing threshold, corresponding to the heat-sink temperature of  $15 \text{ }^\circ\text{C}$ .

Figure 6.2 (c) shows the relative temperature increase as function of dissipated power, i.e., the difference between the absorbed pump power and the output. The absorbed power is calculated by taking into account 30 % reflection, obtained from the experimental data, active structure thickness of  $1.7 \mu\text{m}$ , and the absorption coefficient of GaAs [36]. The VECSEL chip with copper as a heat-spreader heats up significantly faster than the diamond-bonded device. Thermal resistance  $R$  is obtained by extracting the slope of the plotted curves yielding  $R_c = 2.5 \text{ K W}^{-1}$  and  $R_d = 1.3 \text{ K W}^{-1}$  for copper and diamond heat-spreaders, respectively. Even though diamond turns out to be clearly superior to copper, the ratio of thermal resistances  $R_c/R_d = 1.9$  is significantly lower than expected from the thermal conductivity ratio of 4.5 for the two materials. The output-power characteristics plotted in Fig. 6.2 (d) support these results. The slope efficiency is equal for the two chips, indicating comparable loss channels in both devices. The thermal rollover, however, occurs at about a factor of two higher output power in the diamond-soldered VECSEL, confirming its superior performance as a heat-spreader.

### 6.2.2 Heat removal

Eventually, the heat has to be transferred into the heat-sink after it is distributed across the large area of a heat-spreader to keep the temperature of the device below its thermal rollover point. In a simple picture, the heat transport between two reservoirs increases linearly with the respective temperature difference. Therefore, the most intuitive way to enhance cooling is to increase the temperature gradient between the back-side of the device and the heat-sink. The standard cooling scheme involves four Peltier-elements, each capable to dissipate  $50 \text{ W}$ , transferring the heat to a water bath with  $T = 15 \text{ }^\circ\text{C}$ . Such

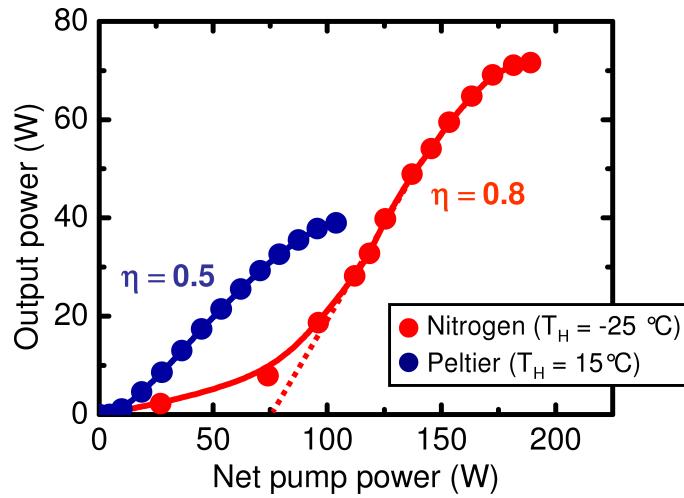


Figure 6.3: Output power as function of net pump power for two different cooling concepts: Peltier-elements (squares) and liquid nitrogen bath (circles). The heat-sink temperatures are  $15\text{ }^\circ\text{C}$  and  $-25\text{ }^\circ\text{C}$ , respectively.

Peltier-elements are easy to operate and yet still capable of removing a significant amount of heat. However, they reach their maximum cooling power for a zero temperature difference between the heat-sink and the water bath. Thus, the cooling efficiency decreases strongly for any heat-sink temperatures lower than  $15\text{ }^\circ\text{C}$ .

An alternative approach to overcome the restrictions of the Peltier-elements is to cool the heat-sink directly. The requirements of reaching low temperatures and simultaneously removing several hundreds of Watts in heat load are best met by liquid nitrogen. Hence, a liquid nitrogen bath connected directly to the heat-sink is used, capable of dissipating more than  $300\text{ W}$  determined by keeping the system at a stable temperature using electrically-driven heat elements. Figure 6.3 shows the output curves of the VECSEL device with Peltier elements and nitrogen cooling. The heat-sink temperatures are set to  $15\text{ }^\circ\text{C}$  and  $-25\text{ }^\circ\text{C}$ , respectively. In case of the nitrogen cooling the active area of the sample is kept above condensation temperature due to the dissipated heat from the pump beam. Any further temperature decrease beyond  $-25\text{ }^\circ\text{C}$  causes severe mechanical stress in the structure due to the thermal expansion, resulting in very probable damage of the device. A pump spot of about  $780\text{ }\mu\text{m}$  width is used for the experiment. The device reaches  $40\text{ W}$  of output power for the Peltier-cooled heat-sink with a slope efficiency of  $\eta = 0.5$  and a threshold power of about  $9\text{ W}$ . In case of nitrogen the thermal rollover is significantly delayed. A maximum output power of  $72\text{ W}$  is obtained, almost doubling the previous result. The threshold pump power and the relative slope efficiency are also increased due to the higher initial detuning between the gain medium and the sub-cavity at lower heat-sink temperature. The high power performance of the VECSEL is thus significantly improved by using the nitrogen cooling concept.

### 6.2.3 Power scaling

Heat management does not only rely on appropriate heat transfer solutions but also depends on the heat generation. In this last subsection the performance of the VECSEL device is studied under variations of the pump spot size, altering the density of the generated heat. Diamond heat-spreader and Peltier-cooling are used for reliable and more comfortable handling of the device.

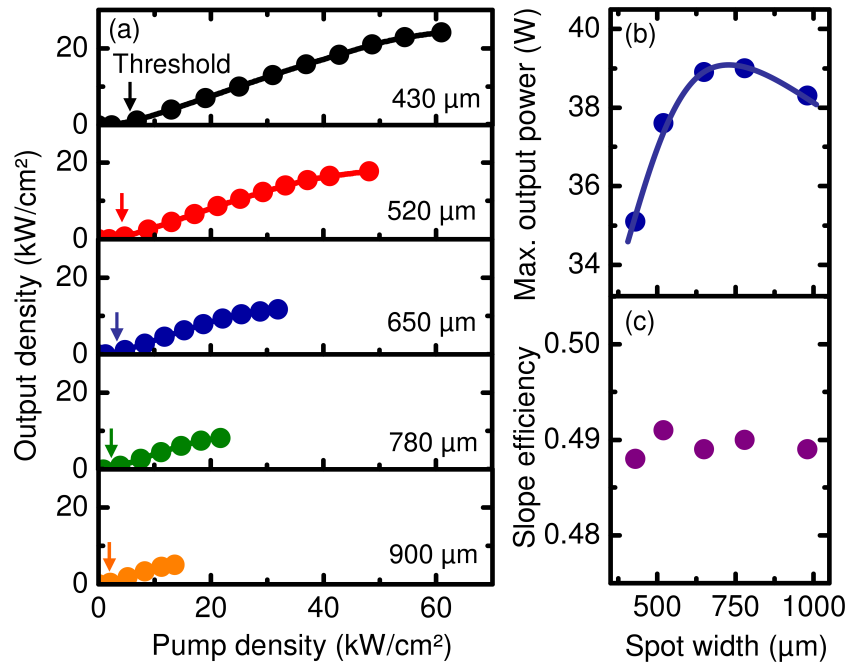


Figure 6.4: (a) Output density as function of the net pump density for spot sizes between  $430\ \mu\text{m}$  and  $900\ \mu\text{m}$ . Lasing threshold is marked by the arrows. Maximum output power and slope efficiency for different spot widths are shown in (b) and (c), respectively. Heat-sink temperature is set to  $15\ ^\circ\text{C}$ .

In Fig. 6.4(a), the output density is plotted as a function of the pump density for different spot sizes between  $430\ \mu\text{m}$  and  $900\ \mu\text{m}$ . The data clearly shows that the thermal roll-over occurs at much lower excitation densities for the large pump spots compared with the small spots. The laser is thus not power-scalable under these operation conditions. The maximum output power is still slightly increased for higher spot sizes, as it is shown in Fig. 6.4 (b). However, the difference of only 13 % for the spot widths between  $430\ \mu\text{m}$  and  $780\ \mu\text{m}$  is negligible compared to the factor of three, expected from power scaling. In addition, the slope efficiency remains constant at about 0.5, see Fig. 6.4 (c), confirming that no additional loss channels are introduced as the spot size is increased. Thus, it is clearly excluded that the inhomogeneity of the VECSEL chip is responsible for the observed decrease of the device performance. The spatial homogeneity of the device is further supported by the position-dependent measurements of the input-output



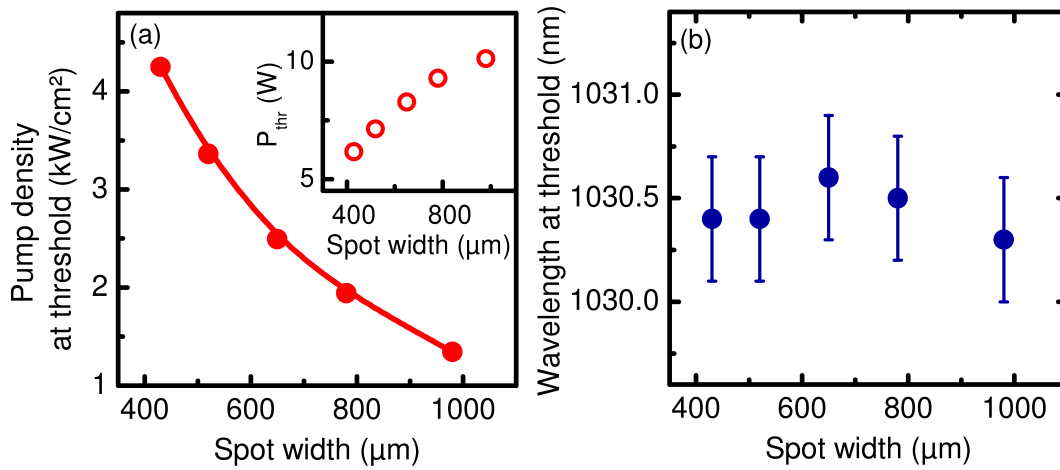


Figure 6.5: (a) Pump density at the lasing threshold as function of the spot width. The inset shows the absolute pump power. (b) Laser emission wavelength for different pump spots.

characteristics applying a small pump spot size of about  $300\ \mu\text{m}$  (not shown here). For better understanding of the observed reduced power-scalability, the threshold and emission wavelength dependence on the spot width is plotted in Fig. 6.5 (a) and (b), respectively. For a scalable device, one would usually expect the absolute pump power to increase and the pump density to remain constant as the spot size is increased. In the data, however, only the absolute pump power increases slightly as shown in the inset of Fig. 6.5 (a). Contrary to expectations, the power density at threshold decreases significantly. Also, the emission wavelength at threshold remains independent from the chosen spot width. Constant emission wavelength implies constant temperature inside the device. Therefore, the lasing activity occurs as soon as the VECSEL reaches a certain temperature, i.e., at a specific spectral position of the gain and the sub-cavity mode. Generally, the pump power at the lasing threshold is determined by the light amplification matching the cavity losses. In a VECSEL structure this is influenced not only by the magnitude of the material gain but also by the overlap with the sub-cavity mode. As mentioned above, the device is intentionally designed for operating in high power regime at increased temperatures. However, if the pump density and the temperature are low, the initial detuning between the gain and the cavity resonance leads only to a small overlap. On the other hand, a temperature increase inside the active structure lowers the detuning. Thus, a sufficient match of the gain spectrum and the sub-cavity mode occurs at a smaller pump density. Therefore, the experimental findings strongly indicate that a decrease in the pump density at threshold for large pump spots is due to the less effective heat removal, leading to temperature increase in the active area. The latter also leads to the thermal rollover at lower pump densities.



### 6.3 Study of spatial temperature distribution via PL spectroscopy

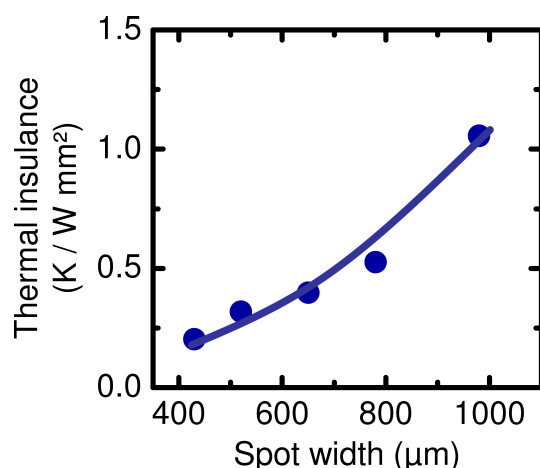


Figure 6.6: Thermal insulance, calculated by multiplying the thermal resistance with the active area, as function of the spot width.

To confirm the interpretation, the thermal properties of the VECSEL are studied as function of the spot size, similar to the analysis in the previous subsection 6.2.1. To compare the heat transfer through different areas, the so-called *thermal insulance* is investigated. The quantity is calculated by multiplying the thermal resistance with the pumped area and thus depends only on thermal properties of the VECSEL chip itself. Figure 6.6 shows the thermal insulance as function of different spot sizes. An increase by about a factor of five is found as the pump spot is increased from  $430\ \mu\text{m}$  to  $900\ \mu\text{m}$  in diameter. The efficiency of the heat transfer from the active area is thus significantly lower for large pump spots. To understand the decrease of cooling efficiency, spatially resolved temperature measurements are proposed.

### 6.3 Study of spatial temperature distribution via PL spectroscopy

To determine the temperature in the active area of the device, the spectrally and spatially resolved PL signal is measured. The experimental setup is shown schematically in Fig. 6.7. The PL emission from the active area is collected by a large aperture lens in a 4f-geometry. A single-mode fiber of about  $10\ \mu\text{m}$  core diameter mounted on a two-dimensional translation stage is used to scan the image plane. The emission signal is detected by an optical spectrum analyzer with a spectral resolution of  $0.3\ \text{nm}$ , thus providing a resolution of  $3\ \text{K}$  for the temperature estimation. For the calibration of the setup, the PL is measured as function of the spatial position on the chip at low power densities below the lasing threshold for a constant heat sink temperature. As previously discussed in section 2.2.3, the spectrum of the QW luminescence is determined by the optical modes

## 6 Vertical-external-cavity surface-emitting lasers for NIR applications

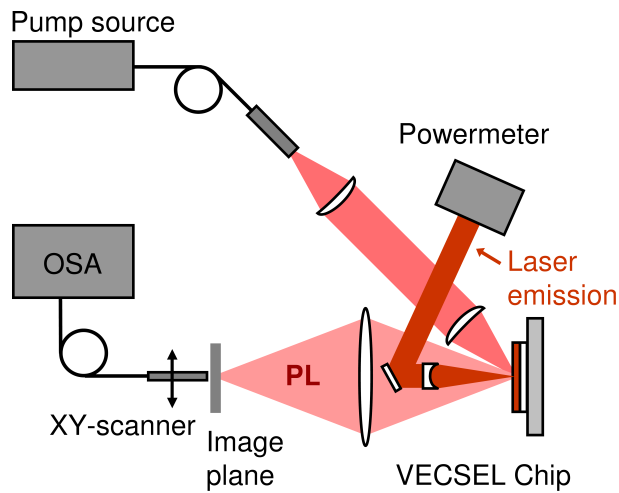


Figure 6.7: Experimental setup for the spatially resolved temperature measurement in the active area of the VECSEL device

of its surrounding dielectric structure, i.e., the sub-cavity resonance, in analogy to the laser emission, c.f. section 6.2.1. A typical temperature-induced shift of the PL maximum  $E_{PL}$  of about 0.1 nm/K [17, 185, 198] is measured as function of the heat sink temperature for an excitation intensity below lasing threshold. Thus, the lattice temperature is extracted from the spectral shift of the PL signal. The spatially resolved measurements of the temperature in the active region are then performed during the VECSEL operation, using the same optics as in the calibration measurement. An exemplary PL spectrum is shown in Fig. 6.8.

To investigate the lack of power scalability at well-defined experimental conditions, the role of the shape of the pump profile on the output characteristics is studied first. Different pump profiles are chosen at constant excitation power in the intermediate pump regime. The temperatures in the active region are shown in Fig. 6.9 as function of a lateral space coordinate for a super-Gaussian, the so-called "flat-top" (a), and a nearly Gaussian (b) pump spot profile, respectively. The pump profiles are represented by the grey areas. The corresponding fit curves by a super-Gaussian function  $I_{pump}(x) \propto \exp(-x^p)$  are shown by the solid lines. The values  $p$  obtained from the fit are 5 and 2 for the spots (a) and (b), respectively. The super-Gaussian pump profile yields 22 W output power and exhibits a relatively narrow temperature distribution. In comparison, the Gaussian profile provides only 4.2 W of the laser emission for the same pump intensity. Also, the temperature on the flank of the pump spot is much higher than for the super-Gaussian distribution. The additional heat is generated mostly in the weakly pumped area far from the center where the system does not reach the lasing threshold. The super-Gaussian profile provides a nearly homogeneous distribution of the incident pump light and is clearly superior in comparison to the Gaussian spot. Aside from the operation directly at the lasing threshold, this

### 6.3 Study of spatial temperature distribution via PL spectroscopy

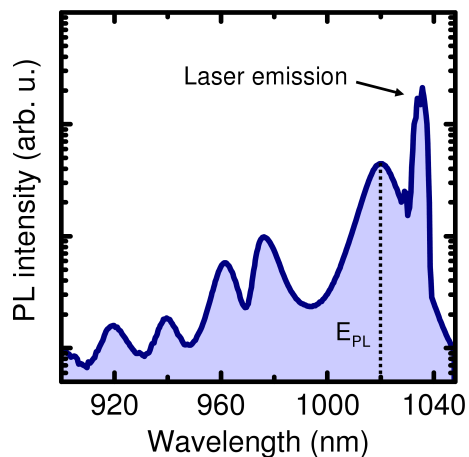


Figure 6.8: Exemplary PL spectrum measured during operation of the VECSEL above the lasing threshold.

conclusion is valid for all pump density regimes. Figure 6.9 (c) shows the output characteristic for the Gaussian and super-Gaussian pump profiles. Increased efficiency and significantly higher maximum output power are obtained for the super-Gaussian pump distribution.

Now, the thermal behavior of the VECSEL is studied for different pump spot sizes using the optimal spot profile. Figure 6.10 shows the temperature distribution in the lasing region at intermediate and high pump densities, the latter being just below the thermal roll-over of the laser. The corresponding pump spots of  $430\ \mu\text{m}$  and  $780\ \mu\text{m}$  FWHM are indicated by the grey areas in Fig. 6.10 (a) and (c), respectively. For both spot sizes, a temperature rise in the active region is observed as the pump density is increased. Whereas the temperature distribution is rather flat for the smaller spot, it is more peaked at the center of the larger pumped area.

These observations clearly show that the heat generated in the active area is not only transferred towards the heat sink, but also in the lateral directions, parallel to the surface. The center of the active region heats up first due to the less efficient heat removal in comparison to the borders of the active region. Interestingly, the laser roll-over occurs as soon as the temperature of  $(87 \pm 2)\ ^\circ\text{C}$  is reached in the center of the respective lasing region, independent of the spot size. For large pump spots, the three-dimensional heat transfer is strongly suppressed, leading to the thermal roll-over already at relatively low pump densities, c.f. Fig. 6.4. Thermal lensing effects from the thermal expansion of the chip surface and refractive index change in the active structure are negligible. The heating of the central region leads to a surface curvature of about 12 m radius which is insignificant compared to 10 cm radius of curvature of the cavity mirror. Additionally, the thermally induced change of the refractive index produces a weak focusing lens. The resulting refractive power of the laser cavity changes only slightly. Carefully choosing

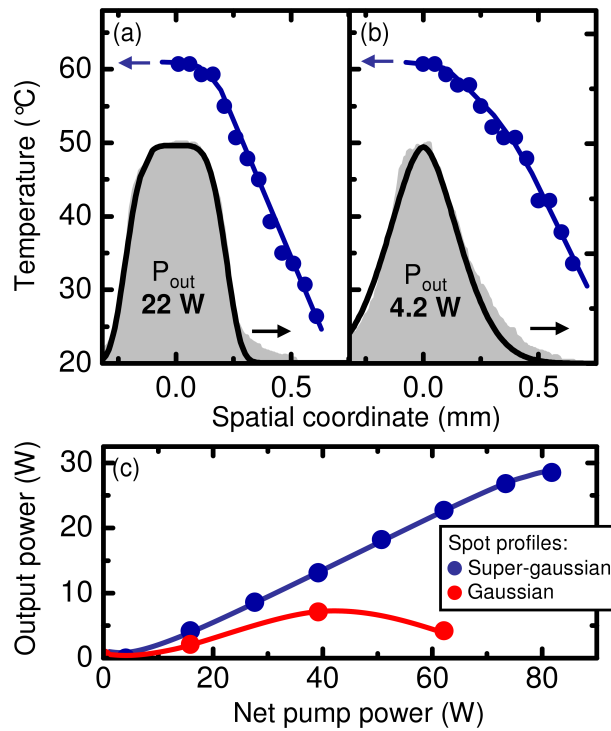


Figure 6.9: Temperature distribution in the active region of the VECSEL chip for a super-Gaussian (a) and a Gaussian (b) pump spots. Corresponding profiles are shown by the grey areas. The solid lines represent super-Gaussian fits with  $I_{pump}(x) \propto \exp(-x^p)$ . The FWHM of the pumped area is  $430 \mu\text{m}$  and the net pump power is set to 60 W. (c) Input-output characteristics of the laser for the super-Gaussian and Gaussian profiles.

the cavity length to 50 % of the curvature radius of the output coupler, the effect of the thermal lens on the laser cavity is minimized. Thus, the laser operation is not affected.

To support the interpretation, a numerical model is used to analyze the heat flow in the VECSEL structure. The simulations are performed by Dr. Maik Scheller in the group of Prof. Martin Koch at the Phillips-Universität Marburg. In this model, a 3 mm thick copper heat sink is assumed with constant temperature at the lower boundary controlled by the thermal electro cooling. The copper is connected by a  $1 \mu\text{m}$  layer of thermal grease to the diamond heat spreader. Between the diamond and the semiconductor device, a  $2.5 \mu\text{m}$  indium sheet is placed, taking into account the bonding process. Since the experiments are performed with nearly circular pump spots, a two-dimensional axial symmetry around the  $z$  axis is assumed. Furthermore, the simulations are based on the experimentally measured pump profiles. A commercial finite element solver, COMSOL, is used to perform the simulations. The results are shown in Fig. 6.10 (b) and (d). The temperature within the center of the pump spot rises nonlinearly with increasing pump area meaning that the same peak value in for the  $780 \mu\text{m}$  spot is reached already at a lower pump density. Therefore, in the case of larger pump areas the temperature contrast between spot center and

### 6.3 Study of spatial temperature distribution via PL spectroscopy

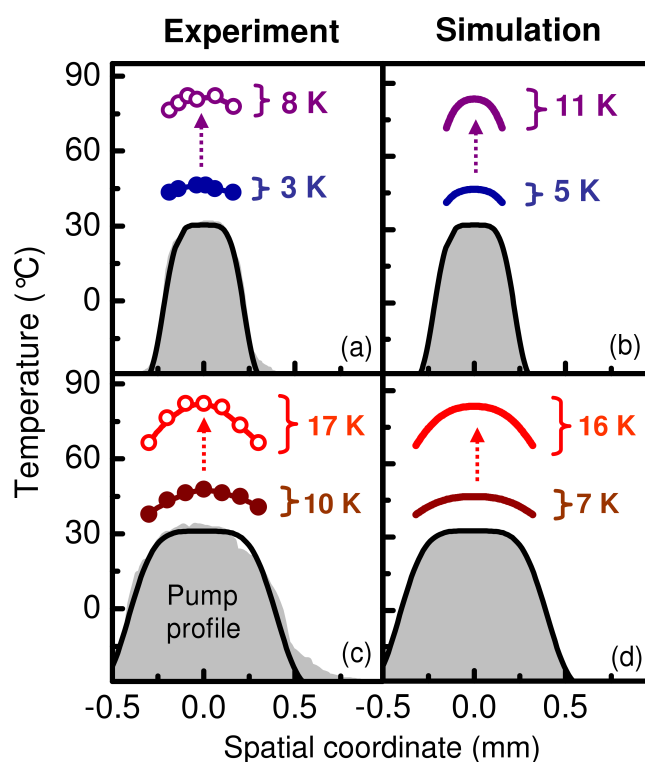


Figure 6.10: Temperature distribution in the active region for the pump spots with the FWHM of  $430\ \mu\text{m}$  (a) and  $780\ \mu\text{m}$  (c) at intermediate (full circles) and high (empty circles) pump densities; corresponding simulation results are plotted in (b) and (d), respectively. The numbers give the respective temperature drop across the FWHM of the pump profiles, shown as grey-shaded areas.

perimeter is higher. Altogether, an excellent agreement is obtained between the numerical simulation and the experiment.

In summary, thermal properties of a high-power 1040 nm VECSEL are studied experimentally investigating the generation, the distribution and the removal of excess heat. To optimize the heat-spreading in the device the behavior of a CVD diamond is compared to a copper plate, each soldered to a VECSEL chip. The diamond-bonded device turns out to be superior displaying an up to a factor of two higher output power and substantially lower thermal resistance. Additionally, the heat removal is addressed by applying liquid nitrogen cooling instead of the standard Peltier-cooling scheme. This alternative concept provides a large temperature gradient between the heat-sink and the heat-spreader leading to a significant increase of the laser output to more than 70 W of maximum power. In addition, the performance of a 1040 nm VECSEL is studied for various spatial profiles of the optical pump distribution via spatially resolved PL measurements. Input-output characteristics are monitored under simultaneous temperature tracking by measuring the spatially-resolved PL from the active region. The results clearly show that not only that

## *6 Vertical-external-cavity surface-emitting lasers for NIR applications*

the shape of the pump spot strongly influences the laser output but also that larger pump areas do not lead to the expected increase of the maximum power. As a consequence, the device is not power-scalable for pump spot sizes between  $430\ \mu\text{m}$  and  $780\ \mu\text{m}$  FWHM. Lateral heat flow is identified to be responsible for the observed behavior. The flow is strongly suppressed at high pump densities and large spot areas and leads to intrinsic limitations of the VECSEL performance.

## 7 Summary and conclusions

This last chapter gives a brief summary of the experimental findings and the resulting conclusions. In chapter 4, the influence of the carrier-carrier Coulomb scattering on the interaction between electrons and lattice-vibrations is studied. In the first part, an unambiguous experimental evidence for phonon-assisted plasma emission is presented, clearly confirming the predictions of the many-body theory. Characteristic signatures of exciton and plasma luminescence, supported by the quantitative analysis of the PL dynamics, are observed. As a main result, the emission at the excitonic PSB resonances can definitely not be considered as an evidence of the exciton population. The PL from electron-hole plasma can, indeed, strongly contribute or even dominate the PSBs. Both exciton- and plasma-dominated regimes are accessible by the specific choice of the excitation conditions.

In the second part of chapter 4, exciton-phonon interaction mechanisms in polar semiconductors CdS, CdSe, and ZnO are studied. The experimental results are compared to the calculations via microscopic many-body approach to identify the dominant scattering processes. Fröhlich coupling is found to govern the exciton-phonon interaction in CdS while deformation potential scattering turned out to be the dominant mechanism in ZnO, with both processes contributing about equally in ZnS. Particularly for ZnO, Fröhlich contributions are suppressed by the strong Coulomb-coupling of electrons and holes in excitons rendering deformation potential scattering the overall dominant mechanism responsible for the sideband emission. This result holds, even if the scattering between single electrons and optical phonons are dominated by the Fröhlich interaction in all studied cases due to the strong polarity of the respective materials. The conducted studies clearly show that Coulomb scattering strongly influences the interaction between charge carriers and lattice vibrations in a semiconductor as well as the resulting optical response. The obtained results, published in [199, 200], expand the traditional picture of the phonon-assisted emission, providing additional insight in the interpretation of the PSB spectroscopy.

The experiments discussed in chapter 5 are focused on the study of carrier dynamics in ZnO/(ZnMg)O heterostructures, (GaAs)Bi QWs, as well as the GaN quantum QWires. In case of the ZnO/(ZnMg)O, carrier localization is found to play a major role for the

## 7 Summary and conclusions

optical response of the (ZnMg)O layers as well as of the ZnO QWs. However, despite possible carrier trapping in the (ZnMg)O barriers, carrier relaxation into the ZnO QW occurred on an ultra-fast time-scale below 3 ps. This result is obtained by exploiting the build-up of screening of the internal electric fields for direct observation of carrier population inside the QW. Hence, carrier capture into the QW occurs on the same or even faster time-scale than the carrier-trapping processes within the barriers. In addition, the experimental study of recombination processes strongly indicates that radiative recombination dominates the PL dynamics at low temperatures in the homoepitaxially grown ZnO/(Zn<sub>0.9</sub>Mg<sub>0.1</sub>)O QW samples without the QCSE as well as in the ZnO/(Zn<sub>0.8</sub>Mg<sub>0.2</sub>)O QW samples with strong QCSE contributions. The overall results are rather encouraging regarding possible applications of the material. On the one hand, fast carrier capture into the QW combined with a potentially high quantum efficiency should be advantageous for the ZnO QW-based edge-emitters or surface-emitting lasers. On the other hand, carrier localization is favourable when LED applications are considered. Hence, even if there is still room for the optimization of the material quality as well as a need for p-doped ZnO samples, the ZnO/(ZnMg)O system appears highly capable for light-emitting applications in the UV spectral range. The envisioned subsequent studies are the non-linear absorption and gain measurements as well as the development of the optically pumped laser on the ZnO QW-basis, circumventing the issue of the p-doping. Part of this work is published in [135, 201].

In the second part of chapter 5, carrier localization dynamics in a Ga(AsBi) epitaxial layer are experimentally studied. Typical disorder-induced effects appeared in the TRPL and are attributed to the interplay between relaxation- and recombination-dominated processes. The experimental investigations are supported the kinetic Monte-Carlo simulations applying the two-scale approach taking into account alloy disorder as well as the Bi clusters. The comparison of the measured data with the simulations provided a complete set of the individual disorder parameters. Faster carrier hopping among localized sites with fluctuating alloy compositions is found, compared to a much slower carrier diffusion between the formation of Bi clusters. In addition, carrier capture into the cluster states occurs on an ultra-fast time-scale of about 5 ps. The overall results show that the two-scale disorder should always be taken into account when optical response of Ga(AsBi) is considered, at least at the current stage of the material development. In the near future, depending on the optimized growth as well as on the successful doping of (GaAs)Bi layers, the material system will have to prove its potential for NIR laser applications. Part of this work is published in [202, 203, 204].

In the third part of chapter 5, the PL emission from the quasi-1D GaN QWires is clearly identified and the evidence of a significant confinement effect is found. The estimated QWires diameters of several nm, smaller than the excitonic Bohr radius of GaN, are in a



good agreement to TEM data. Also, the optical response of the QWires does not show any indications of the internal electric fields perpendicular to the length of the QWires. The light-matter coupling in the GaN QWires is thus not inhibited by the charge separation effects. A further advantage is the comparably high stability of the overall PL intensity as well as the carrier lifetimes as function of the lattice temperature. Since the material system is still in development and the growth parameters are to be optimized, further studies of the structural as well as the optical properties should follow. However, this seems a rather encouraging task, since the QWires appear to be a promising playground for the basic research of quasi-1D semiconductors, offering various intriguing applications based on the well-developed, mature GaN technology.

In chapter 6, the thermal properties of a high-power NIR VECSEL are studied experimentally investigating the generation, the distribution and the removal of heat. The developed cooling concept provides a significant increase of the laser output to more than 70 W of maximum power from a single semiconductor chip. In addition, the input-output characteristics are monitored under simultaneous temperature tracking by measuring the spatially-resolved PL from the active region. The results clearly show that not only the shape of the pump spot strongly influenced the laser output but also that larger pump areas did not lead to the expected increase of the maximum power. As a consequence, the device is found to be not power-scalable for pump spot sizes larger than 400  $\mu\text{m}$  full-width-at-half-maximum (FWHM). Lateral heat flow is identified to be responsible for the observed behavior. The flow is strongly suppressed at high pump densities and large spot areas, leading to intrinsic limitations for the maximal output power of the VECSEL. Thus, additional sophisticated cooling concepts should be applied to enable even more efficient performance of the device. Still, in the present configuration, the VECSEL appears to be an excellent choice for frequency mixing and high-power applications. Part of this work is published in [205, 206, 196].



# Appendix

## 1 Photon density calculator

*Mathematica 6.0* script for the calculation of the photon densities during the excitation pulse at the sample surface. Main input parameters are the central wavelength as well as the time-averaged power of the incident laser, pump spot size, magnification of the image and the spectrometer entrance slit-width. The script calculates two-dimensional power density distribution and averages over the range of interest, defined by the imaging parameters.

$\text{nm} = 10^{-9}$ ;  $\mu\text{m} = 10^{-6}$ ;  $\text{MHz} = 10^6$ ;  $\text{mW} = 10^{-3}$ ;  $\text{cm} = 10^{-2}$ ;  $\text{eV} = 1.602 * 10^{-19}$ ;  
 $\text{fs} = 10^{-15}$ ;  $\text{ps} = 10^{-12}$ ;  $\text{ns} = 10^{-9}$ ;  $\text{kHz} = 10^3$ ;  
(\* SI units \*)

$\text{Rep} = 80\text{MHz}$ ; (\* repetition rate \*)

$t_{\text{pulse}} = 100\text{fs}$ ; (\* pulse length \*)

$\lambda = 290\text{nm}$ ; (\*wavelength\*)

$\text{FWHM}_{\text{spot}} = 30\mu\text{m}$ ; (\* pump spot \*)

$d_{\text{slit}} = 40\mu\text{m}$ ; (\* slit width spectrometer \*)

$P_{\text{cw}} = 0.001\text{mW}$ ; (\*time – integratedpower\*)

$T = 0.7$ ; (\* sample surface transmission \*)

$h\nu = \frac{1240\text{nm}}{\lambda}\text{eV}$

(\* photon energy \*)

$N_{\text{pulse}} = N \left[ T * P_{\text{cw}} * \frac{1}{\text{Rep} * h\nu} \right]$ ; (\* pulse photon number \*)

$r_{\text{eff}} = d_{\text{slit}} * \frac{1}{2} * \frac{1}{2}$ ; (\* effective detection width \*);

$2\pi * \int_0^{+\infty} \left( e^{-2 \frac{r^2}{(\text{FWHM}_{\text{spot}}/1.18)^2}} * r \right) dr$ ;

$\text{Int}[r\_] = e^{-2 \frac{r^2}{(\text{FWHM}_{\text{spot}}/1.18)^2}} * \frac{N_{\text{pulse}}}{2\pi * \int_0^{+\infty} \left( e^{-2 \frac{r^2}{(\text{FWHM}_{\text{spot}}/1.18)^2}} * r \right) dr}$ ;

(\*photonnumber[r]normalized\*)

$\text{stepFktA}[x\_]:= \text{If}[x \geq r_{\text{eff}}, 0, 1]$ ;

## Appendix

stepFktB[x\_]:=If[x ≥ -r<sub>eff</sub>, 1, 0];

A<sub>eff</sub> = ∫<sub>0</sub><sup>r<sub>eff</sub></sup> Int[r] \* 2π \* r dr;

App[r\_] =  $\left( \frac{1}{2\pi \int_0^{+\infty} \text{stepFktA}[r] * \text{stepFktB}[r] * r dr} \right) * \text{stepFktA}[r] * \text{stepFktB}[r] * A_{\text{eff}}$ ;

(\*averagepumppowerofApp =

avg.powerofIntwithin det.spot\*)

Plot[{Int[r \* μm] \* cm<sup>2</sup>, App[r \* μm] \* cm<sup>2</sup>}, {r, -100, 100},

PlotRange → {0, All},

AxesLabel → {"radius/um", "photon density / cm<sup>-2</sup>"}

Print["p<sub>cw</sub> = ", N[hv \* Rep \* 1/T \* App[0] \* cm<sup>2</sup>], " W/cm<sup>2</sup>"];

Print["p<sub>pulse</sub> = ", N[T \*  $\frac{hv}{t_{\text{pulse}}}$  \* App[0] \* cm<sup>2</sup>], " W/cm<sup>2</sup>"];

Print["N<sub>pulse</sub><sup>compl</sup> = ", N[N<sub>pulse</sub>]];

Print["E<sub>pulse</sub><sup>compl</sup> = ", N[N<sub>pulse</sub> \* hv], " J"];

Print["e<sub>pulse</sub><sup>det</sup> = ", N[App[0] \* hv \* cm<sup>2</sup>], " J/cm<sup>2</sup>"];

Print["(n<sup>2D</sup>)<sub>photons</sub> = ", (n<sup>2D</sup>)<sub>photons</sub> = N[App[0] \* cm<sup>2</sup>], " 1/cm<sup>2</sup>"];

L = 300nm(\* sample thickness \*);

α = 1 \* 10<sup>4</sup>cm<sup>-1</sup>(\*absorption\*);

Print["(n<sup>3D</sup>)<sub>avg</sub> = ", N[(n<sup>2D</sup>)<sub>photons</sub> \* (1 - e<sup>-α\*L</sup>) \*  $\frac{\text{cm}}{L}$ ], " 1/cm<sup>3</sup>"];

## 2 Decay-time extraction algorithm

*Mathematica 6.0* script for the extraction of long, i.e.,  $> 5$  ns, PL decay times from the intensity ratios between the "back-sweep" and PL peak short after the excitation. The input parameters are repetition rate of the pump laser as well as the rise- and the decay-time of the PL signal. The script simulates an exponentially decaying PL signal measured by the streak-camera in "synchro-scan" mode for the given parameters and calculates the "back-sweep"-to-PL-maximum ratio. The decay time is then adjusted to the experimentally measured value.

```

t0 = 0.5; (* t-offset *)
NPump = 4.5 * 1012; (* pump density *)
stufenFktA[x_] := If[x ≥ 0, 1, 0];
stufenFktB[x_] := If[x ≥ 0, 0, 1];
rep = 12.6;
Ninit = NPump * 0; (* initial fast nonrad. recombining carriers *)
τfd = 0.04; (* fast initial decay time *)

τd = 5.0; (* decay time in ns *)
τR = 0.005; (* rise-time *)

N0 = 0; (* residual carrier density at t = 0 *)
N02 = 0;
For[i = 0, i < 1000, i++, (* calculating N0 *)
N0 = N02;
InoBS[t_] = N0 *  $\frac{1}{\tau_d}$  * stufenFktB[t] +
stufenFktA[t] *  $\left( \left( \left( 1 - e^{-\frac{t}{\tau_R}} \right) * N_{Pump} + N_0 \right) * \frac{1}{\tau_d} * e^{-\frac{t}{\tau_d}} + \left( 1 - e^{-\frac{t}{\tau_R}} \right) * N_{init} * \frac{1}{\tau_{fd}} * e^{-\frac{t}{\tau_{fd}}} \right)$ ;
N02 = InoBS[rep] * τd
]; (* InoBS : real PL intensity without back-sweep,
only intrinsic saturation effect at t < 0 *)
IBS[t_] = InoBS[3.15] *  $e^{-\frac{(3.15-t)}{\tau_d}}$ ; (* only back-sweep *)
Ifull[t_] = IBS[t] + InoBS[t]; (* measured PL *)
Ifull[0 - t0] / Ifull[0.6 - t0]
Plot[{Ifull[t - t0] / Ifull[1.5 - t0]}, {t, 0, 2}, PlotRange → {0.0, All},
AxesLabel → {"Zeit / ns", "Ladungsträger-2D Dichte / cm2"}]
Clearall;

```



# Bibliography

- [1] R. Hall, G. Fenner, J. Kingsley, T. Soltys, and R. Carlson, "Coherent light emission from GaAs junctions," *Physical Review Letters* **9**, 366 (1962).
- [2] N. Holonyak and S. F. Bevacqua, "Coherent (visible) light emission from Ga(AsP) junctions," *Applied Physics Letters* **1**, 82 (1962).
- [3] J. C. Ion, *Laser processing of engineering materials: principle, procedures and industrial applications* (Elsevier Butterworth-Heinemann, 2005).
- [4] J. Singh, *Electronic and Optoelectronic Properties of Semiconductor Structures* (Cambridge University Press, 2003), 1st ed.
- [5] M. M. Rao, *Optical Communication* (Universities Press, 2000).
- [6] T. K. Hatwar and J. Spindler, "Development of white OLED technology for application in full-color displays and solid-state lighting," in "Luminescent materials and applications," , A. Kitai, ed. (John Wiley & Sons Ltd., 2008).
- [7] W. S. Boyle and G. E. Smith, "Charge coupled semiconductor devices," *Bell Sys. Tech. J.* **49**, 587 (1970).
- [8] [Http://www.nobelprize.org/nobel\\_prizes/physics/laureates/2009/](http://www.nobelprize.org/nobel_prizes/physics/laureates/2009/), "The Nobel Prize in Physics 2009," .
- [9] C. Klingshirn, *Semiconductor Optics* (Springer, Berlin Heidelberg New York, 2007), 2nd ed.
- [10] H. Haug and S. W. Koch, *Quantum theory of the optical and electronic properties of semiconductors* (World Scientific, Singapore, 2009), 5th ed.
- [11] T. Feldtmann, "Influence of phonons on semiconductor quantum emission," Ph.D. thesis, Philipps Universität Marburg (2009).
- [12] C. F. Klingshirn, B. K. Meyer, A. Waag, A. Hoffmann, and J. Geurts, *Zinc Oxide*, vol. 120 of *Springer Series in Materials Science* (Springer Berlin Heidelberg, Berlin, Heidelberg, 2010).
- [13] S. Nakamura, S. Pearton, and G. Fasol, *The blue laser diode: the complete story* (Springer, 2010).
- [14] K. Oe and H. Okamoto, "New semiconductor alloy GaAsB grown by metal organic vapor phase epitaxy," *Japanese Journal of Applied Physics* **37**, L1283 (1998).
- [15] S. Paul, J. B. Roy, and P. K. Basu, "Empirical expressions for the alloy composition and temperature dependence of the band gap and intrinsic carrier density in GaInAs," **69**, 827 (1991).

## Bibliography

- [16] M. Kuznetsov, F. Hakimi, R. Sprague, and A. Mooradian, "High-power ( $>0.5\text{W}$  cw) diode-pumped vertical-external-cavity surface-emitting semiconductor lasers with circular TEM<sub>00</sub> beams," *IEEE Phot. Techn. Lett.* **9**, 1063 (1997).
- [17] A. C. Tropper, H. D. Foreman, A. Garnache, K. G. Wilcox, and S. H. Hoogland, "Vertical-external-cavity semiconductor lasers," *Journal of Physics D: Applied Physics* **37**, R75 (2004).
- [18] L. Cerutti, A. Garnache, F. Genty, A. Ouvrard, and C. Alibert, "Low threshold, room temperature laser diode pumped Sb-based VECSEL emitting around 2.1 microns," *Electronics Letters* **39**, 290 (2003).
- [19] J. L. A. Chilla, "Blue and green optically pumped semiconductor lasers for display," in "Proceedings of SPIE," , vol. 5740 (SPIE, 2005), vol. 5740, p. 41.
- [20] M. Holm, D. Burns, A. Ferguson, and M. Dawson, "Actively stabilized single-frequency vertical-external-cavity AlGaAs laser," *IEEE Photonics Technology Letters* **11**, 1551 (1999).
- [21] A. Garnache, S. Hoogland, A. C. Tropper, I. Sagnes, G. Saint-Girons, and J. S. Roberts, "Sub-500-fs soliton-like pulse in a passively mode-locked broadband surface-emitting laser with 100 mW average power," *Applied Physics Letters* **80**, 3892 (2002).
- [22] S. Tixier, M. Adamcyk, T. Tiedje, S. Francoeur, A. Mascarenhas, P. Wei, and F. Schietekatte, "Molecular beam epitaxy growth of GaAsBi," *Applied Physics Letters* **82**, 2245 (2003).
- [23] S. Baranovskii, R. Eichmann, and P. Thomas, "Temperature-dependent exciton luminescence in quantum wells by computer simulation," *Physical Review B* **58**, 13081 (1998).
- [24] M. Kira, F. Jahnke, and S. Koch, "Microscopic Theory of Excitonic Signatures in Semiconductor Photoluminescence," *Physical Review Letters* **81**, 3263 (1998).
- [25] M. Kira, F. Jahnke, W. Hoyer, and S. Koch, "Quantum theory of spontaneous emission and coherent effects in semiconductor microstructures," *Progress in Quantum Electronics* **23**, 189 (1999).
- [26] M. Kira and S. W. Koch, "Microscopic theory of optical excitations, photoluminescence, and terahertz response in semiconductors," *The European Physical Journal D* **36**, 143 (2005).
- [27] N. Ashcroft and N. Mermin, *Solid State Physics* (Cengage Learning Emea, 1976).
- [28] C. Cohen-Tannoudji, B. Diu, and F. Laloe, *Quantum Mechanics* (Wiley-International, 2006), 1st ed.
- [29] M. Kira and S. Koch, "Many-body correlations and excitonic effects in semiconductor spectroscopy," *Progress in Quantum Electronics* **30**, 155 (2006).
- [30] S. Chatterjee, C. Ell, S. Mosor, G. Khitrova, H. Gibbs, W. Hoyer, M. Kira, S. Koch, J. Prineas, and H. Stolz, "Excitonic photoluminescence in semiconductor quantum wells: plasma versus excitons," *Physical Review Letters* **92**, 2 (2004).
- [31] N. Balkan, ed., *Hot electrons in semiconductors* (Clarendon Press, Oxford, 1998).



- [32] S. Arlt, U. Siegner, J. Kunde, F. Morier-Genoud, and U. Keller, “Ultrafast dephasing of continuum transitions in bulk semiconductors,” *Physical Review B* **59**, 14860 (1999).
- [33] R. A. Kaindl, M. A. Carnahan, D. Hägele, R. Lövenich, and D. S. Chemla, “Ultrafast terahertz probes of transient conducting and insulating phases in an electron-hole gas.” *Nature* **423**, 734–8 (2003).
- [34] M. Umlauff, J. Hoffmann, H. Kalt, W. Langbein, J. Hvam, M. Scholl, J. Söllner, M. Heuken, B. Jobst, and D. Hommel, “Direct observation of free-exciton thermalization in quantum-well structures,” *Physical Review B* **57**, 1390 (1998).
- [35] K. Kash and J. Shah, “Carrier energy relaxation in In<sub>0.53</sub>Ga<sub>0.47</sub>As determined from picosecond luminescence studies,” *Applied Physics Letters* **45**, 401 (1984).
- [36] K.-H. Hellwege, O. Madelung, M. Schulz, and H. Weiss, eds., *Landolt-Börnstein: Semiconductors* (Springer-Verlag Berlin / Heidelberg / New York, 1982).
- [37] H. Polland, W. Rühle, J. Kuhl, K. Ploog, K. Fujiwara, and T. Nakayama, “Nonequilibrium cooling of thermalized electrons and holes in GaAs/AlGaAs quantum wells,” *Physical Review B* **35**, 8273 (1987).
- [38] J. Shah, “Photoexcited hot LO phonons in GaAs,” *Solid State Communications* **8**, 1089 (1970).
- [39] S. Koch, T. Meier, F. Jahnke, and P. Thomas, “Microscopic theory of optical dephasing in semiconductors,” *Applied Physics A: Materials Science & Processing* **71**, 511 (2000).
- [40] K. Hantke, “Einfluß von Stickstoff auf die Photolumineszenz von metastabilen III-V-Nitriden K,” Ph.D. thesis (2005).
- [41] S. Rudin, T. Reinecke, and B. Segall, “Temperature-dependent exciton linewidths in semiconductors,” *Physical Review B* **42**, 11218 (1990).
- [42] H. Ibach and H. Lüth, *Festkörperphysik*, vol. 62 of *Springer-Lehrbuch* (Springer Berlin Heidelberg, Berlin, Heidelberg, 2009).
- [43] Y. Varshni, “Temperature dependence of the energy gap in semiconductors,” *Physica* **34**, 149 (1967).
- [44] J. Hader, J. V. Moloney, and S. W. Koch, “Suppression of carrier recombination in semiconductor lasers by phase-space filling,” *Applied Physics Letters* **87**, 201112 (2005).
- [45] L. Andreani, “Radiative lifetime of free excitons in quantum wells,” *Solid State Communications* **77**, 641 (1991).
- [46] G. Khitrova and H. M. Gibbs, “Nonlinear optics of normal-mode-coupling semiconductor microcavities,” *Reviews of Modern Physics* **71**, 1591 (1999).
- [47] J. Szczytko, L. Kappei, J. Berney, F. Morier-Genoud, M. Portella-Oberli, and B. Deveaud, “Determination of the exciton formation in quantum wells from time-resolved interband luminescence,” *Physical Review Letters* **93**, 13 (2004).
- [48] D. Oberhauser, K. H. Pantke, W. Langbein, V. G. Lyssenko, H. Kalt, J. M. Hvam, G. Weimann, and C. Klingshirn, “Coherent and incoherent exciton dynamics in AlGaAs/GaAs multiple quantum wells,” *Physica Status Solidi (b)* **173**, 53 (1992).

## Bibliography

- [49] P. Landsberg, *Recombination in semiconductors*, vol. 5 (Cambridge University Press, Cambridge, 1991).
- [50] K. Huang and A. Rhys, “Theory of light absorption and non-radiative transitions in F-centres,” *Proceedings of the Royal Society A: Mathematical, Physical and Engineering Sciences* **204**, 406 (1950).
- [51] H. Zhao and H. Kalt, “Energy-dependent Huang-Rhys factor of free excitons,” *Physical Review B* **68**, 125309 (2003).
- [52] C. Klingshirn, “The luminescence of ZnO under high one- and two-quantum excitation,” *Physica Status Solidi (b)* **71**, 547 (1975).
- [53] H. D. Sun, Y. Segawa, M. Kawasaki, A. Ohtomo, K. Tamura, and H. Koinuma, “Phonon replicas in ZnO/ZnMgO multiquantum wells,” *Journal of Applied Physics* **91**, 6457 (2002).
- [54] D. Hägele, R. Zimmermann, M. Oestreich, M. Hofmann, W. Rühle, B. Meyer, H. Amano, and I. Akasaki, “Cooling dynamics of excitons in GaN,” *Physical Review B* **59**, R7797 (1999).
- [55] S. Permogorov, “Optical emission due to exciton scattering by LO phonons in semiconductors,” in “Excitons,” E. I. Rashba and M. Sturge, eds. (North-Holland, Amsterdam, 1982).
- [56] T. Feldtmann, M. Kira, and S. W. Koch, “Phonon sidebands in semiconductor luminescence,” *Physica Status Solidi (b)* **246**, 332 (2009).
- [57] T. Feldtmann, M. Kira, and S. Koch, “Theoretical analysis of higher-order phonon sidebands in semiconductor luminescence spectra,” *Journal of Luminescence* **130**, 107 (2010).
- [58] H. Fröhlich, “Electrons in lattice fields,” *Advances in Physics* **3**, 325 (1954).
- [59] H. Haken, *Quantenfeldtheorie des Festkörpers* (Teubner, Stuttgart, 1973).
- [60] F. Giustino, M. L. Cohen, and S. G. Louie, “Small phonon contribution to the photoemission kink in the copper oxide superconductors.” *Nature* **452**, 975–8 (2008).
- [61] W. Harrison, “Scattering of electrons by lattice vibrations in nonpolar crystals,” *Physical Review* **104**, 1281 (1956).
- [62] D. Braun, W. Rühle, C. Trallero-Giner, and J. Collet, “Spectroscopic determination of the optical deformation-potential constant in semiconductors,” *Physical Review Letters* **67**, 2335 (1991).
- [63] K. Reimann, R. Kaindl, and M. Woerner, “Optical deformation-potential scattering of holes in multiple quantum well structures,” *Physical Review B* **65**, 045302 (2001).
- [64] P. Yu and M. Cardona, *Fundamentals of Semiconductors: Physics and Material Properties* (Springer-Verlag Berlin / Heidelberg / New York, 2005), 3rd ed.
- [65] W.-K. Hong, G. Jo, M. Choe, T. Lee, J. I. Sohn, and M. E. Welland, “Influence of surface structure on the phonon-assisted emission process in the ZnO nanowires grown on homoepitaxial films,” *Applied Physics Letters* **94**, 043103 (2009).

- [66] A. Minnaert, A. Silov, W. van der Vleuten, J. Haverkort, and J. Wolter, “Fröhlich interaction in InAs/GaAs self-assembled quantum dots,” *Physical Review B* **63**, 075303 (2001).
- [67] T. Itoh, M. Nishijima, A. Ekimov, C. Gourdon, A. Efros, and M. Rosen, “Polaron and exciton-phonon complexes in CuCl nanocrystals,” *Physical Review Letters* **74**, 1645 (1995).
- [68] C. Lange, N. S. Köster, S. Chatterjee, H. Sigg, D. Chrastina, G. Isella, H. von Känel, B. Kunert, and W. Stolz, “Comparison of ultrafast carrier thermalization in GaInAs and Ge quantum wells,” *Physical Review B* **81** (2010).
- [69] F. Bernardini, V. Fiorentini, and D. Vanderbilt, “Spontaneous polarization and piezoelectric constants of III-V nitrides,” *Physical Review B* **56**, R10024 (1997).
- [70] M. Leroux, N. Grandjean, M. Lügt, J. Massies, B. Gil, P. Lefebvre, and P. Bigenwald, “Quantum confined Stark effect due to built-in internal polarization fields in (Al,Ga)N/GaN quantum wells,” *Physical Review B* **58**, R13371 (1998).
- [71] D. Miller, D. Chemla, T. Damen, A. Gossard, W. Wiegmann, T. Wood, and C. Burrus, “Electric field dependence of optical absorption near the band gap of quantum-well structures,” *Physical Review B* **32**, 1043 (1985).
- [72] A. Hangleiter, F. Hitzel, S. Lahmann, and U. Rossow, “Composition dependence of polarization fields in GaInN/GaN quantum wells,” *Applied Physics Letters* **83**, 1169 (2003).
- [73] D. Turchinovich, B. S. Monozon, and P. U. Jepsen, “Role of dynamical screening in excitation kinetics of biased quantum wells: Nonlinear absorption and ultrabroadband terahertz emission,” *Journal of Applied Physics* **99**, 013510 (2006).
- [74] R. Huber, F. Tauser, A. Brodschelm, M. Bichler, G. Abstreiter, and A. Leitenstorfer, “How many-particle interactions develop after ultrafast excitation of an electron-hole plasma.” *Nature* **414**, 286–9 (2001).
- [75] E. Yablonovitch, “Inhibited spontaneous emission in solid-state physics and electronics,” *Physical Review Letters* **58**, 2059 (1987).
- [76] R. Slusher and C. Weisbuch, “Optical microcavities in condensed matter systems,” *Solid State Communications* **92**, 149 (1994).
- [77] E. Hecht, *Optics* (Addison Wesley, 2001), 4th ed.
- [78] M. Schafer, W. Hoyer, M. Kira, S. W. Koch, and J. V. Moloney, “Influence of dielectric environment on quantum-well luminescence spectra,” *Journal of the Optical Society of America B* **25**, 187 (2008).
- [79] N. S. Köster, K. Kolata, R. Woscholski, C. Lange, G. Isella, D. Chrastina, H. von Känel, and S. Chatterjee, “Giant dynamical Stark shift in germanium quantum wells,” *Applied Physics Letters* **98**, 161103 (2011).
- [80] D. Thomas and J. Hopfield, “Exciton spectrum of cadmium sulfide,” *Physical Review* **116**, 573 (1959).
- [81] D. Thomas, “The exciton spectrum of zinc oxide,” *Journal of Physics and Chemistry of Solids* **15**, 86 (1960).

## Bibliography

- [82] M. Cobet, C. Cobet, M. R. Wagner, N. Esser, C. Thomsen, and A. Hoffmann, "Polariton effects in the dielectric function of ZnO excitons obtained by ellipsometry," *Applied Physics Letters* **96**, 031904 (2010).
- [83] J. Gutowski, N. Presser, and I. Broser, "Acceptor-exciton complexes in ZnO: A comprehensive analysis of their electronic states by high-resolution magneto-optics and excitation spectroscopy," *Physical Review B* **38**, 9746 (1988).
- [84] D. Reynolds, D. Look, B. Jogai, C. Litton, G. Cantwell, and W. Harsch, "Valence-band ordering in ZnO," *Physical Review B* **60**, 2340 (1999).
- [85] G. Mak and W. Rühle, "Femtosecond carrier dynamics in Ge measured by a luminescence up-conversion technique and near-band-edge infrared excitation," *Physical Review B* **52**, R11584 (1995).
- [86] S. Takeoka, M. Fujii, S. Hayashi, and K. Yamamoto, "Decay dynamics of near-infrared photoluminescence from Ge nanocrystals," *Applied Physics Letters* **74**, 1558 (1999).
- [87] V. Härle, H. Bolay, E. Lux, P. Michler, A. Moritz, T. Forner, A. Hangleiter, and F. Scholz, "Indirect-band-gap transition in strained GaInAs/InP quantum-well structures," *Journal of Applied Physics* **75**, 5067 (1994).
- [88] S. Fukatsu, "Quantitative analysis of light emission from SiGe quantum wells," *Journal of Crystal Growth* **157**, 1 (1995).
- [89] Y. Zhang, "Behavior of nitrogen impurities in III-V semiconductors," *Journal of Luminescence* **85**, 247–260 (2000).
- [90] W. Shan, K. M. Yu, W. Walukiewicz, J. Wu, J. W. Ager, and E. E. Haller, "Band anticrossing in dilute nitrides," *Journal of Physics: Condensed Matter* **16**, S3355 (2004).
- [91] J. Haynes, "Experimental proof of the existence of a new electronic complex in Silicon," *Physical Review Letters* **4**, 361 (1960).
- [92] G. Perna, V. Capozzi, and M. Ambrico, "Structural properties and photoluminescence study of CdSe/Si epilayers deposited by laser ablation," *Journal of Applied Physics* **83**, 3337 (1998).
- [93] A. Toropov, O. Nekrutkina, T. Shubina, T. Gruber, C. Kirchner, A. Waag, K. Karlsson, P. Holtz, and B. Monemar, "Temperature-dependent exciton polariton photoluminescence in ZnO films," *Physical Review B* **69**, 1 (2004).
- [94] E. Bogardus and H. Bebb, "Bound-exciton, free-exciton, band-acceptor, donor-acceptor, and Auger recombination in GaAs," *Physical Review* **176**, 993 (1968).
- [95] E. Calleja, F. J. Sánchez, D. Basak, M. A. Sánchez-García, E. Muñoz, I. Izpura, F. Calle, J. M. G. Tijero, J. L. Sánchez-Rojas, B. Beaumont, P. Lorenzini, and P. Gibart, "Yellow luminescence and related deep states in undoped GaN," *Physical Review B* **55**, 4689 (1997).
- [96] A. van Dijken, E. Meulenlamp, D. Vanmaekelbergh, and A. Meijerink, "The luminescence of nanocrystalline ZnO particles: the mechanism of the ultraviolet and visible emission," *Journal of Luminescence* **87-89**, 454 (2000).

- [97] W. Stadler, D. Hofmann, H. Alt, T. Muschik, B. Meyer, E. Weigel, G. Müller-Vogt, M. Salk, E. Rupp, and K. Benz, "Optical investigations of defects in Cd<sub>1-x</sub>Zn<sub>x</sub>Te," *Physical Review B* **51**, 10619 (1995).
- [98] B. Guo, Z. R. Qiu, and K. S. Wong, "Intensity dependence and transient dynamics of donor-acceptor pair recombination in ZnO thin films grown on (001) silicon," *Applied Physics Letters* **82**, 2290 (2003).
- [99] Y. J. Ding, J. V. D. Veliadis, and J. B. Khurgin, "Nonradiative recombination and saturation of traps in multiple intrinsic quantum wells," *Journal of Applied Physics* **75**, 1727 (1994).
- [100] W. Shockley and W. Read, "Statistics of the recombinations of holes and electrons," *Physical Review* **87**, 835 (1952).
- [101] R. Westphaling, "Photoluminescence quantum efficiency and dynamics in ZnSeTe and CdSSe mixed crystals," *Journal of Luminescence* **72-74**, 980 (1997).
- [102] T. Fleck, M. Schmidt, and C. Klingshirn, "Absolute external luminescence quantum efficiency of GaAs/Al<sub>0.3</sub>Ga<sub>0.7</sub>As multiple quantum wells," *Physica Status Solidi (a)* **198**, 248 (2003).
- [103] D. P. Popescu, P. G. Eliseev, A. Stintz, and K. J. Malloy, "Temperature dependence of the photoluminescence emission from InAs quantum dots in a strained GaInAs quantum well," *Semiconductor Science and Technology* **19**, 33 (2004).
- [104] D. Ouadjaout and Y. Marfaing, "Localized excitons in II-VI semiconductor alloys: Density-of-states model and photoluminescence line-shape analysis," *Physical Review B* **41**, 12096 (1990).
- [105] A. Ait\_ouali, R. Y.-F. Yip, J. L. Brebner, and R. A. Masut, "Strain relaxation and exciton localization effects on the Stokes shift in InAsP/InP multiple quantum wells," *Journal of Applied Physics* **83**, 3153 (1998).
- [106] O. Rubel, W. Stolz, and S. D. Baranovskii, "Spectral dependence of the photoluminescence decay in disordered semiconductors," *Applied Physics Letters* **91**, 021903 (2007).
- [107] T. Niebling, O. Rubel, W. Heimbrodt, W. Stolz, S. D. Baranovskii, P. J. Klar, and J. F. Geisz, "Spectral and time dependences of the energy transfer of bound optical excitations in GaP(N)," *Journal of Physics: Condensed Matter* **20**, 015217 (2008).
- [108] M. Oueslati, M. Zouaghi, M. Pistol, L. Samuelson, H. Grimmeiss, and M. Balkanski, "Photoluminescence study of localization effects induced by the fluctuating random alloy potential in indirect band-gap GaAsP," *Physical Review B* **32**, 8220 (1985).
- [109] J. Li, K. B. Nam, J. Y. Lin, and H. X. Jiang, "Optical and electrical properties of Al-rich AlGaIn alloys," *Applied Physics Letters* **79**, 3245 (2001).
- [110] K. Hantke, J. D. Heber, S. Chatterjee, P. J. Klar, K. Volz, W. Stolz, W. W. Ruhle, A. Polimeni, and M. Capizzi, "Carrier relaxation dynamics in annealed and hydrogenated GaInNAs/GaAs quantum wells," *Applied Physics Letters* **87**, 252111 (2005).
- [111] O. Rubel, S. Baranovskii, K. Hantke, B. Kunert, W. Ruhle, P. Thomas, K. Volz, and W. Stolz, "Kinetic effects in recombination of optical excitations in disordered quantum heterostructures: Theory and experiment," *Journal of Luminescence* **127**, 285 (2007).

## Bibliography

- [112] A. Miller and E. Abrahams, "Impurity conduction at low concentrations," *Physical Review* **120**, 745 (1960).
- [113] O. Rubel, M. Galluppi, S. D. Baranovskii, K. Volz, L. Geelhaar, H. Riechert, P. Thomas, and W. Stolz, "Quantitative description of disorder parameters in (GaIn)(NAs) quantum wells from the temperature-dependent photoluminescence spectroscopy," *Journal of Applied Physics* **98**, 063518 (2005).
- [114] C. Wagner, "Hopping von Exzitonen in ungeordneten Halbleiterstrukturen und Halbleiternanokristallen," Ph.D. thesis (2011).
- [115] R. Stanley, J. Hegarty, R. Fischer, J. Feldmann, E. Göbel, R. Feldman, and R. Austin, "Hot-exciton relaxation in CdZnTe/ZnTe multiple quantum wells," *Physical Review Letters* **67**, 128 (1991).
- [116] J. Collet, H. Kalt, L. Dang, J. Cibert, K. Saminadayar, and S. Tatarenko, "Relaxation of excitons in coherently strained CdTe/ZnTe quantum wells," *Physical Review B* **43**, 6843 (1991).
- [117] D. Kovalev, B. Averboukh, D. Volm, B. Meyer, H. Amano, and I. Akasaki, "Free exciton emission in GaN," *Physical Review B* **54**, 2518 (1996).
- [118] C. a la Guillaume, J.-M. Debever, and F. Salvan, "Radiative recombination in highly excited CdS," *Physical Review* **177**, 567 (1969).
- [119] P. Wiesner and U. Heim, "Dynamics of exciton-polariton recombination in CdS," *Physical Review B* **11**, 3071 (1975).
- [120] P. Yu and C. Hermann, "Excitation spectroscopies of impurities in CdSe," *Physical Review B* **23**, 4097 (1981).
- [121] C. Litton, D. Reynolds, T. Collins, and Y. Park, "Exciton-LO-phonon interaction and the anti-Stokes emission line in CdS," *Physical Review Letters* **25**, 1619 (1970).
- [122] S. Prabhu, A. Vengurlekar, and J. Shah, "Picosecond-luminescence study of exciton formation dynamics in CdSe," *Physical Review B* **53**, R10465 (1996).
- [123] W. Pötz and P. Vogl, "Theory of optical-phonon deformation potentials in tetrahedral semiconductors," *Physical Review B* **24**, 2025 (1981).
- [124] S.-H. Park and S.-L. Chuang, "Comparison of zinc-blende and wurtzite GaN semiconductors with spontaneous polarization and piezoelectric field effects," *Journal of Applied Physics* **87**, 353 (2000).
- [125] U. Özgür, Y. I. Alivov, C. Liu, A. Teke, M. A. Reshchikov, S. Dogan, V. Avrutin, S.-J. Cho, and H. Morkoç, "A comprehensive review of ZnO materials and devices," *Journal of Applied Physics* **98**, 041301 (2005).
- [126] C. Klingshirn, J. Fallert, H. Zhou, J. Sartor, C. Thiele, F. Maier-Flaig, D. Schneider, and H. Kalt, "65 years of ZnO research - old and very recent results," *Physica Status Solidi (b)* **247**, 1424 (2010).
- [127] A. K. Sharma, J. Narayan, J. F. Muth, C. W. Teng, C. Jin, A. Kvit, R. M. Kolbas, and O. W. Holland, "Optical and structural properties of epitaxial MgZnO alloys," *Applied Physics Letters* **75**, 3327 (1999).



- [128] T. Makino, C. H. Chia, N. T. Tuan, H. D. Sun, Y. Segawa, M. Kawasaki, A. Ohtomo, K. Tamura, and H. Koinuma, "Room-temperature luminescence of excitons in ZnO/(MgZn)O multiple quantum wells on lattice-matched substrates," *Applied Physics Letters* **77**, 975 (2000).
- [129] W. I. Park, G.-C. Yi, and H. M. Jang, "Metalorganic vapor-phase epitaxial growth and photoluminescent properties of ZnMgO thin films," *Applied Physics Letters* **79**, 2022 (2001).
- [130] A. Bakin, A. El-Shaer, A. C. Mofor, M. Al-Suleiman, E. Schlenker, and A. Waag, "ZnMgO-ZnO quantum wells embedded in ZnO nanopillars: Towards realisation of nano-LEDs," *Physica Status Solidi (c)* **4**, 158 (2007).
- [131] T. V. Shubina, a. a. Toropov, O. G. Lublinskaya, P. S. Kopev, S. V. Ivanov, A. El-Shaer, M. Al-Suleiman, A. Bakin, A. Waag, A. Voinilovich, E. V. Lutsenko, G. P. Yablonskii, J. P. Bergman, G. Pozina, and B. Monemar, "Recombination dynamics and lasing in ZnO/ZnMgO single quantum well structures," *Applied Physics Letters* **91**, 201104 (2007).
- [132] S.-M. Li, B.-J. Kwon, H.-S. Kwack, L.-H. Jin, Y.-H. Cho, Y.-S. Park, M.-S. Han, and Y.-S. Park, "Optical transition dynamics in ZnO/ZnMgO multiple quantum well structures with different well widths grown on ZnO substrates," *Journal of Applied Physics* **107**, 033513 (2010).
- [133] J. Zippel, M. Stölzel, A. Müller, G. Benndorf, M. Lorenz, H. Hochmuth, and M. Grundmann, "Electronic coupling in ZnO/Mg ZnO double quantum wells grown by pulsed-laser deposition," *Physica Status Solidi (b)* **247**, 398 (2010).
- [134] T. A. Wassner, B. Laumer, S. Maier, A. Laufer, B. K. Meyer, M. Stutzmann, and M. Eickhoff, "Optical properties and structural characteristics of ZnMgO grown by plasma assisted molecular beam epitaxy," *Journal of Applied Physics* **105**, 023505 (2009).
- [135] B. Laumer, T. A. Wassner, F. Schuster, M. Stutzmann, J. Schörmann, M. Rohnke, A. Chernikov, V. Bornwasser, M. Koch, S. Chatterjee, and M. Eickhoff, "Exciton confinement in homo- and heteroepitaxial ZnO/ZnMgO quantum wells with  $x < 0.1$ ," *Journal of Applied Physics* **110**, 093513 (2011).
- [136] J. F. Muth, R. M. Kolbas, A. K. Sharma, S. Oktyabrsky, and J. Narayan, "Excitonic structure and absorption coefficient measurements of ZnO single crystal epitaxial films deposited by pulsed laser deposition," *Journal of Applied Physics* **85**, 7884 (1999).
- [137] A. Ohtomo, M. Kawasaki, T. Koida, K. Masubuchi, H. Koinuma, Y. Sakurai, Y. Yoshida, T. Yasuda, and Y. Segawa, "MgZnO as a II-VI widegap semiconductor alloy," *Applied Physics Letters* **72**, 2466 (1998).
- [138] S. Heitsch, G. Zimmermann, D. Fritsch, C. Sturm, R. Schmidt-Grund, C. Schulz, H. Hochmuth, D. Spemann, G. Benndorf, B. Rheinländer, T. Nobis, M. Lorenz, and M. Grundmann, "Luminescence and surface properties of MgZnO thin films grown by pulsed laser deposition," *Journal of Applied Physics* **101**, 083521 (2007).
- [139] B. K. Meyer, H. Alves, D. M. Hofmann, W. Kriegseis, D. Forster, F. Bertram, J. Christen, A. Hoffmann, M. Straßburg, M. Dworzak, U. Haboeck, and a. V. Rodina, "Bound exciton and donor-acceptor pair recombinations in ZnO," *Physica Status Solidi (b)* **241**, 231 (2004).

## Bibliography

- [140] A. Müller, M. Stölzel, C. Dietrich, G. Benndorf, M. Lorenz, and M. Grundmann, "Origin of the near-band-edge luminescence in MgZnO alloys," *Journal of Applied Physics* **107**, 013704 (2010).
- [141] B. Bansal, V. K. Dixit, V. Venkataraman, and H. L. Bhat, "Alloying induced degradation of the absorption edge of InAsSb," *Applied Physics Letters* **90**, 101905 (2007).
- [142] C. Gourdon and P. Lavallard, "Exciton transfer between localized states in CdSSe alloys," *Physica Status Solidi (b)* **153**, 641 (1989).
- [143] C. Morhain, T. Bretagnon, P. Lefebvre, X. Tang, P. Valvin, T. Guillet, B. Gil, T. Taliercio, M. Teisseire-Doninelli, B. Vinter, and C. Deparis, "Internal electric field in wurtzite ZnO/ZnMgO quantum wells," *Physical Review B* **72**, 2 (2005).
- [144] H. D. Sun, T. Makino, N. T. Tuan, Y. Segawa, M. Kawasaki, A. Ohtomo, K. Tamura, and H. Koinuma, "Temperature dependence of excitonic absorption spectra in ZnO/ZnMgO multi-quantum wells grown on lattice-matched substrates," *Applied Physics Letters* **78**, 2464 (2001).
- [145] S.-H. Park and D. Ahn, "Spontaneous and piezoelectric polarization effects in wurtzite ZnO/MgZnO quantum well lasers," *Applied Physics Letters* **87**, 253509 (2005).
- [146] S. Francoeur, M.-J. Seong, A. Mascarenhas, S. Tixier, M. Adamcyk, and T. Tiedje, "Band gap of GaAsBi,  $0 < x < 3.6\%$ ," *Applied Physics Letters* **82**, 3874 (2003).
- [147] S. Imhof, C. Bückers, A. Thränhardt, J. Hader, J. V. Moloney, and S. Koch, "Microscopic theory of the optical properties of Ga(AsBi)/GaAs quantum wells," **23**, 125009 (2008).
- [148] W. Huang, K. Oe, G. Feng, and M. Yoshimoto, "Molecular-beam epitaxy and characteristics of GaNAsBi," *Journal of Applied Physics* **98**, 053505 (2005).
- [149] K. Alberi, O. D. Dubon, W. Walukiewicz, K. M. Yu, K. Bertulis, and A. Krotkus, "Valence band anticrossing in GaBiAs," *Applied Physics Letters* **91**, 051909 (2007).
- [150] A. Mascarenhas, R. Kini, Y. Zhang, R. France, and A. Ptak, "Comparison of the dilute bismide and nitride alloys GaAsBi and GaAsN," *Physica Status Solidi (b)* **246**, 504 (2009).
- [151] A. Janotti, S.-H. Wei, and S. Zhang, "Theoretical study of the effects of isovalent co-alloying of Bi and N in GaAs," *Physical Review B* **65**, 115203 (2002).
- [152] X. Lu, D. a. Beaton, R. B. Lewis, T. Tiedje, and Y. Zhang, "Composition dependence of photoluminescence of GaAsBi alloys," *Applied Physics Letters* **95**, 041903 (2009).
- [153] G. B. Stringfellow, *Organometallic Vapor-Phase Epitaxy: Theory and Practice* (Academic Press, 1999), 2nd ed.
- [154] K. Kazlauskas, G. Tamulaitis, A. Zukauskas, M. A. Khan, J. W. Yang, J. Zhang, G. Simin, M. S. Shur, and R. Gaska, "Double-scaled potential profile in a group-III nitride alloy revealed by Monte Carlo simulation of exciton hopping," *Applied Physics Letters* **83**, 3722 (2003).
- [155] C. Karcher, K. Jandieri, B. Kunert, R. Fritz, M. Zimprich, K. Volz, W. Stolz, F. Gebhard, S. Baranovskii, and W. Heimbrodt, "Peculiarities of the photoluminescence of metastable Ga(N,As,P)/GaP quantum well structures," *Physical Review B* **82**, 245309 (2010).



- [156] S. Francoeur, S. Tixier, E. Young, T. Tiedje, and A. Mascarenhas, "Bi isoelectronic impurities in GaAs," *Physical Review B* **77**, 1 (2008).
- [157] S. Yoon, M. J. Seong, B. Fluegel, A. Mascarenhas, S. Tixier, and T. Tiedje, "Photogenerated plasmons in GaAsBi," *Applied Physics Letters* **91**, 082101 (2007).
- [158] C. Metzner, K. Schrüfer, U. Wieser, M. Lubert, M. Kneissl, and G. Döhler, "Disorder effects on luminescence in delta-doped n-i-p-i superlattices," *Physical Review B* **51**, 5106 (1995).
- [159] M. Kozhevnikov, B. Ashkinadze, E. Cohen, and A. Ron, "LO-phonon sideband photoluminescence in pure GaAs," *Solid State Communications* **106**, 73 (1998).
- [160] M. Kozhevnikov, B. Ashkinadze, E. Cohen, and A. Ron, "LO phonon sideband photoluminescence in pure GaAs and GaAs/AlGaAs QWs," *Journal of Luminescence* **72-74**, 312 (1997).
- [161] G. Ciatto, E. Young, F. Glas, J. Chen, R. Mori, and T. Tiedje, "Spatial correlation between Bi atoms in dilute GaAsBi: From random distribution to Bi pairing and clustering," *Physical Review B* **78**, 1 (2008).
- [162] R. A. Mair, J. Y. Lin, H. X. Jiang, E. D. Jones, A. A. Allerman, and S. R. Kurtz, "Time-resolved photoluminescence studies of InGaAsN," *Applied Physics Letters* **76**, 188 (2000).
- [163] S. Strite and H. Morkoc, "GaN, AlN, and InN: A review," *J. Vac. Sci. Technol. B* **10**, 1237 (1992).
- [164] S. J. Pearton, B. S. Kang, S. Kim, F. Ren, B. P. Gila, C. R. Abernathy, J. Lin, and S. N. G. Chu, "GaN-based diodes and transistors for chemical, gas, biological and pressure sensing," *Journal of Physics: Condensed Matter* **16**, R961 (2004).
- [165] X. W. Zhang and J. B. Xia, "Optical properties of GaN wurtzite quantum wires," *Journal of Physics: Condensed Matter* **18**, 3107 (2006).
- [166] B. Amstatt, J. Renard, C. Bougerol, E. Bellet-Amalric, B. Gayral, and B. Daudin, "Growth of m-plane GaN quantum wires and quantum dots on m-plane 6H-SiC," *Journal of Applied Physics* **102**, 074913 (2007).
- [167] R. Dwiliski, R. Doradzinski, J. Garczyski, L. Sierzputowski, B. J. M., and M. Kasminska, "Exciton photo-luminescence of GaN bulk crystals grown by the AMMONO method," *Materials Science and Engineering B* **50**, 46 (1997).
- [168] F. Furtmayr, M. Vilemeyer, M. Stutzmann, A. Laufer, B. K. Meyer, and M. Eickhoff, "Optical properties of Si- and Mg-doped gallium nitride nanowires grown by plasma-assisted molecular beam epitaxy," *Journal of Applied Physics* **104**, 074309 (2008).
- [169] C. Adelman, E. Sarigiannidou, D. Jalabert, Y. Hori, J.-L. Rouviere, B. Daudin, S. Fanget, C. Bru-Chevallier, T. Shibata, and M. Tanaka, "Growth and optical properties of GaN/AlN quantum wells," *Applied Physics Letters* **82**, 4154 (2003).
- [170] J. Renard, R. Songmuang, G. Tourbot, C. Bougerol, B. Daudin, and B. Gayral, "Evidence for quantum-confined Stark effect in GaN/AlN quantum dots in nanowires," *Physical Review B* **80**, 121305(R) (2009).

## Bibliography

- [171] F. Furtmayr, J. Teubert, P. Becker, S. Conesa-Boj, J. R. Morante, A. Chernikov, S. Schäfer, S. Chatterjee, J. Arbiol, and M. Eickhoff, "Carrier confinement in GaN/AlGaIn nanowire heterostructures ( $0 < x < 1$ )," *Physical Review B* **84**, 205303 (2011).
- [172] M. E. Levinshtein, S. L. Rumyantsev, and S. S. Shur, *Properties of advanced semiconductor materials: GaN, AlN, InN, BN, SiC, SiGe* (Wiley-Interscience, 2001), 1st ed.
- [173] H. Lobentanzer, H.-J. Polland, W. W. Rühle, W. Stolz, and K. Ploog, "Cooling of hot carriers in GaInAs," *Applied Physics Letters* **51**, 673 (1987).
- [174] J. Coleman, "Strained-layer quantum well heterostructure lasers," *Thin Solid Films* **216**, 68 (1992).
- [175] P. Michler, A. Lohner, W. W. Rühle, and G. Reiner, "Transient pulse response of InGaAs/GaAs microcavity lasers," *Applied Physics Letters* **66**, 1599 (1995).
- [176] Y. Goldberg and N. Schmidt, *Handbook Series on Semiconductor Parameters* (World Scientific, London, 1999).
- [177] C. Lange, S. Chatterjee, C. Schlichenmaier, A. Thränhardt, S. W. Koch, W. W. Rühle, J. Hader, J. V. Moloney, G. Khitrova, and H. M. Gibbs, "Transient gain spectroscopy of (GaIn)As quantum wells: Experiment and microscopic analysis," *Applied Physics Letters* **90**, 251102 (2007).
- [178] M. A. Holm, D. Burns, P. Cusumano, A. I. Ferguson, and M. D. Dawson, "High-power diode-pumped AlGaAs surface-emitting laser," *Applied Optics* **38**, 5781 (1999).
- [179] S. Smith, J.-M. Hopkins, J. Hastie, D. Burns, S. Calvez, M. Dawson, T. Jouhti, J. Kontinen, and M. Pessa, "Diamond-microchip GaInNAs vertical external-cavity surface-emitting laser operating CW at 1315 nm," *Electronics Letters* **40**, 935 (2004).
- [180] W. Diehl, P. Brick, S. Chatterjee, S. Horst, K. Hantke, W. W. Rühle, W. Stolz, A. Thränhardt, and S. W. Koch, "Dynamic behavior of 1040 nm semiconductor disk lasers on a nanosecond time scale," *Applied Physics Letters* **90**, 241102 (2007).
- [181] N. Schulz, M. Rattunde, C. Ritzenthaler, B. Rösener, C. Manz, K. Köhler, J. Wagner, and U. Brauch, "Resonant optical in-well pumping of an (AlGaIn)(AsSb)-based vertical-external-cavity surface-emitting laser emitting at 2.35 microns," *Applied Physics Letters* **91**, 091113 (2007).
- [182] T. D. Raymond, W. J. Alford, M. H. Crawford, and A. A. Allerman, "Intracavity frequency doubling of a diode-pumped external-cavity surface-emitting semiconductor laser," *Optics Letters* **24**, 1127 (1999).
- [183] J. Lee, S. Lee, T. Kim, and Y. Park, "7 W high-efficiency continuous-wave green light generation by intracavity frequency doubling of an end-pumped vertical external-cavity surface emitting semiconductor laser," *Applied Physics Letters* **89**, 241107 (2006).
- [184] Y. Kaneda, J. M. Yarborough, L. Li, N. Peyghambarian, L. Fan, C. Hessenius, M. Fallahi, J. Hader, J. V. Moloney, Y. Honda, M. Nishioka, Y. Shimizu, K. Miyazono, H. Shimatani, M. Yoshimura, Y. Mori, Y. Kitaoka, and T. Sasaki, "Continuous-wave all-solid-state 244 nm deep-ultraviolet laser source by fourth-harmonic generation of an optically pumped semiconductor laser using CsLiB<sub>6</sub>O<sub>10</sub> in an external resonator," *Optics Letters* **33**, 1705 (2008).

- [185] S. Calvez, J. Hastie, M. Guina, O. Okhotnikov, and M. Dawson, "Semiconductor disk lasers for the generation of visible and ultraviolet radiation," *Laser & Photonics Review* **3**, 407 (2009).
- [186] S. Hoogland, S. Dhanjal, A. Tropper, J. Roberts, R. Haring, R. Paschotta, F. Morier-Genoud, and U. Keller, "Passively mode-locked diode-pumped surface-emitting semiconductor laser," *IEEE Photonics Technology Letters* **12**, 1135 (2000).
- [187] R. Haring, M. Paschotta, A. Aschwanden, E. Gini, F. Morier-Genoud, and U. Keller, "High-power passively mode-locked semiconductor lasers," *IEEE Journal of Quantum Electronics* **38**, 1268 (2002).
- [188] W. Zhang, A. McDonald, T. Ackemann, E. Riis, and G. McConnell, "Femtosecond synchronously in-well pumped vertical-external-cavity surface-emitting laser," *Optics Express* **18**, 187 (2009).
- [189] A. Siegman, *Lasers* (Herndon, VA: Univ. Science Books, 1986).
- [190] J. Moloney, J. Hader, and S. Koch, "Quantum design of semiconductor active materials: laser and amplifier applications," *Laser & Photonics Review* **1**, 24 (2007).
- [191] S. Lutgen, T. Albrecht, P. Brick, W. Reill, J. Luft, and W. Späth, "8-W high-efficiency continuous-wave semiconductor disk laser at 1000 nm," *Applied Physics Letters* **82**, 3620 (2003).
- [192] J. L. A. Chilla, *High-power optically pumped semiconductor lasers* (SPIE, 2004).
- [193] A. Maclean, A. Kemp, and D. Burn, "Power-scaling of a 1060nm semiconductor disk laser with a diamond heatspreader," *Conf. on Lasers and Electro-Optics*, San Jose p. JThA10 (2008).
- [194] W. J. Alford, T. D. Raymond, and A. A. Allerman, "High power and good beam quality at 980 nm from a vertical external-cavity surface-emitting laser," *Journal of the Optical Society of America B* **19**, 663 (2002).
- [195] A. J. Maclean, R. B. Birch, P. W. Roth, A. J. Kemp, and D. Burns, "Limits on efficiency and power scaling in semiconductor disk lasers with diamond heatspreaders," *Journal of the Optical Society of America B* **26**, 2228 (2009).
- [196] T.-L. Wang, Y. Kaneda, J. M. Yarborough, J. Hader, J. V. Moloney, A. Chernikov, S. Chatterjee, S. W. Koch, B. Kunert, and W. Stolz, "High-power optically pumped semiconductor laser at 1040 nm," *IEEE Photonics Technology Letters* **22**, 661 (2010).
- [197] E. Kühn, A. Thränhardt, C. Bückers, S. W. Koch, J. Hader, and J. V. Moloney, "Numerical study of the influence of an antireflection coating on the operating properties of vertical-external-cavity surface-emitting lasers," *Journal of Applied Physics* **106**, 063105 (2009).
- [198] C. Bückers, E. Kühn, C. Schlichenmaier, S. Imhof, A. Thränhardt, J. Hader, J. V. Moloney, O. Rubel, W. Zhang, T. Ackemann, and S. W. Koch, "Quantum modeling of semiconductor gain materials and vertical-external-cavity surface-emitting laser systems," *Physica Status Solidi (b)* p. 789 (2010).

- [199] A. Chernikov, V. Bornwasser, M. Koch, S. Chatterjee, C. N. Böttge, T. Feldtmann, M. Kira, T. A. Wassner, S. Lautenschläger, B. K. Meyer, and S. W. Koch, "Phonon-assisted luminescence in polar semiconductors - Fröhlich coupling versus deformation potential scattering," *Physical Review B*, accepted for publication (2011).
- [200] A. Chernikov, T. Feldtmann, S. Chatterjee, M. Koch, M. Kira, and S. W. Koch, "Time-resolved phonon-sideband spectroscopy," *Solid State Communications* **150**, 1733 (2010).
- [201] A. Chernikov, S. Horst, M. Koch, K. Volz, S. Chatterjee, S. Koch, T. Wassner, B. Laumer, and M. Eickhoff, "Investigation of carrier dynamics in ZnMgO by time-resolved photoluminescence," *Journal of Luminescence* **130**, 2256 (2010).
- [202] S. Imhof, C. Wagner, A. Thränhardt, A. Chernikov, M. Koch, N. S. Köster, S. Chatterjee, S. W. Koch, O. Rubel, X. Lu, S. R. Johnson, D. A. Beaton, and T. Tiedje, "Luminescence dynamics in Ga(AsBi)," *Applied Physics Letters* **98**, 161104 (2011).
- [203] S. Imhof, C. Wagner, A. Chernikov, M. Koch, K. Kolata, N. S. Köster, S. Chatterjee, S. W. Koch, X. Lu, S. R. Johnson, D. A. Beaton, T. Tiedje, O. Rubel, and A. Thränhardt, "Evidence of two disorder scales in Ga(AsBi)," *Physica Status Solidi (b)* **248**, 851 (2011).
- [204] S. Imhof, A. Thränhardt, A. Chernikov, M. Koch, N. S. Köster, K. Kolata, S. Chatterjee, S. W. Koch, X. Lu, S. R. Johnson, D. a. Beaton, T. Tiedje, and O. Rubel, "Clustering effects in Ga(AsBi)," *Applied Physics Letters* **96**, 131115 (2010).
- [205] A. Chernikov, J. Herrmann, M. Koch, B. Kunert, W. Stolz, S. Chatterjee, S. W. Koch, T.-L. Wang, Y. Kaneda, J. M. Yarborough, J. Hader, and J. V. Moloney, "Heat management in high-power vertical-external-cavity surface-emitting lasers," *IEEE Journal of Selected Topics in Quantum Electronics* **17**, 1772 (2011).
- [206] A. Chernikov, J. Herrmann, M. Scheller, M. Koch, B. Kunert, W. Stolz, S. Chatterjee, S. W. Koch, T. L. Wang, Y. Kaneda, J. M. Yarborough, J. Hader, and J. V. Moloney, "Influence of the spatial pump distribution on the performance of high power vertical-external-cavity surface-emitting lasers," *Applied Physics Letters* **97**, 191110 (2010).

# Wissenschaftlicher Werdegang

Alexej A. Chernikov

geboren am 17. November 1982 in Sankt-Petersburg (Russland)

2003 Abitur am Humboldt-Gymnasium Bad Homburg

2003 - 2008 Studium der Physik an der Philipps-Universität Marburg (Diplom)

seit 2008 Promotion an der Philipps-Universität Marburg, Fachbereich Physik, AG Experimentelle Halbleiterphysik bei Prof. Dr. Martin Koch

## Originalveröffentlichungen

- [1] A. Chernikov, V. Bornwasser, M. Koch, S. Chatterjee, C. N. Böttge, T. Feldtmann, M. Kira, T. A. Wassner, S. Lautenschläger, B. K. Meyer, and S. W. Koch, "Phonon-assisted luminescence in polar semiconductors - Fröhlich coupling versus deformation potential scattering", *Physical Review B*, accepted for publication (2011).
- [2] E. Gatti, E. Grilli, M. Guzzi, D. Chrastina, G. Isella, A. Chernikov, V. Bornwasser, N. S. Köster, R. Woscholski, M. Koch, and S. Chatterjee, "Photoluminescence and ultra-fast intra-subband relaxation in Ge/SiGe multiple quantum wells" *Physical Review B*, accepted for publication (2011).
- [3] A. Chernikov, M. Koch, B. Laumer, T. A. Wassner, M. Eickhoff, S. W. Koch, and S. Chatterjee, "Intra-excitonic relaxation dynamics in ZnO", *Applied Physics Letters* **99**, 231910 (2011).
- [4] F. Furtmayr, J. Teubert, P. Becker, S. Conesa-Boj, J. R. Morante, A. Chernikov, S. Schäfer, S. Chatterjee, J. Arbiol, and M. Eickhoff, "Carrier confinement in GaN/AlGaN nanowire heterostructures", *Physical Review B* **84**, 205303 (2011).
- [5] B. Laumer, T. Wassner, F. Schuster, M. Stutzmann, J. Schörmann, M. Rohnke, A. Chernikov, V. Bornwasser, M. Koch, S. Chatterjee, and M. Eickhoff, "Exciton confinement in homo- and heteroepitaxial ZnO/ZnMgO quantum wells with  $x < 0.1$ ", *Journal of Applied Physics*, **84**, 093513 (2011).
- [6] E. Gatti, A. Giorgioni, E. Grilli, A. Chernikov, S. Chatterjee, D. Chrastina, G. Isella, and M. Guzzi, "Photoluminescence decay of direct and indirect transitions in Ge/SiGe multiple quantum wells", *Journal of Applied Physics*, accepted for publication (2011).

- [7] A. Chernikov, J. Herrmann, M. Koch, B. Kunert, W. Stolz, S. Chatterjee, S. W. Koch, T.-L. Wang, Y. Kaneda, J. M. Yarborough, J. Hader, and J. V. Moloney, "Heat management in high-power vertical-external-cavity surface-emitting lasers, *IEEE Journal of Selected Topics in Quantum Electronics* **17**, 1772 (2011).
- [8] S. Imhof, C. Wagner, A. Thränhardt, A. Chernikov, M. Koch, N. S. Köster, S. Chatterjee, S. W. Koch, O. Rubel, X. Lu, S. R. Johnson, D. A. Beaton, and T. Tiedje, "Luminescence dynamics in Ga(AsBi)", *Applied Physics Letters* **98**, 161104 (2011).
- [9] A. Chernikov, S. Horst, T. Waitz, M. Tiemann, and S. Chatterjee, "Photoluminescence properties of ordered mesoporous ZnO", *The Journal of Physical Chemistry C* **115**, 1375 (2011).
- [10] S. Imhof, C. Wagner, A. Chernikov, M. Koch, K. Kolata, N. S. Köster, S. Chatterjee, S. W. Koch, X. Lu, S. R. Johnson, D. A. Beaton, T. Tiedje, O. Rubel, and A. Thränhardt, "Evidence of two disorder scales in Ga(AsBi)", *Physica Status Solidi (b)* **248**, 851 (2011).
- [11] A. Chernikov, C. N. Böttge, T. Feldtmann, S. Chatterjee, M. Koch, M. Kira, and S. W. Koch, "Plasma-related phonon-sideband emission in semiconductors", *Physica Status Solidi (c)* **8**, 1129 (2011).
- [12] A. Chernikov, S. Horst, M. Koch, K. Volz, S. Chatterjee, S. W. Koch, T. A. Wassner, B. Laumer, and M. Eickhoff, "Carrier dynamics in (ZnMg)O alloy materials", *Physica Status Solidi (c)* **8**, 1149 (2011).
- [13] A. Chernikov, J. Herrmann, M. Scheller, M. Koch, B. Kunert, W. Stolz, S. Chatterjee, S. W. Koch, T. L. Wang, Y. Kaneda, J. M. Yarborough, J. Hader, and J. V. Moloney, "Influence of the spatial pump distribution on the performance of high power vertical-external-cavity surface-emitting lasers", *Applied Physics Letters* **97**, 191110 (2010).
- [14] A. Chernikov, T. Feldtmann, S. Chatterjee, M. Koch, M. Kira, and S. W. Koch, "Time-resolved phonon-sideband spectroscopy", *Solid State Communications* **150**, 1733 (2010).
- [15] A. Chernikov, S. Horst, M. Koch, K. Volz, S. Chatterjee, S. Koch, T. Wassner, B. Laumer, and M. Eickhoff, "Investigation of carrier dynamics in ZnMgO by time-resolved photoluminescence", *Journal of Luminescence* **130**, 2256 (2010).
- [16] A. Chernikov, S. Chatterjee, M. Koch, C. Bückers, S. W. Koch, S. Imhof, A. Thränhardt, X. Lu, S. R. Johnson, D. A. Beaton, and T. Tiedje, "Optical spectroscopy of Bi containing semiconductors", in "Conference on Lasers and Electro-Optics", JWA94(2010).
- [17] S. Imhof, A. Thränhardt, A. Chernikov, M. Koch, N. S. Köster, K. Kolata, S. Chatterjee, S. W. Koch, X. Lu, S. R. Johnson, D. A. Beaton, T. Tiedje, and O. Rubel, "Clustering effects in Ga(AsBi)", *Applied Physics Letters* **96**, 131115 (2010).

- [18] A. Chernikov, S. Horst, S. W. Koch, S. Chatterjee, W. W. Rühle, J. Sweet, B. C. Richards, J. Hendrickson, G. Khitrova, H. M. Gibbs, D. Litvinov, D. Gerthsen, and M. Wegener, "Polarization conservation and dephasing in InAs quantum dot ensembles", in Proc. SPIE, 75971R (2010),
- [19] T.-L. Wang, Y. Kaneda, J. M. Yarborough, J. Hader, J. V. Moloney, A. Chernikov, S. Chatterjee, S. W. Koch, B. Kunert, and W. Stolz, "High-power optically pumped semiconductor laser at 1040 nm", IEEE Photonics Technology Letters **22**, 661 (2010).
- [20] S. Jankowski, S. Horst, A. Chernikov, S. Chatterjee, and W. Heimbrodt, "Energy transfer processes in ZnSe/(Zn,Mn)Se double quantum wells", Physical Review B **80**, 155315 (2009).
- [21] A. Chernikov, S. Horst, S. W. Koch, S. Chatterjee, W. W. Rühle, J. Sweet, B. Richards, J. Hendrickson, G. Khitrova, and H. M. Gibbs, "Intra-dot relaxation and dephasing rates from time-resolved photoluminescence from InAs quantum dot ensembles", Solid State Communications **149**, 1485 (2009).
- [22] M. Schwalm, S. Horst, A. Chernikov, W. W. Rühle, S. Lautenschläger, P. J. Klar, B. K. Meyer, T. Waitz, M. Tiemann, and S. Chatterjee, "Time-resolved photoluminescence study of mesoporous ZnO nanostructures", Physica Status Solidi (c) **6**, 542 (2009).



# Danksagung

An dieser Stelle möchte ich allen von Herzen danken, die mich in der Zeit meiner Promotion und bei der Entstehung dieser Arbeit unterstützt und begleitet haben:

- Prof. Dr. Martin Koch, für die Aufnahme in die Arbeitsgruppe sowie für die Möglichkeit und die Freiheit spannende Physik zu machen
- PD. Dr. Sangam Chatterjee für seine langjährige Betreuung, interessante, hitzige Diskussionen, rettende "Deus-ex-machina"-Auftritte im Labor, Mama-Qualitäten, Gummibärchen-Flatrate und eine vage Aussicht auf eine "Drive-through"-Eisdiele inklusive
- Prof. Dr. Stephan W. Koch für seine Zeit, seine Geduld und so manchen guten Ratschlag, den man mit der Zeit um so mehr zu schätzen weiß
- Prof. Dr. Wolfgang W. Rühle für die Möglichkeit ihn jederzeit mit Fragen über die zeitaufgelöste PL-Spektroskopie zu belästigen
- Meinen Studenten, Jens Herrmann, Verena Bornwasser und Sören Schäfer für ihre unermüdliche Laboreinsätze, wissbegierige Fragen und die schönen Daten
- Meinen Gefährten, insbesondere Michael Drexler, Benjamin Ewers, Swantje Horst, Tilmann Jung, Kolja Kolata, Kapil Koli, Niko Köster, Bjorn Metzger, Khaled Shakfa, Ricardo Scott, Matthias Stecher, Ajanth Velauthapillai und der ganzen AG Halbleiterphysik für die warme Arbeitsatmosphäre, so manchen lebenswichtigen Labortipp, spannende Physikdebatten und natürlich für die ganz besonderen Freitag-Nachmittage
- Den elektronischen und feinmechanischen Werkstätten für das "Auf-der-Grundlage-einer-Serviettenskizze-was-richtig-tolles-Bauen" und für die magische Gabe, Weihnachten mehrmals im Jahr stattfinden zu lassen
- Rüdiger Rink für jegliche Hilfe mit eigenwilligen Geräten und für die Fähigkeit aus jedem Entwurf zu entlocken, was man wirklich will aber es noch nicht weiß
- Anne Ehlers und Annegret Webel für ihre Arbeit, gezieltes und hilfreiches Nachfragen und auch für ihr Verständnis
- Allen Kollegen und Kollaborateuren (ich weiß, das Wort ist etwas eingefärbt...), ohne die viele der Arbeiten niemals entstanden wären, für die interessanten Diskussionen und für ihre Geduld den Ausblick "über den Tellerrand" leichter und angenehmer zu gestalten
- Meinen Freunden und meiner WG für die Unterstützung und Ablenkung sowie das gelungene Vortäuschen der Interesse für meine Arbeit im speziellen und für die Physik im allgemeinen.

Besonders möchte ich meinen Eltern danken, die in allen Lebenslagen immer hinter mir standen und mir das alles selbstlos ermöglicht haben. Bolschoje vam Spasibo, Aljoscha.